

Abstract

Circuit Quantum Electrodynamics

David Isaac Schuster

2007

This thesis describes the development of circuit quantum electrodynamics (QED), architecture for studying quantum information and quantum optics. In circuit QED a superconducting qubit acting as an artificial atom is electrostatically coupled to a 1D transmission line resonator. The large effective dipole moment of the qubit and high energy density of the resonator allowed this system to reach the strong coupling limit of cavity QED for the first time in a solid-state system. Spectroscopic investigations explore effects of different regimes of cavity QED observing physics such as the vacuum Rabi mode splitting, and the AC Stark effect. These cavity QED effects are used to control and measure the qubit state, while protecting it from radiative decay. The qubit can also be used to measure and control the cavity state, as shown by experiments detecting and generating single photons. This thesis will describe the theoretical framework, implementation, and measurements of the circuit QED system.

Circuit Quantum Electrodynamics

A Dissertation

Presented to the Faculty of the Graduate School

of

Yale University

in Candidacy for the Degree of

Doctor of Philosophy

by

David Isaac Schuster

Dissertation Director: Professor Robert J. Schoelkopf

May 2007

©2007 by David Schuster.

All rights reserved.

Acknowledgements

I would first like to thank my advisor Rob Schoelkopf. He gave me the freedom to explore an amazing world of quantum physics, while his guidance prevented me from ever feeling lost in all of its complexity. He taught me what it means to be a scientist, and the importance of eliminating ground loops. I will always remember our late night brainstorming sessions, and his willingness to suspend more critical demands to provide advice. Most of all I thank him for creating RSL and giving me the opportunity to participate.

I have been fortunate to work with many amazing people in the course of this research. In particular, most of the work presented in this thesis was the joint effort of Andreas Wallraff and myself. His influence on me runs deep extending from small things like my (near fanatical) use of mathematica and my much improved graphics design skills to the way I now approach experimental questions. More importantly, Andreas has become one of my closest friends. More recent work, presented in sections 4.3, 8.3.1, and 9.3, related to the “Transmon” was performed with my evil twin, Andrew Houck. His scientific abilities are matched only by his unbounded enthusiasm, and hopefully the former is as contagious as his excitement. I thank Alexandre Blais and Jay Gambetta for teaching me everything I know about cavity QED and quantum measurement. Their patience exceeds even Andrew’s optimism. I also owe a great debt to Luigi Frunzio for teaching me everything I know about the dark arts of fabrication.

Steve Girvin has an uncanny ability to make tangible connections between theory and experiment, while simultaneously telling a hilarious story. Similarly, I often found myself emerging from Michel Devoret’s office with new understanding of a question much deeper than the one with which I had entered. Dan Prober is to be thanked not only for his direct role in helping to convince me to come to Yale, serving on my committee, and advising me throughout my time here, but also for helping to build such an amazing community on the 4th floor.

My lab mates have made graduate school the best of times, providing help, camaraderie, and close

friendship. All of my friends from graduate, undergraduate, and high school have provided invaluable support. I would especially like to thank my roommate(s) Matt and Sam for their tolerance and friendship.

Most importantly I would like to thank my family, who have encouraged my curiosity and provided me with unending love. Finally, I thank Carol who helped me to grow as a person as well as a scientist.

Contents

1	Introduction	18
1.1	Quantum Computation	18
1.2	Cavity Quantum Electrodynamics	21
1.3	Quantum Circuits	26
1.4	Circuit Quantum Electrodynamics	29
1.5	Thesis Overview	32
2	Cavity Quantum Electrodynamics	34
2.1	Dispersive Limit	37
2.2	Strong Dispersive Interactions	41
3	Cavity QED with Superconducting Circuits	45
3.1	Transmission Line Cavities	45
3.1.1	The LCR Oscillator	46
3.1.2	Transmission Line as Series of LC Circuits	47
3.1.3	Capacitively Coupled LCR Resonator	50
3.1.4	Capacitively Coupled Transmission Line Resonator	51
3.1.5	Coplanar Waveguide Cavities	53
3.1.6	Kinetic Inductance	55
3.1.7	Intrinsic Resonator Losses	56
3.1.8	Quantization of the LC Oscillator	60
3.2	Cooper Pair Box	61
3.2.1	Charge Basis	61
3.2.2	Phase Basis	65

CONTENTS	4
3.2.3 Split CPB	66
3.3 Coupling CPB to Cavity	68
3.3.1 Comparison with Traditional Cavity QED	71
3.4 Measurement Theory	73
3.4.1 Quantum Non-Demolition Measurements	73
3.4.2 Mapping Qubit State onto Cavity State	73
3.4.3 Distinguishing Cavity States	75
3.4.4 Small Phase Shift Limit	77
3.4.5 Optimizing SNR	78
4 Decoherence in the Cooper Pair Box	82
4.1 Relaxation and Heating	82
4.1.1 Voltage Noise	83
4.1.2 Voltage Noise Inside a Cavity	85
4.1.3 Material Loss	89
4.1.4 Dipole Radiation	91
4.2 Dephasing	92
4.2.1 Charge Noise	95
4.2.2 Flux Noise	100
4.2.3 Critical Current/Josephson Energy $1/f$ Noise	101
4.2.4 E_C Noise	102
4.2.5 Summary of Cooper pair box decoherence	102
4.3 Transmon	103
4.3.1 Charge Dispersion	103
4.3.2 Anharmonicity	105
4.3.3 Transmon as a Josephson Oscillator	108
4.3.4 Transmon for Circuit QED	111
4.3.5 Other Sources of Decoherence	115
4.3.6 Transmon Summary	117
5 Design and Fabrication	119
5.1 Cavity	119

CONTENTS	5
5.1.1 Design Considerations	119
5.1.2 Optical Lithography	123
5.1.3 Deposition and Liftoff	126
5.1.4 Substrates	127
5.2 Cooper Pair Box	129
5.2.1 Josephson Energy	129
5.2.2 Charging Energy and Voltage Division	130
5.2.3 Electron Beam Lithography	133
5.2.4 Veil of Death	135
5.3 Transmon	137
5.4 Printed Circuit Boards and Sample Holders	137
6 Measurement Setup	141
6.1 Cryogenics and Filtering	143
6.2 Pulse Synthesis	146
6.3 Demodulation	147
6.3.1 Digital Homodyne	148
7 Characterization of CQED	154
7.1 Cavity	154
7.1.1 Temperature Dependence	155
7.1.2 Magnetic Field Dependence	157
7.2 Cooper pair box	159
7.2.1 Charge Noise	164
7.2.2 Measured CPB properties	166
7.3 Transmon	166
8 Cavity QED Experiments with Circuits	169
8.1 Resonant Limit	171
8.1.1 Vacuum Rabi Mode Splitting with CPB	171
8.1.2 Vacuum Rabi Mode Splitting With Transmon	173
8.2 Dispersive Weak Limit	177

CONTENTS	6
8.2.1 AC Stark Effect	177
8.2.2 Off-Resonant AC Stark Effect	182
8.2.3 Sideband Experiments	185
8.3 Dispersive Strong Limit	191
8.3.1 Photon Number Splitting	191
8.3.2 Anharmonic Strong Dispersive Limit	197
9 Time Domain Measurements	200
9.1 Single Qubit Gates	200
9.2 Single Shot Readout	207
9.3 Single Photon Source	211
10 Future work	220
10.1 Evolution of Circuit QED	220
10.1.1 New Cavity and Qubit Designs	220
10.1.2 Scaling Circuit QED	221
10.1.3 Other quantum circuits	222
10.1.4 Hybrid Circuit QED	223
11 Conclusions	225
Appendices	226
A Operators and Commutation Relations	227
A.1 Harmonic Oscillators	227
A.2 Spin 1/2	227
A.3 Jaynes-Cummings Operators	227
A.3.1 Interaction with Harmonic oscillator operators	228
A.3.2 Interaction with Spin 1/2 Operators	228
B Derivation of Dressed State Atom Picture	229
C Mathematica Notebooks	233
C.1 Cooper Pair Box	233

D Recipes	234
------------------	------------

List of Figures

1.1	Relaxation and dephasing of qubits leads to decoherence	21
1.2	Cavity QED setup with alkali atoms at optical frequencies	24
1.3	Cavity QED setup with Rydberg atoms at microwave frequencies	24
1.4	Cavity QED setup with quantum dots in semiconductors	25
1.5	Gallery of superconducting qubits	28
1.6	Cooper pair box as tunable atom	29
1.7	Cavity QED setup with superconducting circuits	30
1.8	Circuit QED sample	31
2.1	Illustration of atomic cavity QED system	35
2.2	Energy level diagrams of Jaynes-Cummings Hamiltonian	36
2.3	Exact calculation of vacuum Rabi avoided crossing and indirect decay rates	38
2.4	A phase diagram for cavity QED	42
2.5	Spectra of cavity and atom in strong dispersive limit	43
3.1	LCR oscillator	46
3.2	Transmission line as series of LC oscillator	48
3.3	Impedance of transmission line resonator	50
3.4	Capacitive coupling to an LCR resonator	51
3.5	Transmission of asymmetric cavity	53
3.6	Coplanar waveguide cavity	54
3.7	Dependence of characteristic impedance, Z_0 , on the CPW geometry.	55
3.8	Dependence of kinetic inductance prefactor on geometry.	57
3.9	Dependence of kinetic inductance on penetration depth and center-pin width.	57

3.10 CPB circuit diagram / junction diagram	62
3.11 CPB energy levels and charge staircase	63
3.12 Energy in two state approximation and fictitious field figure	64
3.13 CPB Matrix elements	65
3.14 Split CPB sketch	67
3.15 Dipole moment of the Cooper Pair Box	70
3.16 Measurement schematic and derivatives of CPB energy levels	74
3.17 State dependent transmission	75
3.18 Q function of coherent states	76
3.19 State dependent transmission with small phase shift	77
3.20 Selecting Δ_r for optimal SNR	79
3.21 Selecting $\kappa/2\chi$ for optimal SNR	80
4.1 Decoherence through gate voltage coupling circuit diagram and $S_V(\omega)$ at different temperatures	84
4.2 Quality factor of qubits coupled to transmission line and cavity	86
4.3 CPB coupling to slotline mode in resonator	87
4.4 Flux noise circuit diagram and flux transition matrix elements	88
4.5 Electric Field distribution in CPB	90
4.6 Derivatives of energy with respect to gate charge	96
4.7 Thermal Dephasing of the qubit	97
4.8 Dephasing of qubit due to $1/f$ charge noise	98
4.9 Dephasing times due to flux and critical current noise	101
4.10 CPB energy bands at different E_J/E_C ratios	104
4.11 Anharmonicity vs. E_J/E_C ratios	107
4.12 Anharmonic barrier and dimensionless dephasing rates	107
4.13 Sketch and circuit diagram of the transmon	108
4.14 Analogy of transmon as quantum rotor	110
4.15 Transmon matrix elements	112
4.16 Transmon dispersive couplings	114
5.1 Resonator sample and gap capacitors	120
5.2 Optical lithography equipment	124

5.3 Resist Profile	124
5.4 Optical image of gap capacitor in resist	125
5.5 Pictures of sputtered Nb resonators showing the “apron” and “flagging”	127
5.6 Diagram of rotating angle evaporation process	128
5.7 Edge profiles of deposited Aluminum	128
5.8 CPB sample and equivalent circuit including parasitic capacitances	131
5.9 Dolan bridge process	134
5.10 SEM images of tunnel junctions	135
5.11 Photograph of scanning electron microscope and electron beam evaporator	136
5.12 Transmon pictures	136
5.13 Sample mounts	138
5.14 “Coffin” style printed circuit board	139
5.15 Next generation PCB schematics	140
6.1 Measurement setup for cQED experiments	142
6.2 Annotated images of the cryostat	144
7.1 Transmission of a high Q resonator	155
7.2 Quality factor as a function of temperature	156
7.3 a) Comparison of Q ’s between under and over coupled resonators and their harmonics	157
7.4 Resonance frequency shift with temperature due to kinetic inductance	158
7.5 Resonator quality factor dependence on magnetic field	158
7.6 Resonance frequency shift due to magnetic field	159
7.7 “Footballs” showing phase shift of cQED system as function of gate voltage and magnetic field.	161
7.8 3D images of qubit spectroscopy	163
7.9 Spectroscopic determination of qubit energy	164
7.10 Saturation and power broadening of the qubit	165
7.11 “Footballs” showing parity effects and the presence of charge “switchers”	166
7.12 Spectroscopic characterization of the transmon	168
8.1 A phase diagram for cavity QED	170
8.2 Vacuum Rabi avoided crossing as function of bias charge	172

8.3	Transmission spectra of cQED system at and away from cavity-qubit degeneracy	172
8.4	Vacuum Rabi avoided crossing as function of bias flux	174
8.5	Level separation and linewidth near flux avoided crossing	176
8.6	Vacuum Rabi mode splitting at different drive powers	176
8.7	Density plot showing the AC Stark shift and slices at different drive powers	178
8.8	AC Stark shift and dephasing rate vs. input power	179
8.9	Non-linear corrections to the AC Stark effect	180
8.10	Dephasing due to measurement photons showing higher powers and a more comprehensive theory	183
8.11	Measurement setup for off-resonant AC Stark effect and sideband experiments	184
8.12	Lorentzian cavity transmission spectrum and experimental signal frequencies	185
8.13	AC Stark shift using tone detuned from cavity frequency	186
8.14	Plots of AC Stark shifted qubit transition frequency and linewidth with and off-resonant tone	186
8.15	Qubit-cavity energy levels illustrating sideband transitions.	187
8.16	Sideband spectroscopy density plot and spectrum	188
8.17	Tracking sidebands as function of spectroscopy and AC Stark drive tone parameters	190
8.18	Strong dispersive spectral features	193
8.19	Direct spectroscopic observation of quantized cavity photon number	195
8.20	Density and waterfall plots of the dispersive cavity's inherited non-linearity from its coupling to the qubit	196
8.21	Anharmonic cavity shifts and linewidths	199
9.1	Time resolved measurement setup	202
9.2	Rabi oscillation experiment and individual time slices	204
9.3	Rabi oscillations	206
9.4	Ramsey fringes	206
9.5	Histograms of single shot measurements	210
9.6	Single photon source protocol	212
9.7	Mapping of qubit state onto photon states	215
9.8	Spontaneous emission from qubit Rabi oscillations in cavity	217
9.9	Single photon fluorescence tomography	218
10.1	Sketch of two cavities and two qubits	221
10.2	Sketch of hybrid circuit QED with molecules	223

B.1 Radiative decay in the presence of coupling	231
---	-----

List of Tables

1.1	Types of qubits and effects of different types of noise	27
3.1	Table of superconductor properties	59
3.2	Key rates and parameters for different CQED systems	72
4.1	Comparison of representative relaxation and dephasing times for various superconducting qubit designs. T	
7.1	Sample Info	167
D.1	Optical Lithography Recipe	235
D.2	Electron beam resist spinning recipe	235
D.3	Electron beam resist development recipe	236
D.4	Nb sputtering recipe	237
D.5	Deposition and Liftoff recipe	238

List of Symbols and Abbreviations

(a^\dagger, a)	Photon creation and annihilation operators
(b^\dagger, b)	Transmon excitation creation and annihilation operators
(C_g)	Gate capacitance
$(C_{\text{in/out}})$	Resonator input/output coupling capacitor
(C_n)	Effective resonator capacitance for the n^{th} cavity mode
(C_j)	Junction capacitance
(C_s)	Stray capacitance between islands
(C_Σ)	Total capacitance between islands
(C_s)	Shunting capacitance used to increase C_Σ and lower E_C and g
(CPB)	Cooper Pair Box - consisting of two small superconducting islands connected by a Josephson junction
$(CNOT)$	Conditional Not, a two qubit gate in which one qubit is flipped depending on the state of the other
$(E_{\pm,n})$	Energies with n excitations from exact diagonalization of Jaynes-Cummings Hamiltonian
$(g/e, n\rangle)$	State vector with atom in ground/excited state and n -photons
$\left(\overline{ \pm, n\rangle}\right)$	Exact eigenstates of Jaynes-Cummings Hamiltonian, n is total number of excitations (not photon number)
(E_C)	Cooper pair box charging energy (in single e units)
(E_J)	Josephson energy
(g)	Interaction rate between qubit and photon
(g_{ij})	Cavity-qubit coupling between qubit levels i and j

(I_c)	Josephson critical current
(J_c)	Josephson critical current density (per unit area)
(L_J)	Josephson inductance
(L_{J0})	Josephson inductance in zero current limit
(L_K)	Kinetic inductance per unit length of the (superconducting) CPW
(L_m)	Magnetic inductance per unit length of the CPW
(L_n)	Effective resonator inductance for the n^{th} cavity mode
(\bar{n})	Average photon number in the cavity
(n_{crit})	Number of photons before dispersive approximation fails to converge, $n_{\text{crit}} = \Delta^2/4g^2$
(n_κ)	Number of photons before second order term in dispersive Taylor expansion of energy is comparable to cavity linewidth, $n_\kappa = \frac{\kappa\Delta^3}{2g^4}$
(n_g)	Gate polarization charge
(n_s)	Density of Cooper pairs
(n_n)	Density of quasiparticles
(Q)	Cavity quality factor ($Q = \omega_r/\kappa$)
$(Q_{\text{int/ext}})$	Quality factor due to internal/external losses
(Q_{op})	Operations quality factor, defined as number of oscillations in one decay time T_{op}/T_2
(Q_ϕ)	Pure dephasing quality factor
(Q_{res})	Quality factor due to resistivity of CPW
(Q_{rad})	Quality factor due to radiative losses
$(q_{\text{in/out}})$	External inverse q factor, the external resonator quality factor is $Q_{\text{int}} = 1/q_{\text{in/out}}^2$
(QED)	quantum electrodynamics
$(qubit)$	A quantum mechanical bit, referring to any quantum system with two levels
(R_K)	The resistance quantum (Von Klitzing constant) $R_K = h/e^2 \approx 25.8 \text{ k}\Omega$
(R_n)	Resistance of tunnel junction in normal state

(RSA)	Rivest-Shamir-Adelman public key cryptosystem, which bases its security on the computational difficulty of factoring products of large primes
(S_I)	Spectral density of current noise in units of $A^2/\text{Hz}^{1/2}$
(S_Φ)	Spectral density of flux noise in units of $\Phi_0^2/\text{Hz}^{1/2}$
(S_V)	Spectral density of voltage noise in units of $V^2/\text{Hz}^{1/2}$
(S_Q)	Spectral density of charge noise in units of $e^2/\text{Hz}^{1/2}$
$(1/T)$	Inverse transit time for atom to leave the cavity
(T_1)	Qubit state relaxation time
(T_2)	Total dephasing time
(T_2^*)	Inhomogenous dephasing time, due to ensembles of different qubit frequencies (usually due to $1/f$ noise)
(T_{op})	Operation time
(T_ϕ)	Pure dephasing time
(V_g)	Cooper pair box gate voltage
(V_j)	Voltage across the junction when a gate voltage is applied elsewhere
(Z_L)	Load impedance
(Z_C)	Characteristic impedance
(α)	Fine structure constant or anharmonicity (depending on context)
(α_r)	Relative anharmonicity α/ω_a
(Δ)	Atom-cavity detuning $\Delta = \omega_a - \omega_r$
(ϵ_m)	Charge dispersion of m^{th} CPB energy level
(ϵ_{eff})	Effective dielectric constant of CPW mode
$(\epsilon_{\text{re/im}})$	Real and imaginary parts of the substrate dielectric constant
(ϵ_r)	Relative dielectric constant
(γ_\perp)	Decay rate of atom into modes other than the cavity
(Γ_{eff})	Decay rate of atom including all channels of decay
(γ_κ)	Radiative decay of the atom by radiating through the cavity

(κ)	Decay rate of photon out of the cavity
(κ_γ)	Decay of photons by decaying through the atom via non-radiative means
$(\kappa_{\text{in/out}})$	Photon decay rate due to the input/output coupling
(λ_L)	The London penetration depth, describing the depth within which currents flow
(μ_r)	Relative magnetic permeability
(σ^\pm)	Qubit excitation creation and annihilation operators
$(\sigma_{x,y,z})$	Pauli matrices for a spin 1/2 particle used to measure x,y,z components of qubit
(σ_n)	Conductivity of the normal fluid
(τ_n)	Scattering time of the normal fluid (Drude model), which is a measure of the real part of the conductivity
(χ)	Cavity shift or Stark shift per photon, $\chi = g^2/\Delta$ for a two level atom
(χ_{ij})	Dispersive shift between cavity and qubit levels i and j
(χ_{eff})	Effective dispersive shift due to interactions of all qubit levels with the cavity
(ω_a)	Ground-excited state transition (angular) frequency
(ω_r)	Cavity resonance (angular) frequency
(ω_s)	Spectroscopy (angular) frequency

Chapter 1

Introduction

Progress in science is often a result of exchanging principles and techniques between seemingly disparate disciplines. Often this interaction leads both fields in new directions. The subject of this dissertation, “circuit quantum electrodynamics” is an excellent example of such cross-pollination. In this work, techniques imported from atomic cavity quantum electrodynamics (QED), a field developed to study the quantum interaction of light and matter, are applied to superconducting circuits to realize the building blocks of a quantum computer. Amazingly, some circuits, though containing billions of atoms, can be accurately described as a single atom. Leveraging techniques from atomic physics, this metaphor is exploited to enhance the circuits’ fidelity and develop new ways of coupling them together. While circuits can behave much like “artificial” atoms, their properties are quite supernatural, allowing circuit QED to explore new regimes of cavity QED that are difficult to reach with ordinary atoms. The introduction will first discuss quantum computation, its importance, and the challenges associated with its realization. Next, some “simple” questions that arise in a quantum theory of light lead to a brief discussion of beautiful experiments in cavity QED. Finally, these ideas are brought together to describe an architecture for quantum computing employing a superconducting circuit version of cavity QED.

1.1 Quantum Computation

Information is inherently a physical quantity, and the physics of information is the physics of all matter [Landauer1991]. The concept of the computer was developed in part as a concrete means to answer fundamental questions about information, such as “What questions can and cannot be answered?” The idea of a *quantum* computer arose out of studying the thermodynamics of compu-

tation [Bennett1982], and asking what is information in a world described by quantum mechanics, where apparently there exist inherent randomness and non-locality. The pursuit of a quantum computer can be thought of as a way to improve current computer technology, as a way to simulate quantum mechanics, or simply as a universal quantum problem stimulating interaction between disparate scientific disciplines.

In 1985 David Deustch proposed a simple algorithm [Deutsch1985] exploiting quantum information to solve a model problem inherently faster than could be done classically. While the particular problem was somewhat contrived, it was the first demonstration that the richer physics available to a quantum computer might allow it to perform faster than a classical computer. Later, in 1994 Peter Shor devised quantum algorithms which could factor and take discrete logarithms of large numbers, exponentially faster than the best known classical algorithm [Shor1994]. These two longstanding computational problems are particularly important because they are “one-way,” that is, it’s easy to pose the problem and verify the solution (e.g. by multiplying two numbers together), but extremely difficult (the best known classical algorithm requires exponentially more steps than the size (in bits) of the number) to factor. Multiplying numbers with hundreds of digits can be completed essentially instantaneously, while with the best current algorithms and classical computers, it would take the lifetime of the universe to factor them. The ease of multiplication and difficulty of factoring has been exploited to create the Rivest-Shamir-Adelman (RSA) “public-key” cryptography system [Rivest1978]. The idea that a quantum computer could mount a successful attack on RSA (and other similar systems) has stimulated much interest in both the theory and construction of quantum computers. Since then, new algorithms have been developed, most notably the Grover search algorithm [Grover1997] which speeds the time to search unstructured data quadratically, and though there is not an exponential speed-up, searching is quite important.

The physical basis of information not only allows current encryption schemes to be defeated, but also provides for new quantum encryption schemes which are based not on the computational difficulty of a one-way problem, but instead on limits of measurement imposed by quantum mechanics [Bennett1984, Bennett1992]. When properly implemented, such systems are unbreakable with known physics. Quantum cryptography systems have now been demonstrated and are even sold commercially.

While cryptography is relevant to national security and central in the study of computational complexity, there is another important application for quantum computing, namely simulating quan-

tum physics. Classical computers are ill-equipped to simulate quantum physics, folding under the weight of even small problems involving only a modest number of degrees of freedom. Richard Feynman noticed this difficulty and postulated that it might be possible to use a quantum computer to simulate quantum physics more efficiently [Feynman1982]. For very small quantum systems involving only a few degrees of freedom, brute force calculations can sometimes capture the important physics of a system. For quantum systems with a large number of degrees of freedom, consisting of millions, even 10^{23} objects, usually individual fluctuations can be ignored. The mean behavior can usually be described in classical terms using parameters derived from quantum considerations. However, there exists a large class of physical situations, involving from tens to hundreds of degrees of freedom, which cannot be addressed by these methods. This class of problems are central in topics including nuclear physics, atomic physics, and chemistry. If a quantum computer could be harnessed to predict from first principles the behavior of many-body systems in these areas, it could revolutionize every aspect of technology.

The rest of this dissertation will concern itself with the physical realization of a quantum computer. A computer is built of bits that store information and gates which operate on those bits. To create a quantum computer one must first build these fundamental components. A classical bit can be made from any system with two states, a coin or a MOSFET transistor. Of course the transistor is a superior choice for most applications. Similarly, a quantum bit or qubit can be created from any two quantum states, and while coins are not likely candidates, we have yet to find the equivalent of the quantum transistor. This means that essentially any quantum system could be used to create qubits, with attempts underway using ion traps [Monroe1995], nuclear [Gershenfeld1997, Cory1997] and electron spins [Loss1998], neutral atoms [Deutsch2000], photons [Knill2001], and also superconducting circuits [Wallraff2004, Devoret2004, Chiorescu2004, Martinis2002] among others.

The primary requirements for a physical system used to study quantum information are that it be controllable. That is, it must be easy to couple multiple qubits together and for the experimenter to measure them [DiVincenzo2000]. More challenging still, it must be coherent, avoiding both decay and dephasing. Much like a classical bit, when set to one it should not change, or relax back to zero (see Fig. 1.1a). Unlike a classical bit though, a qubit can be in a superposition of states. In this state, much like a spinning top (why qubits are often called spins), it precesses, acting as a sort of clock measuring the frequency difference between the two states. If the qubit is subject to noise (internal or external) the clock can lose time or dephase, a subtle form of decoherence that

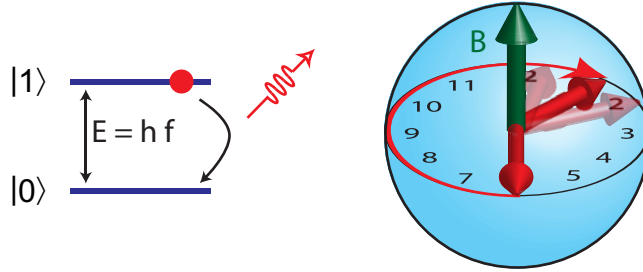


Figure 1.1: **a.** Any two quantum energy levels can be used as a qubit. Relaxation occurs when the qubit decays from the excited state to the ground state. **b.** When in a superposition, the phase, ϕ , of the qubit precesses at a frequency determined by the energy difference between the two levels. If this energy varies in time, the clock speed will vary causing it to lose time or dephase.

is the bane of most would-be qubits (see Fig. 1.1b). It is for this reason that there is an intimate relationship between the study of atomic clocks and quantum bits [Monroe1995].

In order to prevent decoherence, this loss of quantum character, the elements of a quantum computer must both be isolated from sources of noise, and yet be strongly coupled to each other, all the while being controlled by the classical experimenter. These nearly antithetical requirements pose a shared challenge for all quantum computing experiments, and have stimulated the flow of ideas among disciplines. In this project, we apply analogies of atomic physics to superconducting circuits, as a means of taming the large decoherence present in solid-state environments. Applying these analogies in reverse we use superconducting circuits to access areas difficult or impossible to study in natural atomic systems.

1.2 Cavity Quantum Electrodynamics

The electromagnetic field, though it has a wave-like nature, is composed of discrete packets known as photons. At first glance, this seems like a rather innocuous postulate, a matter of bookkeeping rather than a qualitative shift from classical waves. This discretization, however, has subtle and far reaching effects, explaining many mysteries, including the color of a hot object such as our sun, and why excited atoms decay, emitting light only at certain frequencies. The complexities of the photon postulate become more apparent when asking even a simple question like, “What is the shape of a photon?” The answer to this is subtle. Both the spatial and temporal distributions of energy are not fixed, but are dependent and *controllable* by the boundary conditions imposed upon the photon by matter. If a photon is so malleable how can it be discrete? How does matter interact

with light on the single photon level? Quantum optics [Walls2006] which studies the implications of quantum mechanics on light, attempts to answer such questions. The laser, one of the most important inventions of the past century, and one of the first fruits of such endeavors, exploits the principles of quantum mechanics to generate exquisitely well defined, but *classical* light. Much like the transistor, this device uses quantum properties to perform with incredible speed and precision in a *classical* task. As it is possible to make a bit that is inherently quantum mechanical, it is also possible to make states of light which bear no classical analogue. Both classical and quantum states of light must have some intrinsic noise, but using quantum optics, one can redistribute this noise to create states in which the noise is reduced in one parameter (i.e. the number of photons) at the expense of another (i.e. the phase of those photons). Such “squeezed” states can be used to measure with superior precision [Huelga1997] and also to transport quantum information [Duan2001].

Perhaps the truest quantum state of light is an electromagnetic field containing exactly one photon. The first way one might think to do this is to take a coherent or incoherent light source, and attenuate it until there is on average a single photon. However, despite having on average one photon an attenuated classical state will retain most of its classical nature, and there will still be a probability to have more or less than a single photon. To get a single photon one needs a non-linear system, ideally one with only two states, such as an atom. If this atom is put into its excited state, it will decay, emitting exactly one photon. Typically the cross-section for interactions between a single atom and photon is quite small, making it difficult to observe their effect on one another.

Cavity quantum electrodynamics [Berman1994] (QED) gives a means by which to overcome these technical difficulties to experimentally answer fundamental questions about photons and their interaction with matter. The prototypical cavity QED system is an atom modeled as a two-level system coupled to a harmonic oscillator, whose excitations are photons. The system has the theoretical virtue that it is relatively easy to describe while capturing the essence of the matter-light interaction. Discussed in section 2, the ubiquity of this type of interaction makes the concept generalizable to many different physical systems, including ions [Monroe1995], semiconductors [Reithmaier2004, Yoshie2004], nanomechanical structures [Irish2003], and the subject of this work, superconducting electrical circuits [Blais2004].

Normally, when an atom couples to its electromagnetic environment, noise present even in the vacuum will cause it to spontaneously decay, emitting a photon never to be seen again, and destroying the atom’s coherence. In cavity QED, a very different environment is created, in which the cavity acts

like a hall of mirrors, reflecting photons back and forth as many as one million times [Vahala2003] before they leak out. In this way, the cavity confines photons to a small volume, increasing their energy density and giving them many chances to interact with the atom, and thereby enhancing the effective interaction strength. One might think that this would enhance the atom decay, however only photons of a precisely defined energy (the resonant frequency of the cavity) can fit in this cavity. If the atom and cavity do not share the same frequency, the emitted photon does not fit inside the cavity, and the spontaneous decay can be suppressed, allowing it to remain coherent far longer than in free space. When they are resonant, and the cavity is designed to be very leaky, the atom can be made to decay even faster than in free space. When they are resonant and the cavity is not leaky, then an even stranger thing happens. If this interaction strength is large enough, the strong coupling limit is reached, and the atom can emit and reabsorb a single photon many times before the atom decays or the photon has time to escape. Apparently, inside a cavity the spontaneous decay can be made coherent! Cavity QED allows one to suppress, enhance, and even make coherent the radiative decay of an atom, allowing one to study and engineer this mysterious quantum process.

The last process, a periodic oscillation between photon and atom excitation, is known as a vacuum Rabi oscillation, called such in honor of I. I. Rabi and because it is as if the oscillation is stimulated by the zero point noise of the vacuum (see Fig. 1.3b). Another way to think about this phenomenon, is that the atom and cavity share a single quantum of energy, in an analogous manner to that of two atoms sharing an electron in a molecule. Like in a molecule, this system has two states similar to a bonding and anti-bonding orbital, which can be measured spectroscopically by looking at the energies of photons allowed to pass through the atom-cavity system (1.2b). Our observation of this vacuum Rabi splitting in a solid state system is one of the central results of this work and is discussed further in section 8.1.

Because the physics of cavity QED is so fundamental there are many systems in which it can be observed. One such system traps a cloud of hydrogen-like alkali atoms above an optical cavity formed by two highly reflective mirrors (see Fig. 1.2a). Atoms are then released from the trap such that on average only a single atom falls into the cavity. As the atom drops through, it slightly changes the cavity's properties, which can then be probed by shining a laser through the cavity. This allows one to count how many atoms are in the cavity [McKeever2004] (see Fig. 1.2c) and even detect the state of a single atom. An analogous measurement technique is used in this work and is discussed in sections 2.1 and 3.4.

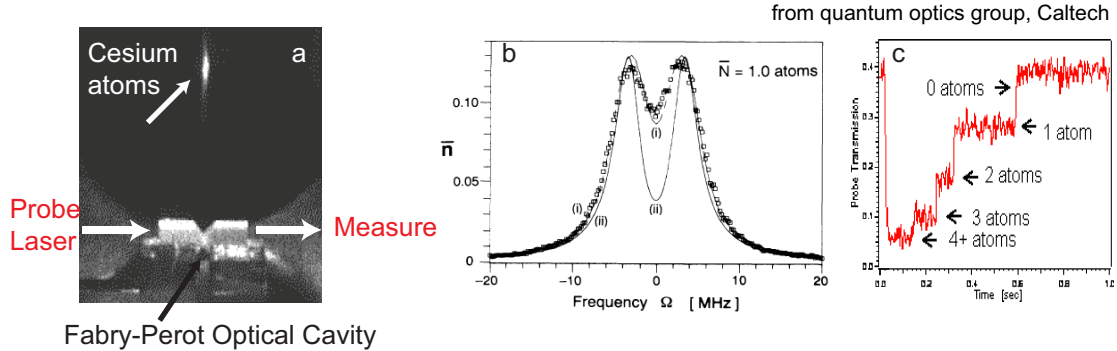


Figure 1.2: **a.** Cavity QED setup dropping a cloud of cesium atoms into a Fabry-Pérot optical cavity. Transmission of a laser through a cavity is monitored to determine the atomic state. **b.** First observation of vacuum Rabi splitting. The spectrum is similar to that of the response of a molecule with two a pair energy levels split by the bond strength. **c.** Plot of cavity transmission used to count the number of atoms inside it.

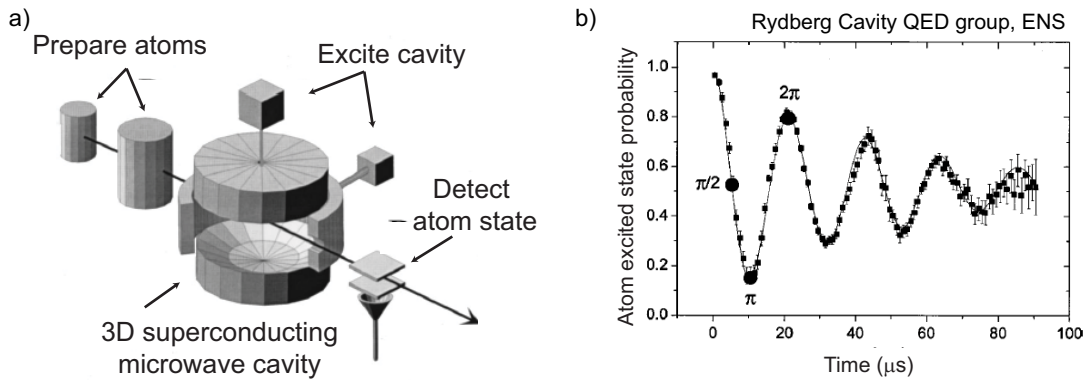


Figure 1.3: **a.** Model of Rydberg atom cavity QED setup. At left atoms are prepared into highly excited Rydberg states, then prepared into an initial state and filtered for velocity. They then pass through a high finesse three-dimensional microwave cavity which is cooled to ~ 1 K interacting with photons inside. Finally the atom state is measured by selective ionization. **b.** First observation of vacuum Rabi oscillation. An excited state atom is sent into the cavity where it coherently emits and absorbs a single photon, the excited state population of the atom is then measured as a function of time spent in the cavity.

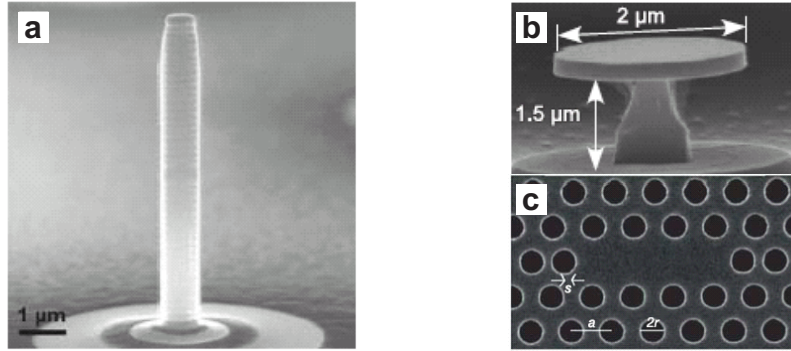


Figure 1.4: **a.** A self assembled quantum dot inside a micro-pillar of alternating dielectrics (GaAs and AlAs) to create a distributed bragg reflector cavity [Reithmaier2004]. **b.** A two-dimensional photonic band gap crystal supported by a micro pillar [Yoshie2004]. **c.** Top view of the photonic crystal showing defect in crystal forming the cavity. The quantum dot is located underneath the surface inside the defect.

Another atomic cavity QED system that heavily influences this work, uses Rydberg atoms and three-dimensional microwave cavities [Raimond2001]. Rydberg atoms are highly excited alkali atoms, with much larger electron orbits than ground state atoms (1000 \AA vs. 1 \AA). Their large size allows them to possess much larger dipole moments, and thus to interact more strongly with light. In addition, radiative decay is much slower for microwave excitations than optical excitations, giving more time for the atoms to interact with the photons. However, these benefits come at the price of having less energy available, making direct detection of the photons difficult and requiring cryogenic cooling of the cavity to $\sim 1 \text{ K}$. Fortunately, the atoms can be detected directly by selective ionization. This leads to a different and interesting reversal of focus from the previous implementation, with atoms as “meters,” probing the cavity photons. In addition to measuring the vacuum Rabi oscillations described above (see Fig. 1.3b), the Rydberg atoms can be used to count the number of photons in the cavity [Brune1996] (see Fig. 1.3c). Another experiment measured the presence of a single photon without destroying it, constituting a quantum non-demolition (QND) measurement of a single photon [Nogues1999], while a more recent experiment measured quantum jumps as the number of cavity photons changed [Gleyzes2007]. In section 8.3 we present a new technique for counting photons without destroying them.

In addition to atomic systems, rapid progress is also being made in semiconducting systems, using quantum dots as artificial atoms. In one technique, self assembled dots and a distributed Bragg reflector cavity made from alternating layers of epitaxially grown dielectric materials are

used [Reithmaier2004](see Fig. 1.4a). Another uses a quantum well in a defect of two dimensional photonic band gap crystal acting as a cavity to confine the photon [Yoshie2004] (see Fig. 1.4a). While not yet as sophisticated as atomic cavity QED, these efforts provide a natural path to integrate quantum optics techniques with current solid state optical technology.

1.3 Quantum Circuits

The goal of this project is to realize a cavity QED system using superconducting electrical circuits rather than natural atoms. Superconducting circuits can be engineered to have discrete, non-linear spectra and long coherence times, making them resemble artificial atoms. The toolbox of superconducting circuit elements consists of capacitors, inductors, and the Josephson element. The Josephson junction is the only¹ known dissipationless non-linear circuit element[Devoret2004]. It acts much like a non-linear inductor which, like the semiconductor transistor, provides the basis for gain, and non-trivial logic. These building blocks are the elements of a circuit periodic table, which has its own unique and highly versatile chemistry. By arranging the elements in different topologies, one can realize circuits which operate on quantized photon number, charge, flux, or phase states (see Fig. 1.5).

The simplest combination is the LC circuit, which creates an electrical simple harmonic oscillator². This circuit, if built at high enough frequencies (gigahertz) and operated at low enough temperatures ($< 100 \text{ mK}$), will have thermally resolvable energy levels corresponding to microwave photons. Unfortunately, because it is harmonic (the levels are evenly spaced), there is no way, with an LC oscillator alone, to observe the discrete nature of these photons. In order to detect the quantization of energy one must have a non-linear element. If the inductor is replaced with a small Josephson junction, then one realizes a Cooper pair box, a type of charge qubit [Nakamura1999]. The junction allows Cooper pairs to tunnel between sides of the capacitor but weakly enough that the states of the qubit can be labeled by the charge difference between the islands. The conjugate quantum variable to charge is flux. One can also make a qubit, by storing a flux quantum in a loop interrupted by a Josephson junction [Mooij1999]. The quantum variable is then the number of flux quanta (or sign of the persistent current). One can also replace the inductor in the harmonic oscil-

¹Some microscopic ferromagnetic or ferroelectric materials might also be usable to make non-linear inductors or capacitors.

²While it is possible to make a lumped element LC oscillator, one can also use a distributed cavity approximating the resonance as that of an effective LC (see Sec. 3.1).

Control	Readout	Charge Noise	Flux Noise	Critical Current Noise
Charge	Charge	High	Low	Medium
Flux	Flux	Low	High	Medium
Phase	Phase	Low	Low	High
Flux	magnetic susceptibility	Low	Medium	Medium
Charge	electric susceptibility	Medium	Low	Medium

Table 1.1: Each qubit is sensitive to different types of noise. Simple qubits which use the same quantum variable for controlling and reading out the qubit tend to be more sensitive to noise in that parameter. Qubits which exploit dispersive readout techniques can moderate the effects of noise by working at first order insensitive points and measuring second order properties.

lator with a large Josephson junction. By itself this configuration would also be nearly harmonic, but clever application of a bias current can enhance the nonlinearity¹.

The atom is nature’s quantum system, built from a small number of tightly bound fundamental particles, able to exist in the exquisite isolation of an ultra high vacuum environment, an atom can easily maintain its quantum purity for an astonishing 10^{14} oscillation periods [Diddams2001]! Artificial atoms made with quantum circuits are made from billions of atoms, allowing the engineer to tune the “atom” parameters at a level difficult or impossible with natural atoms. However, these macroscopically coherent systems, also involve many more degrees of freedom which can contribute to decoherence. Any fluctuation or imperfection in the system that couples to the circuit is a potential source of decoherence. Noise which couples to a circuit’s preferred quantum variable (or its conjugate) is particularly harmful (see Table 1.1). Minimizing sources of environmental noise and its coupling to the circuit is a primary goal of all quantum circuit research.

Circuits must be measured to project their quantum state, and this can provide a natural channel for noise to couple to the circuit. This has led to new designs, which rather than measuring charge, flux, or phase directly measure a second order (dispersive) property, such as the electric [Blais2004], or magnetic susceptance (dipole moment) [Born2004, Siddiqi2006]. These methods allow one to reduce the sensitivity of the qubit to noise via the measurement port. There has been rapid progress in improving resilience to noise in all of these flavors of qubit, via a very productive exchange of ideas between the various groups. These issues are discussed in depth in chapter 4.

For this work we chose to explore the Cooper pair box (CPB) [Buttiker1987, Bouchiat1998, Cottet2002] as an artificial atom and a qubit. This qubit was chosen because, with clever readout technique to measure the dipole moment (see Sec. 3.4), it is only moderately sensitive to known

¹This type of qubit is especially sensitive to fluctuations in the bias current.

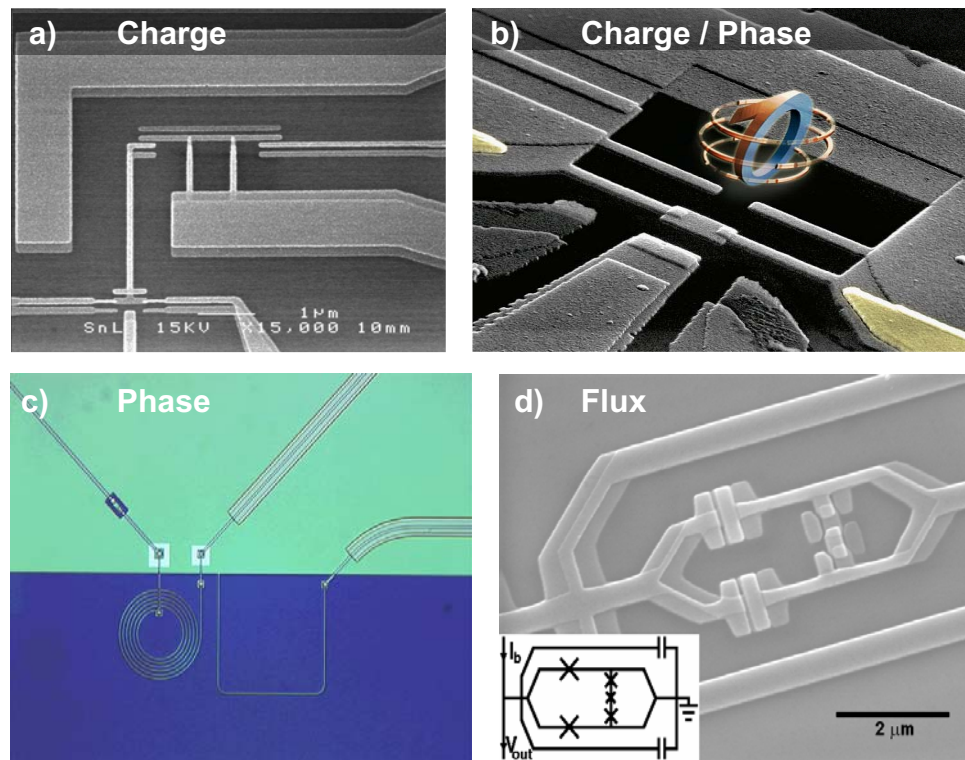


Figure 1.5: A gallery of superconducting qubits. **a)** A charge qubit based on a Cooper pair box (CPB) with single electron transistor (SET) readout. **b)** A charge/phase qubit “quantronium” which is a CPB which is excited via charge but readout in phase. **c)** A phase qubit which uses phase both for its quantum variable and its readout. **d)** A flux qubit which uses the direction of a persistent current as its quantum state and is readout using flux.

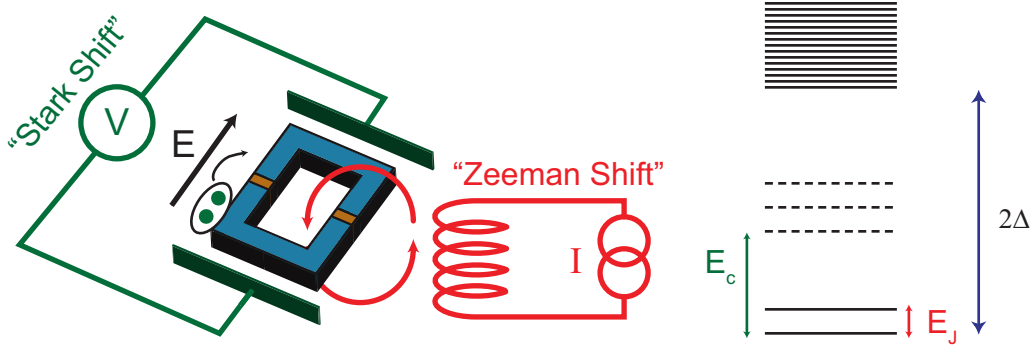


Figure 1.6: The Cooper pair box as a tunable atom. Cooper pairs (pair of green circles) can tunnel between islands (light blue) separated by the two tunnel junctions (orange), under the influence of an applied gate voltage (electric field, E) and current (magnetic flux through the ring). The Cooper pair box can be thought of as an atom, with tunable energy scales. The electrostatic energy ($\sim E_c$) can be modified by applying an electric field (Stark shift), while the Josephson tunneling energy ($\sim E_J$) can be tuned with a magnetic field (Zeeman shift). These low lying excitations are protected from a lossy continuum of normal electron states by the superconducting gap (2Δ).

sources of noise (see Ch. 4). The Cooper pair box, discussed theoretically in section 3.2 and experimentally in sections 5.2 and 7.2, consists of two small superconducting islands coupled via a Josephson tunnel junction [Josephson1962, Tinkham2004] (see Fig. 1.8 for an image of an actual CPB sample). The CPB has two energy scales, the charging energy, which is the energy to add an electron to one of the islands, and the Josephson energy gained when a Cooper pair tunnels between islands through the tunnel junction (a thin ~ 1 nm insulating barrier between the islands). In the Cooper pair box, both of these energy scales correspond to gigahertz frequencies. The maximum values of both the charging and Josephson energies can be designed by specifying the geometry of the box, and further can be tuned in-situ by applying a gate voltage or magnetic field respectively (see Fig. 1.6).

1.4 Circuit Quantum Electrodynamics

Superconducting circuits can be made to act like coherent artificial atoms. Such circuits typically operate at microwave frequencies and their quantum variables manifest themselves in familiar macroscopic parameters such as current and voltage. Though the circuits themselves are manifestly quantum, the electromagnetic fields used to interact with them were, prior to the present work, used in a classical manner. This is analogous to the interactions between a laser and atom before the

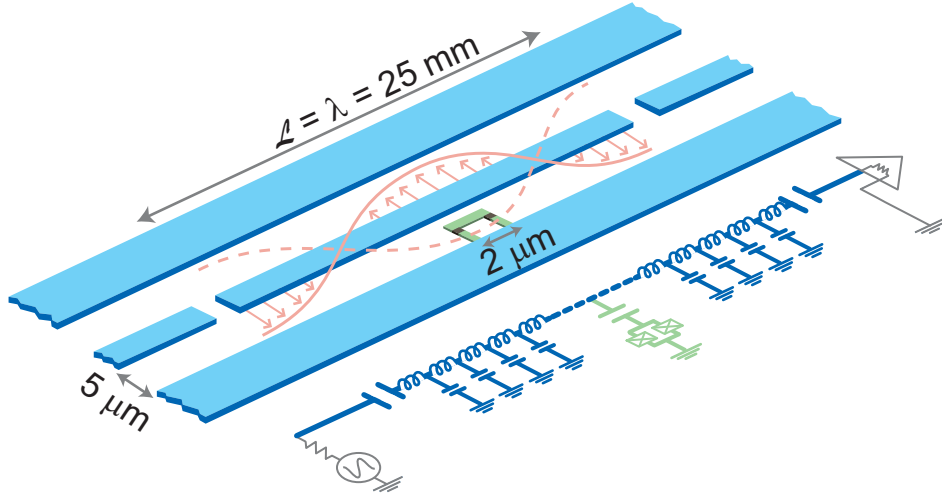


Figure 1.7: Schematic representation of cavity QED with superconducting circuits. Cooper pair box (green) at the center of a coplanar waveguide resonator (blue). The cavity resonant frequency (~ 5 GHz) is set by the length between two gap capacitors at the ends, which act as highly reflective microwave mirrors. The cavity is driven from one side and the transmitted signal is measured on the other side. The box is placed at an antinode in the spatial voltage profile for the first harmonic (pink). The system can be accurately modeled as a series of lumped element circuits.

advent of cavity QED. The primary contribution of this thesis is to apply the notions of cavity QED to the study of quantum circuits, a notion we dub “Circuit Quantum Electrodynamics”.

Though microwaves do not seem to have much in common with visible light, they are both electromagnetic fields and thus composed of photons. Even when studying qubits, the quantum properties of microwaves are often ignored. However cavity QED shows that these properties can be an asset rather than just a complication, enabling one to engineer the decoherence properties of these circuits, making them decay slower or faster. By embracing the quantum nature of microwaves, we are able to solve many problems associated with measuring quantum circuits without exposing them to sources of decoherence. We can protect them from radiative decay, and use single microwave photons as a means of coupling distant qubits together.

The circuit QED architecture [Blais2004] places a superconducting qubit, which can be thought of as an artificial atom, inside of a transmission line resonator that forms a microwave cavity (see Fig. 1.7).

The key to this cavity QED readout is the use of a one-dimensional coplanar waveguide resonator as a cavity, which is discussed in detail in sections 3.1, 5.1.4, and 7.1. The coplanar waveguide (transmission line) can be thought of as a two-dimensional version of a coaxial cable for television,

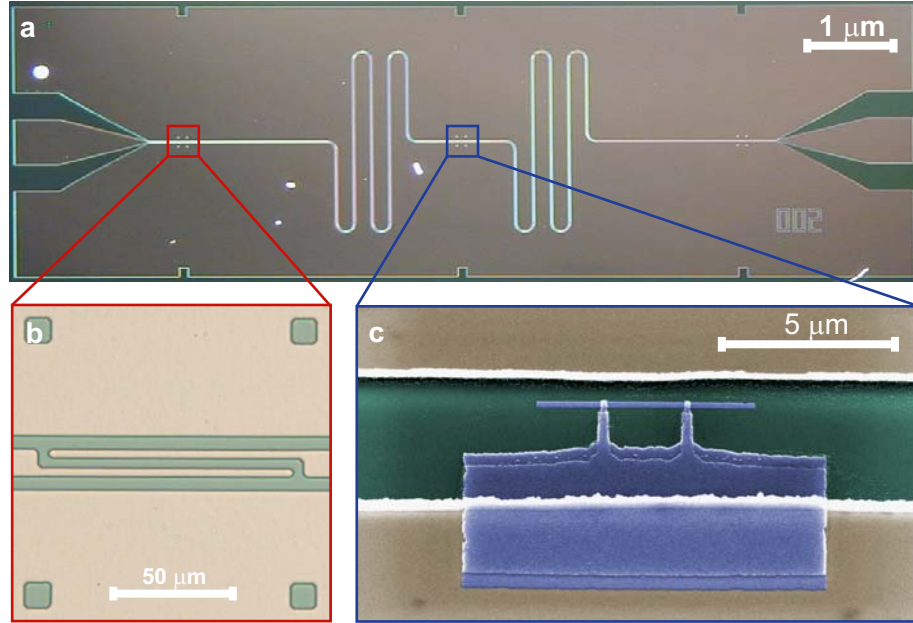


Figure 1.8: **a.** Optical image of transmission line resonator. The metal is superconducting niobium, and the substrate is silicon. **b.** Optical microscope image of one of the coupling capacitors (metal is beige, substrate is green). **c.** False colored scanning electron micrograph of Cooper pair box (blue) inside the cavity (beige) on the silicon substrate (green). The box consists of two aluminum islands (blue) connected by a small tunnel junction (the overlap of the two fingers on the thin island).

which has a center-pin and a coaxial shield separated by an insulator (see Fig. 1.7). As anyone who has tried to install cable knows, if there is a gap in the cable the signal is reflected, and if the connection is almost but not quite right there can be interference, seen on the television as waves in the picture. In a transmission line resonator, gaps in the center-pin at either end of the resonator act as mirrors for the microwave photons inside. In TV, cable signals can only travel the line a few times before being absorbed as heat, but in a superconducting transmission line, there are almost no losses and the gaps can be designed to cause anywhere from a few hundred to nearly a million reflections before allowing the photons to escape. This shows that the losses in the superconductor are so low that a microwave photon can travel tens of kilometers (10^6 cm = 10 km) without being absorbed. Thus the CPW transmission lines act much like optical fibers do for visible photons. Microwave resonators have long been used as filters to block all but a narrow band of frequencies. This filtering is the circuit analogy to the suppression of spontaneous decay in atomic cavity QED, and it helps protect the qubit from undesired environmental noise. One of the reasons it is so difficult to maintain coherence in circuits is that with many wires and other circuits around it is difficult

to control the environment seen by the qubit. The transmission line resonator has a very simple geometry making it an environment that is relatively easy to model and control. The simplicity of the environment, though not glamorous, is one of the most important aspects of this architecture.

Cavity QED offers many benefits to quantum circuits, but circuit QED also contributes to traditional cavity quantum electrodynamics. Quantum circuits are fabricated on a microchip using conventional lithography techniques, eventually allowing complex integrated quantum circuits to be manufactured. Unlike natural atoms, the properties of artificial atoms made from circuits can be designed to taste, and even manipulated in-situ. However, with this flexibility comes more channels for decoherence. Because the qubit contains many atoms, the effective dipole moment can be 10,000 times larger than an ordinary alkali atom and 10 times larger than even a Rydberg atom! This allows circuits to couple much more strongly to the cavity. Further, in atomic cavity QED the three dimensional cavities must be a minimum of one wavelength in each dimension. In our one-dimensional transmission line cavity (see Figs. 1.7 and 1.8), the other two dimensions have been compressed to much less than a wavelength, increasing the energy density by 1,000,000 over 3D microwave cavities (see Fig. 1.3a), and further increasing the dipole coupling by 1,000. This large coherent coupling allows circuits to achieve strong coupling even in the presence of the larger decoherence present in the solid state environment. In both cases, the strength of coherent interactions is larger than the rates of decoherence, allowing one to observe the quantum interactions of matter with single photons. Because circuits arrive at this end by such different means (exceptional coupling strength and moderate coherence) than atoms (using exceptional coherence and moderate coupling) circuit QED can explore new regimes of cavity QED.

1.5 Thesis Overview

The dissertation first puts the experiment on firm theoretical footing. Chapter 2 gives a theoretical review of cavity QED, exploring the Jaynes-Cummings Hamiltonian, wavefunctions, and lifetime of excited states. We explore resonant and dispersive regimes of cavity QED, introducing new regimes exploiting the strength of the dipole coupling we can attain in circuit QED. Chapter 3 discusses how to realize cavity QED with superconducting circuits. The focus in this section is to connect electrical engineering intuition of classical circuits with a second quantization based quantum optics approach. The cavity, Cooper pair box, and coupling between them are discussed in both languages and compared with traditional cavity QED implementations. Chapter 4 analyzes decoherence pro-

cesses in the Cooper pair box, with a focus on how the CPB can be made robust against each type of noise. As a result of this type of analysis a new derivative of the CPB called the “transmon” is introduced that has very promising characteristics. Next, in chapter 5, the design and fabrication of the cavities and qubits is discussed. This section is meant to be a design guide, by which one can realize the desired parameters in a physical circuit. The appendices associated with these chapters, while not necessary for understanding, present some more involved derivations and perhaps most importantly provide a convenient formulary for circuit QED. The measurements are performed at gigahertz frequencies at one-hundredth of a degree above absolute zero, requiring demanding microwave and cryogenic engineering. The cryogenic and microwave engineering techniques used in these experiments are explained in chapter 6. The data begins to flow in chapter 7 where the cavities and circuit QED system are experimentally characterized, with a focus on how to find one’s way in a rather large parameter space. The rest of the results are divided into two general classes of experiments focusing on spectroscopic and time domain results respectively. In Chapter 8 spectroscopic experiments observe the vacuum Rabi splitting, emphatically demonstrating that these circuit QED experiments reach the strong coupling limit. Spectroscopy in the dispersive limit shows the ac Stark effect, where the transition frequency of the qubit is shifted proportional to the number of photons in the cavity. Further experiments take this one step further making the dispersive coupling so strong that the qubit absorption spectrum splits into photon-number peaks, the first demonstration of the strong dispersive coupling regime. Chapter 9 then studies time resolved measurements performing detection and manipulation of the qubit state. While spectroscopic measurements are well suited to study the static energy spectrum of the system, time domain measurements are particularly adept at observing the dynamics of a single qubit or photon. In this section we realize the first high visibility measurement of a superconducting qubit, and study the fidelity of single-shot readout. Using the cavity-qubit coupling we are also able to map the qubit state onto a single photon, creating an on-demand single photon source. This thesis work was not a single experiment, but the creation of a platform for studying cavity QED and quantum information in a new way. Chapter 10 discusses a few possible directions for further experiments.

Chapter 2

Cavity Quantum Electrodynamics

A prototype system for studying the interaction between matter and light is a two-level atom, interacting via a dipole coupling with a cavity, described by a harmonic oscillator whose excitations are photons (see Fig. 2.1). The coherent behavior of this coupled system is described by the Jaynes-Cummings Hamiltonian [Walls2006]:

$$H_{JC} = \hbar\omega_r(a^\dagger a + 1/2) + \hbar\frac{\omega_a}{2}\sigma_z + \hbar g(a^\dagger\sigma^- + a\sigma^+) \quad (2.1)$$

where the first term represents the energy of the electromagnetic field, where each photon contains an energy, $\hbar\omega_r$. The second term represents the atom as a spin-1/2, with transition energy $\hbar\omega_a$, and will be henceforth referred to as a spin, qubit, atom, or simply two level system. Finally, the third term describes a dipole interaction¹ where an atom can absorb ($\sigma^+ a$) and emit ($a^\dagger\sigma^-$) a photon from/to the field at rate g . There are many systems besides atoms and photons which can be represented by this Hamiltonian, circuits [Wallraff2004], quantum dots [Reithmaier2004, Yoshie2004], and nanomechanical [Irish2003] systems, with the values of these parameters arising from the specific physics of the system. Chapter 3 contains a derivation of these parameters and typical approximations made in using the Jaynes-Cummings Hamiltonian to describe superconducting circuits. While specific to superconducting circuits, the techniques are general and could be applied to any physical system which couples Bosonic (harmonic oscillator) and Fermionic (two level system) degrees of freedom.

In addition to the coherent behavior described by the Jaynes-Cummings Hamiltonian, there are also incoherent phenomena that obscure the evolution of the coupled system(see Fig. 2.1). Any

¹The dipole interaction term is the result of a rotating wave approximation, valid in all experiments performed here and discussed in more depth in section 3.3.

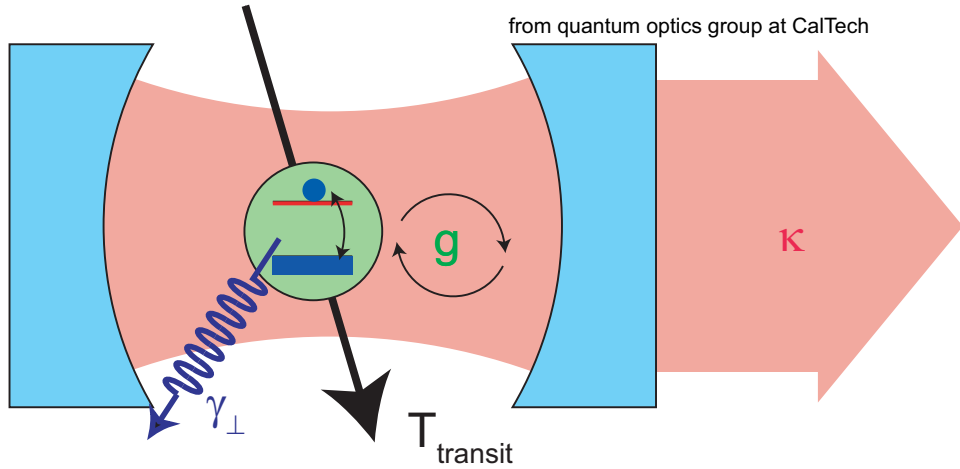


Figure 2.1: A two level atom interacts with the field inside of a high finesse cavity. The atom coherently interacts with the cavity at a rate, g . Also present are decoherence processes that allow the photon to decay at rate κ , the atom to decay at rate γ_{\perp} into modes not trapped by the cavity, and the rate at which the atom leaves the cavity, $1/T$. To reach the strong coupling limit the interaction strength must larger than the rates of decoherence $g > \kappa, \gamma_{\perp}, 1/T_{\text{transit}}$.

leakage or absorption by the cavity results in a photon decay rate, κ , sometimes expressed in terms of the quality factor $Q = \omega_r/\kappa$. Often, and particularly in circuit QED, κ is set by the desired transparency of the mirrors to allow some light to be transmitted to a detector as a means of probing the dynamics of the system. In the absence of other decay mechanisms, the radiative decay of the atom can be completely described in terms of the *coherent* interaction with the cavity and decay of cavity photons (which are measured). This very well modeled (and often slow) decay makes cavity QED a good test-bed for studying quantum measurement and open systems [Mabuchi2002]. In practice, the atom may also decay at rate, γ_{\perp} , into non-radiative channels or radiative modes not captured by the cavity. Finally in atomic implementations, the atoms have a finite lifetime or transit time T_{transit} , before exiting the cavity.

The competition between coherent and incoherent processes is most evident when the atom is resonant with the cavity, and the two systems can freely exchange energy. In the absence of decay, an excitation placed in the system will coherently oscillate between an atomic excitation and a photon in the cavity. This is often called a vacuum Rabi oscillation because it can be interpreted as vacuum fluctuations which stimulate photon emission and absorption by the atom to and from the cavity. When many oscillations can be completed before the atom decays or the photon is lost, the system reaches the *strong coupling* limit of cavity QED ($g > \gamma_{\perp}, \kappa, 1/T_{\text{transit}}$).

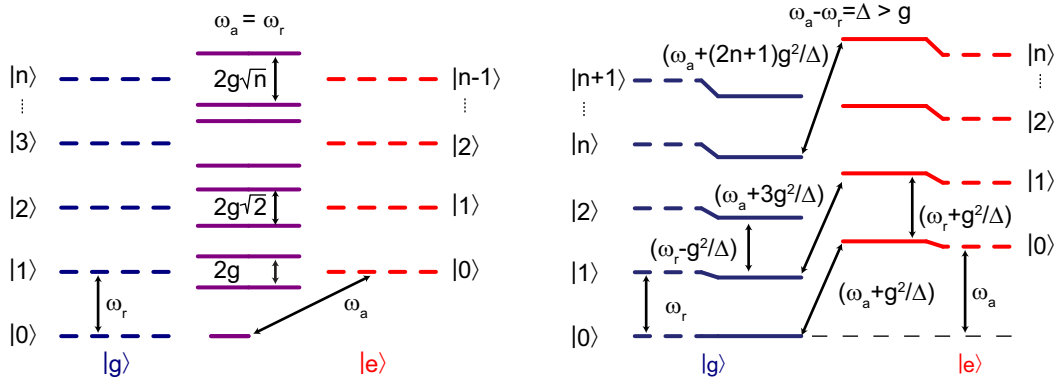


Figure 2.2: Energy level diagrams of the Jaynes-Cummings Hamiltonian¹. The dashed lines are the eigenstates of the uncoupled Hamiltonian, where left is qubit in the $|g\rangle$ state and right in the $|e\rangle$ state, and $|n\rangle$ corresponding to the photon number. The solid lines are the energies in the presence of the dipole coupling. **a.** When the uncoupled qubit and resonator are resonant ($\omega_a - \omega_r \ll g$) the levels split forming new eigenstates that have both photon and qubit character. These levels are split proportional to the dipole coupling strength, and to the square root of the number of excitations, $2g\sqrt{n}$, making the system very anharmonic. **b.** The energy levels in the dispersive limit ($\omega_a - \omega_r \gg g$) of the Jaynes-Cummings Hamiltonian. The effective cavity frequency is the difference between successive number states, $\omega'_r \approx \omega_r \pm g^2/\Delta$ depending on the atom state. The effective atom frequency is $\omega'_a \approx \omega_a \pm (2n + 1)g^2/\Delta$, where n is the number of photons in the cavity.

Another way to see the significance of the strong coupling limit is to look at the energy levels of the joint system. When the cavity and atom frequencies are degenerate, photon number states, $|n\rangle$, and atom ground and excited states denoted by $|g\rangle$ and $|e\rangle$, are no longer eigenstates of the full Hamiltonian (Eq. 2.1). The eigenstates must also diagonalize the interaction term, which (for exact resonance) is accomplished by superpositions of atom states and cavity states of the form, $|\psi_{\pm}\rangle = (|g\rangle|n\rangle \pm |e\rangle|n-1\rangle)/\sqrt{2}$. The energies of these new states are split by $2g\sqrt{n}$ (see Fig. 2.2a). The finite lifetime due to decay or dephasing manifests itself by giving the energy levels a finite width. When the width of the levels becomes so great that the splitting is obscured, it means that the atom/photon decays before a single oscillation is complete. When in the strong coupling limit (i.e. the levels are resolved), the atom-cavity system becomes anharmonic even for a single photon, allowing creation of photon number states, squeezed states, and other quantum optics phenomena [Birnbaum2005].

One should not get the idea that once in the strong coupling limit decoherence is unimportant. On the contrary, strong coupling cavity QED can be used to study decoherence. Decoherence is often the bane of experimental attempts to observe naked quantum effects, but it is also the source of irreversibility and entropy in an otherwise unitary world. Decoherence literally moves the

universe forward! A canonical example of an irreversible process, cooling of trapped atoms relies on spontaneous decay to break the symmetry between heating and cooling. Long decay times associated with atomic microwave transitions, while good for coherence, make it difficult to cool and trap such atoms based on their microwave transitions. Because excitations are equally shared between atoms and the cavity, they decay at the average of the two rates, $\Gamma_{\text{eff}} = (\gamma_{\perp} + \kappa)/2$. When $\kappa \gg \gamma$ the cavity speeds up the atom decay, allowing faster extraction of energy. Future experiments might couple circuit based cavities to increase the cooling efficiency of atom trapping/cooling. In fact, this particular trick known as the Purcell effect [Purcell1946] works even if $g < \kappa$, where the effective decay rate becomes $\Gamma_{\text{eff}} = g^2/\kappa$. In addition, the Purcell effect allows one to redirect decay from lossy internal modes (γ_{\perp}) to controlled radiative modes (κ), a property sometimes used to enhance the emission of LED's [Boroditsky1999].

Exercise 2.0.1. Using degenerate perturbation theory find the eigenstates and energies for the resonant ($\omega_a = \omega_r$) Jaynes-Cummings Hamiltonian in Eq. 2.1.

Exercise 2.0.2. Derive the Purcell effect, by calculating the overlap of the cavity and qubit wavefunctions. Does the decay depend on the photon number? Why or why not?

2.1 Dispersive Limit

In the resonant limit ($\omega_a - \omega_r \ll g$), the atom and photon can exchange energy causing them to lose their individual character, and forming a strongly coupled system. In many cases it is preferable for the interaction to be dispersive, where no actual photons are absorbed by the atom. This can be achieved by detuning the atom and cavity by $\Delta = \omega_a - \omega_r$ where $g \ll \Delta$. In this dispersive limit, the effect of the dipole interaction can be modeled using (non-degenerate) perturbation theory (see Ex. 2.1.1)). Expanding in powers of g/Δ to second order yields the approximate Hamiltonian:

$$H \approx \hbar \left(\omega_r + \frac{g^2}{\Delta} \sigma_z \right) (a^\dagger a + 1/2) + \hbar \omega_a \sigma_z / 2 \quad (2.2)$$

The atom and cavity still interact through the dispersive shift term proportional to g^2/Δ . Because it commutes with the rest of the Hamiltonian it conserves both the photon number and the atom state, but shifts the energies of both the atom and the photons (see Fig. 2.2b). The first term remains the Hamiltonian of a harmonic oscillator, but the effective frequency $\omega'_r = \omega_r \pm g^2/\Delta$, depends on the state of atom (see Fig 2.2b). This atom state dependent cavity shift can be used to

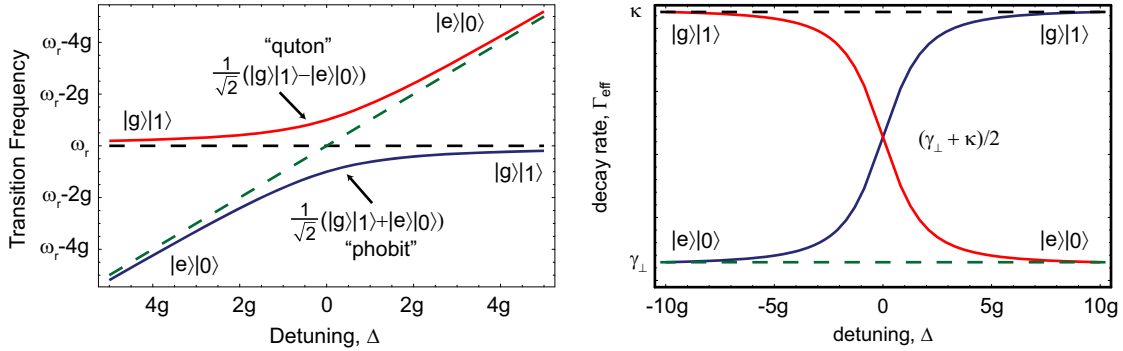


Figure 2.3: **a.** A plot of the avoided crossing in the transition frequency between the ground state in the one excitation manifold. The dashed lines show the uncoupled resonator frequency, ω_r (black) and qubit frequency, ω_a (green). The solid red and blue lines show the energy for the $|\overline{+,1}\rangle$ and $|\overline{-,1}\rangle$ states as a function of detuning. At large detunings these energies and the associated eigenstates approach that of the uncoupled system. When $\Delta \rightarrow 0$ the photon and qubit become entangled forming “phobit” and “quton” states. **b.** Indirect decay rates γ_κ and κ_γ

perform a Quantum Non-Demolition (QND) measurement of the atom state. QND measurements are important because they project the atom into the state they measure, allowing a measurement to be repeated to improve its fidelity and results in squeezing [Caves1980]. This type of QND measurement is discussed in depth in section 3.4.

The interaction can also be rewritten to highlight the interaction’s effect on the atom instead writing the Hamiltonian in Eq. 2.2 as

$$H \approx \hbar\omega_r (a^\dagger a + 1/2) + \frac{\hbar}{2} \left(\omega_a + \frac{2g^2}{\Delta} a^\dagger a + \frac{g^2}{\Delta} \right) \sigma_z \quad (2.3)$$

In this grouping, one can see that the interaction gives the atom frequency a “light” shift consisting of a photon number-dependent “Stark” shift ($2ng^2/\Delta$) and vacuum noise induced “Lamb” shift (g^2/Δ). Physically when the atom state is changed it must electrically compress (or expand) the photons’ wavelength, increasing (or decreasing) the frequency of each photon in the cavity, which will require extra energy ($\hbar g^2/\Delta$). The atom-photon symmetry of the dispersive interaction is a manifestation of the Heisenberg uncertainty principle required backaction. It means that photons which are used to measure the state of the atom will also modify its frequency. This quantum Stark Hamiltonian is special because the interaction can also perform a QND measurement on the photon number. Experiments measuring photon number and measurement induced dephasing are the topics of sections 8.2 and 8.3.

Because the Jaynes-Cummings Hamiltonian connects only states with the same number of excita-

tions, it is relatively straightforward to go beyond perturbation theory diagonalizing the Hamiltonian exactly, to calculate the energy levels and eigenstates (see appendix B). A plot of the transition frequency between the ground state and one excitation manifold based on these calculations is shown in figure 2.3. The energies are:

$$\begin{aligned} E_{\pm,n} &= \hbar n \omega_r \pm \frac{\hbar}{2} \sqrt{4ng^2 + \Delta^2} \\ E_{g,0} &= -\frac{\hbar\Delta}{2} \end{aligned} \quad (2.4)$$

Where the n used in Eq. 2.4 is the total number of excitations¹ in the system *not* the number of photons and \pm refer to the higher energy or lower energy state in the n excitation manifold *not* the atom state. Well into the dispersive limit, one can Taylor expand the square root in eq. 2.4 in the small dispersive energy shift, $n(g/\Delta)^2$, yielding

$$E_{\pm,n} \approx \hbar n \omega_r \pm \left(\Delta + \frac{\hbar}{2} ng^2 / \Delta \right) \quad (2.5)$$

The coupling effectively scales with the number of excitations, so for a given detuning there is a critical number of excitations, n_{crit} , which will make the dispersive limit break down (and the Taylor expansion diverge).

$$n_{\text{crit}} = \frac{\Delta^2}{4g^2} \quad (2.6)$$

While n_{crit} sets an upper limit on the number of photons in the dispersive limit, a more quantitative measure of dispersiveness is the orthogonality of the wavefunctions. The eigenstates can be expressed as:

$$|-\bar{n}\rangle = \cos \theta_n |g, n\rangle - \sin \theta_n |e, n-1\rangle \quad (2.7)$$

$$\begin{aligned} |+\bar{n}\rangle &= \sin \theta_n |g, n\rangle + \cos \theta_n |e, n-1\rangle \\ \theta_n &= \frac{1}{2} \arctan \left(\frac{2g\sqrt{n}}{\Delta} \right) \end{aligned} \quad (2.8)$$

If the system is well into the dispersive limit, then these can be approximated by (or computed directly using perturbation theory)

¹This also differs slightly from the convention in [Blais2004]. My n is his $n+1$ so that $n=1$ is one excitation.

$$|\overline{-, n}\rangle = |g, n\rangle - (g\sqrt{n}/\Delta) |e, n-1\rangle \quad (2.9)$$

$$|\overline{+, n}\rangle = (g\sqrt{n}/\Delta) |g, n\rangle + |e, n-1\rangle \quad (2.10)$$

In the presence of a dispersive coupling (when $\Delta > 0$), the $|\overline{\pm}\rangle$ most resemble qubit states, but they also have some photon component. This overlap can be interpreted to mean that the qubit excitation lives some of the time as a photon in the cavity. If multiple qubits are strongly coupled to the same cavity the photonic part of their wavefunctions can overlap, creating an “entanglement” bus. The atoms or qubits could be centimeters apart creating a non-local gate. The photonic aspect of the qubit also gives a new decay means that the qubit has some probability to decay as a photon emitted from the cavity, which occurs at a rate γ_κ . Similarly photons live partly as qubit excitations and so can be emitted by the qubit into non-radiative modes at a rate κ_γ . These rates are derived in appendix B. Well into the dispersive limit they are given by

$$\gamma_\kappa \approx \left(\frac{g}{\Delta}\right)^2 \kappa \quad (2.11)$$

$$\kappa_\gamma \approx \left(\frac{g}{\Delta}\right)^2 \gamma \quad (2.12)$$

Were an atom coupled to an infinite transmission line, it would radiatively decay at a rate g^2/ω . The atom inside the cavity decays at rate $g^2\kappa/\Delta$, which can be over 100,000 (Q) times slower than an atom coupled to a continuum bath! Thus, even atoms/qubits very strongly coupled to the cavity, the effective decay rates from these indirect radiative processes are very favorable for quantum computation [Blais2004] and the study of cavity QED, but often non-radiative sources of decay (γ_\perp) will begin to dominate before the limit set by suppressed radiative decay. By eliminating radiative sources of decay, we can begin to understand these non-radiative sources more quantitatively.

Exercise 2.1.1. Derive the dispersive JC Hamiltonian to second order in g/Δ using the Baker-Haussdorf Lemma [Sakurai1994] to find a unitary transformation of the form

$$U = \exp [i(\phi\sigma^+a + \phi^*a^\dagger\sigma^-)]$$

for which the transformed Hamiltonian UHU^\dagger gives Eq. 2.2 to second order in g/Δ . If you prefer

(i.e. dislike the BH Lemma) you may expand the exponential to the appropriate order and compute the Hamiltonian directly to the requested order in g/Δ .

Exercise 2.1.2. Applying the unitary transformation found in exercise 2.1.1 instead to the wavefunctions, find the eigenstates of the dispersive Hamiltonian to first order in g/Δ . Show that these agree with the exact eigenstates first order.

Exercise 2.1.3. Apply (to first order) the unitary transformation found in exercise 2.1.1 to the photon annihilation operator UaU^\dagger . What does this say about the radiative decay of the qubit?

Exercise 2.1.4. Using Fermi's Golden Rule find the decay rate of a qubit-like excitation in the dispersive Jaynes-Cummings Hamiltonian with a decay Hamiltonian $H_\kappa = \sqrt{\kappa}(b^\dagger a + a^\dagger b)$. The solution can be found in appendix B. **b.** Along similar lines derive the rate of photon loss through the atom decay channel.

Exercise 2.1.5. **a.** Derive the energy levels of Eq. 2.4 by diagonalizing the n -excitation manifold exactly. See appendix B for solution. **b.** By taking appropriate energy differences to second order find the cavity, Stark, and Lamb shifts.

Exercise 2.1.6. The $1/2$ in the harmonic oscillator Hamiltonian $H = \hbar\omega_r(a^\dagger a + 1/2)$ is often neglected as it appears to be a constant offset which can be eliminated by appropriate gauge choice. The Lamb shift arises from this $1/2$ term. Using CQED, design an experiment to measure the Lamb shift.

2.2 Strong Dispersive Interactions

In the previous section, nothing was mentioned about the strength of the coupling relative to decay, the only constraint was that $ng/\Delta \ll 1$ (outside of blue region in Fig. 2.4). In fact in the dispersive limit the old definition of strong coupling, that the rate of atom-photon oscillations were faster than decay, contradicts the notion of dispersiveness, that no (very little) mixing occurs between atom and photon. Instead one can compare the manifestation of the dipole coupling, the dispersive frequency shifts, to the decay rates. To access the strong dispersive regime one must have $\chi = g^2/\Delta > \gamma, \kappa$ (white region in Fig. 2.4). The hallmark of this type of strong coupling is that the qubit spectrum resolves into individual photon number peaks. Also above this threshold, the cavity shift is larger than the cavity linewidth, “splitting” the cavity, based on the state of the atom (see Fig. 2.5). When

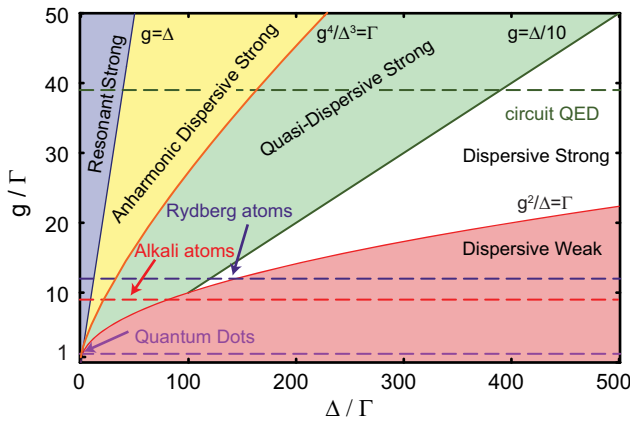


Figure 2.4: A phase diagram for cavity QED. The parameter space is described by the atom-photon coupling strength, g , and the detuning, Δ , between the atom and cavity frequencies, normalized to the rates of decay represented by $\Gamma = \max[\gamma, \kappa, 1/T]$. Different cavity QED systems, including Rydberg atoms, alkali atoms, quantum dots, and circuit QED, are represented by dashed horizontal lines. In the blue region the qubit and cavity are resonant, and undergo vacuum Rabi oscillations. In the red, weak dispersive, region the ac Stark shift $g^2/\Delta < \Gamma$ is too small to dispersively resolve individual photons, but a QND measurement of the qubit can still be realized by using many photons. In the white region, quantum non-demolition measurements are in principle possible with demolition less than 1%, allowing 100 repeated measurements. In the green region single photon resolution is possible but measurements of either the qubit or cavity occupation cause larger demolition. In the yellow region the cavity becomes anharmonic, allowing it to create squeezed states and inherit some inhomogeneous broadening, and the Stark shift becomes non-linear.

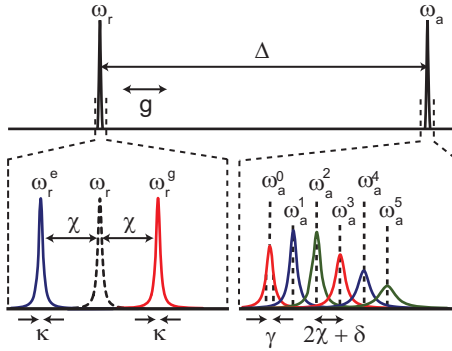


Figure 2.5: Spectrum of coupled cavity and atom system in strong dispersive limit. (left) Cavity spectrum when atom is in ground (blue), excited (red) state or not present (dashed black). (right) Atom spectrum when cavity has different (exact) photon numbers.

measuring the state of a single atom using the cavity, one has the luxury of using many photons to compensate for a small dispersive shift $\chi < \kappa$, even in the weak dispersive limit (pink region in Fig. 2.4). Because there is only a single atom in the cavity, single photon precision requires dispersive strong coupling.

Perhaps even more interesting is when the Stark shift per photon exceeds the atom decay ($\chi > \gamma$). In this case the atom is shifted by more than a linewidth for each photon, only responding when driven at a given frequency when a specific number of photons are present in the cavity. By probing the response of the atom at different frequencies one can measure the exact photon number distribution (see section 8.3). The qubit can not only measure the photon number but be coherently controlled by it. If the qubit is made only to respond when a single photon is present this can be considered a conditional-not (CNOT) gate. If multiple atoms in the cavity (which might be far apart from each other) perform a CNOT on the same photon state they can be entangled without ever interacting directly.

In the weak dispersive limit (red region in Fig. 2.4), the cavity, though its frequency became atom state-dependent, remained harmonic at photon numbers below n_{crit} . If the coupling becomes strong enough, even in the dispersive limit well below n_{crit} (where perturbation theory is still accurate) higher order terms in the expansion of equations 2.4 and 2.7 can become significant compared with the cavity linewidth. A new critical photon number can be defined for when the 4th order shift ($n\chi^2/\Delta$), changes the resonator frequency by more than a linewidth per photon.

$$n_\kappa = \frac{\kappa\Delta}{\chi^2} = \frac{\kappa\Delta^3}{g^4} \quad (2.13)$$

While the wavefunction overlap between atom and cavity is small in absolute terms ($(g/\Delta) \ll 1$), the coupling can be large enough ($g \gg \kappa$) for the cavity to inherit a significant non-linearity. Note that the qubit remains mostly in the ground state. Depending on how the cavity is being used, this could be a blessing or a curse. If linearity is desired, then it is not sufficient to stay below n_{crit} , one must also keep the number of photons to be much less than n_κ . However, an anharmonic oscillator can also be an extremely useful device. It can be used to squeeze light (in a less extreme way than in the resonant case), or as a hysteretic latching measurement of another atom [Siddiqi2006].

If the coupling is stronger still, it is even possible to have $n_\kappa < 1$ (the orange line in Fig. 2.4). In this limit, the cavity becomes anharmonic on the single photon level, acting more like a many level atom than a harmonic oscillator. As such it can also be used as a “photonic” qubit which is discussed briefly in section 8.3.2.

Cavity QED can be used to explore a wide variety interaction types and decoherence effects. All of these regimes have useful properties for quantum information. The resonant interaction between an atom and a single photon can be used to transport quantum information. The dispersive shifts can be used to measure the photon number or qubit state, while the radiative lifetime enhancement can be used to protect it from decoherence. In the strong dispersive regime, one can use the dispersive shifts to measure photons, creating and characterizing exotic states of light, which could be used for communication of quantum information or to be studied in their own right. It might even be possible to make fundamentally new quantum bits based on the non-linearities present in cavity QED. As the phase diagram in figure 2.4 and as chapter 3 will show, superconducting circuits can be made into an excellent CQED system, exhibiting a wealth of interesting physics.

Chapter 3

Cavity QED with Superconducting Circuits

This chapter describes the process of building a cavity QED system out of circuits. A special emphasis is placed on connecting the languages of microwave engineering to that of quantum optics. First, each component is described in classical circuit terms. Because the energy scales of these circuits ($E/\hbar \sim 5$ GHz) correspond to temperatures of ~ 250 mK and the experimental temperature is ~ 20 mK ($k_B T \sim 400$ MHz) the circuits are quantized to understand their full behavior. Special attention is paid to the conditions under which it is valid to approximate the quantum circuits, a coplanar waveguide resonator and Cooper pair box, to a single mode harmonic oscillator and two level atom. With these approximations in mind, we can then describe these circuits in the language of quantum optics. Dissipation can mask any coherent quantum effects so attention is given to decoherence, with several sections describing engineering of the cavity decay and all of chapter 4 devoted to describing various decoherence mechanisms in the CPB.

3.1 Transmission Line Cavities

In cavity QED, the cavity creates a single harmonic mode¹, which couples to the qubit state. In the microwave domain, a cavity can be realized using electrical circuits. In order to observe the quantum properties of a cavity it should have a high quality factor so that each energy state lives for a long time. This is important both so that its discreteness can be resolved and so that the cavity does not contribute decay to any qubits which are coupled to it.

¹The cavity actually creates an infinite number of discrete modes spaced by ω_r , but there is only one near the atom frequency.

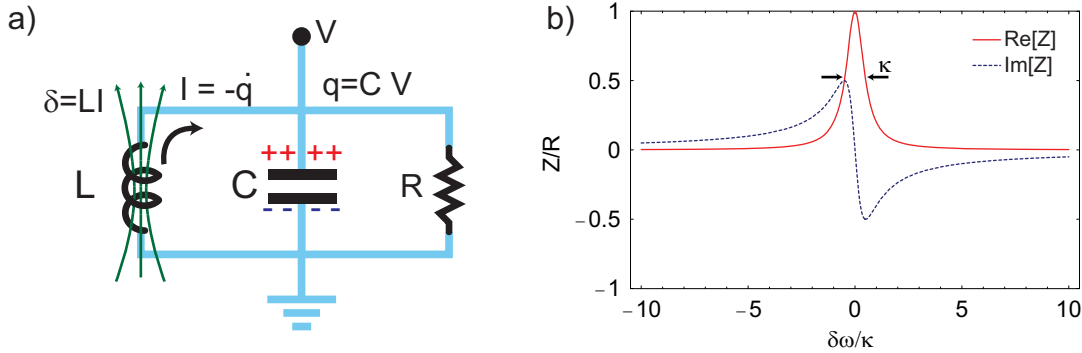


Figure 3.1: **a.** A parallel LCR circuit can be described in terms of the canonical variables, $q = CV$, the charge on the capacitor, and $\delta = LI$, the magnetic flux in the inductor. They are linked by Lenz's law and the fact that the current draws charge from the capacitor. **b.** Plot of real (solid) and imaginary (dashed) parts of the impedance $Z(\omega)$ of an LCR circuit (Eq. 3.3). The frequency is normalized to the full width at half max and the impedance is normalized to the resistance at resonance.

First, we will analyze the LCR oscillator, a simple lumped element circuit which realizes a harmonic oscillator Hamiltonian. However, at microwave frequencies, it is difficult to realize a true lumped element circuit. This is because to measure the lumped element we must attach wires which extend more than a wavelength, and so there is almost invariably at least one large dimension. Therefore it is much easier to make a 1D oscillator, a transmission line cavity, which can be modeled as a series of LCR circuits. We will then discuss coupling these resonant circuits to the input and output transmission lines. After gaining a classical intuition for these circuits, we can quantize the LCR circuit connecting our basic intuition from electrical engineering to fully quantum mechanical notions of decoherence and measurement.

3.1.1 The LCR Oscillator

The equation of motion for the amount of charge on the capacitor (from currents summing to zero and voltages all equal) in a parallel LCR oscillator can be written

$$\frac{d^2q}{dt^2} - \frac{1}{RC} \frac{dq}{dt} + \frac{q}{LC} = 0 \quad (3.1)$$

The solution to this differential equation is

$$q(t) = q_0 \exp \left[i(\omega_0 + i\frac{\kappa}{2})t + \phi \right] \quad (3.2)$$

which describes a charge oscillation with frequency $\omega_0 = 1/\sqrt{LC}$ and decay rate $\kappa = 2/RC$. In the frequency domain the circuit can be described by its impedance $Z(\omega)$ or its admittance $Y(\omega) =$

$1/Z(\omega)$. For a parallel LCR oscillator the impedance is given by

$$Z_{\text{LCR}}(\omega) = \left(j\omega C + \frac{1}{j\omega L} + \frac{1}{R} \right)^{-1} \quad (3.3)$$

The imaginary¹ part of this impedance will be zero at the resonance frequency $\omega_0 = 1/\sqrt{LC}$. Near resonance, this expression can be expanded to first order in $\delta\omega = \omega - \omega_0$, allowing the approximation $\omega^2 - \omega_0^2 \sim 2\omega(\omega - \omega_0)$, and yielding

$$Z_{\text{LCR}}(\omega) = \frac{R}{1 + 2jQ\delta\omega/\omega_0} \quad (3.4)$$

where the quality factor is $Q = \omega_0 RC = \omega_0/\gamma$. The quality factor is dimensionless and can be thought of as the number of oscillations in a cavity decay time $2/\kappa = RC$, before the system comes to equilibrium. Large resistance results in high Q , with the limit as $R \rightarrow \infty$ giving the lossless impedance

$$Z_{\text{LC}}(\omega) = \frac{1}{2jC(\omega - \omega_0)} \quad (3.5)$$

which now approaches infinity at $\delta\omega = 0$. As with the differential equation one can use the lossless expression with a complex frequency $\omega'_0 = \omega_0(1 + j/2Q)$ to represent the decay.

3.1.2 Transmission Line as Series of LC Circuits

The microwave frequency regime is a particularly interesting slice of the electromagnetic spectrum because its characteristic wavelength, $\lambda = c/f$, occurs at human size scales of $100 \mu\text{m}$ to 1 m . Because the waves interfere constructively and destructively on these scales, the electrical response of a structure becomes highly dependent on its geometry. In a microwave circuit both the topology and the geometry are critical, which presents a challenge when engineering microwave circuits. It is well worth facing this challenge, as the geometric dependence brings the opportunity to make fantastically sharp resonances, and even to make a short act as an open! Here, a section of transmission line is used to create an effective LCR resonator.

A quick review of transmission line resonators following [Pozar1990] chapters 2 and 3 is given. A transmission line can be modeled as consisting of many small lumped elements that have the same impedances (admittances) per unit length as the transmission line (see Fig. 3.2). The impedance of one small section is

$$Z_0 = \sqrt{\frac{R_\ell + j\omega L_\ell}{G_\ell + j\omega C_\ell}} \quad (3.6)$$

¹In electrical engineering it is conventional to use $\exp(j\omega t)$ whereas quantum mechanics uses $\exp(i\omega t)$ and $j = -i$.

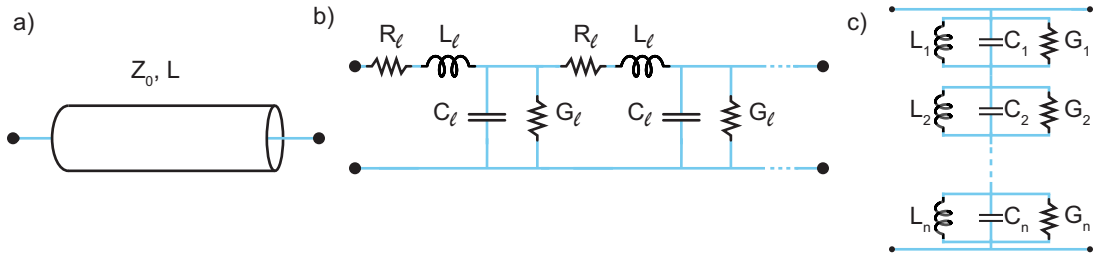


Figure 3.2: **a.** A transmission line with characteristic impedance Z_0 and length L . **b.** The transmission line can be represented as an infinite series of L's and C's which have the correct inductance (δL) and capacitance (δC) per unit length, to give the transmission line characteristic impedance $Z_0 = \sqrt{\delta L/\delta C}$. **c.** This circuit can be transformed into a series of parallel LCR oscillators, whose characteristic impedance is Z_0 and whose inductances/capacitances are given by the values in Eq. 3.13. It is interesting to note that model **c** incorrectly predicts the DC impedance (see Fig. 3.3).

where R_ℓ, L_ℓ, G_ℓ , and C_ℓ are the resistance, inductance, conductance, and capacitance per unit length of the transmission line. The R_ℓ can usually be associated with conductor loss, while the G_ℓ can be thought of as leakage in the dielectric (see sec. 3.1.7). If the loss is small, the impedance simplifies to $Z_0 = \sqrt{L_\ell/C_\ell}$. Signals on a transmission line propagate as waves with a complex propagation coefficient $\gamma = \sqrt{(R_\ell + j\omega L_\ell)(G_\ell + j\omega C_\ell)}$. The imaginary part of the propagation coefficient ($\beta = \text{Im}[\gamma]$) describes the phase of the wave. For a given frequency ω , this defines a phase velocity $v = \omega/\beta$. If the line is nearly lossless, $v \approx \sqrt{1/L_\ell C_\ell}$ and the wavelength $\lambda = 2\pi/\beta = 2\pi v/\omega$. The attenuation is described by the real part of the propagation constant

$$\alpha = \text{Re}[\gamma] \approx R_\ell/Z_0 + G_\ell Z_0 \quad (3.7)$$

The effective input impedance of an arbitrary load Z_L , at a distance ℓ , through a transmission line of characteristic impedance Z_0 , is

$$Z_{\text{in}} = Z_0 \frac{Z_L + Z_0 \tanh \gamma \ell}{Z_0 + Z_L \tanh \gamma \ell} \quad (3.8)$$

When the load impedance is an open or a short, this expression simplifies to

$$Z_{\text{in}}^{\text{short}} = Z_0 \tanh \gamma \ell \quad (3.9)$$

$$Z_{\text{in}}^{\text{open}} = Z_0 \coth \gamma \ell$$

In this thesis, transmission lines terminated with high impedances (opens or nearly opens) are usually used. With these boundary conditions there will be two types of resonance (see Fig. 3.3). Whenever the length of line is an integer multiple of a half wavelength ($\ell = n\lambda/2 = \pi v/\omega_0$), there

will be a high impedance resonance. Whenever the length is odd multiple of a quarter wavelength ($\ell = (2n + 1)\lambda/4$), there will be a high admittance resonance. The input impedance will determine which case applies, and for this thesis, we selected a near open, which selects the $\lambda/2$ high impedance resonances.

$$Z_{\text{in}}^{\text{open}} = Z_0 \frac{1 + j \tan \beta \ell \tanh \alpha \ell}{\tanh \alpha \ell + j \tan \beta \ell} \quad (3.10)$$

Note that when $\alpha \rightarrow 0$ the impedance returns to the lossless case, $Z_{\text{in}}^{\text{open}} \rightarrow -j \cot \beta \ell$, which will have poles when $\beta \ell \approx (n + 1)\pi$.

$$\beta \ell = (\omega/v)(\pi v/\omega_{\lambda/2}) = \pi(n\omega_{\lambda/2} + \delta\omega_n)/\omega_{\lambda/2} \quad (3.11)$$

Expanding $Z_{\text{in}}^{\text{open}}$ for small $\delta\omega_n$ and α yields

$$Z_{\text{in}}^{\text{open}} = \frac{Z_0/\alpha \ell}{1 + 2j \left(\frac{n\pi}{2\alpha \ell} \right) \left(\frac{\delta\omega_n}{n\omega_{\lambda/2}} \right)} \quad (3.12)$$

This looks exactly like the impedance in Eq. 3.3 where

$$\omega_n = n\omega_{\lambda/2} \quad (3.13a)$$

$$Q_n = R_n/Z_{\text{cn}} = \frac{n\pi}{2\alpha \ell} \quad (3.13b)$$

$$R_n = \frac{Z_0}{\alpha \ell} = \frac{\pi Z_0^2}{2R_\ell \ell} \quad (3.13c)$$

$$C_n = \frac{Q}{\omega_n R} = \frac{\pi}{2Z_0 \omega_{\lambda/2}} = \frac{1}{2} C_\ell \ell \quad (3.13d)$$

$$L_n = \frac{1}{\omega_n^2 C} = \frac{2Z_0}{\pi n^2 \omega_{\lambda/2}} = \frac{2}{\pi^2 n^2} L_\ell \ell \quad (3.13e)$$

$$Z_{\text{cn}} = \sqrt{L_n/C_n} = \frac{2Z_0}{n\pi} \quad (3.13f)$$

A comparison of the model in Fig. 3.2 using the effective LCR values in Eq. 3.13, is shown in Fig. 3.3a. The agreement is quite close except for the DC behavior (see Fig. 3.3b). The error is reduced to $1/Q$ at about 10% of the fundamental frequency independent of Q , and the imaginary part is suppressed much faster by ω_0/Q . The agreement in both the real and imaginary parts gets better at higher Q , contributing a negligible error due to the use of a single pole model.

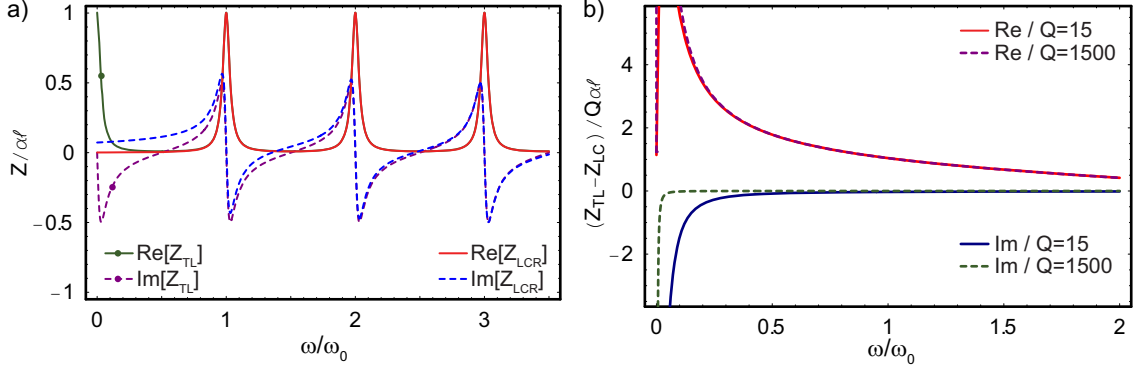


Figure 3.3: **a)** Real and imaginary parts of the impedance of resonator formed terminating a transmission line with an open-circuit (green and purple) and model of LCR resonators (red and blue) normalized to the attenuation ($\alpha\ell$). **b)** Error in normalized impedance, $(Z_{TL} - Z_{LC})/\alpha\ell$, in units of $1/Q$ between the impedance predicted by the LCR model and exact impedance of an open terminated transmission line. As can easily be seen in **a**, both the real and imaginary parts of the impedance differ significantly between the transmission line and the simple LC model. The solid red and dashed purple curves show the error in the real part of the impedance at $Q \approx 15$ and $Q \approx 1500$. Note that while the frequency scale on which the error falls off is independent of the Q , the error in the normalized impedance scales with $1/Q$ (and the absolute impedance with $1/Q^2$). The solid blue and dashed green curves show the error in the imaginary part of the impedance. The error falls off, does on scale proportional to $1/Q$, so that it becomes negligible (even measured in units of $1/Q$) very quickly.

3.1.3 Capacitively Coupled LCR Resonator

The previous subsection discusses a transmission line resonator with no coupling to the outside world, a rather lonely circuit. One could directly connect the resonator to a transmission line, but this would allow the radiation to escape too quickly by shunting the effective impedance to Z_0 and destroying the Q . A less invasive technique connects the resonator to a transmission line via a small capacitor (see Fig. 3.4a). The large impedance mismatch the capacitor causes is analogous to a dielectric mirror, since it is lossless and reflects most incident radiation, but transmits a small amount. Through this “mirror,” photons can be added to the cavity or allowed to leak out. To see how this coupling affects the resonator, it is convenient to transform the source impedance into its Norton equivalent (see Fig. 3.4b). The effective admittance of this circuit is

$$Y_{in} = \frac{j\omega C_{in}}{1 + j\omega C_{in}Z_0} = \frac{j\omega C_{in} + q_{in}^2/Z_0}{1 + q_{in}^2} \quad (3.14)$$

where $q_{in} = \omega C_{in}Z_0$ is small when the $\omega C_{in} \gg Z_0$. In this limit, one can approximately ignore the denominator in Eq. 3.14 ($1+q_{in}^2 \approx 1$). Thus the effect of the coupling is to add an effective capacitance C_{in} , which will shift the resonance frequency, and an effective parallel resistance $1/Re[Y_{in}] = Z_0/q_{in}^2$,

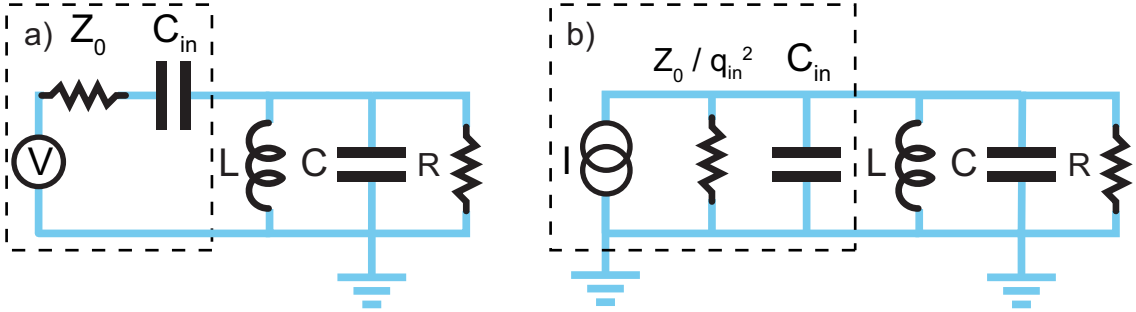


Figure 3.4: The capacitive coupling (a) to an environment of impedance Z_0 through a capacitor, C_{in} , such that $C_{\text{in}}\omega \ll Z_0$ can be modeled by an effective circuit (b). The transformed input impedance, seen by the oscillator, can be made much larger than the impedance of the environment.

which will change the Q . The quality factor will be the ratio of the impedance on resonance to the characteristic impedance¹ Z_{res}/Z_0 . If the internal resistance is negligible then²

$$Q_{\text{ext}} = \frac{1}{Z_{\text{cn}} \text{Re}[Y_{\text{in}}]} = \frac{1}{q_{\text{in}}^2} \frac{Z_0}{Z_{\text{cn}}} \approx \frac{n\pi}{2q_{\text{in}}^2} \quad (3.15)$$

If the internal resistance is significant compared to the loading then

$$\frac{1}{Q_L} = \frac{1}{Q_{\text{ext}}} + \frac{1}{Q_{\text{int}}} \quad (3.16)$$

where $Q_{\text{int}} = R_n/Z_{\text{cn}}$. This gives some insight on how coupling to the system gives an effective loss (effectively loading the resonator), and how that can be engineered (by adding a large impedance in series).

3.1.4 Capacitively Coupled Transmission Line Resonator

In the previous subsection we discussed a one-sided cavity, which could be measured in reflection, however when measuring in this mode the important signal sits on top of a large background of reflected power that contains no information. This is not in principle a limitation, but in practice it is more convenient to use transmission of a two sided cavity where only the signal is present³, making it easier to analyze the signal. If the internal losses are negligible and $Q \gg 1$, then the transmission coefficient can be expressed as

$$S_{21} = \frac{T_0}{1 - j \frac{\delta\omega_n}{(\kappa_{\text{in}} + \kappa_{\text{out}})/2}} \quad (3.17)$$

¹The characteristic impedance is $Z_{\text{c1}} = \sqrt{L/C}$ and need not be Z_0 but for all cases here the resonator has been designed such that $Z_c = Z_0$.

²Note that even though it appears that Q increases at higher harmonics, $q_{\text{in}} = \omega_{\text{in}} C_{\text{in}} Z_0 \propto n$, so overall, for fixed C_{in} the quality factor is inversely proportional to n ($Q_{\text{ext}} \propto 1/n$).

³Control pulses applied to the atom are strongly detuned from the cavity and are heavily filtered by the cavity.

where

$$\kappa_{\text{in/out}} = \left(\frac{2}{\pi} \right) q_{\text{in/out}}^2 \omega_n \quad (3.18)$$

$$T_0 = \frac{\sqrt{\kappa_{\text{in}} \kappa_{\text{out}}}}{(\kappa_{\text{in}} + \kappa_{\text{out}})/2} \quad (3.19)$$

$$\omega_n = n\omega_{\lambda/2} (1 - (q_{\text{in}} + q_{\text{out}})) \quad (3.20)$$

One can also measure the reflection of incident radiation which will be proportional to

$$S_{11} = \frac{\kappa_{\text{in}}}{\frac{\kappa_{\text{in}} + \kappa_{\text{out}}}{2} - j\delta\omega_n} - 1 \quad (3.21)$$

Equation 3.17 describes transmission with a Lorentzian line shape, which looks much like the expression for the impedance of an LCR circuit (Eq. 3.3). Here the resonance frequency is shifted by the extra capacitance contributed by the coupling capacitors (as in Eq. 3.14). The numerator of the expression gives the peak transmission (when $\delta\omega_n = 0$). If the input/output coupling is symmetric ($\kappa_{\text{in}} = \kappa_{\text{out}}$) then the transmission will be unity ($T_0 = 1$). If the resonator is asymmetric some of the input power will be reflected, satisfying energy conservation. To be concrete, let the input capacitor be smaller than the output. In equilibrium, the amount of power flowing out must equal the amount coming in, but if the input capacitor is smaller, then the input rate will not be sufficient to maintain the internal voltage, which is drained at a faster rate by the output, unless it is driven with a higher input amplitude to compensate. Since there is no loss, the remaining input power must be reflected. A similar argument holds for if the output is smaller.

The Q of the capacitively coupled transmission line resonator comes from the parallel combination of the input and output Q 's

$$Q_{\text{CCTL}} = \frac{\omega_n}{\kappa_{\text{in}} + \kappa_{\text{out}}} = \frac{n\pi}{2(q_{\text{in}}^2 + q_{\text{out}}^2)} \approx \frac{\pi}{2} \frac{1}{n\omega_{\lambda/2}^2 Z_0^2 (C_{\text{in}}^2 + C_{\text{out}}^2)} \quad (3.22)$$

Note that the quality factor for the capacitively coupled resonator $Q_{\text{CCTL}} \propto 1/n$. This can be thought of as the result of a competition between the higher frequency and the increase in conductive losses, which is proportional to the square of the frequency, resulting in overall decrease in Q at higher harmonics.

Thus far, we have only discussed the magnitude of the transmitted signal. The complex transmission coefficient of Eq. 3.17 indicates the signal will also acquire a phase shift,

$$\phi = \arctan (Im[S_{21}]/Re[S_{21}]) = \arctan \left(\frac{\delta\omega}{\kappa/2} \right) \quad (3.23)$$

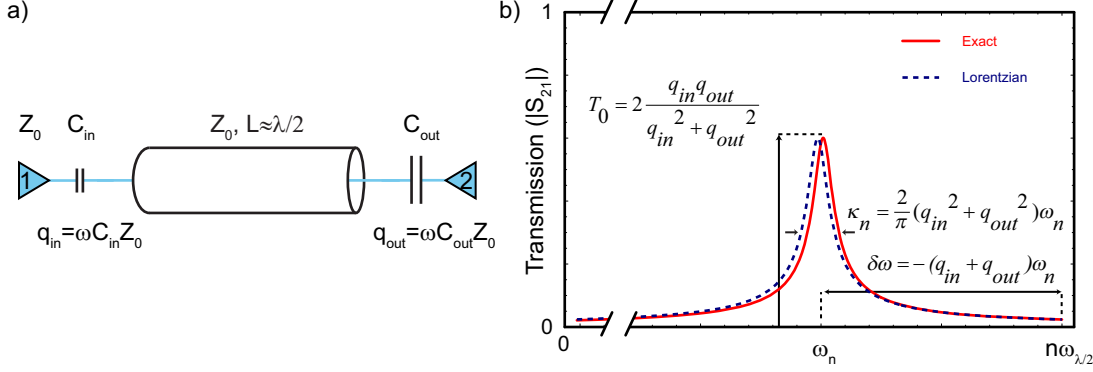


Figure 3.5: Transmission of asymmetric cavity near one of its resonances (ω_n), using an exact analytic calculation (solid red) and a lorentzian model (dashed blue). The lorentzian is a very good approximation to the full transmission spectrum near resonance. The input and output capacitor act as extra stray capacitance to ground shifting the center frequency of the resonance, ω_n , down by $\delta\omega_n$ from the unloaded half-wave resonance $n\omega_{\lambda/2}$. The width of the resonance is proportional to the square of the capacitances. If the input and output couplings are the same and the line is lossless transmission will be unity. This plot was generated using $q_{out}/q_{in} = 5$ and $Q = 2/\pi q_{out}^2 + 2/\pi q_{in}^2 = 20$.

Both the magnitude, $|S_{21}|$, and phase ϕ of the transmitted amplitude, can be exquisitely sensitive probes of the cavity frequency (see Fig. 3.5) with a relative frequency shift of $1/Q$ giving a change in transmitted amplitude/phase of order unity. As will be discussed in detail in sections 3.3 and 3.4, the effective cavity resonance frequency is shifted differently depending on the state of the qubit. The resulting change in the transmitted amplitude or phase of a tone passing through the cavity is then used as a readout of the qubit state.

- Exercise 3.1.1.**
- Derive an exact expression for the transmission coefficient S_{21} in Eq. 3.17 using the $ABCD$ representation for the coupling capacitors and transmission line (see Pozar [Pozar1990]).
 - Use a similar technique but this time approximately expand about a frequency such that $\beta\ell \sim n\pi$.
 - Make the approximate substitution $\omega C_{in/out} Z_0 \rightarrow q_{in/out}$. In reality the capacitors are frequency dependent. By approximating $q_{in/out}$ as constant this dependence is neglected in the small range near resonance. To connect to the quantum optics language in the following sections one can then substitute $q_{in/out} \rightarrow \sqrt{\kappa_{in/out}/\omega_n}$.

3.1.5 Coplanar Waveguide Cavities

Thus far the description of transmission line resonators and their properties has been geometry independent. In any physical realization a transmission line geometry must be chosen. A myriad of options exist, including balanced lines such as the coplanar stripline (CPS), or unbalanced lines

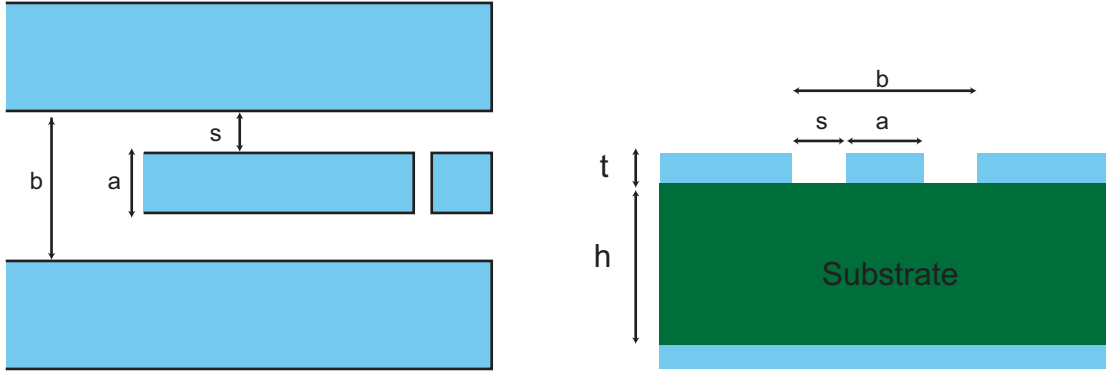


Figure 3.6: Sketch of coplanar waveguide. Length is defined by gap capacitors at end. The ratio s/a determines the impedance, Z_0 . The extent of the ground planes should be much larger than s so that they can be approximated as infinite.

like microstrip and coplanar waveguide (CPW). In deciding to use CPW, the primary factor was the method of grounding. In the microstrip geometry, the ground is beneath the substrate, meaning that it would either be far away ($300\ \mu m$), involve a potentially lossy deposited dielectric, or require more complicated fabrication techniques (strained silicon or molecular beam epitaxy). Balanced lines such as the CPS have no ground by definition, a blessing and curse as it requires less metal (allowing it to be fabricated with electron beam lithography in the same step as the qubit), but since the cryostat uses all balanced (coaxial) lines a balun is required to make the transition, potentially complicating the mode structure. The CPS is certainly a viable choice and is currently being tested by the QuLab group at Yale. The CPW has its ground in the same plane, separated by a gap from the centerpin, resembling a 2d version of a coaxial cable. This gap can be scaled from microns (where the fields are intense and well localized) to millimeters (to easily interface with printed circuit boards) while maintaining the same impedance. These convenient grounding and scaling properties led us to choose the CPW geometry for these experiments.

While any of these lines can be described by the general transmission line equations, their properties, especially the impedance (Z_0) and wave propagation velocity (v), will depend on the exact geometry (see Fig. 3.7). For a CPW these parameters are given by [Simons2002]

$$Z_0^{CPW} = \frac{60\pi}{\sqrt{\epsilon_{\text{eff}}}} \left(\frac{K(k)}{K(k')} + \frac{K(k_3)}{K(k'_3)} \right)^{-1} \quad (3.24)$$

The speed of propagation is $v_{\text{eff}} = \frac{c}{\sqrt{\mu_{\text{eff}}\epsilon_{\text{eff}}}} \approx \frac{c}{\sqrt{\epsilon_{\text{eff}}}}$ (for non-magnetic substrates) and the effective dielectric constant ϵ_{eff} is

$$\epsilon_{\text{eff}} = \frac{1 + \epsilon_r \tilde{K}}{1 + \tilde{K}} \quad (3.25)$$

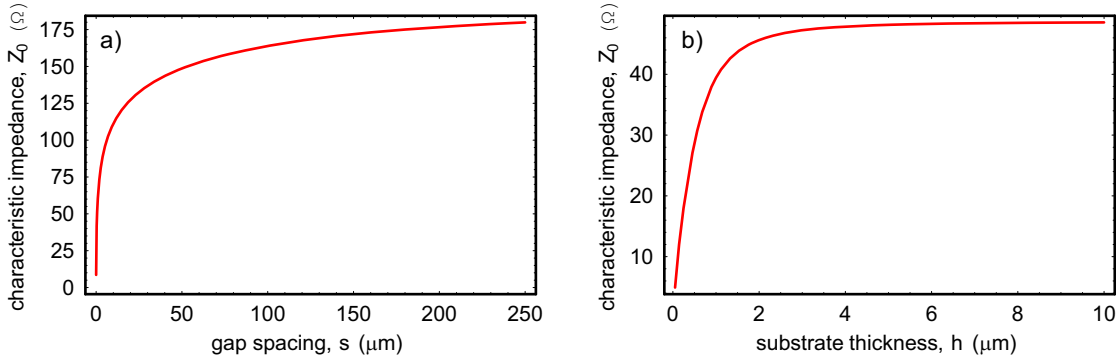


Figure 3.7: Dependence of characteristic impedance, Z_0 , on the CPW geometry. **a)** Plot of characteristic impedance, Z_0 vs. the gap spacing, s assuming a $h = 300 \mu\text{m}$ thick substrate and $a = 1 \mu\text{m}$ center-pin thickness. The importance is that regardless of the ratio of a/s the impedance will be from $\sim 10 - 200 \Omega$. This puts constraints on how well (and with how much bandwidth) one can match to a very high or low impedance load. **b)** Dependence of characteristic impedance on substrate thickness showing that as soon as $h \gg s$, Z_0 is independent of the substrate thickness.

where K is the complete elliptic integral of the first kind¹

$$\tilde{K} = \frac{K(k')K(k_3)}{K(k)K(k'_3)} \quad (3.26a)$$

$$k = \frac{a}{b} \quad (3.26b)$$

$$k_3 = \frac{\tanh(\frac{\pi a}{4h})}{\tanh(\frac{\pi b}{4h})} \quad (3.26c)$$

$$k' = \sqrt{1 - k^2} \quad (3.26d)$$

$$k'_3 = \sqrt{1 - k_3^2} \quad (3.26e)$$

and ϵ_r is the relative dielectric constant of the substrate of height h , with center conductor width a and s the width of the gap, $b = 2s + a$, as shown by Fig. 3.6.

3.1.6 Kinetic Inductance

When current flows in a wire it induces a magnetic flux. In addition to energy stored in these magnetic fields, there is also the kinetic energy present in the electrons themselves. Normally this kinetic inductance is masked by the conductivity of normal metals. In a superconductor, where the resistivity is suppressed this hidden inductance can become significant. The total inductance per unit length of a superconductor is the sum of the magnetic and kinetic inductances, $L_\ell = L_m + L_K$.

¹Complete elliptic integrals of the first kind can be calculated using the *Mathematica* function *EllipticK*.

In a coplanar waveguide geometry the magnetic inductance per unit length is given by [Yoshida1995]

$$L_m = \frac{\mu}{4} \frac{K(k')}{K(k)} \quad (3.27)$$

The kinetic energy of a current can be expressed as [Tinkham2004]

$$E = \int \frac{1}{2} n_s m v^2 dV = \int \frac{1}{2} \frac{n_s m}{A e^2} I^2 = \frac{1}{2} \mu \lambda_L^2 \frac{\ell}{A} I^2 \quad (3.28)$$

where $A = at$ is the cross sectional area and $\lambda_L = (\mu m / n_s e^2)^{-1/2}$ is the London penetration depth. Because this kinetic energy is proportional to I^2 it can be interpreted as a kinetic inductance of the form

$$L_K = \mu \frac{\lambda_L^2}{at} g(s, a, t) \quad (3.29)$$

where $g(s, a, t) \approx 5$ is a geometric factor arising from the conformal mapping to the coplanar waveguide configuration [Yoshida1995]

$$g(s, a, t) = \frac{1}{2k^2 K(k)^2} \left(-\ln \left(\frac{t}{4a} \right) + \frac{2(a+s)}{(a+2s)} \ln \left(\frac{s}{a+s} \right) - \frac{a}{(a+2s)} \ln \left(\frac{t}{4(a+2s)} \right) \right) \quad (3.30)$$

Because $g(s, a, t)$ is only weakly dependent on t and a (see Fig. 3.8), the kinetic inductance decreases with the cross sectional area of the center-pin. In addition to the geometry of the CPW, the kinetic inductance depends strongly on the London penetration depth, λ_L , the depth to which supercurrents flow. λ_L depends on magnetic field, temperature, and any optical radiation which could break Cooper pairs (as is discussed in Sec. 7.1). This derivation implicitly assumes that the thickness of the film is smaller than the depth of current flow (λ_L), such that the current distribution is uniform. If it is much thicker then it may be more accurate to approximate the thickness as $t \approx 2\lambda_L$. The penetration depth itself also depends on the film thickness and this may lead to further corrections. If any kinetic inductance dependencies have any temporal fluctuations on timescales faster than the decay time, the resulting shifts in the resonance frequency ($\propto L^{-1/2}$), will cause inhomogeneous broadening of the resonance. Since the kinetic inductance makes up only a fraction of the total inductance (see Fig. 3.9), such fluctuations will be suppressed by roughly $L_K/L_m \sim 10^{-1} - 10^{-2}$, depending on the geometry of the CPW and superconductor chosen.

3.1.7 Intrinsic Resonator Losses

Ideally, all of the cavity loss would be determined by intentional coupling as in section 3.1.4. Though the primary experiments in this dissertation were performed in this over coupled case, at higher

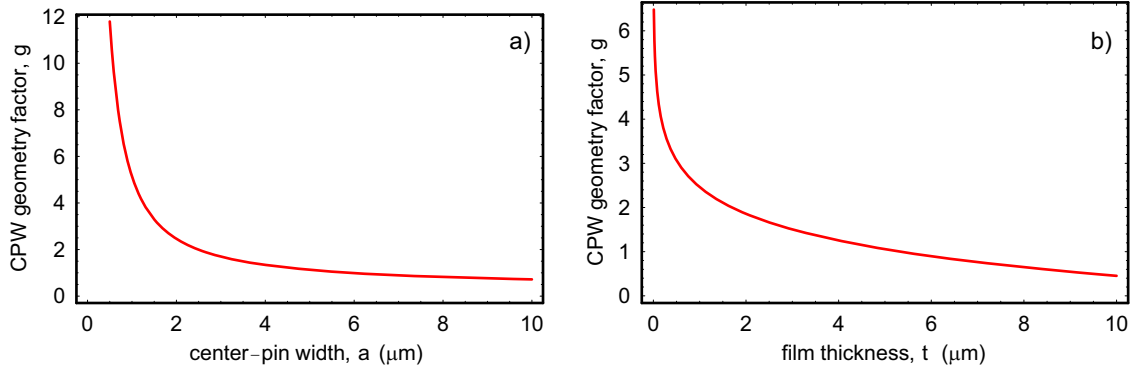


Figure 3.8: Dependence of kinetic inductance prefactor on geometry as in Eq. 3.30. **a.** Plot of $g(s, a, t)$ vs. the centerpin width a . For this plot $s = a/2$ and $t = 0.2 \mu\text{m}$. **b.** Plot of $g(s, a, t)$ vs. the film thickness t . Here $a = 10 \mu\text{m}$ and $s = 5 \mu\text{m}$.

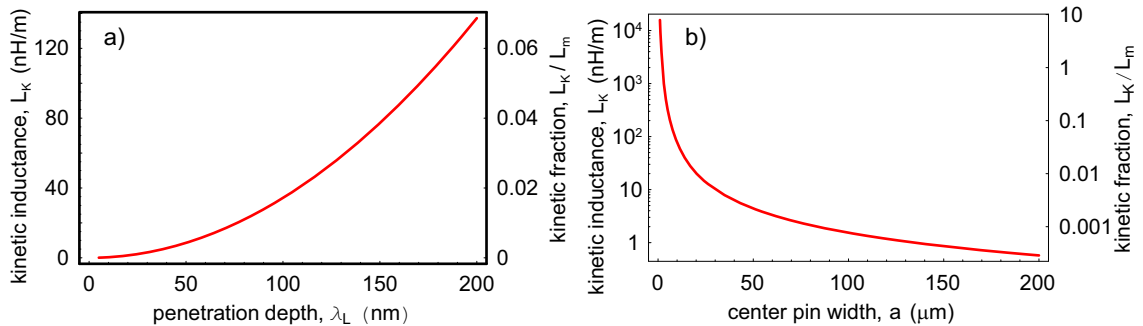


Figure 3.9: **a.** Kinetic inductance vs. penetration depth (with $a = 10 \mu\text{m}$) and **b.** kinetic inductance vs. center-pin width (with $\lambda_L = 105 \text{ nm}$). Depending on parameters the kinetic inductance can be a significant percentage of the total resonator inductance.

temperatures or at ultrahigh quality factors, even in a superconducting resonator intrinsic losses can be the dominant factor limiting the photon lifetime. Three primary mechanisms of internal loss are resistive, dielectric, and radiative losses. These mechanisms are also present as qubit relaxation processes. Understanding these processes in the cavity, a simpler system, is very important for improving qubit lifetimes and is sure to be explored further in future dissertations. Here, the focus is to describe the basis of these loss mechanisms and show that they do not prevent resonators from attaining $Q \sim 10^6$.

Resistive Losses

A superconductor can be thought of as consisting of two fluids consisting of a density, n_n , of normal quasiparticles with finite resistance and n_s , of superconducting Cooper pairs, having zero DC resistance but finite AC kinetic inductance. These fluids can be modeled as an inductor (the superfluid) and resistor (the quasiparticles) in parallel. The normal fluid's resistance is inversely proportional to the number of quasiparticles, so at temperatures below the critical temperature it becomes very large, and most of the current goes through the inductor. At any finite temperature and frequency, some current will flow through the lossy resistor, limiting the maximum Q due to resistive loss.

The conductance of a superconductor

$$\sigma = \sigma_n + i \frac{A}{\omega L_K} \quad (3.31)$$

where the normal conductivity $\sigma_n = n_n e^2 \tau_n / m$, A is the cross-sectional area, and $\tau_n \sim 10^{-12} s$ is the scattering time [Tinkham2004] of the quasiparticles. One can transform this parallel conductance per unit length to a series resistance per unit length [Yoshida1995],

$$R_\ell = L_K^2 \omega^2 \sigma_n = \frac{n_n}{n_s} L_K \omega^2 \tau_n g(s, a, t) \quad (3.32)$$

This form of the effective resistance per unit length shows the strong temperature dependence as the BCS theory predicts $n_n/n_s = \exp(-1.76 T_c/T)$, and $L_K \propto \lambda_L^2 \approx \lambda_L(0)^2 (1 - (T_c/T)^4)$. Substituting R_ℓ into Eq. 3.6, the Q due to resistive losses can be expressed as

$$Q_{\text{res}} = \frac{Z_{cn}}{R_n} = \frac{n \pi Z_0}{2 R_{\ell,n} \ell} = \frac{n_s}{n_n} \frac{Z_0 \epsilon_r^{-1/2}}{n L_K \omega_{\lambda/2} \tau_n c g(s, a, t)} \quad (3.33)$$

where the last step is achieved by substituting $\ell = c \pi / \omega_{\lambda/2} \epsilon_r^{-1/2}$. Ideally, the resistive Q can be increased exponentially in T_c/T , to values $> 10^{10}$ [Kuhr2006]. Resonators are often characterized (see Sec. 7.1) at temperatures near T_c , where the resistive Q can be a limiting factor. For ultra high

Material	T_c (K)	H_{C1} (G)	Coherence length, ξ (nm)	London length, λ_L (nm)	λ_L/ξ
Aluminum	1.14	105	1600	16	0.01
Niobium	9.5	1980	38	39	1.02
Tantalum	4.48	830	90	54	0.6

Table 3.1: Important length scales and temperatures for superconductors of interest. Data taken from [Kittel1996] and tantalum data from [Hauser1964, Kittel1996].

Q resonators non-equilibrium effects could also result in higher than expected residual quasiparticle population, and resistive losses.

Dielectric Losses

Even if a resonator could employ perfect conductors, energy would be lost if the electric (or magnetic) field lines pass through a lossy material. The dielectric loss is can be expressed as an imaginary component in the dielectric constant $\epsilon = \epsilon_{re} + i\epsilon_{im}$. A capacitor made from this material with capacitance C , will acquire a conductance

$$G = C\omega \tan \delta \quad (3.34)$$

where $\tan \delta = -\epsilon_{im}/\epsilon_{re}$ is called the loss tangent of the dielectric. The Q of an LCR resonator made with such a capacitor is

$$Q_{\text{diel}} = \frac{\omega_r C}{G} = \frac{1}{\tan \delta} \quad (3.35)$$

One must take the utmost care to use only the most lossless dielectrics such as sapphire, high resistivity silicon, and thermally grown (or crystalline) SiO₂. Specifically it is almost certainly wise to avoid deposited dielectrics. The substrate is thought to be the Q limiting factor [Mazin2004] and one might hope to reduce losses by using a suspended resonator.

Radiative Losses

Even with no material loss the resonator can still lose energy to microwaves radiated into space. A simple model [Mazin2004, Mazin2002] which treats the cavity as a straight CPW transmission line, gives a radiation quality factor,

$$Q_{\text{rad}} \approx 3.5 \left(\frac{\ell}{b} \right)^2 \quad (3.36)$$

where ℓ is the length of the resonator and b is the distance between the CPW ground planes (see Fig. 3.6). For the experimental parameters $\ell \approx 2.5$ cm and $b \approx 20$ μ m, giving $Q_{\text{rad}} \approx 5 \times 10^{-6}$. This formula is approximate and does not take into account the meanders or the ground plane backing, and multiple dielectrics, but says that radiation should allow high quality factors to be achieved.

3.1.8 Quantization of the LC Oscillator

In the previous subsections, lumped element and distributed effective LC circuits were used to make an electronic harmonic oscillator. In this subsection, a LC circuit will be described as a (quantum) harmonic oscillator, with the operators expressed in terms of electrical circuit quantities[Devoret2003].

For a lossless parallel LC circuit the inductor and capacitor share the same voltage so

$$V = -L \frac{\partial I}{\partial t} = q/C \quad (3.37)$$

The energy of the LC oscillator is

$$E = \frac{1}{2}LI^2 + \frac{1}{2}CV^2 \quad (3.38)$$

Which can be conveniently expressed as the Hamiltonian

$$H = \frac{q^2}{2C} + \frac{\delta^2}{2L} \quad (3.39)$$

where q is the charge stored in the capacitor, and $\delta = LI$, is the flux stored in the inductor. I have rewritten the energy in these variables because in this formulation

$$\frac{\partial H}{\partial q} = q/C = -L \frac{\partial I}{\partial t} = -\dot{\delta} \quad (3.40)$$

$$\frac{\partial H}{\partial \delta} = \delta/L = I = \dot{q} \quad (3.41)$$

which defines δ and q as generalized canonical position and momentum variables. In this form, the classical variables map directly to quantum mechanical operators ($\hat{H}, \hat{q}, \hat{\delta}$) and because they are canonical the commutator is

$$[\hat{q}, \hat{\delta}] = -i\hbar \quad (3.42)$$

The Hamiltonian for a particle moving in a harmonic potential is

$$H = \hat{p}^2/2m + \frac{1}{2}m\omega^2\hat{x}^2 \quad (3.43)$$

By analogy, the charge is the momentum ($\hat{q} \sim \hat{p}$), the flux is the position ($\hat{\delta} \sim \hat{x}$), and $\omega \sim 1/\sqrt{LC}$. As with the mechanical oscillator, this Hamiltonian can be written in terms of dimensionless operators

$$H = \hbar\omega(a^\dagger a + 1/2) \quad (3.44)$$

where the photon annihilation operator is given by

$$a = \frac{1}{\sqrt{2\hbar Z_c}} (\delta + iZ_c q) \quad (3.45)$$

where $Z_c = \sqrt{L/C}$ is the characteristic impedance of the circuit. In this language, the charge and flux can be expressed in terms of creation and annihilation operators as

$$q = i\sqrt{\frac{\hbar}{2Z_c}}(a^\dagger - a) \quad (3.46)$$

$$\delta = \sqrt{\frac{\hbar Z_c}{2}}(a + a^\dagger) \quad (3.47)$$

Note the prefactors of $Z_c \sim \sqrt{\mu/\epsilon} \sim 50\Omega$ which can have implications when coupling to an atom or qubit via charge or phase/flux. Using input-output theory, described in chapter 7 of *Walls and Milburn* [Walls2006], the effect of coupling to the environment can be modeled. In their treatment, the cavity is represented by a single electromagnetic mode, coupled to a continuum of bath modes. A quick read through this chapter is highly recommended for a quantum optics view of the cavity, as it is well written and very penetrable.

3.2 Cooper Pair Box

The Cooper pair box (CPB)¹ consists of a superconducting island connected to a reservoir via a Josephson junction. The Josephson junction can be thought of as a circuit element which allows Cooper pairs to coherently couple between the island and reservoir, with a stray capacitance in parallel. A gate voltage (V_g) can be used to electrostatically induce Cooper pairs to tunnel. Usually, a two junction “SQUID” geometry is used which allows the tunnel coupling to be adjusted by application of a magnetic flux (Φ). In this section, the CPB Hamiltonian will be described, first in the charge basis, which naturally incorporates the voltage bias and gives intuitive meaning to the two logical qubit states. Next, the Hamiltonian is rederived in the phase basis, which allows for analytic calculation of the energy levels and wavefunctions. The phase basis will also provide a natural way of approaching a new manifestation of the CPB in section 4.3.

3.2.1 Charge Basis

To lowest order, the CPB can be thought of as a superconducting island with total capacitance to ground, $C_\Sigma = C_g + C_j + C_s$, a gate induced polarization charge, $n_g = C_g V_g/e$, which can be thought of as the preferred amount of excess island charge (in electrons). However, the actual excess charge is a quantized, integer number, \mathbf{N} , of excess Cooper pairs, allowing the box to be electrostatically

¹Two particularly good resources for learning about the CPB are the Cottet [Cottet2002] and Bouchiat [Bouchiat1998] theses. Much of the following discussion closely follows these works.

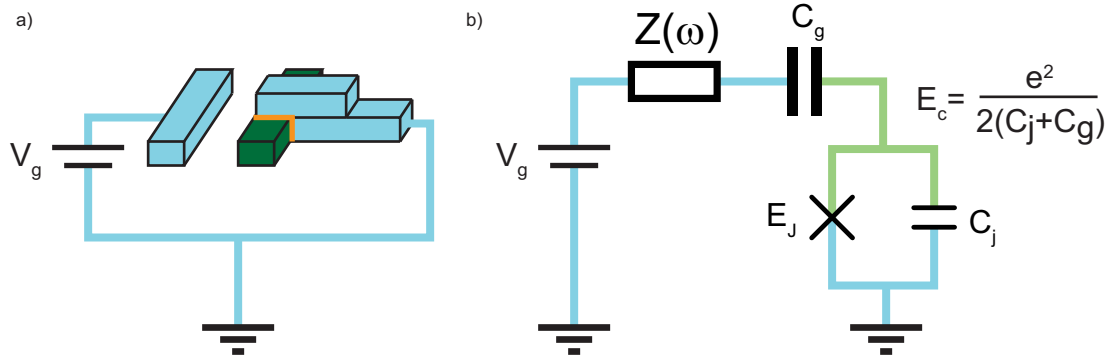


Figure 3.10: **a.** Sketch of CPB circuit. The CPB consists of an island connected to a reservoir via a tunnel junction and is electrostatically biased by a voltage coupled through a small capacitor. **b.** A circuit diagram of the CPB. The island (green) is connected to a ground via a Josephson junction which is represented by a pure Josephson element with energy E_J and a stray capacitance C_j . The charging energy, which sets the scale of electrostatic excitations, is determined by the total capacitance of the island to ground.

frustrated by the gate voltage. The Hamiltonian for this electrostatic component¹,

$$H_{\text{el}} = 4E_C \left(\hat{N} - n_g/2 \right)^2 \quad (3.48)$$

where $E_C = e^2/2C_\Sigma$ is the electrostatic charging energy to add a single electron² to the island. These electrostatic energy levels, the parabolas (dashed and dotted lines) in Fig. 3.11, are just the energies of a capacitor with some fixed charge. If the junction were only capacitive, allowing no tunneling, then Eq. 3.48 would fully describe the Cooper pair box. Charge would be perfectly quantized, but there would be no way of changing the charge state, a rather uninteresting quantum circuit. However, the Josephson effect allows Cooper pairs to coherently tunnel across the junction, described by the Hamiltonian

$$H_J = \frac{E_J}{2} \sum_n (|n\rangle \langle n+1| + |n+1\rangle \langle n|) \quad (3.49)$$

where E_J is the Josephson energy and n is the number of Cooper pairs on the island. This operator in the Hamiltonian allows Cooper pairs to hop on and off the island, acting much like a discrete kinetic energy term in a tight binding model of a lattice.

The shape of the energy bands and composition of the wave functions can be expressed purely in

¹An energy $-C_g V_g^2/2$ has been subtracted off as a gauge choice because it does not depend on any of the dynamical qubit variables.

²The convention in this thesis is that all electrostatic energies and polarization charges are expressed in terms of single electrons.

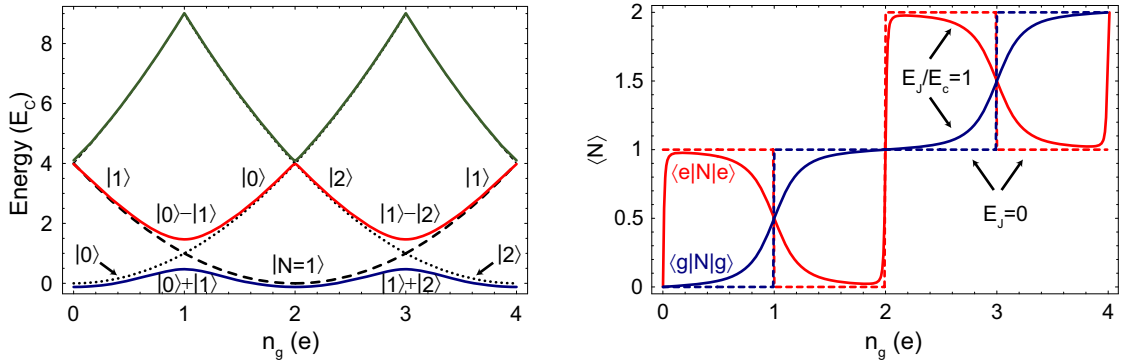


Figure 3.11: **a)** CPB energy levels. Dotted and dashed black lines show electrostatic energy of island for 0 and 1 Cooper pairs present on the island. The (from bottom to top) blue, red, and green solid bands show the ground, and first two excited state energy levels with $E_J = E_C$. At $n_g = 1$ there is an avoided crossing, where the eigenstates are superpositions of n and $n + 1$ Cooper pairs. The midpoint of the avoided crossing occurs at an energy E_C , and the difference between states at even n_g of Cooper pairs is $4E_C$. **b)** A plot of the expected number of Cooper pairs (each with charge of $2e$) of the ground (blue) and first excited (red) state. The dashed/dotted curves have $E_J = 0$ and so the expected value is just the lowest energy integer charge state, whereas the solid curves with $E_J = E_C$ have non-integer expected charge values indicating strongly overlapping superpositions of charge states. At $n_g = 1$ they have the same expected charge $2e\langle \hat{N} \rangle = 1e$, meaning that they can not be distinguished by a charge based measurement or affected (to first order) by charge noise.

terms of the ratio¹ E_J/E_C . When the characteristic tunneling energy is much less than the charging energy ($E_J \ll 4E_C$), in the charge qubit regime, then the qubit state can be accurately expressed in terms of the nearest two charge states. In the charge qubit regime, the most important effect shown in Fig. 3.11a is that the Josephson coupling lifts the degeneracy present when the Cooper pair box is electrostatically frustrated at $n_g = 1$. At this bias condition, the ground and excited eigenstates are superpositions of charge states $(|0\rangle \pm |1\rangle)/\sqrt{2}$ with a ground-excited state energy difference $E_{eg} = E_J$. When $E_{eg} > k_B T$ then there will be no thermal population of the first (or any higher lying) excited state.

When using the CPB as a qubit, it is convenient to reexpress the lowest two levels of the Hamiltonian in the language of a spin-1/2, which can be done by taking the first two levels, subtracting their mean energy, and approximating the operators as $|n\rangle \langle n+1| + |n+1\rangle \langle n| \rightarrow \sigma'_x$ and $\hat{N} \rightarrow \sigma'_z/2$.

$$H_{\text{CPB}} = -\frac{1}{2}(4E_C(1-n_g)\sigma'_z + E_J\sigma'_x) \quad (3.50)$$

This is the Hamiltonian of a spin² (with $\mu = 1$) subject to a fictitious magnetic field, $B = E_J\hat{x}' +$

¹The effects of different E_J/E_C ratios will be discussed in more detail chapter 4.

²Even well into the “transmon” regime, where $E_J \geq 4E_C$, the CPB can be expressed in this form, but the field

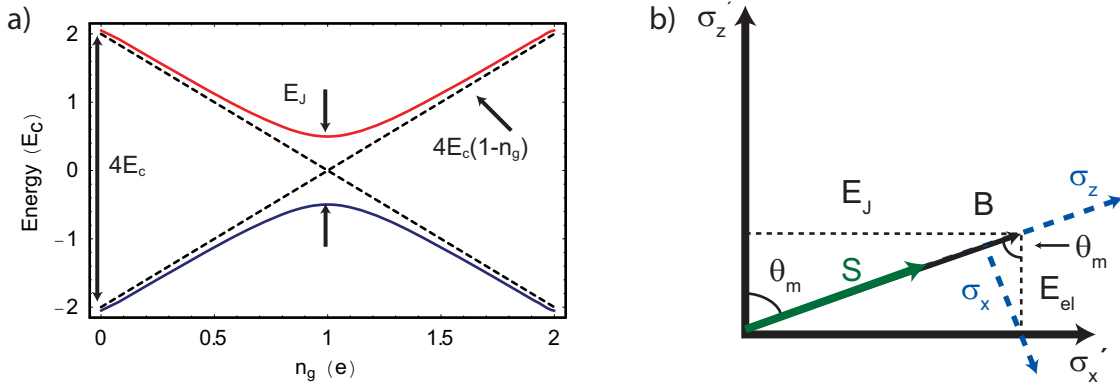


Figure 3.12: **a.** Energy levels from the two state approximation in Eq. 3.52, are (solid) hyperbolas, which asymptote (dashed lines) to $4E_C(1 \pm n_g)$. **b.** Fictitious field picture of a point close to $n_g = 1$, in the $x' - z'$ basis and the showing transformation to the basis where \hat{z} is along the quantization axis.

$$4E_C(1 - n_g)\hat{z}'.$$

As can be seen from Fig. 3.12 the Coulomb energy away from degeneracy depends nearly linearly on n_g . Fluctuations in n_g , which arise from noise on the voltage bias and charge noise due to impurities in the box itself, can lead to fluctuations in the qubit transition energy. At $n_g = 1$ however the transition energy is insensitive, to first order, to small fluctuations of n_g . This allows one to obtain much longer coherence times (see section 4.2). For this reason, the CPB is usually operated at $n_g = 1$, and the discussion that follows will focus on this bias condition. More detail on optimizing the CPB parameters and operating point to minimize decoherence will be discussed in chapter 4.

The effective field and quantization axis is parallel to the net magnetic field (see Fig. 3.12). It is often convenient to work in a coordinate system rotated about the \hat{y}' -axis by a mixing angle

$$\theta_m = \arctan\left(\frac{E_J}{4E_C(1 - n_g)}\right) \quad (3.51)$$

In this new coordinate system, quantization is along the \hat{z} -axis and $H_{CPB} = \hbar\omega_a\sigma_z$ where

$$\hbar\omega_a = \sqrt{E_J^2 + (4E_C(1 - n_g))^2} \quad (3.52)$$

At $n_g = 1$, the electrostatic component is $H_{el} = 0$ and $\theta_m = \pi/2$, leaving the Josephson component

strengths will have a more complicated functional form. The two energy level (not charge state) approximation is useful as long as the ground-excited energy difference is not harmonic with the next transition. The dependence of this anharmonicity on E_J/E_C and its implications for using the CPB as a qubit will be discussed in chapter 4.

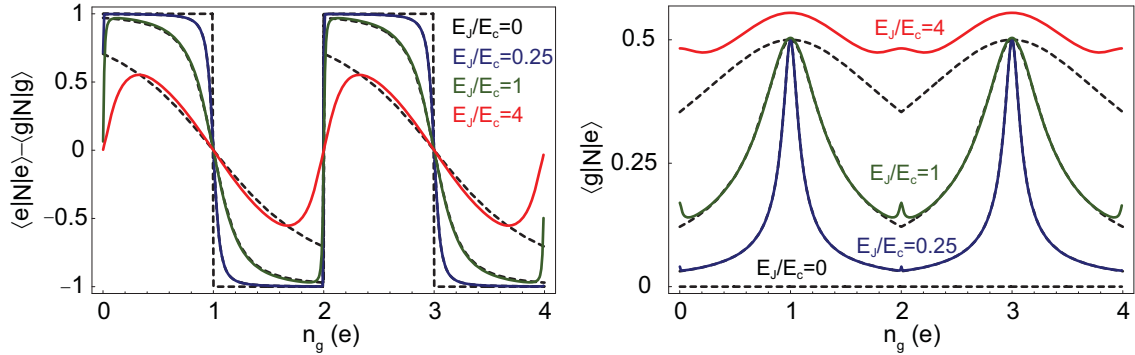


Figure 3.13: **a)** Charge difference between ground and first excited state ($\langle e | \hat{N} | e \rangle - \langle g | \hat{N} | g \rangle$) at different E_J/E_C ratios. The charge difference is largest away from $n_g = 1$. The dashed black lines are calculated using a two charge-state approximation $\cos(\theta_m)$ **b)** The transition (dipole) matrix element ($\langle g | \hat{N} | e \rangle$) however does not go to zero at degeneracy, and in fact is largest at $n_g = 1$. The dashed two charge approximation is $|\sin(\theta_m)|/2$, which is $1/2$ at $n_g = 1$ because the state is an even superposition of charge states. The cusps at $n_g = 2$ are due to the coupling of the first and second excited states. In both cases the approximations begin to break down as E_J/E_C increases. In the two charge approximation one would expect the transition matrix element to never rise above $1/2$ (an even superposition of two states one Cooper pair apart). At $E_J/E_C = 4$ the superpositions contain more states raising the expectation value.

to determine the quantization axis, $\sigma'_x \rightarrow \sigma_z$. Qubit manipulations are performed via electrostatic excitation along what is now the σ_x direction. At an arbitrary n_g , gate excitations affect both the perpendicular (as $\sigma_x \sin \theta_m$), allowing the qubit to be flipped, and the longitudinal component (as $\sigma_z \cos \theta_m$) allowing implementation of electrostatic phase gates. Thermal and vacuum fluctuations are similarly divided, affecting the CPB decoherence properties discussed in chapter 4.

3.2.2 Phase Basis

The charge basis provides an intuitive framework for visualizing the states of the Cooper pair box. However, because it is an unbounded discrete basis most calculations must be done approximately by numerically diagonalizing a subspace including many nearest charge states. Phase is the canonical conjugate to charge and while the charge is discrete the phase is continuous (though periodic). In the phase basis the energies and wavefunctions can be solved analytically, making it cheaper computationally and less susceptible to truncation error¹. The superconducting phase difference, $\hat{\theta}$,

¹The number of charge states increases when $E_J \geq 4E_C$, making the phase basis more appropriate for analysis of CPB's with large E_J/E_C .

is related to the tunneling current across the junction and can be defined by the relations

$$\hat{n} = i \frac{\partial}{\partial \theta} \quad (3.53)$$

$$\hat{n} \exp{i\theta} = \exp{i\theta} (\hat{n} + 1) \quad (3.54)$$

and eigenstates corresponding to

$$|\theta\rangle = \sum_{n=-\infty}^{\infty} e^{i\theta n} |n\rangle \quad (3.55)$$

$$|n\rangle = \int_0^{2\pi} d\theta e^{-i\theta n} |\theta\rangle \quad (3.56)$$

Rewriting the $|n\rangle$'s in Eqs. 3.48 and 3.49 in the $|\theta\rangle$ basis, one can rewrite the box Hamiltonian $H_{\text{CPB}} = H_{\text{el}} + H_{\text{J}}$ in the phase basis as¹

$$H_{\text{CPB}} = 4E_C \left(i \frac{\partial}{\partial \theta} - n_g/2 \right)^2 |\theta\rangle \langle \theta| - \frac{E_J}{2} (e^{i\theta} + e^{-i\theta}) |\theta\rangle \langle \theta| \quad (3.57)$$

The time independent Schrödinger equation becomes $H_{\text{CPB}} |k\rangle = E_k |k\rangle$. The phase wave function $\psi_k(\theta) \equiv \langle \theta | k \rangle$ is then the solution of the differential equation

$$4E_C \left(i \frac{\partial}{\partial \theta} - n_g/2 \right)^2 \psi_k - E_J \psi_k \cos \theta = E_k \psi_k \quad (3.58)$$

This equation resembles the equation of motion of a pendulum which is allowed to make large angular excursions, and lies in the class of Mathieu equations, which can be solved analytically[Cottet2002, Arscott1964]. Their solutions are prepackaged in *Mathematica* and a specific implementation is presented in Appendix C, or for a more detailed derivation see ref.[Cottet2002].

3.2.3 Split CPB

In the previous Hamiltonian, the electrostatic (\hat{x} field) component can be tuned by application of a gate voltage (V_g). The ability to tune the tunneling (E_J) portion of the Hamiltonian is readily achieved by splitting the Josephson junction, as shown in Fig. 3.14. Each junction will have a characteristic tunneling energy (E_{J1}, E_{J2}) and superconducting phase ($\hat{\theta}_1, \hat{\theta}_2$) across it. The Josephson part of the Hamiltonian is just the sum of the contributions of the two junctions.

$$H_J = E_{J1} \cos(\theta_1) + E_{J2} \cos(\theta_2) \quad (3.59)$$

¹The implicit integral over θ has been suppressed in Eq. 3.57 for clarity.

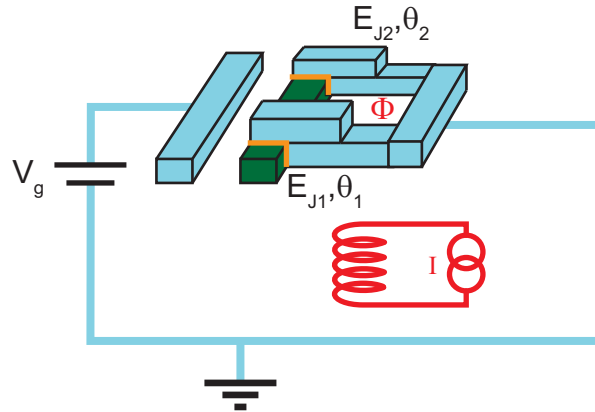


Figure 3.14: Sketch of the split Cooper pair box. The island is connected to a reservoir by two junctions, each with a Josephson energy E_{J1}, E_{J2} and phase difference $\hat{\theta}_1, \hat{\theta}_2$. Splitting the box gives the ability to tune the effective $E_J = (E_{J1} + E_{J2}) \cos(\pi\Phi/\Phi_0)$ by applying a magnetic flux Φ .

It is convenient to define two new variables

$$\theta = \frac{\theta_1 + \theta_2}{2} \quad (3.60)$$

$$\varphi = \theta_1 - \theta_2 \quad (3.61)$$

Using flux quantization¹ the phase difference, φ , can be rewritten in terms of the magnetic flux piercing the loop (see Fig. 3.14), Φ , as $\varphi = 2\pi\Phi/\Phi_0$ where $\Phi_0 = h/2e$ is the superconducting flux quantum. Substituting the relations in Eq. 3.61, and using trigonometric substitutions one can rewrite this expression as

$$H_J = (E_{J1} + E_{J2}) \cos\left(\pi\frac{\Phi}{\Phi_0}\right) \cos\theta + (E_{J2} - E_{J1}) \sin\left(\pi\frac{\Phi}{\Phi_0}\right) \sin\theta \quad (3.62)$$

If the two junctions are symmetric ($E_{J1} = E_{J2}$), or there is no external flux ($\Phi = 0$), the expression simplifies to the single junction Hamiltonian (as in Eq. 3.57), with a flux tunable effective Josephson energy

$$E_J^{\text{sum}} = (E_{J1} + E_{J2}) \quad (3.63)$$

$$d = \frac{E_{J1} - E_{J2}}{E_J^{\text{sum}}} \quad (3.64)$$

¹Flux quantization [Tinkham2004] arises because the wavefunction inside of a superconductor must be single valued meaning that, $\oint \nabla\varphi \cdot ds = 2\pi n$. For a superconducting loop interrupted by a junction, this integral is most conveniently expressed in terms of the phase difference across the junction, φ and the magnetic flux enclosed as $\Delta\varphi + 2\pi \oint (m^*v_s/h + A/\Phi_0) \cdot ds = 2\pi n$, where because no current flows inside the bulk of the superconductor the net Cooper pair velocity, $v_s = 0$. Using Stokes' theorem the integral can be rewritten as $\Phi/\Phi_0 = \int_S B/\Phi_0 \cdot dA$. Substituting and solving for $\Delta\varphi$, yields $\Delta\varphi = 2\pi\Phi/\Phi_0 + 2\pi n$. It is valid to treat this phase as a classical variable because the asymmetric mode of the squid has the junctions effectively shunted by the rest of the loop[Cottet2002].

In our typical devices the junction asymmetry is $d \sim 10\%$ and so the Josephson terms in Eq. 3.62 cannot be suppressed completely. Typically the CPB is operated with integer flux in the ring, $\Phi = n\Phi_0$, then $\sin(\pi\Phi/\Phi_0) = 0$, further suppressing the difference term, and one can hope to ignore its effects to first order. When E_J^{sum} is suppressed by applying a field, then flux noise in the difference term could potentially contribute to decoherence. Also the $\sin \theta$ term presents an opportunity couple the qubit states through flux, even at $n_g = 1$. This might allow a non-cavity excitation channel, and may also be relevant with the transmon geometry, where charge noise is almost completely suppressed, potentially leaving flux noise to dominate the decoherence properties (see Sec. 4.3).

One can transform this split CPB Hamiltonian in the phase basis back to the charge basis using the Eq. 3.55 to map

$$\cos \theta \rightarrow \frac{1}{2} (|n\rangle \langle n+1| + |n+1\rangle \langle n|) \sim \sigma'_x \quad (3.65)$$

$$\sin \theta \rightarrow \frac{i}{2} (|n\rangle \langle n+1| - |n+1\rangle \langle n|) \sim \sigma'_y \quad (3.66)$$

so the junction Hamiltonian in the charge basis is

$$H_J = E_J^{\text{sum}} \sum_n \frac{\cos(\pi\Phi/\Phi_0)}{2} (|n\rangle \langle n+1| + |n+1\rangle \langle n|) + \frac{id \sin(\pi\Phi/\Phi_0)}{2} (|n\rangle \langle n+1| - |n+1\rangle \langle n|) \quad (3.67)$$

In the two state approximation the total Hamiltonian can be written

$$H_{\text{CPB}} = \frac{E_J^{\text{sum}}}{2} (\cos(\pi\Phi/\Phi_0) \sigma_x + d \sin(\pi\Phi/\Phi_0) \sigma_y) + 4E_C(1 - n_g)\sigma_z \quad (3.68)$$

The transition energy of the split CPB is

$$E = \sqrt{E_J^{\text{sum}}{}^2 (\cos^2(\pi\Phi/\Phi_0) + d^2 \sin^2(\pi\Phi/\Phi_0)) + 16E_C^2(1 - n_g)^2} \quad (3.69)$$

3.3 Coupling CPB to Cavity

The electrostatic Hamiltonian, H_{el} of Eq. 3.48, depends on a polarization charge $n_g = C_g V_g/e$. Inside of a cavity, the gate voltage, V_g , is the voltage between the center-pin and ground planes (See Fig. 3.15). The total voltage can be written as the sum of a classical DC voltage and a quantum voltage due to the photons inside the resonator.

$$V_g = V_{\text{DC}} + \hat{V} \quad (3.70)$$

where $\hat{V} = \hat{q}/C$. Substituting into Eq. 3.46 yields¹

$$\hat{V} = \sqrt{\frac{\hbar\omega_r}{2C}}(a + a^\dagger) \quad (3.71)$$

Plugging this into the H_{el} (Eq. 3.48) and expanding the square gives

$$H_{\text{el}} = 4E_C \left(\hat{N} - n_g/2 \right)^2 + \frac{4E_C C_g \hat{V} (2V_g + \hat{V})}{e} - \frac{4E_C C_g \hat{V} \hat{N}}{e} \quad (3.72)$$

The first term is just the original electrostatic Hamiltonian with classical bias. The second term is extra energy stored in the geometric capacitance of the qubit, and is not qubit state dependent, thus it does not affect any of the qubit(-cavity) dynamics. The final term, which represents the resonator-CPB coupling Hamiltonian, H_c , depends both on the CPB state and the quantum field state of the resonator.

$$H_c = 2\hbar g(a^\dagger + a)\hat{N} \quad (3.73)$$

$$g = \frac{eV_0}{\hbar}\beta \quad (3.74)$$

$$V_0 = \sqrt{\frac{\hbar\omega_r}{2C}} \quad (3.75)$$

Where $\beta = C_g/C_\Sigma$ accounts² for the division of voltage in the CPB. The coupling constant $2\hbar g$ can be seen as the energy in moving a Cooper pair ($2e$) across the portion ($\beta = C_g/C_\Sigma$) of the rms vacuum voltage fluctuations (V_0) in the resonator. Eq. 3.75 for the zero point voltage can be derived from the following relation,

$$\frac{1}{2} \left(\frac{1}{2} \hbar\omega_r \right) = \frac{1}{2} CV_0^2 \quad (3.76)$$

where the first $1/2$ is because half of the zero point energy is stored in the electric field and half is in the magnetic field. How large can this dipole coupling get? To answer this critical question most generally, one can look at the dimensionless coupling g/ω_r

$$\frac{g}{\omega_r} = \frac{\beta e V_0}{\hbar\omega_r} = \beta \sqrt{\frac{Z_c e^2}{2\hbar}} \quad (3.77)$$

where we have employed $Z_c = 1/\omega_r C$ to reexpress the coupling in terms of the characteristic impedance. One can rewrite the characteristic impedance of the effective resonance in terms of

¹I have made a slight change of convention changing to $q \propto (a + a^\dagger)$ rather than $(a - a^\dagger)$ so that the resulting Jaynes-Cummings Hamiltonian will be in its standard form. For a harmonic oscillator this is purely a phase convention.

² $\beta = C_g/C_\Sigma$ assumes a well grounded box with $C_g \ll C_\Sigma$. By judicious design of the capacitance network (see Sec. 5.2) β can be engineered to be anywhere between zero and one.

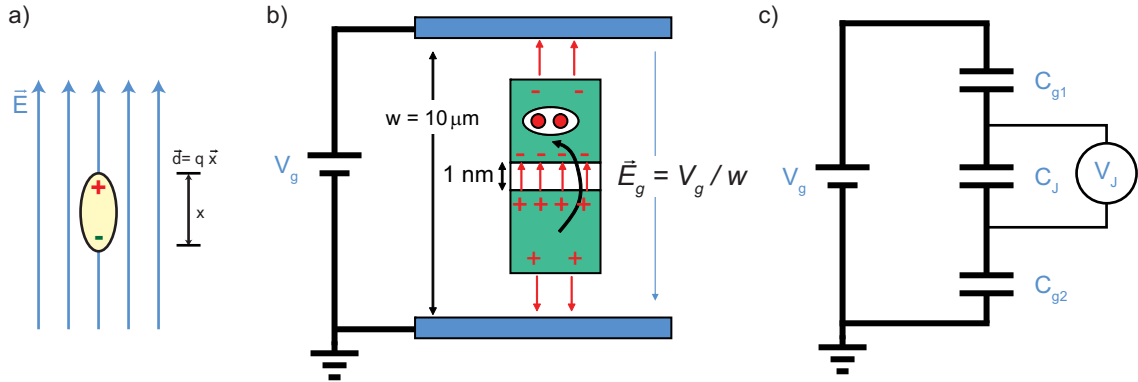


Figure 3.15: a) Schematic depiction of dipole moment of an atom $\vec{d} = q\vec{x}$ in an electric field \vec{E} , which has energy $U = -\vec{E} \cdot \vec{d}$. b) The CPB can be thought of as molecule inside of an electric field produced by applying a gate voltage V_g across a gap of width w . Because the Cooper pairs can move freely on each island, a Cooper pair can move by microns even though the junction is only $\sim 1 \text{ nm}$, allowing the dipole moment to be adjusted. c) A more appropriate picture of the dipole energy of a circuit is $U = -2eV_j$, where $V_j = \beta V_g$ is the voltage dropped across the actual junction, a fraction β of the original gate voltage (See chapter 5 for details).

the transmission line impedance $Z_0 = n\pi Z_C/2$ (Eq. 3.13)

$$\frac{g}{\omega_r} = \beta \sqrt{\frac{2Z_0}{nh/e^2}} = \beta \sqrt{\frac{2}{n} \frac{Z_0}{R_K}} \quad (3.78)$$

where $R_K = h/e^2 \approx 25.8 \text{ k}\Omega$ is the resistance quantum. The line impedance is $Z_0 = \xi \eta_0 \sqrt{\mu_r/\epsilon_r}$, where $\eta_0 = \sqrt{\mu_0/\epsilon_0} \approx 377 \Omega$ is the impedance of free space and $\xi \sim 0.4$ (for a CPW) is a dimensionless geometry dependent factor of order unity. Substituting for Z_0 yields

$$\frac{g}{\omega_r} = \beta \xi \sqrt{\frac{2\alpha}{n}} \left(\frac{\mu_r}{\epsilon_r} \right)^{1/4} \quad (3.79)$$

which consists of dimensionless constants, and amazingly, the fine structure constant, α ! Here we see the fine structure constant in circuit form as the ratio of the vacuum impedance and the resistance quantum

$$\alpha = \frac{\eta_0}{R_K} = \frac{e^2}{2\epsilon_0 hc} \approx \frac{1}{137} \quad (3.80)$$

If the coupling is maximized ($\beta = 1$) the maximum dimensionless coupling strength can be made about $\sim 10\%$. The Hamiltonian in Eq. 3.73 describes the interaction between any two CPB states. At $n_g = 1$ in the charge regime¹

$$\hat{N} \approx \langle g | \hat{N} | e \rangle \sigma_x \approx \sin \theta_m \sigma_x / 2 + \cos \theta_m \sigma_z / 2 \quad (3.81)$$

¹At high E_J/E_C one has to be more careful when evaluating $\langle g | \hat{N} | e \rangle$.

At $n_g = 1$ where the CPB is usually operated $\hat{N} = \sigma_x/2$. In addition one can make the dipole or rotating wave approximation that

$$(a^\dagger + a)\sigma_x = a^\dagger\sigma^- + a\sigma^+ \quad (3.82)$$

which ignores terms like $a^\dagger\sigma^+$ and $a\sigma^-$ which change the number of excitations in the system. This assumption is valid when the energy of adding both a photon and qubit excitation is much larger than the coupling and the energy difference between a photon and a qubit excitation ($\omega_r + \omega_a \gg g, |\omega_r - \omega_a|$).

$$H_c = \hbar g(a^\dagger\sigma^- + a\sigma^+) \quad (3.83)$$

adding this to the harmonic oscillator and qubit contributions gives the Jaynes-Cummings Hamiltonian

$$H_{jc} = \hbar\omega_r(n + 1/2) + \hbar\frac{\omega_r}{2}\sigma_z + \hbar g(a^\dagger\sigma^- + a\sigma^+) \quad (3.84)$$

Exercise 3.3.1. Derive the fine structure limit of g/ω for a dipole inside a three-dimensional cavity.

- a.** $g/\omega = dE_0/\hbar\omega$. Find rms vacuum electric field, E_0 , inside a 3D cavity assuming that the electric field is uniformly distributed in the volume $\sim \lambda^3$ of the cavity. **b.** Assuming that the dipole moment is $d = e\Delta x$, rewrite g/ω in terms of the fine structure constant α . What quantity plays the role of β ? What does this say about relative coupling strengths of atoms to 3D cavities and 1D cavities?

3.3.1 Comparison with Traditional Cavity QED

A cavity QED experiment can be characterized by several frequency scales. The transition frequencies of the atom/qubit (ω_a) and cavity (ω_r) determine the overall energy scale of the system. The dipole coupling rate g sets the interaction rate of the cavity and qubit. Finally the decoherence times $1/\gamma$ and $1/\kappa$ set the length of time before the interactions are polluted. To study interactions between these quantum systems, the ratios of the coupling to the decoherence rates (N_0 , m_0 , and n_{Rabi}) are most important. For example, $N_0 \equiv 2\gamma\kappa/g^2$, is the critical atom number, which can be interpreted as the number of atoms required in the cavity to split the cavity line, and characterizes the maximum rate at which a single photon measures the qubit state. Similarly the critical photon number, $m_0 = \gamma^2/2g^2$, tells how many photons in the cavity in its steady state are required to saturate the qubit, and indicates how sensitive the qubit is as a photon detector. Finally the number of vacuum Rabi oscillations possible, $n_{\text{Rabi}} = \frac{2g}{\kappa+\gamma}$, determines whether one is in the strong coupling regime ($n_{\text{Rabi}} > 1$) and is related to the maximum efficiency of converting an excitation between a

qubit state and a photon. Table 3.3.1 shows circuit QED attains similar values to traditional atomic cavity QED. It does so by having a much stronger dimensionless coupling $g/\omega \approx 1 - 10\%$.

To compare the CPB to an atom independent of the cavity one can define a transition dipole moment. The dipole moment can be reexpressed as $\hbar g = (ew)\frac{1}{w}V_0 = dE_0$ where w is the transverse dimension of the CPW, E_0 is the rms vacuum electric field, and d is the effective dipole moment of the CPB. While this language furthers the image of CPB as artificial atom, from this definition it is clear that circuit QED behaves fundamentally differently from atomic QED where the dipole moment is a fixed property of the atom. Here the dipole moment of the box can be adjusted to give the maximum g for any E_0 . If the cavity is made larger or smaller (reducing E_0) the box can be adjusted to maintain the same coupling. With circuits the properties of the two systems really are inextricably linked. Currently atomic experiments have truly fantastically coherent atoms and resonators, but achieve only a small fraction of their maximum potential dimensionless coupling g/ω . One promising avenue for increasing this coupling is to use cavities with higher E_0 (smaller transverse dimension). The 1D transmission line resonators, might be very promising as they allow the field to be adjusted by changing the gap between center conductor and ground planes.

parameter	symbol	3D optical	3D microwave	Semiconductor	1D circuit
resonator/atom frequency	$\omega_r/2\pi, \Omega/2\pi$	350 THz	51 GHz	250 THz	5 GHz
vacuum Rabi frequency	$g/\pi, g/\omega_r$	$220 \text{ MHz}, 3 \times 10^{-7}$	$47 \text{ kHz}, 5 \times 10^{-7}$	$41 \text{ GHz}, 8 \times 10^{-5}$	$100 \text{ MHz}, 10^{-2}$
transition dipole	d/ea_0	~ 1	1×10^3	2×10^4	30
cavity lifetime	$1/\kappa, Q$	$10 \text{ ns}, 3 \times 10^7$	$1 \text{ ms}, 3 \times 10^8$	$4 \text{ ps}, 6 \times 10^3$	$160 \text{ ns}, 10^4$
atom lifetime	$1/\gamma$	61 ns	30 ms	7 ps	$2 \mu\text{s}$
atom transit time	t_{transit}	$\geq 50 \mu\text{s}$	$100 \mu\text{s}$	∞	∞
critical atom number	$N_0 = 2\gamma\kappa/g^2$	6×10^{-3}	3×10^{-6}	1.1	$\leq 6 \times 10^{-5}$
critical photon number	$m_0 = \gamma^2/2g^2$	3×10^{-4}	3×10^{-8}	0.5	$\leq 1 \times 10^{-6}$
# of vacuum Rabi flops	$n_{\text{Rabi}} = \frac{2g}{\kappa+\gamma}$	~ 10	~ 5	1.3	$\sim 10^2$

Table 3.2: Key rates and parameters for atomic [Hood2000] and microwave [Raimond2001] atomic systems using 3D cavities, semiconductors [Reithmaier2004, Yoshie2004] and superconducting circuits. For the 1D superconducting system, a full-wave ($L = \lambda$) resonator, $\omega_r/2\pi = 10$ GHz, a relatively low Q of 10^4 and coupling $\beta = C_g/C_\Sigma = 0.1$ are assumed. For the 3D microwave case, the number of Rabi flops is limited by the transit time. For the 1D circuit case, the intrinsic Cooper-pair box decay a conservative value equal to typical experimental $\gamma \sim 1/(2 \mu\text{s})$ is assumed.

3.4 Measurement Theory

3.4.1 Quantum Non-Demolition Measurements

Measurement is the process of coupling a small ephemeral system quantity, A , to a robust quantity, M , of a meter system. Quantum mechanically, this is done by performing a projective measurement with a measurement operator $\chi \hat{M} \hat{A}$, with χ characterizing the measurement strength. An ideal classical measurement maps the system state to the measurement apparatus perfectly and without destroying the original state. However, even assuming that the meter is otherwise independent of the system, the Heisenberg uncertainty principle requires that reducing the uncertainty in one system variable (measuring A) increases the uncertainty in (modifies) another conjugate system variable. To illustrate this effect concretely, imagine two quantities measured by the operators \hat{A} and \hat{B} . If both operators leave the state they measure intact, then the order of measurement should not matter, and the following quantity should be zero.

$$\hat{A}\hat{B}|\Psi\rangle - \hat{B}\hat{A}|\Psi\rangle = [\hat{A}, \hat{B}]|S\rangle \quad (3.85)$$

If the commutator $[\hat{A}, \hat{B}]$ is zero, then a measurement of A does not effect a measurement of B , though it may change ψ . Because an operator always commutes with itself, it is possible in principle to measure an observable and then faithfully obtain the same result many times. In order to perform repeated measurements over a finite period of time, the measurement operator (or state property) cannot change during the measurement process, implying

$$\frac{d\hat{M}\hat{A}}{dt} = \frac{1}{i\hbar}[\hat{M}\hat{A}, \hat{H}] = 0 \quad (3.86)$$

When equation 3.86 is satisfied, repetitions are possible, and the measurement is said to be quantum non-demolition (QND). Demolition can occur either if the probe is not exactly along the desired measurement axis, or if the observable itself is not an eigenstate of the Hamiltonian. QND measurements are important because in addition to allowing more faithful measurements, the same type of interactions generate entanglement, which can be used to generate logic gates.

3.4.2 Mapping Qubit State onto Cavity State

The interaction between the cavity and the qubit can be used to map the qubit state onto the phase or amplitude of the cavity photons. A single qubit can be mapped on to many photons, giving energy gain, which can be used to overcome any detector inefficiencies, such as photons lost in the line, or

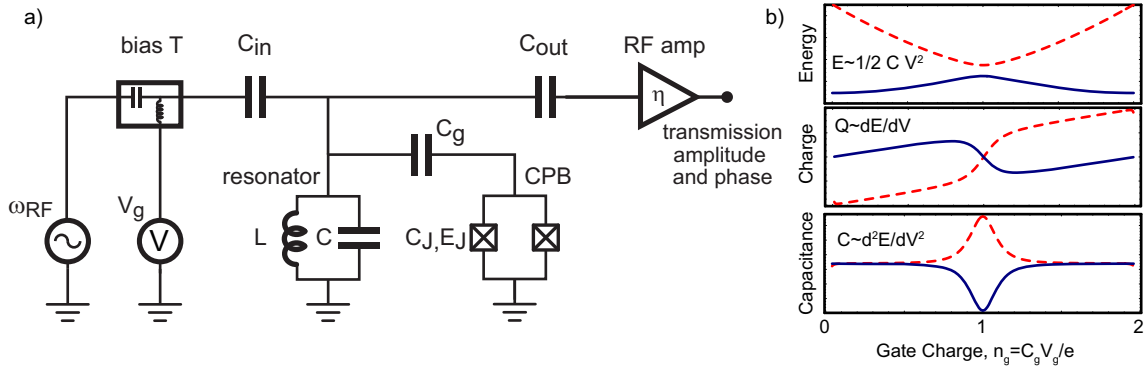


Figure 3.16: a) Simplified measurement schematic. The amplifier adds $k_B T_N B$ of noise for an effective efficiency $\eta = \hbar \omega_r / k_B T_N$. The CPB box acts as a state dependent capacitance which adds to the resonator capacitance, shifting its resonance frequency. b) Energy levels and derivatives of the CPB vs. gate charge. Measurements of the CPB can use the charge, which is similar to the first derivative of the energy, or the effective capacitance which (at low frequencies) is related to the curvature of the bands.

masked by noise inside the amplifier. First, let us describe the interaction in electrical engineering terms. The CPB acts as a capacitor except near degeneracy where there is an avoided crossing. For a capacitor $E = CV^2/2$ and one can define a dynamical capacitance by the relation

$$C = \frac{d^2E}{dV^2} \quad (3.87)$$

As shown in Fig. 3.16 the capacitance is approximately constant (and state-independent) everywhere except near $n_g = 1$, where it becomes positive or negative depending on the state. This “quantum capacitance” [Widom1984, Averin2003] will load the resonator differently depending on the qubit state, changing its resonance frequency slightly. Because both the capacitance of the CPB and the resonator impedance are purely reactive, or dispersive, no energy is deposited on the chip, an important property since excess energy can excite quasi-particles [Lutchyn2005, Lutchyn2006] or two-level fluctuators [Simmonds2004]. Because it can be so non-invasive, the technique has since been adapted to make dispersive readouts of other systems like single Cooper pair transistors [Duty2005]. This semiclassical argument should be considered the low frequency limit of a more general dipole coupling. It is valid when variations in gate voltage are very slow compared to the transition frequency. At high frequencies, the simple dynamical capacitance argument gets the sign wrong, and at high E_J/E_C the simple argument incorrectly predicts that the capacitance goes to zero. It is more appropriate to treat the system quantum mechanically, where the frequency shift of the resonator can be computed directly by diagonalization. One can avoid this confusion entirely by

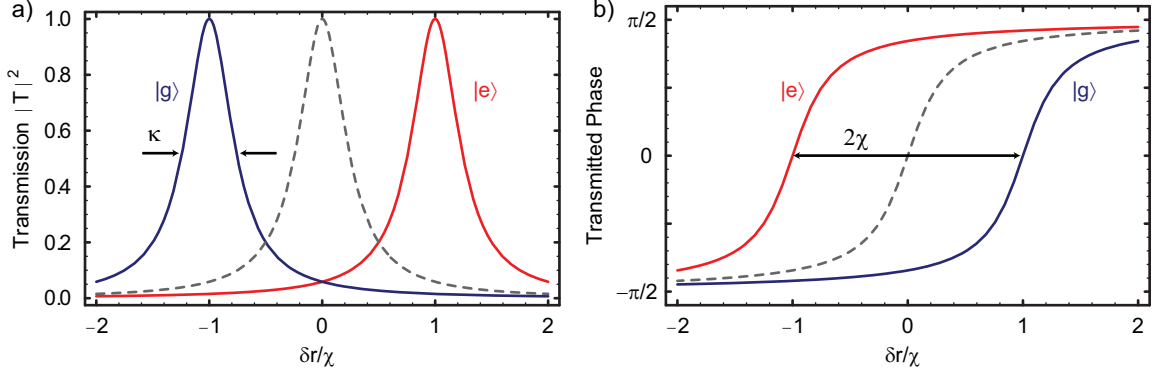


Figure 3.17: State dependent transmitted amplitude (a) and phase (b) of the resonator in the qubit ground (blue) and excited (red) states, as well as the bare resonator spectrum (dashed). The peaks are located at $\pm\chi$ and can be distinguished either by measuring in amplitude or in phase.

looking directly at the dispersive Hamiltonian (Eq. 2.2 repeated below).

3.4.3 Distinguishing Cavity States

The following discussion is based on the steady state solutions derived in reference [Gambetta2006], which contains more detailed derivations and transient effects that can lead to additional inhomogeneous broadening, and number splitting (discussed in section 8.3).

$$H \approx \hbar(\omega_r + \chi\sigma_z)(a^\dagger a + 1/2) + \hbar\omega_a \sigma_z/2 \quad (3.88)$$

The first term in the dispersive Hamiltonian describes a cavity, which now has a resonance frequency, $\omega_r \pm \chi$, where $\chi = g^2/\Delta$ is a qubit state dependant frequency shift. The problem of measuring the CPB can now be rephrased as the problem of determining the frequency of the cavity. The cavity is interrogated with a coherent drive of amplitude (inside the cavity), ϵ_{rf} , at a detuning of $\delta_{rf} = \omega_{RF} - \omega_r$ from the bare resonator frequency. The coherent state phasor inside the cavity is

$$\alpha_\pm = \frac{\epsilon_{rf}}{\frac{\kappa_{in}+\kappa_{out}}{2} + i(\delta_{rf} \pm \chi)} \quad (3.89)$$

with amplitudes

$$|\alpha_\pm|^2 = n_\pm = \frac{\epsilon_{rf}^2}{\frac{(\kappa_{in}+\kappa_{out})^2}{4} - (\delta_{rf} \pm \chi)^2} \quad (3.90)$$

The amplitude inside the cavity is related to the input amplitude by $\epsilon_{rf} = \epsilon_{in}\sqrt{\kappa_{in}}$. The amplitude of the transmitted wave (to the amplifier) is related to the cavity amplitude¹ as $\epsilon_{out} = \epsilon_{rf}\sqrt{\kappa_{in}}$.

¹Note that ϵ_{in} , ϵ_{rf} , and ϵ_{out} have different units. This is due to some issues in the way discrete and continuous modes are normalized.

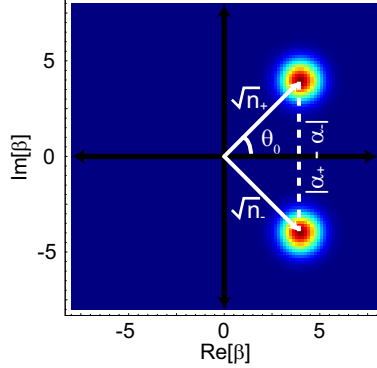


Figure 3.18: Plot in phase space of the Q-function defined in Eq. 3.91, which shows the probability of measuring a given coherent state. This would be the plot of the superposition $|\alpha_+\rangle + |\alpha_-\rangle$ with $n_{\pm} = 16$ photons. Since the Q-function of a coherent state is a gaussian, the overlap of the states can be expressed in terms of the distance between their centers $D = |\alpha_+ + \alpha_-|^2$. It is often useful to think about this distance per photon, equivalent to $\sin \theta_0$, where $\theta_0 = \arctan(2\chi/\kappa)$. In this plot the $|\alpha_{\pm}\rangle$ states are symmetric about the real axis ($\Delta_r = 0$) and $\theta_0 = \pi/2$, which is typically optimal for measurement.

Coherent states are conveniently plotted in phase space (see Fig. 3.18), where the amplitude and phase of the wave are the radius and angle respectively. The probability distribution or Q function, can be expressed as

$$Q(\beta, \psi) \equiv \langle \psi | \beta \rangle \langle \beta | \psi \rangle \quad (3.91)$$

which if $|\psi\rangle = |\alpha\rangle$ is a coherent state then the overlap probability is

$$Q(\beta, \alpha) = \exp(-D^2) \quad (3.92)$$

where the distinguishability $D^2 = |\alpha_+ - \alpha_-|^2$, can be thought of as the information about the qubit state stored in the cavity. From figure 3.18 one can see that this quantity represents the difference in IQ space of the coherent states associated with either qubit state, or more practically the difference signal when the cavity is measured at the optimal phase. The cavity is not really a classical meter, having coherent dynamics of its own, therefore we will say the information becomes classical or measured once it leaves the cavity. Information leaks out of the cavity to the amplifier at rate [Gambetta2006]

$$\Gamma_m = \frac{D\kappa_{out}}{2} = \frac{(n_+ + n_-)\chi^2\kappa}{\Delta_r^2 + (\kappa_{in} + \kappa_{out})^2/4 + \chi^2} \quad (3.93)$$

While the qubit is being measured it also has a rate of decay γ , limiting the integration time before the qubit state changes. Therefore one should compare the measurement rate to its decay rate to

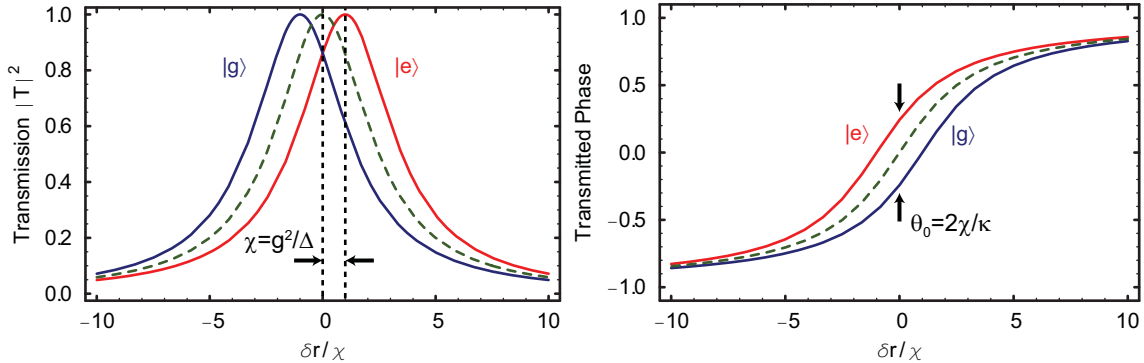


Figure 3.19: State dependent transmitted amplitude (a) and phase (b) of the resonator in the qubit ground (blue) and excited (red) states, as well as the bare resonator spectrum (dashed). The peaks are located at $\pm\chi$ and though they overlap significantly they can be distinguished by measuring the phase shift of transmitted photons.

compute a dimensionless signal-to-noise ratio (SNR)

$$SNR = \frac{\eta\Gamma_m}{\gamma} \quad (3.94)$$

where $\eta = \hbar\omega_r/k_B T_N$ and T_N is the noise temperature of the amplifier in Fig. 3.18a.

3.4.4 Small Phase Shift Limit

Before continuing with the formal optimization of the measurement efficiency it is instructive to explore the small phase shift limit. This limit is both simplest to understand and most important for small couplings or large detunings. Most of the intuition gained here can be applied to some extent in the large shift limit. As before, the cavity is given a dispersive frequency shift $\pm\frac{g^2}{\Delta}$ which will be assumed small when compared to the cavity linewidth κ (see Fig. 3.19). In this limit, the ground excited state phase shift is $\theta_0 = 2g^2/\Delta\kappa$. The amount of signal can be calculated very easily. If the local oscillator phase is adjusted so that the transmitted tone is in-phase then the out-of-phase (quadrature) component of the transmitted signal will by definition be null. The qubit state dependent phase shift will manifest itself as an increase of the quadrature transmission coefficient, $\sin^2(\theta_0)$, which was expressed more fully as D this distance between the ‘blobs’ in Fig. 3.18. The signal in power will be the change in coefficient times the average number of photons, \bar{n} , in the cavity and the rate, κ , that they pass through the cavity. For a given integration time (usually related to T_1) this signal is to be compared with effective number of noise photons, $k_B T_N / \hbar\omega_r$, of the amplifier.

This yields an expression for the signal to noise,

$$\text{SNR} = \sin^2(\theta_0) \frac{\hbar\omega_r \kappa T_1}{k_B T_N} \approx \frac{4g^4 T_1}{\Delta^2 \kappa} \frac{\hbar\omega_r}{k_B T_N} \quad (3.95)$$

What this equation says is that when in the small phase shift limit, the vacuum Rabi coupling, g , is extremely important. Also important are T_1 and the noise temperature of the amplifier, T_N . While this form gives an intuition for the signal-to-noise, one must be careful to only apply it when $g^2/\Delta \ll \kappa$. Because Δ can be tuned, if one is in the strong limit ($g > \kappa, \gamma$) then it is always possible to violate this approximation. However, by using the formalism introduced above it is possible to optimize the SNR for arbitrarily strong dispersive shifts.

3.4.5 Optimizing SNR

The signal-to-noise ratio depends on many variables, and some of those variables are implicitly linked by both theoretical constraints (the break down of the dispersive limit), and practical constraints (limits on ability to fabricate devices with arbitrary g , ω_r , etc.). While the exact optimization depends on the specific experiment being performed, in this subsection, the SNR is optimized under various “typical” experimental limits. A specific warning is that while the general ideas apply to the high E_J/E_C qubits, the smaller anharmonicity in such qubits means that one must take into account the presence and location of several auxiliary levels which can significantly alter the SNR.

Under nearly all circumstances increasing κ_{in} lowers SNR by making it less sensitive without increasing the rate of photons leaking to the amplifier. In principle, one could make it identically zero and use a one-sided cavity, but as a practical matter it is easier to measure in transmission than reflection because the amplifier is not disturbed by control pulses reflected from the cavity. Instead one typically works in the limit $\kappa_{\text{in}} \ll \kappa_{\text{out}}$ but with κ_{in} large enough that ϵ_{in} can be made large enough to achieve the desired ϵ_{rf} .

If the formula for Γ_m (Eq. 3.93) held for any photon number, then it would be possible to achieve arbitrary SNR, but at high enough photon numbers the dispersive Hamiltonian (Eq. 3.88) breaks down, mixing occurs, and parasitic modes can be excited. A typical constraint is to maximize the SNR at a given photon number¹, but which photon number, n_+, n_- , or $(n_+ + n_-)$ should be constrained? In order for one to never exceed a specified photon number when measuring either the ground or excited state one should constrain $\max[n_+, n_-]$. With this additional constraint, one

¹Note that for a given n_{\pm} that ϵ_{rf} must be adjusted based on the values of χ , κ_{out} , and Δ_r .

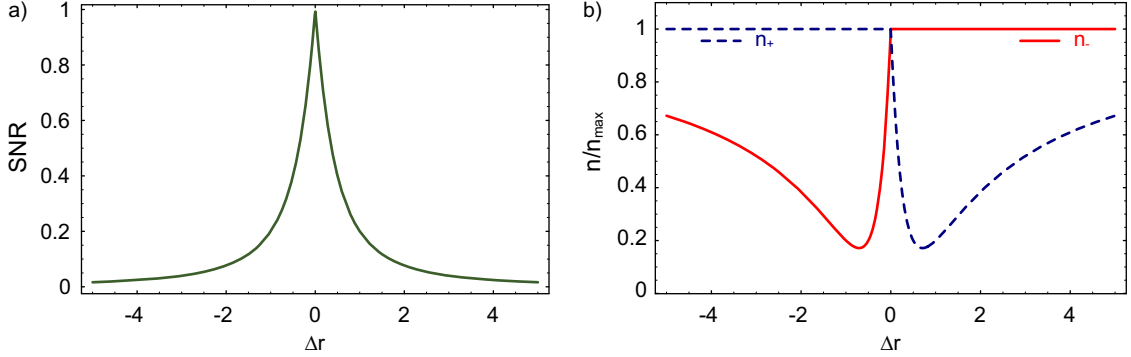


Figure 3.20: **a)** Plot of SNR at fixed κ , χ , and $\max[n_+, n_-] = n_{\max}$ vs Δ_r . The optimum is created by the intersection of the constraints on n_+ and n_- rather than by a local maximum in $SNR[\Delta_r]$. **b)** Plot of n_+ (blue dashed) and n_- (red solid) vs Δ_r . Because SNR is always improved by increasing n_{\pm} , one of the two amplitudes is always constrained. Deviations from optimum Δ_r lose signal to noise because they decrease one of n_{\pm} from n_{\max} .

can find the optimum Δ_r , whose main effect is to control the ratio n_+/n_- . As can be seen from Fig. 3.20, SNR is maximized when $n_+ = n_-$ and $\Delta_r = 0$. Using this information, the optimal SNR can be simplified to

$$SNR = \eta \frac{\kappa}{\gamma} \frac{\bar{n}\chi^2}{\kappa^2/4 + \chi^2} \quad (3.96)$$

where $\bar{n} = (n_+ + n_-)/2$ and $\kappa = \kappa_{\text{in}} + \kappa_{\text{out}} \approx \kappa_{\text{out}}$. First let's take Eq. 3.96 at face value and optimize assuming control at design of κ and χ , but that \bar{n} and γ are fixed constants which cannot be changed.

At constant \bar{n} and γ , and assuming that Δ cannot be made infinitely small (as the dispersive limit breaks down), at the optimum point $\chi = \kappa/2$ (see Fig. 3.21) the phase difference between α_+ and α_- is $\pi/2$ and

$$SNR = \frac{\eta \bar{n} \chi}{\gamma} \quad (3.97)$$

Unfortunately, even ideally, the maximum number of photons \bar{n} is not independent of g, κ , and Δ , but is limited (by the dispersive limit) to a maximum (see Eq. 2.6) $n_{\text{crit}} = \Delta^2/4g^2$. This extra dependence does not change the optimum point of $\chi = \kappa/2$, but the extra condition makes the maximum SNR

$$SNR = \frac{\eta \bar{n} g^2}{2\kappa\gamma} = \frac{\eta}{N_0} \quad (3.98)$$

where $N_0 = 2\gamma\kappa/g^2$ is the critical atom number often used in traditional cavity QED to measure how many atoms must be used to detect a single photon in the cavity. In the strong coupling limit by definition, $N_0 \ll 1$, allowing single shot measurement with an ideal detector. Complications

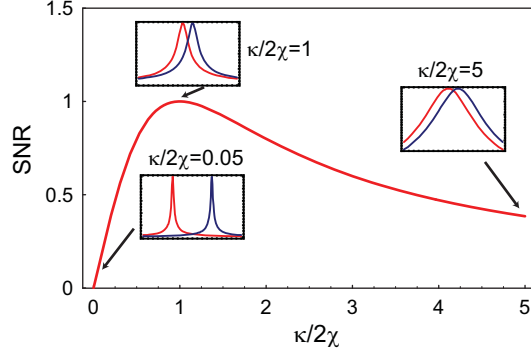


Figure 3.21: Plot of SNR vs. $\kappa/2\chi$, with insets demonstrating transmission of α_+ (red) and α_- (blue) to show effect of $\kappa/2\chi$. When $\kappa \gg 2\chi$, photons exit the cavity out very fast but they carry very little information. When $\kappa \ll 2\chi$, each photon carries a full bit of information, but because κ is small they don't come out fast enough to acquire that information in a T_1 . Thus, one would increase κ to get photons faster until the two states begin to have significant overlap at the optimum $\kappa = 2\chi$.

may arise even at the smaller critical photon number $\bar{n} = n_\kappa = \frac{\kappa\Delta}{\chi^2}$, where the cavity becomes inhomogeneously broadened due to its inherited non-linearity from the qubit. In the future, it may be possible to use this non-linearity as an asset to make a latching measurement of the qubit state as is done with the Josephson Bifurcation Amplifier [Siddiqi2006], but for now the effect is treated as a complication to be avoided. In the limit of γ constant and $\bar{n} = n_\kappa$, SNR is maximized by making $\kappa \sim \Delta$ while still being small compared to ω_r .

$$SNR = \frac{\eta}{2} \frac{\Delta\kappa^2/4}{\gamma\kappa^2/4 + \gamma\chi^2} \approx \frac{2\eta\omega_r^5}{4g^4\gamma + \gamma\omega^4} \approx \frac{2\eta\omega_r}{\gamma} \quad (3.99)$$

If this expression does not make a lot of sense, that is partially because it is not terribly realistic. If the qubit is very long lived then even well into the dispersive limit ($4ng^2/\Delta^2 \ll 1$) the decay into cavity modes may contribute to the total decay rate $\gamma = \gamma_\perp + \gamma_\kappa$, meaning that γ can no longer be treated as a constant in the optimization. The Purcell effect (Eq. 2.11 and appendix B) gives $\gamma_\kappa = (g^2/\Delta^2)\kappa$.

To get a feel for the effect of γ_κ let us temporarily work in the limit where $\gamma_\perp = 0$. This means that without γ_κ one could measure forever achieving arbitrary SNR, so the optimum in Eq. 3.99 occurs as $\kappa \rightarrow 0$

$$SNR = \frac{g^2}{\Delta^2} \frac{\eta\bar{n}}{g^2/\Delta^2 + \kappa^2/4} \approx \eta\bar{n} \frac{\Delta^2}{g^2} \quad (3.100)$$

The above equation states the obvious result, that when γ_\perp is infinite then one must be as dispersive as possible, trading speed ($\kappa \rightarrow 0$) for longevity. When n_{crit} is factored in, the dispersiveness counts

double, limiting the number of photons and the lifetime making $SNR = \eta(\Delta^4/4g^4)$. This points to a looming obstacle, whereby as qubits become more long lived one will have to measure more slowly. This issue could be circumvented by having a κ that can be pulsed on and off, which could be implemented by coupling to the outside world through a junction or other qubit.

For current experiments, γ_\perp is anything but negligible. Letting γ_\perp be held constant (since it seems to be relatively independent of any variable we have measured it against), and allowing γ_κ to enter the optimization one can find the optimal γ_κ at fixed photon number

$$\gamma_\kappa = \gamma_\perp \left(\frac{\kappa}{2\chi} \right)^2 \quad (3.101)$$

substituting γ_κ into Eq. 3.96 and optimizing to find $\kappa \rightarrow (g^2\gamma)^{1/3}$ the SNR becomes

$$SNR = \eta \frac{4\bar{n}g^2}{(2g(\gamma_\perp/\kappa)^{1/2} + \kappa)^2} = \eta\bar{n} \frac{4}{9} \left(\frac{g}{\gamma_\perp} \right)^{1/3} \quad (3.102)$$

At n_{crit} the pressure to be dispersive is strong enough that one wants to make Δ as large as possible once more yielding

$$SNR = \frac{\eta g^2 \Delta^4 \kappa}{(\gamma_\perp \Delta^2 + g^2 \kappa)(4g^4 + \Delta^2 \kappa^2)} \approx \frac{\eta}{N_0} \quad (3.103)$$

Exercise 3.4.1. Show that the Q -function of two coherent states is

$$Q(\alpha, \beta) = \exp(|\alpha - \beta|^2)$$

Chapter 4

Decoherence in the Cooper Pair Box

This chapter will focus on the decoherence properties of the CPB, both inside and outside of a cavity. The first section will discuss relaxation and mixing processes which incoherently change the state of the qubit. The second section discusses dephasing, a form of decoherence which does not cause the qubit to change state but results in noise in the relative phase of superpositions of the two states. In addition to identifying mechanisms which impede progress in quantum computing, and obscure aspects of cavity QED, studying decoherence in the CPB provides a tool to measure quantum noise [Schoelkopf2001], a window onto the underlying physics of the decoherence mechanisms, and a concrete test-bed for observing the collapse of a quantum wavefunction. In both cases the focus will be to optimize the design of the CPB rather than developing the exact lineshapes or functional form of the phase correlator. Good references for these topics include [Cottet2002] and [Martinis2003].

4.1 Relaxation and Heating

This section closely follows “Qubits as Spectrometers” reference [Schoelkopf2001], and complete derivations of the results presented here are provided in that work. Heating and relaxation are processes which excite and de-excite the qubit. They can be thought of as arising from random fluctuations at the transition frequency connecting the ground and excited states. Relaxation can be thought of as a perturbation

$$H_1 = \hat{\xi} \hat{M} \quad (4.1)$$

coupling a qubit operator $\hat{\xi}$, to a bath operator \hat{M} . For weak noise sources the excitation (\uparrow) and relaxation (\downarrow) transition rates are given by Fermi's golden rule (FGR)

$$\Gamma_{\uparrow\downarrow} = \frac{1}{\hbar^2} |\langle g | \hat{\xi} | e \rangle|^2 S_M(\mp\omega_a) \quad (4.2)$$

where $S_M(\mp\omega_a)$ is the spectral density of the bath noise. It is often more convenient to characterize these upward and downward transition rates in terms of the (energy) relaxation time which is the inverse sum of the rates

$$T_1 = 1/(\Gamma_\uparrow + \Gamma_\downarrow) \quad (4.3)$$

and the steady state polarization p is given by

$$p = \frac{\Gamma_\downarrow - \Gamma_\uparrow}{\Gamma_\downarrow + \Gamma_\uparrow} = \frac{S_M(\omega_a) - S_M(-\omega_a)}{S_M(\omega_a) + S_M(-\omega_a)} \quad (4.4)$$

The polarization ranges from $p = 1$ when the qubit ensemble is completely in the ground state to $p = -1$ if the qubit population is completely inverted, and is said to be completely depolarized when $p = 0$. Because the qubit transition selects a particular frequency, the qubit acts as a spectrometer of noise at the transition frequency [Schoelkopf2001]. Further, unlike a classical spectrometer the qubit distinguishes between the positive (qubit emits) and negative (qubit is excited) frequency components of the noise. The total magnitude of the noise is given by $1/T_1$ where the ratio of positive to negative frequency components can be deduced from the polarization, p . The process of investigating relaxation and heating can thus be thought of as identifying sources of environmental noise, S_M , understanding the system matrix elements, $\langle g | A | e \rangle$, and coupling rates to each source of noise. The rest of this section will consist of relaxation (heating) processes and models for how they couple to the CPB.

4.1.1 Voltage Noise

The CPB is primarily controlled through a gate voltage coupled to the electrostatic part of the Hamiltonian via a (not-so) small gate capacitor. The strength of this coupling can be found as in section 3.3 and similarly to Eq. 3.72 of that section, is given by

$$\hat{\xi}_V = 2e\beta\delta V_g \hat{N} \quad (4.5)$$

By creating a channel for electrostatic control we have also created a means for decay (or heating). If the qubit is coupled to an electrical environment with impedance $Z(\omega)$ then the associated

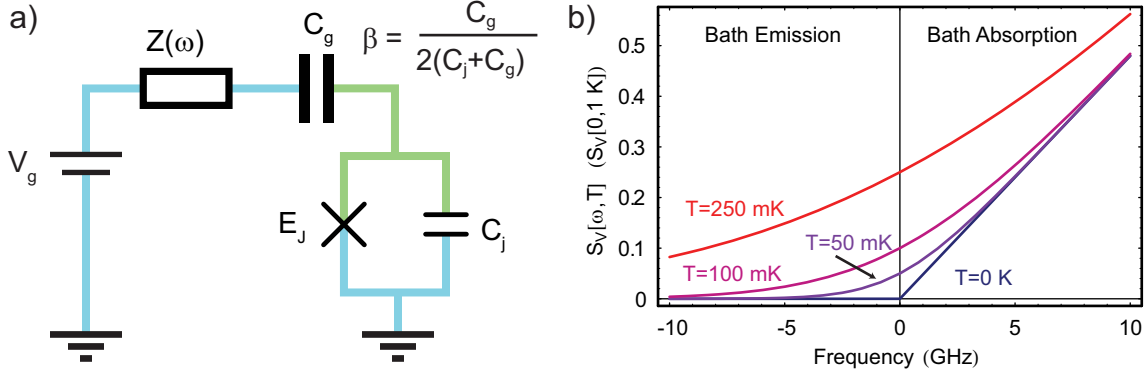


Figure 4.1: **a)** When coupling to the box via a gate capacitance, one opens a channel for decoherence. The impedance presented by the source, as well as the voltage division β between the gate capacitance and junction capacitance, will be critical factors in determining the decoherence. **b)** Plot of the voltage spectral density $S_V(\omega)$ at different temperatures in units of $S_V(0) = 2k_B T R$ at $T = 1 \text{ K}$. At high temperatures and low frequencies the spectral density is relatively symmetric about $\omega = 0$. However at high frequencies $\hbar\omega > k_B T$, most notably at $T = 0$, the spectral density is very asymmetric. It is zero for frequencies $\omega < 0$ (at $T = 0$ the bath cannot emit) and linear ($\approx \hbar\omega R$) in frequencies $\omega > 0$ (the bath can still absorb).

voltage noise of that environment is given by the Johnson-Nyquist formula, which resembles a one-dimensional blackbody (Bose-Einstein) and is described by the voltage spectral density

$$S_V(\omega) = \frac{2\hbar\omega \operatorname{Re}[Z(\omega)]}{1 - e^{\frac{-\hbar\omega}{k_B T}}} \quad (4.6)$$

One thing to note about Eq. 4.6 is that at low temperatures the voltage noise is not symmetric in positive and negative frequencies. This inherently quantum mechanical property has a straight forward meaning. At low temperatures there is not enough energy ($k_B T < \hbar\omega$) to emit any photons and therefore the positive frequency side will approach zero. However, even at absolute zero the environment can absorb photons leaving only a voltage spectral density at positive frequencies.

$$S_V(-\omega) \approx 2\hbar\omega \operatorname{Re}[Z(\omega)] \quad (4.7)$$

The effective decay rate at low temperatures is thus

$$\Gamma_V = 16\pi\beta^2\omega_a \frac{\operatorname{Re}[Z(\omega_a)]}{R_K} |\langle g | \hat{N} | e \rangle|^2 = 2\pi \frac{g^2}{\omega_a} \quad (4.8)$$

where $R_K = h/e^2$ is the resistance quantum. The lifetime $T_1 = 1/\Gamma_V$ is enhanced by having a small real environmental impedance $\operatorname{Re}[Z(\omega_a)]$, and by reducing the coupling (β and $\langle g | \hat{N} | e \rangle$) of

the transition to that impedance.

The dependence on $\langle g | \hat{N} | e \rangle$ gives the decay rate a dependence on the bias charge, n_g (see Fig. 3.13). In the charge regime one can make the approximation

$$\langle g | \hat{N} | e \rangle \approx \frac{1}{2} \sin \theta_m = \frac{E_J}{2\sqrt{16E_C^2(1-n_g) + E_J^2}} \approx \frac{E_J}{2\omega_a} \quad (4.9)$$

This means that the decay rate should be approximately independent of gate charge. It is perhaps better to think about a normalized measure of the coherence, the relaxation quality factor $Q_1 = \omega_a/\Gamma$, which can be thought of as the number of oscillations the qubit makes before decaying. So at fixed ω_a the quality factor is maximized by having $E_J/\hbar \ll \omega_a$ and implicitly operating at small bias charge ($n_g \approx 0$). However, as discussed in section 3.2, having very small E_J means that there is no way to change the qubit state. Though at $n_g = 1$ the matrix element is maximal, it only rises to a constant of order unity $\langle g | \hat{N} | e \rangle \approx 1/2$. In practice the dephasing due to low frequency voltage or charge noise will make $n_g = 1$ a more favorable operating point despite the price of faster relaxation.

The effective environmental impedance is typically of order 50Ω , so for the traditional CPB the lifetime is mainly determined by the choice of β . For these parameters $Q_1 \approx 3/\beta^2$, meaning that if the qubit is connected directly to a transmission line then it would decay almost immediately. In principle the Q_1 due to voltage noise could be made arbitrarily large by making $\beta \ll 1$, but in practice it is difficult to make $\beta = C_g/C_\Sigma$ smaller than $\beta \approx 1 \text{ aF}/1 \text{ fF}$ for a traditional CPB implying a maximum $Q_1 \approx 10^6$. While this Q_1 would not limit current CPBs in the next section we will see how one can improve the lifetime even more!

4.1.2 Voltage Noise Inside a Cavity

Observation of cavity QED phenomena and any non-local gates implemented via the cavity rely on having the qubit strongly coupled to the cavity $\beta \sim 0.1 - 1$ which would appear to reduce the qubit lifetime. Luckily, placing the CPB inside of a cavity allows one to control the impedance $Z(\omega)$ of the environment (see Fig. 3.3), allowing larger coupling with similar or reduced decay. In the dispersive limit ($\Delta \gg g$), one can treat the qubit in a cavity as seeing an effective $\text{Re}[Z(\omega_a)]$ presented by the cavity, which can be modeled by an LCR as in Eq. 3.3.

$$\text{Re}[Z_{\text{LCR}}(\omega)] = \frac{Z_C}{1 + \frac{(\omega_a - \omega_r)^2}{(\kappa/2)^2}} \quad (4.10)$$

At large detunings, the effective impedance seen by the qubit is much smaller than the characteristic impedance of the resonator, dramatically enhancing the qubit lifetime (see Fig 4.2). This can be

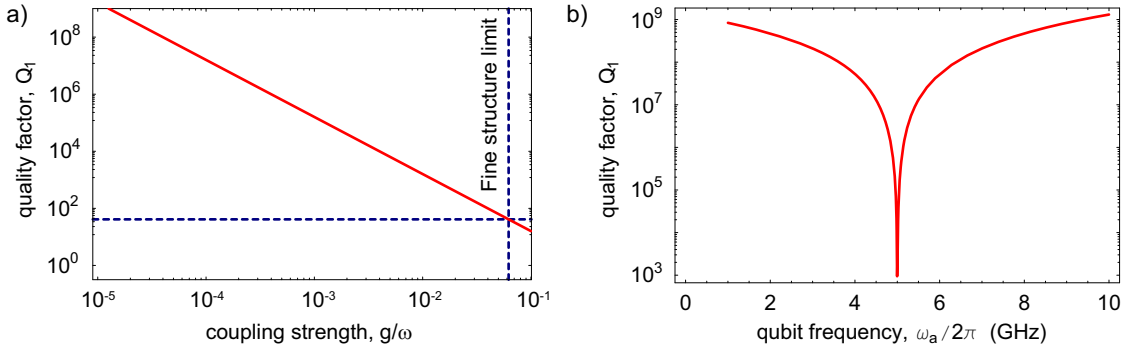


Figure 4.2: Quality factor of qubits coupled to transmission line and cavity. **a)** Plot of Q_1 for a qubit coupled to a bare transmission line as a function of the dimensionless coupling strength g/ω_a . The dashed lines indicate the fine structure limit, where g/ω is made maximal by setting $\beta = 1$. At this maximum coupling strength the relaxation quality factor is only $Q_1 \approx 40$. **b)** Plot of the relaxation Q_1 of the maximally coupled ($\beta = 1$) CPB inside of a cavity due to vacuum noise from outside the resonator. Plot is shown for a cavity frequency $\omega_r/2\pi = 5$ GHz and $Q = 10,000$. The qubit is in the charge regime $\omega_a \approx E_J/\hbar$, and is fully coupled to the resonator and for detunings $\Delta > 10\%$ the relaxation $Q_1 > 10^7$.

thought of as an electrical engineering description of the Purcell Effect¹

Parasitic Cavity Modes

With great coupling, comes great responsibility...to control the environmental impedance! By placing the qubit inside a cavity one can couple strongly while preventing the decay. In doing so one must be especially careful not to excite any modes in which the impedance is not carefully controlled. One must avoid any extra parasitic modes on the circuit board and inside the sample holder which might couple to the CPB. Precautions taken in the design of the circuit board and sample holder are discussed in chapter 5.

One particular suspected loss mode is the parasitic mode which may exist between the ground planes of the resonator. In current designs, the CPB is placed in between one of the ground planes and the center pin. The coupling can be thought of as driving a superposition of two modes, a mode symmetrically (see Fig. 4.3a) driving a voltage between the center-pin and ground planes, and an antisymmetric mode (see Fig. 4.3b) driving a voltage from one ground plane to the other. In the

¹Fermi's Golden Rule assumes that if the qubit decays into the environment (in this case a cavity) that it immediately leaves and does not affect further dynamics of the system. This is effectively true when in the dispersive limit, where the rate of real transitions is by definition small, and when the cavity decay rate is much faster than the coupling rate (the weak limit). However this assumption breaks down in the strong coupling limit when the qubit comes into resonance with the cavity because the photon can be reabsorbed by the qubit.

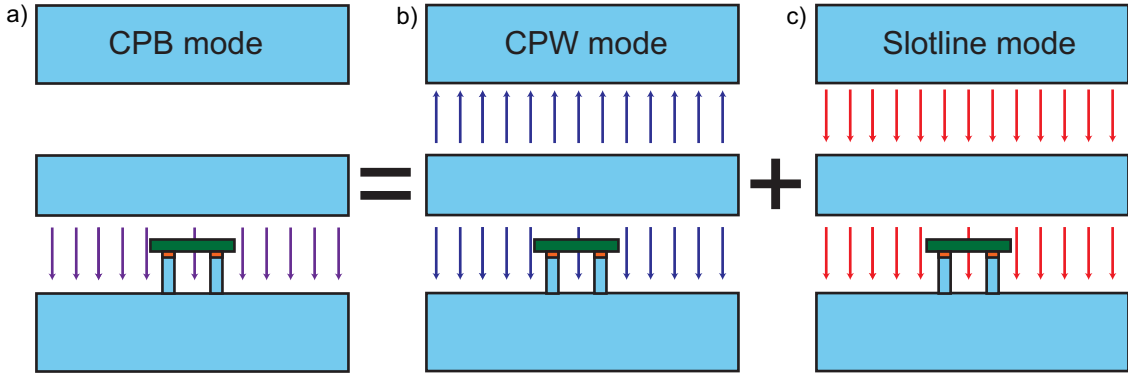


Figure 4.3: The CPB in its current geometry effectively couples only the bottom ground plane and the centerpin. If the two ground planes are not well grounded it is possible that this drives a superposition of the desired CPW mode and a parasitic slot line mode which is not well defined.

design of the resonators and circuit board, care is taken to ensure the two ground planes are always at the same potential, which would eliminate this uncontrolled antisymmetric mode. However due to limitations of local fabrication equipment (inability to make on-chip superconducting vias), there maybe some small but finite inductance between the ground planes. If this inductance presents an effective impedance similar to the intended cavity impedance, then it might be a significant source of decoherence. In addition to improved engineering reducing such impedance, one can also design qubits which do not couple to the mode by symmetry.

The effect of flux noise on the qubit is very similar to that of voltage noise. However, instead of coupling via a voltage division to the electrostatic component of the Hamiltonian, it couples to the Josephson term via a magnetic inductance. Like the voltage noise, it depends both on the coupling of the field to the qubit and on n_g through the matrix elements. For small fluctuations, we can expand the junction Hamiltonian H_J in Eq. 3.62 around the bias point Φ to give a linearized coupling to flux to give

$$\hat{\xi}_\Phi = \frac{\pi \delta\Phi E_J^{\text{sum}}}{\Phi_0} \left(\sin\left(\frac{\pi\Phi}{\Phi_0}\right) \cos\hat{\theta} + d \cos\left(\frac{\pi\Phi}{\Phi_0}\right) \sin\hat{\theta} \right) \quad (4.11)$$

In the two state approximation the fictitious field picture developed in Fig. 3.12 and Eq. 3.68, $\hat{\xi}$ can be thought of as a driving magnetic field. The part of the field that is perpendicular to the quantization axis defined by the net field will drive the $e \rightarrow g$ transition. Using this fictitious field picture

$$|\langle g | \hat{\xi} | e \rangle|^2 = \frac{|B_\xi \times B|^2}{|B|^2} \quad (4.12)$$

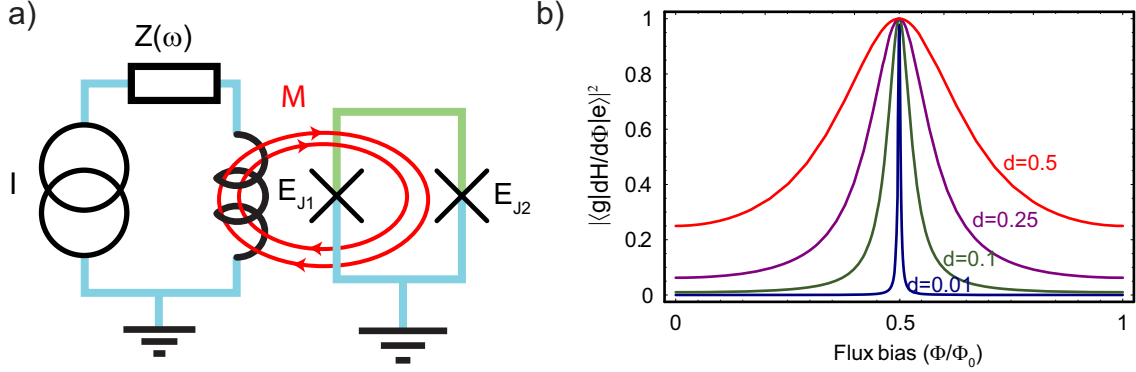


Figure 4.4: **a.** Circuit diagram showing how the environment can couple a flux to the CPB through a mutual inductance M . **b)** Flux transition matrix element vs. Φ/Φ_0 at different junction asymmetries $d = 0.01, 0.1, 0.25, 0.5$. They are very close to zero at $\Phi = 0$ and as long as there is some asymmetry go to 1 at $\Phi = \Phi_0/2$. This occurs because at that point, even if the asymmetry is small it is exactly perpendicular to the field so it couples with order unity. The size of d determines the robustness (flatness) near $\Phi = 0$.

Using this relation the FGR from Eq. 4.2, becomes

$$\Gamma_\Phi = \frac{\pi^2 S_\Phi(\omega)}{\hbar^2 \Phi_0^2} \frac{E_J^4 d^2 + 16 E_C^2 E_J^2 (1 - n_g)^2 \left(\sin^2 \left(\frac{\pi \Phi}{\Phi_0} \right) + d^2 \cos^2 \left(\frac{\pi \Phi}{\Phi_0} \right) \right)}{16 E_C^2 (1 - n_g)^2 + E_J^2 \left(\sin^2 \left(\frac{\pi \Phi}{\Phi_0} \right) + d^2 \cos^2 \left(\frac{\pi \Phi}{\Phi_0} \right) \right)} \quad (4.13)$$

At the degeneracy point ($n_g = 1$) the expression no longer has any dependence on E_C leaving

$$\Gamma_\Phi = \frac{\pi^2 S_\Phi(\omega)}{\hbar^2 \Phi_0^2} \frac{E_J^2 d^2}{\sin^2 \left(\frac{\pi \Phi}{\Phi_0} \right) + d^2 \cos^2 \left(\frac{\pi \Phi}{\Phi_0} \right)} \quad (4.14)$$

and at the most favorable operating point ($n_g = 1$ and $\Phi = 0$) this rate simplifies to

$$\Gamma_\Phi = \frac{\pi^2 d^2 S_\Phi(\omega)}{\Phi_0^2} \left(\frac{E_J}{\hbar} \right)^2 \quad (4.15)$$

If one biases the qubit flux with a current coupled to the CPB loop with a mutual inductance M then one can rewrite S_Φ in terms of S_I the current fluctuations in the bias.

$$S_\Phi = M^2 S_I = M^2 \frac{2\hbar\omega}{Re[Z(\omega)]} \frac{1}{1 - e^{-\frac{\hbar\omega}{k_B T}}} \quad (4.16)$$

At $T = 0$, $n_g = 1$, and $\Phi = 0$, one can use Eqs. 4.15 and 4.16 to find the relaxation quality factor

$$Q_1^\Phi = \frac{\omega_a}{\Gamma_\phi} = \frac{1}{2\pi^2 d^2 M^2} \frac{R\Phi_0^2 \hbar}{E_J^2} \quad (4.17)$$

4.1.3 Material Loss

Resistive (Quasiparticle) Loss

Even though the CPB is superconducting there can still be resistive loss. In this section we will treat the superconductor in the two fluid model where residual normal fluid (quasiparticle) tunneling across the junction in parallel with a finite Josephson inductance leads to loss. In section 4.3.5 a more sophisticated treatment of quasiparticle loss will be applied which takes into account the density of states. These quasiparticle losses in the CPB are analogous to resistive loss in the cavity due to the finite kinetic inductance. The shunting in the CPB is actually even a bit worse because the Josephson inductance $L_J \approx \hbar/2eI_c = R_K/16\pi^2E_J$ is typically larger than the total (magnetic and kinetic) inductance of the cavity (the characteristic impedance $Z_{CPB} \gg 50\Omega$. As for the cavity (Eq. 3.33) the resistive quality factor is

$$Q_{\text{res}} = \frac{R}{\omega L_J} \quad (4.18)$$

Using the Ambegoakar-Baratoff relation one can express the critical current in terms of the superconducting gap and normal state resistance as

$$I_c = \frac{\pi\Delta}{2eR_n} \tanh\left(\frac{\Delta}{2k_B T}\right) \quad (4.19)$$

At degeneracy ($n_g = 1$) for a traditional CPB the transition frequency is the Josephson energy $E_J/\hbar = I_c/2e$. The effective resistance should be inversely proportional to the normal population

$$R = R_n \frac{n_n + n_s}{n_n} = R_n \left(1 + e^{1.76T_c/T}\right) \quad (4.20)$$

Substituting this into Eq. 4.18 yields

$$Q_{\text{res}} = 8\pi \frac{E_J}{\hbar\omega_a} \frac{R_n}{R_K} \left(1 + e^{1.76T_c/T}\right) \quad (4.21)$$

For a CPB with transition frequency $E_J/h \sim 5$ GHz, the ratio $R_n/R_K \approx 1$. The exponential scaling with temperature means that if the quasiparticle population is in equilibrium, then Q_{res} should be 10^5 at 250 mK, and 10^{20} by 50 mK. However, it is possible the effective quasiparticle temperature is higher than the bath temperature. As long as the effective temperature is below ~ 250 mK it probably is not limiting the lifetime of the box.

Dielectric Loss

Another channel for decay is loss in dielectrics in which qubit electrical fields live. For this decay mechanism one can think of a CPB as an LC resonator, whose $Q_1 \approx 1/\tan\delta$ just like the cavities

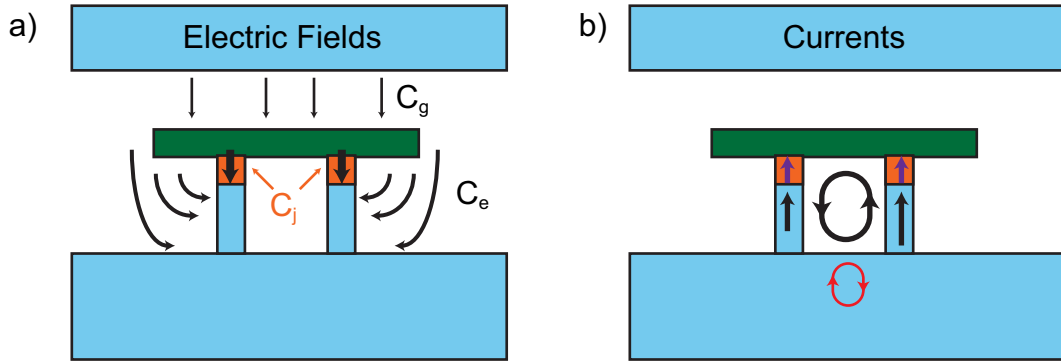


Figure 4.5: **a.** Electric fields in the CPB, black arrows represent E-field lines. Much of the field is in the junctions which form an overlap capacitor with $C_j \sim 4\text{ fF}$ of capacitance. Some of the field is resides in the gate capacitance, C_g and stray or intentional external capacitance C_e . **b.** Currents flowing through the CPB and induced currents in the ground plane. If there is a non-zero flux or asymmetry in the junctions, the amount of current flowing through each junction is different, meaning that there is a net circulating current. This AC circulating current can induce currents in nearby pieces of metal or radiate directly into the vacuum. If quasiparticles are present, the Josephson inductance will shunt some current into the normal, resistive branch, reducing the excited state lifetime.

in section 3.1.7. The electric fields of the CPB pass through many materials with potentially widely varying loss tangents. Thus in addition to the materials themselves, the “participation ratio” of field energy in each material is of paramount importance. A diagram of CPB fields and materials is presented in figure 4.5. In a traditional CPB most of the electrical energy is stored in the junction capacitance whose fields pass through a $1 - 2\text{ nm}$ thick tunnel barrier of AlO_x . The loss tangent of most materials is not that well known at low temperatures, and in fact our current best lifetime $T_1 \sim 10\text{ }\mu\text{s}$ probably sets the current lower limit on the loss tangent of such a barrier ($\tan \delta_{\text{AlO}_x} \sim 10^{-5} - 10^{-6}$). One way to test whether this loss mechanism is limiting the current qubit lifetimes is to add a shunting capacitor to the CPB. The electric fields of this capacitor will ideally¹ live in the substrate which should have less loss. If the lifetime were to improve this would implicate the junction dielectric losses.

Inductive Losses

Inductive losses can be treated in a similar manner to dielectric losses. Because the insulators used have magnetic permeabilities very close to unity, one does not expect them to have much loss. Ideally the superconductors would have no inductive loss, though as seen in section 3.1.7, even

¹Current fabrication processes can leave residue of unknown chemical composition and electrical properties near the qubit. This may make the effective loss of planar capacitors larger than one would expect from the losses in the $\text{Si}/\text{Sapphire}/\text{SiO}_2$ substrate.

superconductors may have some loss. Any magnetic fields in the normal metal circuit board might also induce lossy currents. These mechanisms are not thought to be limiting factors, the loop is quite small $10 \mu\text{m}^2$ compared to the distance to the nearest lossy material. It is possible that local non-equilibrium effects, namely vortices, might present an additional inductive loss mechanism. The magnetic fields produced by the qubit are nominally suppressed at zero flux bias if the junctions are symmetric, and could be eliminated altogether by using a single junction.

4.1.4 Dipole Radiation

One can also calculate the energy radiated by an electric or magnetic dipole in free space. A CPB in free space would have these as ultimate limits to its lifetime. As seen in section 4.1.2, placing the CPB inside a cavity can enhance (or reduce) its lifetime dramatically. However these radiation mechanisms still serve as useful scales of decoherence.

Electric Dipole Radiation

The power emitted by an electric dipole is given by [Griffiths1999]

$$P_{\text{ed}} = \sqrt{\frac{\mu_0}{\epsilon_0}} \frac{d^2}{\lambda^2} \frac{\pi \omega^2}{3} \quad (4.22)$$

where $d = q \cdot x \approx e \times \mu\text{m}$ is the CPB electric dipole moment. The energy relaxation rate is just the power divided by the energy per decay.

$$\Gamma_{\text{ed}} = \frac{P}{\hbar \omega} \quad (4.23)$$

The quality factor of the CPB can then be expressed as

$$Q_{\text{ed}} = \sqrt{\frac{\epsilon_0}{\mu_0}} \frac{\lambda^2}{d^2} \frac{3\hbar}{\pi} \quad (4.24)$$

For the typical CPB at $\sim 5 \text{ GHz}$ transition frequency one expects, depending on the dipole moment, a $Q_{\text{ed}} \sim 10^8 - 10^{10}$! May we one day encounter such limits!

Magnetic Dipole Radiation

The power emitted via magnetic dipole radiation is given [Griffiths1999] is

$$P_{\text{md}} = \frac{4}{3} \pi^3 \sqrt{\frac{\mu_0}{\epsilon_0}} \left(\frac{m}{\lambda^2} \right)^2 \quad (4.25)$$

where $m = I \times A$ is the magnetic dipole moment, with I the current around the SQUID loop of area A . For a typical CPB the current is given by the critical current $I_0 \sim 1 \text{ nA}$, and the loop area is $A \sim 10 \mu\text{m}^2$.

Following the same procedure as for the electric dipole one can derive a quality factor for magnetic radiation.

$$Q_{\text{md}} = \frac{3\hbar}{4\pi^3} \sqrt{\frac{\epsilon_0}{\mu_0}} \left(\frac{\lambda^2}{m} \right)^2 \omega^2 \quad (4.26)$$

For typical parameters the magnetic quality factor is even higher, approximately $Q_{\text{md}} = 10^{14}$!¹

Other Sources of Decay

Other sources of decay have been proposed for the CPB. If there is any piezoelectricity or magnetostriction in any of the nearby materials, the electromagnetic oscillations in the CPB could lose energy in the form of phonons [Ioffe2004]. It is possible that other quasiparticle related phenomena, such as non-equilibrium populations, vortices, or subgap states could affect the lifetime. Vortices might be reduced by better magnetic shielding of the sample and by intentionally pinning vortices which might arise by putting an array of holes in the resonator. Non-equilibrium quasiparticle populations might be reduced by adding a normal metal quasiparticle trap to the box or by making the two halves of the CPB out of superconductors with dissimilar gaps, creating a barrier to quasiparticle tunneling.

4.2 Dephasing

Dephasing is caused by processes that randomly modify the effective transition frequency of the qubit, which cause the qubit to accumulate a random phase. Dephasing is typically caused by low frequency noise far below the transition frequency, and can be treated in a semi-classical manner. There are several types of dephasing. First, any process which causes energy relaxation will also dephase the qubit at a rate¹ $\Gamma_1/2$. Second, there are fluctuations which occur during the course of a single experiment (during one decay lifetime) which dephase at a rate Γ_ϕ . Finally, there are fluctuations which occur on longer timescales from experiment to experiment, creating an ensemble dephasing denoted by the rate Γ_ϕ^* . This last type is analogous to having spatial magnetic field inhomogeneities in nuclear magnetic resonance (NMR), and is often referred to as inhomogeneous broadening. Like its NMR counterpart, because it is not intrinsic to a single experiment, it can theoretically be reduced using spin echo techniques. Though it is possible to compensate for inhomogeneous broadening, doing so can be the bane of practical experiments, because inhomogeneous

¹Dephasing represents decay of an amplitude and so goes at half of the rate of energy relaxation $\Gamma_2 \sim \Gamma_1/2$.

broadening often represents drifting conditions, which significantly complicate experimental protocols. The total dephasing is the sum of all of these rates

$$\Gamma_2 = \Gamma_1/2 + \Gamma_\phi + \Gamma_\phi^* \quad (4.27)$$

and one can define a dephasing quality factor, which is the number of coherent oscillations before the qubit will accumulate a random π phase shift.

$$Q_\phi = \omega_a / \Gamma_\phi \quad (4.28)$$

In the frequency domain Γ_ϕ manifests itself as a broadening of the intrinsic linewidth. To find the deviation of the transition frequency due to (slow) fluctuations in a parameter λ , with spectral density $S_\lambda(\omega)$, one can Taylor expand the frequency about the bias point λ_0 .

$$\delta\omega = \omega - \omega_0 = \delta\lambda \left(\frac{\partial\omega}{\partial\lambda} \right)_{\lambda_0} + \frac{\delta\lambda^2}{2} \left(\frac{\partial^2\omega}{\partial\lambda^2} \right)_{\lambda_0} + \dots \quad (4.29)$$

Typically the first order term dominates the expansion, however it is often possible by artful selection of the bias conditions to null the first term, leaving the second order term at the lowest non-trivial order.

The variance is the time averaged expectation of $\delta\omega^2$

$$\langle \delta\omega^2 \rangle = \langle \delta\lambda^2 \rangle \left(\frac{\partial\omega}{\partial\lambda} \right)_{\lambda_0}^2 + \frac{\langle \delta\lambda^4 \rangle}{4} \left(\frac{\partial^2\omega}{\partial\lambda^2} \right)_{\lambda_0}^2 + \frac{\langle \delta\lambda^3 \rangle}{2} \left(\frac{\partial\omega}{\partial\lambda} \right)_{\lambda_0} \left(\frac{\partial^2\omega}{\partial\lambda^2} \right)_{\lambda_0} + \dots \quad (4.30)$$

For most distributions the last, cross term is small due to the fact if the distribution is not very skewed the average value of $\delta\lambda^3 \approx 0$. Additionally it is convenient to reexpress the kurtosis ($\langle \delta\lambda^4 \rangle$) in terms of the standard deviation $\sigma_\lambda = \sqrt{\langle \lambda^2 \rangle}$ as

$$\langle \lambda^4 \rangle = \sigma_\lambda^4 (\delta K + 3) \quad (4.31)$$

where δK is the excess kurtosis, which may in principle lie between -2 and $+\infty$, but is zero for the normal distribution and typically of order unity for most other distributions encountered. Dropping the cross term and reexpressing Eq. 4.30 in terms of the variance gives

$$\langle \delta\omega^2 \rangle = \sigma_\lambda^2 \left(\frac{\partial\omega}{\partial\lambda} \right)_{\lambda_0}^2 + \sigma_\lambda^4 \frac{3 + \delta K}{4} \left(\frac{\partial^2\omega}{\partial\lambda^2} \right)_{\lambda_0}^2 + \dots \quad (4.32)$$

The time average¹ is most conveniently taken in the frequency domain where can be expressed

¹In general one should take the time average over derivatives as well as λ itself, as they too may have some frequency dependence, which might correlate with the fluctuations in λ . However, for dephasing the maximum cutoff frequency $\omega_{\max} \sim 1/T_2$ is typically still in the adiabatic limit, where the derivatives are frequency independent.

as

$$\langle \lambda^2 \rangle = \int_{\omega_{\min}}^{\omega_{\max}} S_\lambda(\omega) W(\omega) d\omega \quad (4.33)$$

where $W(\omega)$ is the spectral weight function, which depends on the specific experiment being performed [Martinis2003]. While nominally the cut-offs are $\omega_{\min} \rightarrow 0$ and $\omega_{\max} \rightarrow \infty$, in practice the maximum frequency is effectively capped to $\sim 1/T_2$ by the spectral density functions¹. The minimum cut-off is set by the inverse single shot experiment time when calculating Γ_ϕ , and by the total length of ensemble measurements when finding Γ_ϕ^* . Weight functions for common experiments are

Experiment Spectral Weight Function

$$\text{Ramsey/Idle} \quad W_0 = \frac{\sin^2(\pi f t)}{(\pi f)^2} \quad (4.34)$$

$$\text{Rabi} \quad W_R = \left(\frac{\nu_{\text{Rabi}} f}{\nu_{\text{Rabi}}^2 - f^2} \right)^2 W_0 \quad (4.35)$$

$$\text{SpinEcho} \quad W_{\text{SEn}} = \tan^2(\pi f t / 2n) W_0 \quad (4.36)$$

where t is the time at which one wants to know the accumulated phase noise which is often T_2 , ν_{Rabi} is the Rabi oscillation frequency (see section 9.1 for definition and experiments), and n refers to the number of spin echos in a given decay time. In general the accumulated phase noise depends on the experiment being performed and the type of noise. In all cases, the spectral weight function suppresses noise above $1/T_2$. In the Rabi or spin echo experiments noise at very low frequencies is also suppressed. For the examples in this chapter, rates will be calculated using W_0 which is most pessimistic. For noise with gaussian statistics which is white on the scale of the characteristic decay time, the decay will be exponential characterized by a rate, Γ_ϕ . If the noise is predominantly at frequencies lower than Γ_ϕ then the decay will be gaussian. If the statistics are non-gaussian² then one can have an overall loss of contrast rather than decay in time [Martinis2003]. In the charge regime the transition frequency from Eq. 3.69 is

$$\omega_a = \frac{1}{\hbar} \sqrt{E_J^2 \left(\cos^2 \left(\frac{\pi \Phi}{\Phi_0} \right) + d^2 \sin^2 \left(\frac{\pi \Phi}{\Phi_0} \right) \right) + 16 E_C^2 (1 - n_g)^2} \quad (4.37)$$

Variations in any of the parameters in the Eq. 4.37 will lead to fluctuations in the energy and dephasing the qubit. The following subsections investigate the types of noise each parameter experiences, and find optimal bias points to minimize these channels of dephasing.

¹This cut-off is one reason a low-frequency Taylor series approximation is valid

²When many distributions (even non gaussian ones) are added they will typically have gaussian statistics due to the central limit theorem. However if there are not very many distributions (such as a small number of telegraph fluctuators) then one can have non-gaussian statistics.

4.2.1 Charge Noise

When operated in the charge regime, the Cooper pair box is affected most by charge noise. This is both because the charge plays such a critical role in the charge regime CPB and because the fluctuations in charge are both substantial and pathological. Much of the effort on the CPB has been directed towards understanding and minimizing the effects of this charge noise, which can be divided into three categories. The first intrinsic, expected, and relatively benign is the thermal noise introduced by the presence of a gate, in which Johnson-Nyquist voltage noise causes effective fluctuations in the bias charge. The second, pathological, and not well-understood so-called $1/f$ charge noise is thought to arise from local charges in the substrate, or junction barrier, and has fluctuations which diverge at low frequencies [Zorin1996]. In other words; there is unexplained random drifting of charge on large scales and over large times. This presents a significant problem for single shot experiments, but is devastating for long term biasing, and thus, to the efficient scaling of CPB-based qubits. The final mechanism comes in the form of quasi-particles, which when one tunnels across the barrier changes the gate charge by one electron.

To estimate noise and optimize the choice of n_g let us apply formalism in Eq. 4.32. For simplicity we will assume that the CPB is made with a single junction¹ (operated at zero flux). The dimensionless first order decay rate (inverse Q_ϕ) is

$$\frac{1}{Q_\phi} = \frac{\sigma_{n_g}}{\omega_a} \frac{\partial \omega_a}{\partial n_g} = \sigma_{n_g} \frac{(n_g - 1)}{(n_g - 1)^2 + \left(\frac{E_J}{4E_C}\right)^2} \quad (4.38)$$

Before attempting to estimate the dephasing rate, one can immediately see that Eq. 4.38 can be made zero by letting $n_g = 1$. At this ideal bias point, referred to as the “sweet” or “clock” point the energy transition is first order insensitive to any (small) fluctuations in gate [Vion2002]. Further, the ratio $E_J/4E_C$ appears in the denominator, meaning that the insensitive region will grow more robust as this quantity is increased (see Fig 4.6).

The second order contribution to the dimensionless dephasing rate is given by

$$\frac{1}{Q_\phi} = \frac{\sigma_{n_g}^2}{\omega_a} \frac{\partial^2 \omega_a}{\partial n_g^2} = \sigma_{n_g}^2 \left(\frac{4E_C}{E_J} \right)^2 \left(1 + \left(\frac{4E_C}{E_J} \right)^2 (n_g - 1)^2 \right)^{-2} \quad (4.39)$$

Normally, the first order contribution dominates for small fluctuations but when the prefactor in

¹In section 4.2.2 the optimal flux bias point will be $\Phi = 0$. To get the full expression simply let $E_J^2 \rightarrow E_{J1}^2 + E_{J1}E_{J2} \cos\left(\frac{2\pi\Phi}{\Phi_0}\right) + E_{J2}^2$.

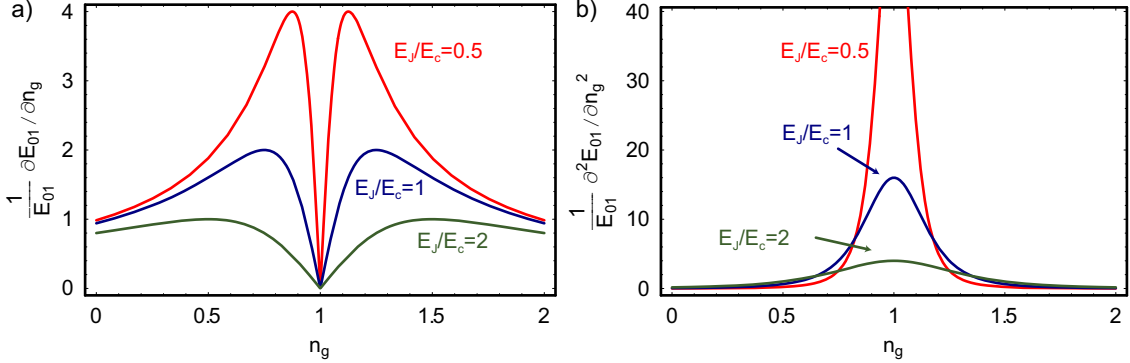


Figure 4.6: **a)** Dimensionless first derivative of energy with respect to charge. Note that the derivative goes to zero at $n_g = 1$ for all E_J/E_C , meaning that the first order charge noise, which is proportional to this derivative will also disappear. At larger E_J/E_C this minimum is more robust. **b)** If the first order noise is eliminated the second order noise will dominate. The robustness in the first derivative at higher E_J/E_C is reflected in the maximum value of the second derivative.

Eq. 4.38 is zero at $n_g = 1$ the second order noise dominates¹, and at this point the dimensionless dephasing rate becomes

$$\frac{1}{Q_\phi} = \frac{\sigma_{n_g}^2}{\omega_a} \left(\frac{\partial^2 \omega_a}{\partial n_g^2} \right) = \sigma_{n_g}^2 \left(\frac{4E_C}{E_J} \right)^2 \quad (4.40)$$

A more complete treatment of dephasing at optimal points can be found in [Makhlin2004], which discusses the rather interesting lineshape produced by the rectification of the parabolic energy dependence on the bias parameter. This behavior confirms that large $E_J/4E_C$ reduces the dimensionless dephasing rate and thus improves Q_ϕ . The two charge state approximation, on which Eq. 4.37 is based, relies on $E_J/4E_C \ll 1$, but the result of Eq. 4.40 provides motivation to explore beyond this regime. This transmon regime (see Sec. 4.3) that lies beyond is fraught with interesting surprises, and looks very promising as a new qubit indeed.

To determine the actual Q_ϕ one must find $S_{n_g}(\omega)$ for each dephasing mechanism. Though each mechanism has a different spectral density and different origin, at present we have little control over these distributions and our attempts to improve the overall performance have mostly centered around optimizing the way that the noise propagates into the qubit itself as shown above.

Voltage Noise

Thermal voltage noise from the 50Ω environment applied to the gate capacitor will make fluctuations in the gate charge $n_g = C_g^* V_g / e$, which is just C_g for the isolated box and $C_g^* \approx (C_{in}/C_r)C_g$ inside a

¹Note that at $n_g = 1$ the cross term in Eq. 4.30 is also zero.

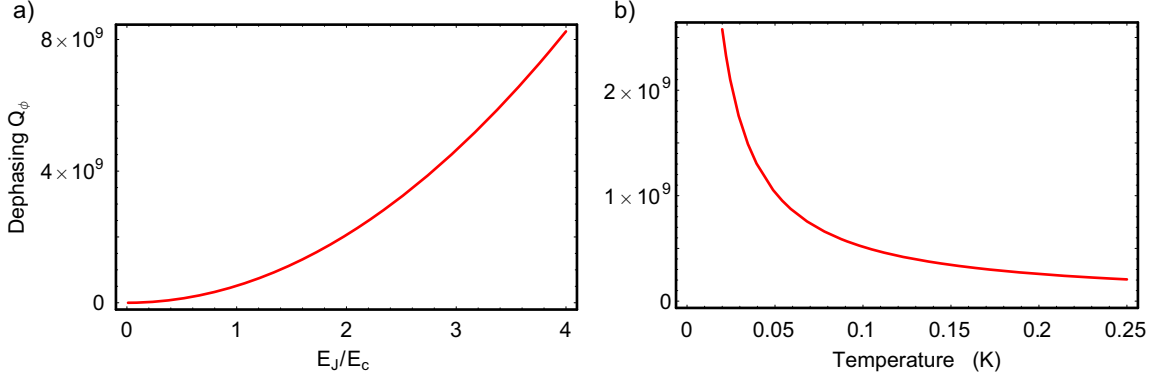


Figure 4.7: **a)** Dephasing of the qubit (at $T = 100$ mK) due to low frequency thermal radiation (Johnson noise) as a function E_J/E_C . **b)** Dephasing of the qubit vs. temperature at $E_J/E_C = 1$. These clearly show that the thermal dephasing is a negligible contributor of dephasing.

resonator. The charge spectral density comes directly from the voltage spectral density of Eq. 4.6, and shown in Fig. 4.1.

$$S_{n_g}^{\text{th}}(\omega) = \frac{C_g^*}{e} \frac{2\hbar\omega \text{Re}[Z(\omega)]}{e^{\frac{\hbar\omega}{k_B T}} - 1} \quad (4.41)$$

If this were a bare CPB than one could integrate this out to the qubit frequency¹ but inside a cavity from Fig. 3.3 one can see that cavity begins filtering heavily at the cavity bandwidth, κ . Therefore one can approximate the RMS charge fluctuations by the low frequency limit of the Eq. 4.41 with bandwidth κ .

$$\sigma_{n_g}^2 \approx \int_0^\infty d\omega W_0 S_{n_g}^{\text{th}}(\omega) = \frac{2C_g^* k_B T \text{Re}[Z(\omega)]}{e} \quad (4.42)$$

Substituting Eq. 4.42 one finds the optimal bias point is $n_g = 1$ giving

$$\frac{1}{Q_\phi} = \sigma_{n_g}^2 \left(\frac{4E_C}{E_J} \right)^2 \quad (4.43)$$

$Q_\phi > 10^7$ even with modest $E_J/4E_C = 1$. (see Fig. 4.7).

1/f Charge Noise

The voltage noise is a remote thermal source of noise which can be filtered and though not white, is well-behaved at low frequencies. In some sense that type of noise is not really charge noise but

¹One must be careful because at high frequencies the adiabatic approximation does not apply so large Stark shifts and real transitions can occur.

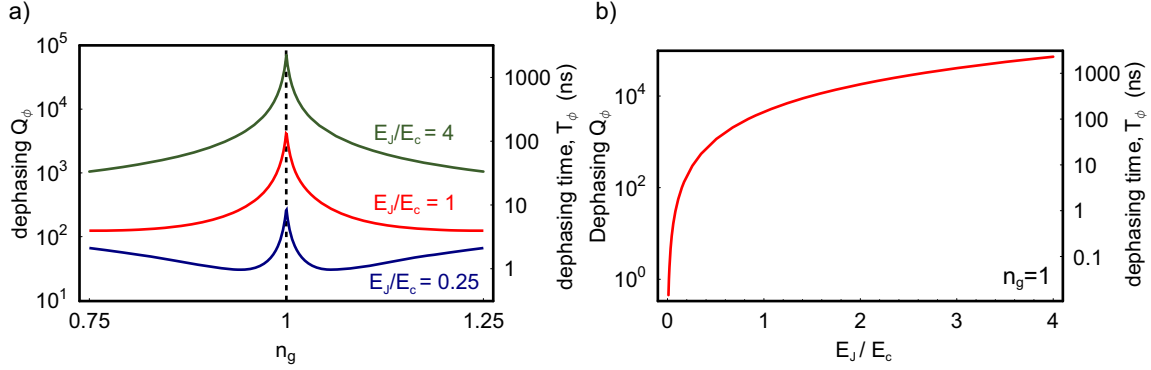


Figure 4.8: **a)** Dephasing quality factor Q_ϕ due to first and second order contributions from $1/f$ noise. Note that there is more than an order of magnitude improvement due to working at the degeneracy point $n_g = 1$, and that the overall Q_ϕ and robustness of the maximum scale favorably with E_J/E_C . **b)** Plot of maximal Q_ϕ at $n_g = 1$ at different E_J/E_C . In both plots a transition frequency of $\nu_a = 5$ GHz and $1/f$ charge noise with magnitude $S_Q(1\text{ Hz}) = 1 \times 10^{-3} e/\text{Hz}^{1/2}$ is assumed.

actually photon noise which just happens to couple through the electrostatic part of the Hamiltonian. Unfortunately, there also exists charge noise in the simple sense of charges moving around near the box, either on in the dielectric nearby or in the barrier of the junction itself. Because such local charge noise can not really be filtered (though its effects can be minimized by proper design of the CPB), it can make large excursions in rare cases, which is typically described using a $1/f$ spectral density given by

$$S_{n_g}^{1/f}(f) = A^2/f \quad (4.44)$$

The origin of this noise is not well-known but is typically of order $A \approx 10^{-3} - 10^{-4} e/\sqrt{\text{Hz}}$. To find the RMS deviations in n_g one must integrate this spectral density over the appropriate bandwidth.

$$\sigma_{n_g}^2 \approx \int_{\omega_{\min}}^{\omega_{\max}} d\omega W_0 S_{n_g}^{1/f}(\omega) \approx A^2 \ln(\omega_{\max}/\omega_{\min}) \quad (4.45)$$

It is more important to set a cutoff frequency, especially on the low side to prevent the distribution from diverging, though for most reasonable choices for cutoffs $\sigma_{n_g} \approx 3 - 5A$. If one desires to find Q_ϕ the single shot dephasing Q , one should set the cutoff to the single shot time ($\omega_{\min} = 1/\tau_{ss}$). If the Q_ϕ^* is desired, then the total experiment time $\omega_{\min} = 1/\tau_{\text{expt}}$ is more appropriate. For an upper bound the spectral density weighting function, or some property of the fluctuators themselves may set an upper bound.

Quasiparticle Noise

A very special form of charge noise is caused by quasi-particles which can tunnel across the junction instantly changing the gate charge by one electron. The treatment developed to treat thermal noise and $1/f$ noise assumes small fluctuations and is inadequate to deal with such large fluctuations. For these, it is best to take the worst case (and most likely) scenario, that the bias point switches over the whole energy range from the lowest $n_g = 1$ to highest $n_g = 0$ transition energy.

$$R = E_{\text{eg}}(n_g = 0) - E_{\text{eg}}(n_g = 1) \quad (4.46)$$

One can characterize the dephasing devastation wrought by a quasiparticle tunneling event by the ratio of $R/\overline{E_{\text{eg}}}$, which can be expressed in the charge regime as

$$\frac{2R}{E_{\text{eg}}(n_g = 0) - E_{\text{eg}}(n_g = 1)} = 1 + 2 \frac{E_J}{4E_C} \left(\frac{E_J}{4E_C} - \sqrt{1 + \left(\frac{E_J}{4E_C} \right)^2} \right) \quad (4.47)$$

This ratio ranges from 1 at $E_J/4E_C = 0$ to about 20% at $E_J/4E_C = 1$, meaning that the relative change in frequency is always of order unity, and that any quasiparticle tunneling event is fatal. However, the Eq. 4.37 is only an approximate expression, valid only when $E_J \ll 4E_C$. The energy range and thus the dephasing clearly gets smaller as $E_J/4E_C$ is increased, so what happens beyond the charge regime? In fact something remarkable happens, and the ground and excited state energy bands become very flat, exponentially suppressing the impact of charge noise.

Before discussing potential cures (see section 4.3) it is prudent to also discuss prevention. While quasiparticle tunneling is devastating, one can take several measures to reduce both the population of quasiparticles available to tunnel and the probability that they will do so. Superconductors possess an energy gap to creating quasiparticles, and thus thermal quasiparticles are suppressed exponentially at temperatures below the critical temperature. In aluminum at 250 mK there might be ~ 1 quasiparticle on a typical CPB island, but at 50 mK there is only about a one in one hundred chance of finding one, and by 20 mK there is ideally less than one chance in one hundred thousand that even a single quasiparticle is present [Lutchyn2005]. If these statistics were followed all the way down to the bath temperature of 20 mK quasiparticles would be only a minor inconvenience. Unfortunately, there are many mechanisms which can limit this scaling. There may be radiation from outside sources which breaks Cooper pairs (unlikely), or impurities which lower the effective gap (possible), magnetic fields which create areas of normal metal (likely though preventable), or

there could just be an odd number of electrons leaving one quasiparticle out of the BCS dance (coin flip).

On average then, one must assume at least one quasiparticle on the island, and since a single tunneling event destroys coherence, it is manifestly important to prevent that quasiparticle from tunneling. One option is to give it a place to go in the form of a quasiparticle trap made of normal metal, though a metal can act as both a source and sink of quasiparticles. Preventing tunneling can also be accomplished by using superconductors of dissimilar gaps, which exponentially suppress tunneling (in one direction at least). This can be done by using two different metals for the two reservoirs, changing the purity of the metals, or using a magnetic field to slightly change the gaps *in situ* [Aumentado2004]. In summary, when quasiparticles are present and mobile, they dephase the qubit quickly, but through proper engineering can be minimized.

4.2.2 Flux Noise

The flux noise is the dual of charge noise. It can arise from thermal fluctuations in nearby wires, vortices in the superconducting ground planes, or if not well shielded, from the motion of external magnetic materials.

The dimensionless first order dephasing rate in the charge regime is

$$\frac{\Gamma_\phi^\Phi}{\omega_a} = \frac{\sigma_\Phi}{\omega_a} \frac{\partial \omega_a}{\partial \Phi} = \frac{\pi \sigma_\Phi}{2\Phi_0} \frac{E_J^2}{\hbar \omega_a^2} (1 - d^2) \sin\left(\frac{2\pi\Phi}{\Phi_0}\right) \quad (4.48)$$

Note that as for charge there exist sweet spots at $\Phi = 0$ and $\Phi = \Phi_0/2$ where the first order dephasing rate goes to zero. When at or near the flux sweet spot the second order noise will dominate the dephasing rate. At the more favorable sweet spot ($\Phi = 0$) and in the charge regime this second order dephasing rate is given by

$$\frac{\Gamma_\phi^\Phi}{\omega_a} = \frac{\sigma_\Phi^2}{\omega_a} \frac{\partial^2 \omega_a}{\partial \Phi^2} = \frac{\pi^2 \sigma_\Phi^2}{\Phi_0^2} \frac{(1 - d^2)}{1 + (4E_C/E_J)^2(1 - ng)^2} \quad (4.49)$$

The dimensionless dephasing rate at the two charge degeneracy points are

$$\left(\frac{\Gamma_\phi^\Phi}{\omega_a}\right)_{n_g=1} = \frac{\pi^2 \sigma_\Phi^2}{\Phi_0^2} (1 - d^2) \quad (4.50)$$

$$\left(\frac{\Gamma_\phi^\Phi}{\omega_a}\right)_{n_g=0} = \frac{\pi^2 \sigma_\Phi^2}{\Phi_0^2} \frac{(1 - d^2)}{1 + (4E_C/E_J)^2} \quad (4.51)$$

In the charge regime where $E_J/4E_C$ is large, $n_g = 0$ is clearly more favorable for flux dephasing, however it is much worse for charge dephasing. In practice, $E_J/E_C \sim 1/4$, so the lever arm is not that

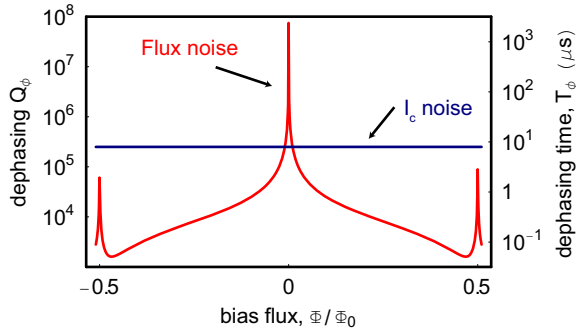


Figure 4.9: Dephasing times at the charge sweet spot ($n_g = 1$) due to flux and critical current noise. These values are independent of the E_J/E_C ratio when in the charge regime. The flux dephasing time is calculated assuming a $1/f$ distribution of flux noise with amplitude $S_\Phi(1\text{Hz}) = 10^{-5}\Phi_0/\text{Hz}^{1/2}$, qubit frequency, $\nu_a = 5\text{GHz}$, and junction asymmetry $d \sim 10\%$. The dephasing due to critical current noise was calculated using a critical current noise amplitude $S_{I_c} = 10^{-6}I_0/\text{Hz}^{1/2}$.

large and thus it is more important to minimize the effects of charge noise and one works at $n_g = 1$. Since $|d| < 1/2$, at this operating point the dimensionless dephasing rate is roughly just the fraction of a flux quantum that the noise presents. Efforts to minimize the impact of flux noise therefore cannot depend on making the matrix elements small and must focus on reducing the amount of flux noise σ_Φ . In addition to external shielding, the qubit can be designed to have a very small loop so as to only couple weakly to any fluctuating magnetic fields, and if one were to get really desperate one could use a single junction CPB, which would deprive oneself of the ability to tune E_J with flux but would eliminate the noise channel completely. Luckily even with modest measures to reduce the flux noise, the residual $1/f$ component is quite small, $\sim 10^{-5}\Phi_0/\sqrt{\text{Hz}}$ [Wellstood1987], and of course at the sweet spot one is only sensitive to second order. In our measurements, flux noise seems to be quite minimal, and can only be noticed if the charge noise is suppressed dramatically (see Sec. 4.3), and then, even without explicit external shielding, only at very low frequencies ($\sim 1\text{Hz}$).

4.2.3 Critical Current/Josephson Energy $1/f$ Noise

Critical current noise is effectively noise in the value of E_J itself. The origin of this noise is not well understood, but is thought to arise from fluctuations inside the tunnel junction barrier which add or remove conductance channels from the junction. The first order dimensionless dephasing rate is

$$\frac{\Gamma_\phi^{E_J}}{\omega_a} = \frac{\sigma_{E_J}}{\omega_a} \frac{\partial \omega_a}{\partial E_J} = \frac{E_J}{\hbar \omega_a^2} \left[\cos^2 \left(\frac{\pi \Phi}{\Phi_0} \right) + d^2 \sin^2 \left(\frac{\pi \Phi}{\Phi_0} \right) \right] \quad (4.52)$$

Unlike charge noise and flux noise there is no sweet spot for critical current/ E_J noise. There is a very general argument why there must always be at least one parameter for which no sweet spot

exists. The shape of the energy bands can be determined completely by dimensionless quantities and for any inputs into these quantities one can in principle arrange a sweet spot. However, if the transition energy is not zero then some parameter must set the absolute scale, $\hbar\omega_a$. The transition frequency must depend linearly on this parameter (by definition) and so any fluctuations in that parameter will translate directly into fluctuations in the transition frequency. While the first order dephasing rate may never be zero, in principle it can be made arbitrarily small by choosing a very stable quantity. This means that if one wants a qubit to have a certain Q then there must be some physical quantity (which the transition frequency is based on) that has that Q . In the case of the CPB that quantity (especially at $n_g = 1$) is E_J . At $n_g = 1$ the dimensionless dephasing rate due to E_J fluctuations is then just

$$\frac{\Gamma_\phi^{E_J}}{\omega_a} = \frac{\sigma_{E_J}}{E_J} \quad (4.53)$$

Variations in E_J (as measured by normal resistance fluctuations) have a $1/f$ like spectral density with $\sigma_{E_J}/E_J \approx 10^{-6}/\sqrt{\text{Hz}}$ [Eroms2006, Wakai1986].

4.2.4 E_C Noise

Another energy scale in the problem is E_C , which physically arises from the capacitance of the reservoirs. While noise in these capacitances has never been quantified, were any present it could contribute to dephasing. The first order dimensionless dephasing rate for noise in E_C is

$$\frac{\Gamma_\phi^{E_J}}{\omega_a} = \frac{\sigma_{E_C}}{\omega_a} \frac{\partial \omega_a}{\partial E_C} = \sigma_{E_C} \frac{16E_C(1-n_g)^2}{\hbar^2 \omega_a^2} \quad (4.54)$$

This dephasing rate does have a sweet spot at $n_g = 1$, so to get the dephasing rate one must go to second order where the rate (at $\Phi = 0$ for simplicity) is

$$\frac{\Gamma_\phi^{E_J}}{\omega_a} = \frac{\sigma_{E_C}^2}{\omega_a} \frac{\partial^2 \omega_a}{\partial E_C^2} = \sigma_{E_C}^2 \frac{16(1-n_g)^2}{(1 + (4E_C/E_J)^2(1-n_g)^2)^2} \quad (4.55)$$

Remarkably the degeneracy point is doubly sweet, and in fact (as we could have observed immediately) since E_C is always multiplied by $(1 - n_g)$ it will not contribute at any order¹.

4.2.5 Summary of Cooper pair box decoherence

Coherent qubit operation of the CPB is limited by the energy relaxation (T_1) processes, which affect the ability to perform single shot measurements, and the dephasing (T_ϕ) processes, which typically

¹The ability to null E_C noise to all orders is only present in the two-state approximation where $E_J \ll 4E_C$. In the transmon regime the behavior is quite different

limit the number of gate operations. When examining the effect of placing the CPB inside of a cavity we found that the qubit could be coupled much more strongly to the gate and other qubits while at the same time improving its radiative relaxation time. This innovation should allow for non-local gates in future experiments.

4.3 Transmon

This section is a bit strange as it describes what is to come and what has just begun rather than that which has been completed. It is a new way of thinking about the Cooper pair box that may be the shape of things to come, and will doubtless be the subject of further investigations and theses. The transmon, as it has come to be called, is a CPB, rediscovered as an anharmonic oscillator rather than a frustrated Cooper pair weakly tunneling between two islands. It was born out of the desire to immunize the CPB from charge noise, by decreasing the charging energy scale. At first glance, it appeared that doing so would destroy the CPB's ability to couple to the cavity, preventing measurement and the qubit-photon interactions we hoped to study. However, a more careful analysis reveals that with appropriate design the CPB can be made even more strongly coupled, and while remarkably suppressing charge noise *exponentially!* When discussed in the language of a charge qubit, these results seem to defy intuition, but when the transmon is described from the perspective of an oscillator, its behavior becomes elegantly simple. The ideas in this section are not fully mature, but they are not simply theoretical, having been employed in the most recent experiments.

The section will proceed by extending analysis of the Cooper pair box out of the charge regime, using exact solutions to the Hamiltonian rather than two-state charge approximations as in previous sections. Next, the asymptotic behavior of the transmon will be derived as an LC oscillator, which employs the non-linear Josephson inductance to achieve anharmonicity. Finally the transmon will be coupled to a cavity, taking care to keep track of auxiliary levels ignored in the two-state approximation. This section follows closely a work in preparation [Koch2007], which will present some additional information.

4.3.1 Charge Dispersion

Charge noise has been the most significant problem for the CPB. In section 4.2.1 we saw that dephasing due to charge noise could be eliminated to first order by operating at the degeneracy point ($n_g = 1$) and that the second order dephasing is reduced by increasing E_J/E_C . The reason

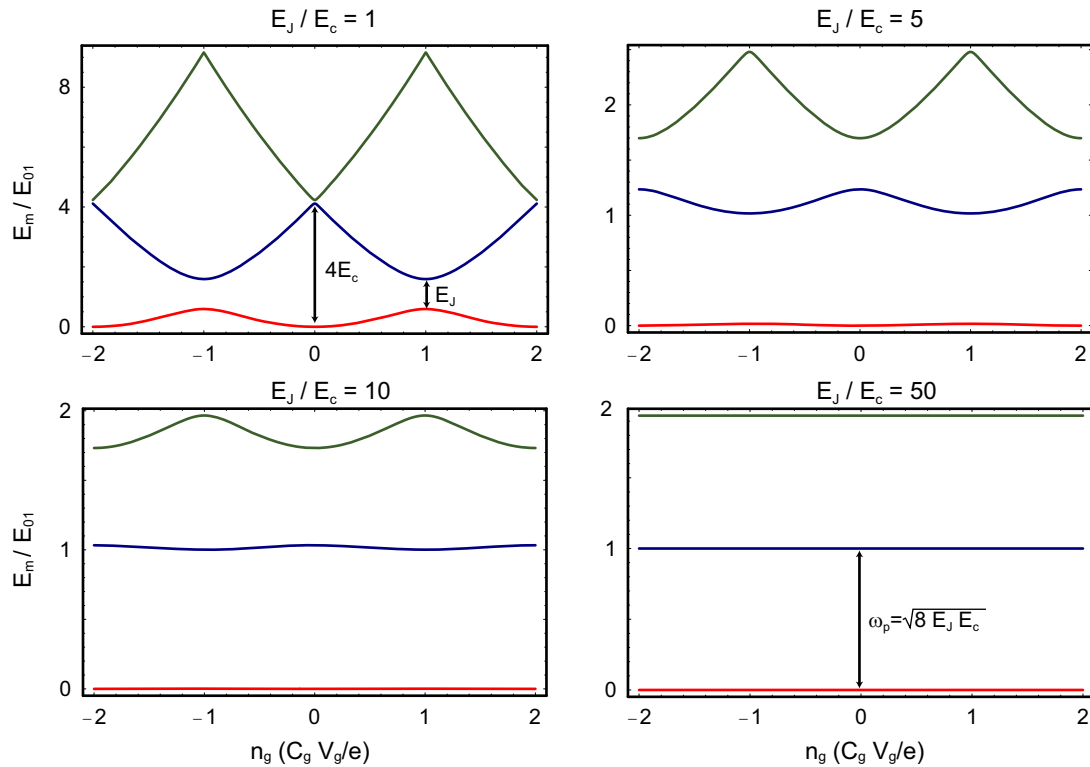


Figure 4.10: CPB energy bands at different E_J/E_C ratios. As the E_J/E_C ratio is increased the charge dispersion (minimum/maximum energy difference) becomes substantially reduced, immunizing the CPB to charge fluctuations. A side effect is that anharmonicity is also reduced (compare differences between levels in different plots). At high enough E_J/E_C the levels resemble a harmonic oscillator.

dephasing is reduced, seen in Fig. 4.10, is that as E_J/E_C increases, the energy bands begin to lose their dependence on the bias charge. In the charge regime this is only noticeable near degeneracy where the electrostatic energy is suppressed, but when $E_J > 4E_C$, it becomes energetically favorable to have currents traveling through the junction, thereby spreading the support of the wavefunction over many Cooper pairs. Looking at the flatness of the bands in Fig. 4.10, it appears that it may be possible to not only reduce the charge noise at degeneracy, but to make the qubit independent of charge all together. To quantify this possibility, one can define the total charge dispersion as the peak to peak difference in the m^{th} energy band over one charge period.

$$\epsilon_m = |E_m(n_g = 0) - E_m(n_g = 1)| \quad (4.56)$$

In the charge regime this is simply

$$\epsilon_m = |0 - 4E_C| = 4E_C = \frac{4E_C}{E_J}E_J \quad (4.57)$$

but a more thorough treatment [Koch2007] shows that this is really just the suppression as E_J/E_C is increased, is just the first term in an exponential reduction in the charge dispersion given by

$$\epsilon_m \simeq E_C \frac{2^{4m+5}}{m!} \sqrt{\frac{2}{\pi}} \left(\frac{E_J}{2E_C} \right)^{\frac{m}{2} + \frac{3}{4}} e^{-\sqrt{8E_J/E_C}} \quad (4.58)$$

This exponential insensitivity to charge holds great promise but as is apparent from the way the energy bands change in Fig. 4.10, it is a significant change that may come with unintended consequences.

4.3.2 Anharmonicity

Another change visible in Fig. 4.10 in addition to the flatness of the bands, is that they become more evenly spaced, that is their anharmonicity is reduced. In order to treat the CPB as a two level qubit, one must ignore its higher excited states. Higher states can be neglected when pulses manipulating the qubit transition do not match the frequency to excite the CPB to the next lowest level. The frequency difference between the qubit transition and the transition from excited state to the lowest unoccupied state, can be classified by the absolute and relative anharmonicity, defined as

$$\alpha \equiv E_{12} - E_{01} \quad (4.59)$$

$$\alpha_r = \alpha/E_{01} \quad (4.60)$$

Because in frequency space, the length of a pulse determines its frequency spread, the anharmonicity places a speed limit on manipulation of the qubit. Initially, as $E_J/E_C \sim 8$ the anharmonicity plummets, even passing through zero, and making it difficult to operate the CPB as a qubit, but later the anharmonicity becomes negative only slowly returning to zero. At large values of E_J/E_C the anharmonicity approaches

$$\lim_{E_J/E_C \gg 1} \alpha \sim -E_C \quad (4.61a)$$

$$\lim_{E_J/E_C \gg 1} \alpha_r \sim -\sqrt{\frac{E_C}{8E_J}} \quad (4.61b)$$

This result will be explained in the following section but for now let's explore its implications. As $E_J/E_C \rightarrow \infty$ the anharmonicity is reduced, $\alpha_r \rightarrow 0$. While the charge dispersion vanished exponentially, the anharmonicity does so only algebraically, allowing the dispersion to be suppressed significantly before the anharmonicity becomes impractically small. While in the previous section we measured the dephasing quality factor Q_ϕ , perhaps a better metric is the operation quality factor (Q_{op}), the number of operations that can be completed in one T_2 . If there were no real decay and we assume a worst case scenario of random bias charge, which gives a dephasing time related to the inverse charge dispersion¹ ($T_2 \sim 1/\epsilon_1$). The operation quality factor can be written as

$$Q_{op} = \alpha/\epsilon_1 \approx 5 \times 10^{-3} \left(\frac{2E_C}{E_J} \right)^{5/4} e^{\sqrt{8E_J/E_C}} \quad (4.62)$$

This means that even at modest E_J/E_C the Q_{op} will become very large, even with no control over charge! This is a huge boon for the scalability of CPB based qubits, as it would eliminate the need for a separate DC charge bias to compensate random offset charges, on each individual qubit. Though Q_{op} goes up, the overall speed of qubit operations does go down. In the presence of some other means of decay there will be an optimum value where the T_2 has equal contributions from decay and pure dephasing. In practice, huge benefits can be gained without any appreciable sacrifice. For example assuming 10 ns pulse length², a typical pulse length in our experiments, is within the anharmonicity for $E_J/E_C \approx 300$. If charge noise were the only limiting factor the operation quality factor would be $Q_{op} > 10^{16}$! If a different mechanism limits the dephasing time, then we still haven't lost any significant bandwidth by limiting ourselves to 10 ns pulses so we've essentially eliminated the charge noise contribution with no obvious performance penalties.

¹For simplicity the charge dispersion of the upper band (ϵ_1) is used to describe the dispersion of the qubit transition energy. This is an approximation but in the large E_J/E_C limit this will tend to dominate over the ground state dispersion (ϵ_0).

²Our arbitrary waveform generator has 1 ns resolution so a shaped (gaussian) pulse usually spans around 10 ns.

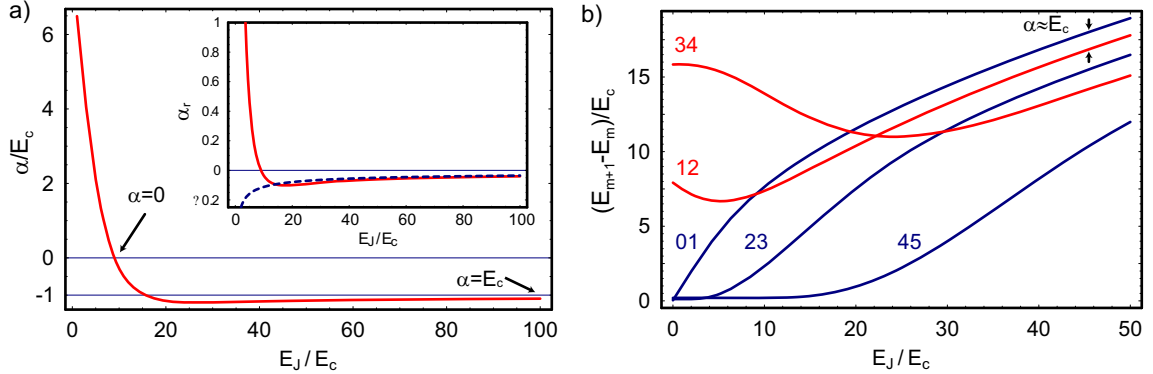


Figure 4.11: a) Anharmonicity vs. E_J/E_C ratio. The anharmonicity, displayed in units of E_C , drops rapidly at low E_J/E_C crossing zero at $E_J/E_C = 0$. It then becomes negative, asymptotizing at $\alpha = -E_C$ at large E_J/E_C . The inset shows the relative anharmonicity, $\alpha_r = \alpha/\omega_a$, and compares the exact calculation (solid) to the asymptotic (dashed) expression $\alpha_r \approx \sqrt{E_C/8E_J}$. The approximate expression proves to be a good approximation above $E_J/E_C \approx 20$. b) The formation of the transmon frequency “comb.” The transition frequency is plotted of transition energies at the degeneracy point ($n_g = 1$). At high E_J/E_C the transition energies become evenly distributed with anharmonicity, $\alpha \approx E_C$. There are two classes of transitions. Note also that at small E_J/E_C the even to odd transitions start degenerate (zero), while the odd to even ones start out large, though eventually they all fall into the comb.

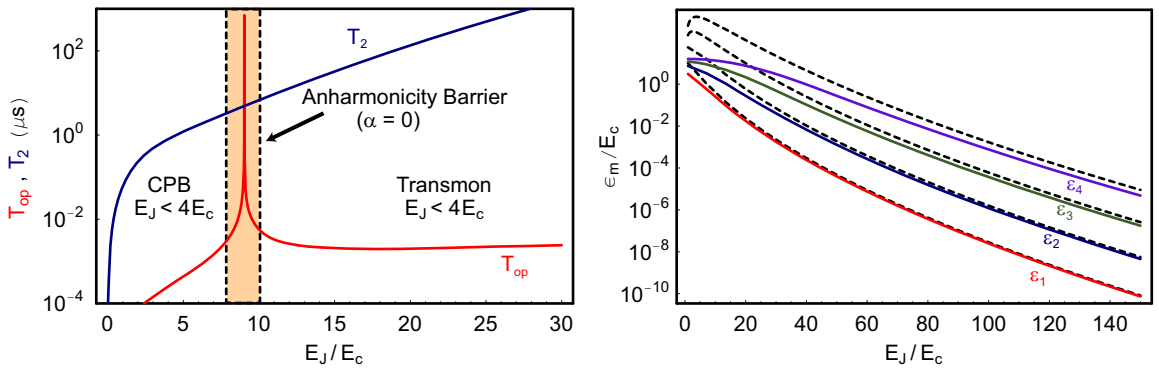


Figure 4.12: a) Plot of T_2 (blue) and $T_{op} = 1/\alpha$ (red) at $n_g = 1$ due to second order charge noise. A $1/f$ spectrum with magnitude $S_Q = 1 \times 10^{-3}e/\text{Hz}^{1/2}$ is assumed for the charge noise. While high Q 's can be obtained in the traditional CPB regime ($E_J/E_C < 4$), once passed the anharmonicity barrier (pink), where $T_{op} \rightarrow \infty$ as $\alpha \rightarrow 0$, the Q can be substantially improved at higher E_J/E_C ratios in the transmon regime. b) Plot of charge dispersion ϵ_m of the first few transmon transitions (solid lines) and asymptotic approximations (dashed lines). Plotting in units of E_C makes this a conservative estimate dimensionless dephasing rate $\Gamma_2/\alpha = 1/Q_{op}$ in the asymptotic limit (where $\alpha \approx E_C$).

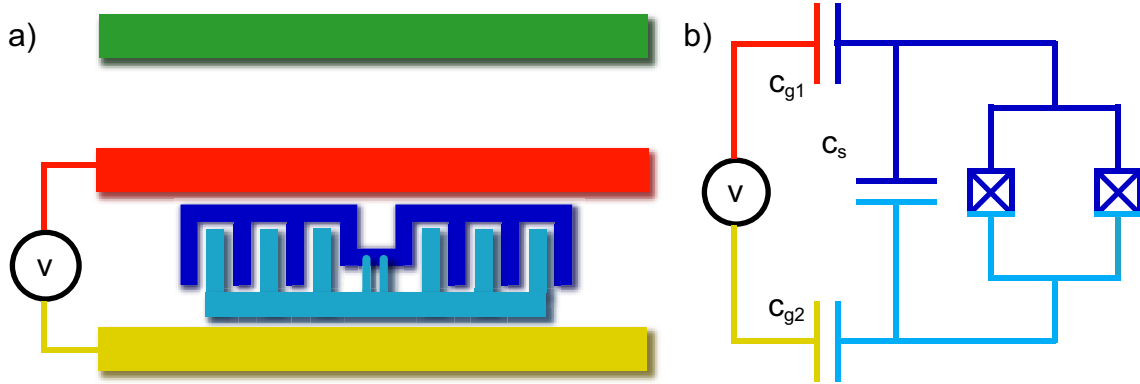


Figure 4.13: **a)** Sketch of the transmon inside of a resonator. The transmon is essentially a CPB with a large geometric gate capacitance which lowers E_C while maintaining β close to unity. The finger capacitor can be used as a shunt capacitance to lower β if unity coupling isn't desired. **b)** Simplified circuit diagram of the transmon which looks very similar to the CPB circuit diagram but with larger values for the capacitors. For a more complete circuit diagram and discussion of capacitance ratios see section 5.3.

4.3.3 Transmon as a Josephson Oscillator

The transmon appears to have the correct spectral characteristics for a qubit (high Q and sufficient anharmonicity) but though topologically the same as a CPB, it is clearly a new type of qubit demanding a new approach for understanding it. The name Cooper pair box arises from thinking about the qubit as a pair of islands where the bit is the location of a single Cooper pair, and intuition for this device is gained from modeling it as two capacitors and small coupling between them. At high E_J/E_C the CPB does not behave like this at all, and is more closely related to an LC oscillator.

The transmon can be thought of as an oscillator based on the Josephson junction and a geometrically defined capacitor (see Fig. 4.13). The argument will proceed similarly to that of the LC oscillator in 3.1.8, but with the inductor replaced by a Josephson element described by the Josephson relations [Tinkham2004]

$$2eV = \hbar \frac{\partial \theta}{\partial t} \quad (4.63)$$

$$I = I_c \sin \theta \quad (4.64)$$

where I_c is the critical current and θ is the superconducting phase difference across the junction. To reveal the Josephson junction's inductive nature, one can find the relation between voltage and

current by substituting Eq. 4.63 into the derivative of Eq. 4.64 to yield

$$V = L_J \frac{\partial I}{\partial t} \quad (4.65)$$

$$L_J = \frac{L_{J0}}{\cos \theta} = \frac{L_{J0}}{\sqrt{1 - I^2/I_c^2}} \quad (4.66)$$

$$L_{J0} = \frac{\hbar}{2eIc} \quad (4.67)$$

To first order the junction behaves as an inductor but it becomes non-linear, the inductance rising as the current approaches the critical current. An oscillator built from this non-linear inductor and a standard capacitor will be anharmonic. According to the RCSJ model [Tinkham2004] the total current can be written as

$$I = C \frac{dV}{dt} + V/R + I_c \sin \theta \quad (4.68)$$

When there is no net current one can use the Josephson relations (Eqs. 4.63 and 4.64) to get the equation of motion (in the phase) of

$$\frac{1}{\omega_p^2} \frac{d^2\theta}{dt^2} + \frac{L_{J0}}{R} \frac{d\theta}{dt} + \sin \theta = 0 \quad (4.69)$$

$$\omega_p = \frac{1}{\sqrt{L_{J0}C}} \quad (4.70)$$

This is the equation of motion for a rigid pendulum, with small angle resonant frequency, ω_p the “plasma” frequency, and viscous drag L_{J0}/R , and mass $\hbar^2/4E_C$. The corresponding Hamiltonian is [Tinkham2004]

$$H_{\text{trans}} = -4E_C \frac{\partial^2}{\partial \theta^2} - E_J \cos \theta \quad (4.71)$$

This is of course exactly the CPB Hamiltonian (though in our simplistic treatment n_g is not present¹). Rather than using the exact Mathieu solution, let’s continue the harmonic oscillator analogy, expanding the cosine potential of Eq. 4.71 as a power series.

$$H_{\text{trans}} \approx -4E_C \frac{\partial^2}{\partial \theta^2} - E_J \left(1 - \frac{\theta^2}{2} + \frac{\theta^4}{4!} + \dots\right) \quad (4.72)$$

As in section 3.1.8 the harmonic oscillator portion can be reexpressed in dimensionless units as

$$b = \sqrt{\frac{R_K}{4\pi Z_C}} \left(\theta + \left(\frac{2\pi Z_C}{\hbar R_K} \right) \hat{N} \right) \quad (4.73)$$

$$\frac{2\pi Z_C}{R_K} = \sqrt{\frac{8E_C}{E_J}} \quad (4.74)$$

¹The effect of n_g is difficult to understand in this interpretation and is best thought of as a constant vector potential added to the momentum, equivalent to acquiring an Aharonov-Bohm phase when the rotor makes a full revolution.

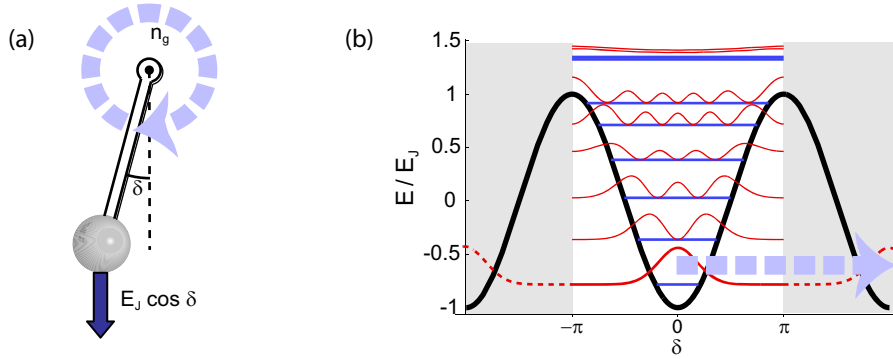


Figure 4.14: **a)** Rotor analogy for the transmon. The transmon Hamiltonian can be understood as a quantum rotor with offset charge n_g acting as a constant vector potential. For large E_J/E_C , there is a significant “gravitational” pull on the pendulum and the system typically remains in the vicinity of vanishing angle δ . Only tunneling events between adjacent cosine wells (i.e. a full 2π rotor movement) will acquire an Aharonov-Bohm like phase due to n_g . The tunneling probability decreases exponentially with E_J/E_C , explaining the exponential decrease of the charge dispersion. **b)** Cosine potential (black solid line) with corresponding eigenenergies and squared moduli of the eigenfunctions.

where as before $R_K = h/4e^2$ is the resistance quantum. Writing the phase θ in terms of the dimensionless operators¹ (as in Eq. 3.46)

$$\theta = \frac{b + b^\dagger}{2} \sqrt{4\pi Z_C/R_K} = \frac{b + b^\dagger}{\sqrt{2}} \left(\frac{8E_C}{E_J} \right)^{1/4} \quad (4.75)$$

$$\hat{N} = \frac{b - b^\dagger}{2} \sqrt{R_K/\pi Z_C} = \frac{b - b^\dagger}{\sqrt{2}} \left(\frac{E_J}{8E_C} \right)^{1/4} \quad (4.76)$$

Substituting Eq. 4.75 into the Hamiltonian of Eq. 4.71 one obtains

$$H_{\text{trans}} \approx \hbar\omega_p (b^\dagger b + \frac{1}{2}) - \frac{E_C}{12} (b + b^\dagger)^4 \quad (4.77)$$

In perturbation theory, the energy will be changed to first order, only by diagonal matrix elements, therefore we can simplify H_{trans} by collecting only the diagonal terms from $(b + b^\dagger)^4$ that can be written in the form $(b^\dagger b)^2$. Plugging these terms (see Ex. 4.3.1 to derive the prefactor) into Eq. 4.77 gives the energy of the j^{th} level to be

$$E_{\text{trans},j} \approx \hbar\omega_p (j + \frac{1}{2}) - \frac{E_C}{12} (6j^2 + 6j + 3) \quad (4.78)$$

Something truly magical has happened here, a mathematical accident or a deep and beautiful piece of physics depending on how one looks at it. The anharmonic (last) term which came from

¹For convenience in section 3.1.8 the charge operator q was chosen as the position coordinate but here the phase θ is chosen as the position coordinate. This is merely a sign convention and has no physical significance. Also where as the operators in section 3.1.8 were written in terms of charge, flux, and impedance, in this section everything is written in terms of dimensionless number, phase, and dimensionless impedance (Z_C/R_K).

the E_J term in the original Hamiltonian only depends on E_C . This is the origin of Eq. 4.61a, and is the equivalent of the anharmonicity of a mass in a quartic potential only depending on the particle mass ($\sim E_C$) not the height of the potential well ($\sim E_J$) in which it resides¹ (see Fig. 4.14). This means that one can pick the anharmonicity by choosing E_C and then choose E_J to get the desired ω_p .

Since to first order in this perturbation the wavefunctions are the same as harmonic oscillator wavefunctions we can easily determine all of the matrix elements of the system, as well as exploit all of the symmetries of the harmonic oscillator, while still getting the anharmonicity of a qubit.

Exercise 4.3.1. *Find*

$$\langle j | (b + b^\dagger)^4 | j \rangle$$

where $|j\rangle$ is a harmonic oscillator number state².

4.3.4 Transmon for Circuit QED

In the previous sections, we saw that the transmon by itself had at least the spectral characteristics to perform as a qubit. In order to use it for circuit QED (or any other application), it must still have a reasonable coupling to the cavity. At first glance, the transmon seems to be doomed. The simple quantum capacitor argument in the measurement was that the curvature in the CPB bands was like a capacitor which shifted the cavity frequency. In order to suppress the charge noise we flattened the bands completely, essentially eliminating all curvature. However, as I said earlier the quantum capacitor/curvature argument is really just an approximate DC limit for the dipole coupling. And though the static dipole moment is suppressed in the large E_J/E_C limit, the transition dipole remains large.

In the asymptotic limit, the proper expression for the dipole coupling is given (as in Eq. 3.73) by

$$g_{ij} = \beta e V_0 \langle i | \hat{N} | j \rangle = \sqrt{2} g \left(\frac{E_J}{8 E_C} \right)^{1/4} \langle i | (b - b^\dagger) | j \rangle \quad (4.79)$$

This is the same expression³ for g derived in section 3.3, but now that the energy eigenstates involve many charge states we take care to include the matrix elements for different transitions explicitly.

¹This would present an interesting if not practical spectroscopic means of determining the local gravitational acceleration g (or other restoring force independent of the inertia of the particle being acted on)

²Hint: Expand $(b + b^\dagger)^4$ and use the commutation relations to rewrite it in terms of the number operator $N = b^\dagger b$.

³Because $\beta = C_g/C_\Sigma$ and $E_C \propto 1/C_\Sigma$ is made large, it might appear that β can no longer be made close to unity for large coupling. However, $C_\Sigma = C_g + C_j + C_s$, so by adding the new capacitance through the C_g , β can actually be made larger in the high E_J/E_C regime. Further as discussed in detail in section 5.2 the extra degree of freedom afforded by the shunt capacitor C_s allows realization of nearly any β independent of other parameters.

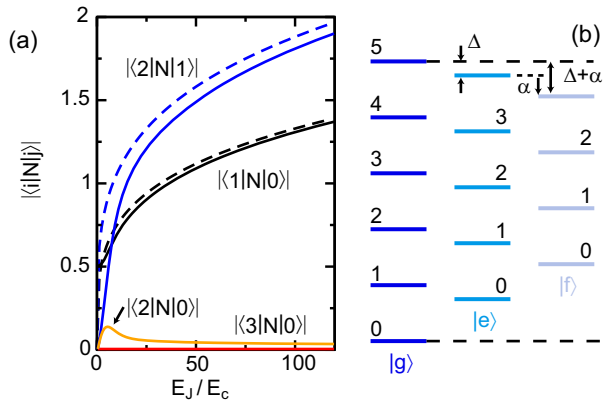


Figure 4.15: **a)** Plot of transmon charge matrix elements vs. E_J/E_C . Note that despite the fact that the curvature in the bands disappears quickly (see Fig. 4.12), the matrix element responsible for the transmon-cavity coupling ($\langle 1 | n | 0 \rangle$) actually increases. Also while the matrix elements for single level transitions remain large, that of two-level transitions are small and are strongly suppressed. This is due to parity of the CPB energy levels which begin to resemble harmonic oscillator eigenstates, which alternate between even and odd parity. The number operator (which resembles the position of the harmonic oscillator) is odd, so transitions involving an even number of excitations are strongly suppressed. This parity property becomes strong as the resemblance of a CPB to a harmonic oscillator grows with E_J/E_C . The quartic potential of the transmon preserves the harmonic oscillator parity while the cubic potential of a phase qubit, which does not, allows such transitions. The fact that higher order transitions are suppressed greatly simplifies the treatment of the transmon in circuit QED. **b)** Energy level diagram for circuit QED with multilevel qubit. The vertical levels represent photon numbers in the cavity while the qubit levels are listed left to right. The cavity levels are detuned from the $g \rightarrow e$ transition by Δ and the higher auxiliary levels are each detuned by α from the previous CPB transition at high E_J/E_C .

A plot of several relevant matrix elements is shown in Fig. 4.15.

For the especially relevant case of adjacent levels one gets a coupling of

$$g_{j,j+1} = g \left(\sqrt{2(j+1)} \left(\frac{E_J}{8E_C} \right)^{1/4} \right) \quad (4.80)$$

The quantity in parenthesis is the scale of $n^{1/2}$, the number of Cooper pairs tunneling in the oscillator. In the traditional CPB, there is one Cooper pair, but even at $E_J/E_C = 100$ there are only ~ 15 Cooper pairs sloshing back and forth. Because more Cooper pairs are involved the dipole moment actually increases¹, but only very slowly. Although it is tempting to again truncate the Hilbert space, ignoring the non-qubit levels, in this new regime of lower anharmonicity one does so at one's peril. The responsibility to keep track of all the CPB levels is in a certain sense the main price one pays using the transmon. One should never have ignored higher levels even in the charge regime, but it was difficult keep track of them since they were at energies difficult to measure directly, and were highly sensitive to charge noise. Now their effects are felt explicitly, but can also be kept track of more easily.

The reason we cannot ignore higher levels is that in this E_J/E_C regime one often works with the charging energy similar to the coupling ($E_C \sim g$). That means that though the transition frequencies are different enough to use fast pulses ($1/\tau \sim E_C/h$) they are similarly detuned $\Delta \gg E_C$, especially well into the dispersive limit. Graphically these auxiliary levels can be accounted for by extending the energy ladder diagrams to the right as in Fig. 4.15. At minimum we must keep the lowest three levels to write down the dispersive Hamiltonian

$$H_{\text{eff}} = \frac{\hbar\omega'_a}{2} + (\hbar\omega'_r + \hbar\chi_{\text{eff}}\sigma_z)a^\dagger a \quad (4.81)$$

with an effective Lamb-shifted transition frequency $\omega'_a = \omega_{01} + \chi_{01}$ and cavity frequency $\omega'_r = \omega_r - \chi_{01} - \chi_{02}$. With these dressed transitions the Hamiltonian looks similar to the traditional CPB case except that one gets an effective dispersive shift which depends on the next highest level

$$\chi_{\text{eff}} = \chi_{01} - \frac{\chi_{12}}{2} + \frac{\chi_{02}}{2} \quad (4.82)$$

where

$$\chi_{ij} \equiv \frac{g_{ij}^2}{\omega_{ij} - \omega_r} \quad (4.83)$$

¹The derivation of the “fine structure limit” assumes only a single Cooper pair tunneling. To make it apply at high E_J/E_C one can multiply by the term in parenthesis in Eq. 4.80.

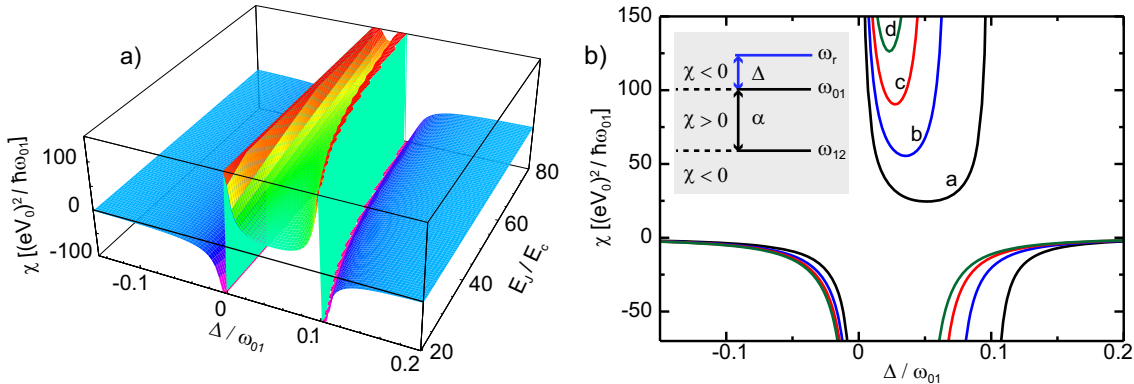


Figure 4.16: **a)** Dispersive frequency shift, χ as a function of detuning Δ between cavity and transmon and energy ratio E_J/E_C , for fixed transition frequency ω_{01} , with $\beta = 1$ and $n_g = 1$. **b)** The bottom panel depicts cross-sections of the 3D plot for $E_J/E_C = 20$ (a), 40(b), 60 (c), and 80(d). Inset shows energy level configuration and regimes for the dispersive shift. When the transmon is detuned negatively or by more than α then the dispersive shift is negative ($\chi < 0$). In the “straddling” regime, when $0 < \Delta < \alpha$, the dispersive shift is positive ($\chi > 0$).

is the dispersive shift for each transition inside the transmon. Using equation 4.79, χ_{ij} can be written as

$$\chi_{ij} = 2 \left(\frac{E_J}{8E_C} \right)^{1/2} \frac{g^2 | \langle i | (b - b^\dagger) | j \rangle |^2}{\Delta_{ij}} \quad (4.84)$$

where $\Delta_{ij} \equiv \omega_{ij} - \omega_r$. Plugging this approximate expression into Eq. 4.82 gives

$$\chi_{\text{eff}} \approx -\frac{g^2}{\Delta} \frac{\hbar \omega_p}{4(\hbar \Delta - E_C)} \quad (4.85)$$

Because of the interplay between the anharmonicity and the detuning there are three distinct regimes of dispersive coupling (see Fig. 4.16). When both Δ and $\Delta - E_C$ are the same sign then $\chi_{\text{eff}} < 0$. In the special case where they are opposite signs, which occurs when $0 < \Delta < E_C$, then $\chi_{\text{eff}} > 0$ and is also significantly enhanced. Another thing to note in Fig. 4.16 is that when $\Delta = \alpha$ or any other integer multiple of the anharmonicity, one of the transitions will be resonant with the cavity. If this occurs even for higher transitions (if there are enough photons in the cavity) then even if the matrix elements for such a process are small the energy denominator will go to zero causing the dispersive shift to explode. This can be a source of charge noise based dephasing because higher levels are more sensitive to charge. Using a negative detuning ($\Delta < 0$) can help avoid some of these complications¹.

Whereas before we only concerned ourselves with the coupling induced decay due to the qubit

¹Negative detuning does not eliminate the problem altogether as high levels may change their energy by more than ω_{01} with charge.

transition (ω_{01}), now we must consider higher lying transitions. If these transitions are resonant with the cavity or its excitations, the qubit could be excited to one of the auxiliary levels, incoherently absorbing one or more photons. During logic operations when the cavity would be empty, this process would not be possible, but it might interfere with a measurement of the qubit state.

4.3.5 Other Sources of Decoherence

While we have already discussed the effects of charge noise we must also consider how the transmon responds to other decay and dephasing mechanisms. In this section we will discuss the action of critical current and flux noise, as well as briefly discuss the transmon's tolerance to charging energy fluctuations and dielectric noise.

Flux noise

At degeneracy flux noise will enter through the dependence of the plasma frequency ω_p on E_J and the effective E_J on the flux. At $\Phi = 0$ the qubit is first order insensitive to flux fluctuations, and so the second order contribution will dominate. The dimensionless dephasing rate is then

$$\frac{\Gamma_\phi^\Phi}{\omega_p} = \frac{\sqrt{3}}{2} \frac{\sigma_\Phi^2}{\omega_p} \frac{\partial^2}{\partial \Phi^2} \sqrt{8E_C E_J \cos\left(\frac{\pi\Phi}{\Phi_0}\right)} = -\frac{\sqrt{3}}{2} \frac{\sigma_\Phi^2 \pi^2}{4\Phi_0^2} \left[\tan^2\left(\frac{\pi\Phi}{\Phi_0}\right) + 2 \right] \approx -\frac{\sqrt{3}}{4} \frac{\sigma_\Phi^2 \pi^2}{\Phi_0^2} \quad (4.86)$$

Assuming a universal flux noise[Wellstood1987] of $\sigma_\Phi = 3 \times 10^{-5} \Phi_0$, gives a quality factor of $Q_\phi \sim 10^8$, well beyond current limitations.

Critical current noise

Noise in the critical current will once again directly translate into noise of E_J . In the large E_J/E_C limit the transition frequency is well approximated by the plasma frequency ω_p and the first order deviations are characterized by

$$\frac{\Gamma_\phi^{E_J}}{\omega_p} = \sigma_{E_J} \frac{\partial \sqrt{8E_J E_C}}{\partial \hbar \omega_p} = \frac{\sigma_{E_J}}{2E_J} \hbar \quad (4.87)$$

which, because of the square root is half as sensitive as it was in the charge regime.

Charging energy fluctuations

The same argument can be made for charging energy fluctuations.

$$\frac{\Gamma_\phi^{E_C}}{\omega_p} = \sigma_{E_C} \frac{1}{2E_C} \quad (4.88)$$

However remember that at degeneracy ($n_g = 1$) the charge qubit could be made nominally insensitive to charging energy fluctuations. That fact was derived using the two charge state approximation, in practice at $E_J/E_C \approx 1$ the first order fluctuations are only reduced by a factor of ten. At present the amount of charging energy fluctuations is unknown and thought not to be a limiting factor. The transmon the capacitance has changed from being mostly in the junction barrier with high fields and small distances to being a large geometric capacitance. If significant charging energy fluctuations exist, studying the transmon would help determine their location.

Dielectric noise

While the dielectric noise has the potential to cause decay in the same manner and at the same rate (half of the energy is always in the electric field), the transmon gives the freedom to choose the participation ratio, the locations of the fields. By choosing a large external capacitance one can make most of the field live in the substrate, whereas by increasing the junction capacitance or making an overlap capacitor one can put the fields in a thin insulating barrier. This freedom will allow (better) controlled experiments on the electrical quality factor of the junctions.

Quasiparticles

The transmon can have a large Q because energy can only be lost by photons at the transmission frequency, and the impedance of the environment at that frequency is very carefully controlled. Quasiparticles once created, can lose arbitrarily small amounts of energy, making them very efficient at dissipating the energy stored in the coherent qubit oscillations. In section 4.1.3, this loss was modeled by assuming a two fluid model, where a resistive fluid (quasiparticles) were shunted by a superconducting but inductive fluid. That model captured much of the essential physics, describing the exponential temperature dependence and effect of junction tunnel resistance on the qubit decay rate.

Here that model is extended to include the density of states of the superconductor and the matrix elements for transitions out of the qubit excited state [Lutchyn2006].

$$\Gamma_1^{\text{QP}} = \frac{N_{\text{qp}}}{4\pi N_e} \frac{R_K}{R_n} \sqrt{\frac{T}{\omega_a}} \sum_j \frac{|\langle i | \text{QP} | e \rangle|^2}{|\langle i | \text{QP} | e \rangle|^2} \quad (4.89)$$

where N_{qp} is the number of quasiparticles in the transmon, N_e is the total number of electrons, and

QP is an operator which represents suddenly changing the gate voltage n_g by one electron.

$$N_{\text{qp}} = 1 + N_e \frac{\Delta}{\epsilon_F} \left(1 + e^{\Delta/k_B T} \right)^{-1} \quad (4.90)$$

There is a lot happening in Eq. 4.89, so let's analyze the origin of each term. The ratio of the resistances and quasiparticle fraction are the same terms as in the more naive treatment in section 4.1.3, though now we have assumed that even at zero temperature there will be one quasiparticle (an odd number of electrons in the metal). If the number of quasiparticles is independent of the volume of the CPB then $N_{\text{qp}}/N_e \propto 1/V$ and quasiparticle dissipation will be reduced in the larger transmon. It is thought that the quasiparticle number may scale with the volume ($N_{\text{qp}}/N_e \sim \text{const}$). The additional quasiparticles able to tunnel would be compensated by additional Cooper pairs shunting them. In addition, there is now a factor representing the density of states $\propto \sqrt{T/\omega_a}$ to which a quasiparticle can tunnel. Finally, a quasiparticle tunneling event can be modeled as a sudden change from $n_g = 1$ to $n_g = 0$, which might not change the state of the qubit. For a CPB in the charge regime, going from $n_g = 1$ to $n_g = 0$ goes from an even superposition of zero and one Cooper pair to a state with zero Cooper pairs, giving a transition probability of 1/2. In the transmon, this amount can be reduced.

4.3.6 Transmon Summary

The transmon is an elegant new qubit which appears to eliminate the effect of charge noise. This should dramatically enhance the ability for such qubits to be operated at high Q's and to later scale (eliminating the need for individual charge biasing) to larger numbers of qubits, where individual voltage biasing and feedback would be difficult. It does so while improving nearly every other performance metric over the traditional CPB and thus is a very promising qubit candidate. The only penalty is that the anharmonicity formerly of order unity is now only 10% requiring much more careful attention to the effects of extra levels. This initial theoretical analysis does not predict the smaller anharmonicity to be a significant barrier, but care must be taken. More information on the design and fabrication of the transmon, which was used for the last two experiments performed, is presented in section 5.3. Experimental work is also reported in sections 8.3 and 9.3.

Noise	transmon $E_J/E_C = 85$	CPB $E_J/E_C = 1$	flux qubit	phase qubit
Dephasing	$1/f$ amp.	T_2	T_2	T_2
charge	$10^{-4}e$ E ^A	0.4 ms T	★ 1 μ s* T	110 ns T ^B – 0.1 s T ^C
flux	$10^{-5}\Phi_0$ E ^D	0.4 ms* T	0.1 ms* T	★ \sim 120 ns E ^E
I_0	$10^{-6}I_0$ E ^F	★ 35 μ s T	17 μ s T	★ \sim 40 ns E ^G
<i>measured</i>		150 ns E	> 500 ns E ^H	20 ns E ^I ; 120 ns E ^J
relaxation	T_1	T_1	T_1	T_1
	90 ns E	$\sim 7 \mu$ s E ^H	900 ns E ^L	110 ns E ^K

Table 4.1: Comparison of representative relaxation and dephasing times for various superconducting qubit designs. The symbol E denotes experimental data, T indicates theoretical predictions, and “★” marks the noise channel most likely limiting the performance of the qubit. Entries marked with “*” are evaluated at a sweet spot (i.e. second-order noise). A: [Zorin1996] B: [Bertet2007] C: [Tian2000] D: [Wellstood1987, Yoshihara2006] E: [Bertet2004] F: [VanHarlingen2004] G: [Simmonds2004] H: [Wallraff2005] I: [Chiorescu2004] J: [Bertet2004] K: [Steffen2006] L: [Chiorescu2004]

Chapter 5

Design and Fabrication

This chapter is intended to be a practical guide for the design and fabrication of circuit QED components. The focus is towards creating robust processes which are tolerant of variations in environmental conditions and operator procedure. Robustness comes not just from making lithography and depositions repeatable, but also from designing circuits which realize optimal parameters with large tolerances. The chapter is divided in to a section for each component, the cavity, the CPB, and the circuit board. For each component the simulations and calculations are performed to estimate the circuit parameters of a given geometry. The circuits are created with different lithography (optical and electron beam) and deposition techniques (evaporation and sputtering), each imposing its own unique constraints. A description of the thought process behind each design decision and examples of what things should look like when they are working are shown for each step of the process.

5.1 Cavity

5.1.1 Design Considerations

There are three primary cavity parameters, the resonator impedance, frequency, and quality factor. The frequency is determined by the length. The impedance is controlled by the ratio of the center pin thickness to the size of the gap between the center pin and ground planes. Finally, the quality factor is determined by the size of coupling capacitors at the input and output. The geometric realizations of these parameters are nearly independent. Small effects such as the loading of the coupling capacitors adjust the frequency and impedance on resonance can be modeled and compensated. In addition, while errors in the design or fabrication will affect the exact values of the cavity parameters, the

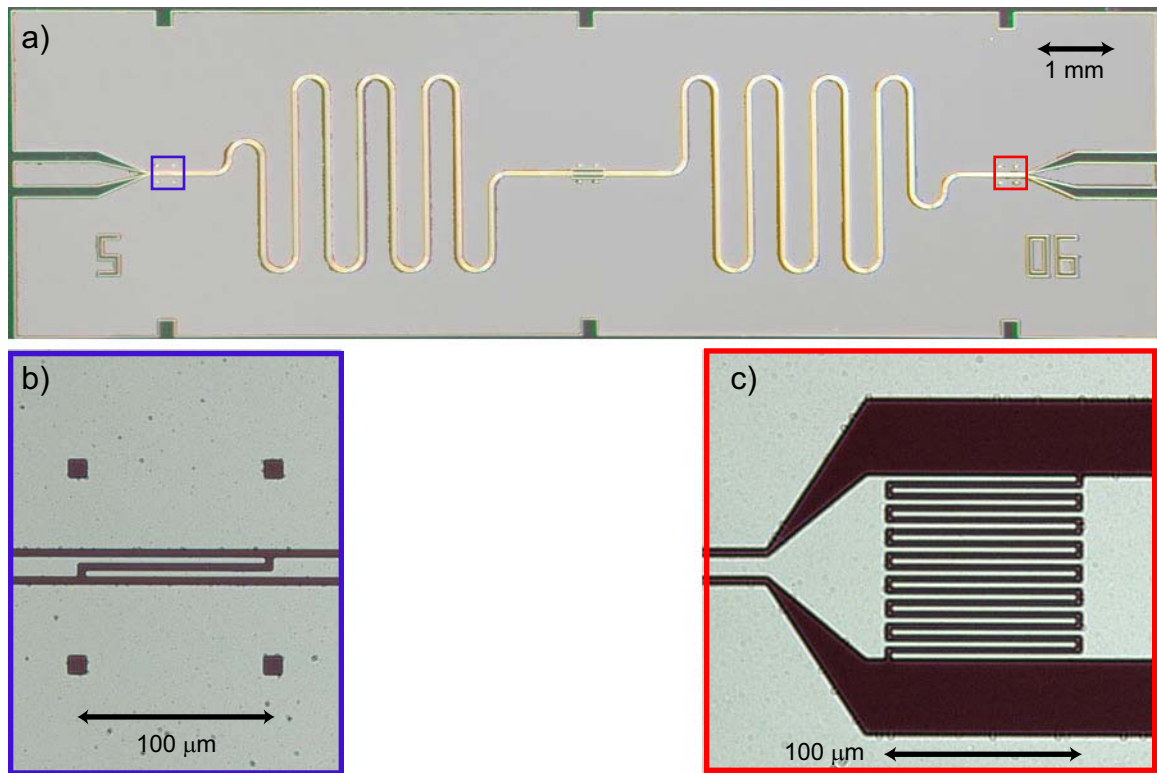


Figure 5.1: Resonator sample and input/output capacitors. **a)** The resonator is composed of a half wave coplanar waveguide. The CPW structure can be resolved at the input and output end with metal being beige and substrate dark. In the resonator itself the magnification cannot be resolved

physics is such that only extreme errors such as metal flakes in the gap will cause device failure. This sort of intrinsic robustness allows us to use the same mask on different substrates and change the coupling or experiment with different qubit geometries without drastically changing the cavity design.

The fundamental frequency of the cavity is set by the effective speed of light and the length of the resonator. When using a substrate made from a single material the effective dielectric constant, and thus effective speed of light can be calculated analytically using Eq. 3.25. The length of transmission line required to attain a $\lambda/2$ resonance frequency is then given by

$$\ell = \frac{c}{\epsilon_{\text{eff}}^{1/2} \omega_r} \frac{\pi}{2} \quad (5.1)$$

The use of multiple dielectrics (such as SiO_2 on Si) is much more difficult to calculate exactly and slightly modify the effective dielectric constant. Small perturbations in the electrical length also arise from the loading due to the kinetic inductance [Yoshida1995] and the coupling capacitors. While it may be difficult to calculate the exact effective speed, the frequency can still be adjusted linearly by adjusting the length. In practice, it is easier to make a set of resonators once, and then adjust the length, keeping all other parameters the same, to compensate these shifts if higher precision is required. The typical shifts due to kinetic inductance (see Sec. 7.1.1) are approximately 5 – 10%. The loading of the coupling capacitors gives a shift $\sim -(q_{\text{in}} + q_{\text{out}})\omega_r$. These shifts are in principle very repeatable, but in practice fabrication errors can lead to some randomness in their values. If the pattern is over or under exposed it can change the effective wave velocity somewhat, and the value of the coupling capacitors significantly. When the same pattern is made it is typically repeatable to within 1 – 2% or about 50 – 100 MHz. Adding a few hundred nanometers of oxide to the silicon substrates changes the frequency by ~ 500 MHz. Resonators are very repeatable on repeated cool downs with resonant frequencies changing by of order 1 MHz which is about one part in 10^{-4} . The resonators are designed to be as modular as possible. In order to allow resonators of substantially different lengths to mate to the same printed circuit board they are made to meander (see Fig. 5.1). This has the additional advantage of making the circuit smaller and thus helping to avoid parasitic modes. If the curvature of the meanders is much less than the gap size the impedance will not be affected (see 5.1).

The characteristic impedance (Z_0) can be calculated using Eq. 3.24. The kinetic inductance and dielectric composition also affect the exact value of the impedance. One might think that the cavity

coupling would be very sensitive to its characteristic impedance, but actually for a Fabry-Perot cavity small differences in the internal impedance are not very important. Rather the coupling is determined almost completely by the ratio and size of the coupling capacitors. The internal impedance does affect the vacuum field strength, but it depends on geometry and dielectric constant rather weakly, so variations away from $50\ \Omega$ are typically small.

The quality factor can be determined by the size of the coupling capacitors using Eq. 3.18. For the highest quality factors the coupling capacitors can be formed by having a gap in the centerpin. The strength of this coupling can be made arbitrarily small by making the gap larger (see Fig. 5.1). For larger coupling (lower external Q), the capacitors are realized using planar interdigitated finger capacitors. The minimum width and spacing of the fingers is set by the minimum feature size for our optical lithography process¹ of $2\ \mu\text{m}$. The length of the fingers can be adjusted as can the number of fingers. In order for the fingers to be accurately represented as a lumped element capacitor they must be much smaller than the wavelength. If the fingers get too long their inductance becomes significant, which can alter the capacitance values or create undesired parasitic resonances. In practice $2\ \mu\text{m}$ fingers with $2\ \mu\text{m}$ spacing that are $200\ \mu\text{m}$ or less are safe. To find the values of the capacitors, we simulate their DC capacitance with *Maxwell*, a commercial electromagnetic simulation package. Their RF performance was also simulated using another simulation program, *Sonnet*. Some capacitance values are given in Table XX, but a good rule of thumb is that a symmetric resonator with coupling capacitors each consisting of one pair of fingers $100\ \mu\text{m}$ in length, gives a quality factor of $\sim 10,000$, and that the Q scales inversely with the square of the number of fingers (as per Eq. 3.18).

The frequency shifts due to the coupling capacitors can be calculated using Eq. 3.20. The transmission coefficient (Eq. 3.19) is determined by the ratio of the coupling capacitors. Initially symmetric capacitors were used, but as described in section 3.4.5, it is more efficient to use asymmetric coupling capacitors with a larger output capacitor limiting the external quality factor.

The desired characteristic impedance determines the ratio of the pin size to the gap, but it does not say what the absolute scale should be. We attempt to keep the gap size as small as possible without straining the design tolerances. This approach keeps the electromagnetic field confined to a small volume, and away from lossy PCB materials and the backing ground plane which might

¹While our optical lithography equipment is in principle capable of realizing sub-micron feature sizes, imposing a $2\ \mu\text{m}$ feature limit, reduces mask costs and more importantly makes the process more robust.

also be lossy or give parasitic modes. For most resonators a center pin width of $10\ \mu\text{m}$ was chosen, though $5\ \mu\text{m}$ has also been tested successfully.

Such a center pin width can be realized with standard optical lithography, but is well beyond the capabilities of commercial PCB makers. Typical PCB tolerances are $\pm 75\ \mu\text{m}$. In order to accommodate these tolerances the input and output CPWs on the PCB have a centerpin width $\sim 500\ \mu\text{m}$. In order to prevent reflections which could reduce the measurement efficiency, one must smoothly taper the centerpin (and gap) width from the PCB to the chip. The overall transverse dimension can be reduced without reflections if the ratio between the gap and centerpin widths is maintained and they are reduced gradually. In a CPW, on a very thick substrate, this can be done with a simple linear taper. However, when the transverse width is comparable to the thickness of the substrate, the CPW mode acquires some microstrip character. This additional length scale is taken into account by equation 3.24 for the impedance, but creates some curvature when going from widths comparable to the substrate thickness to very narrow lines¹. This taper is one of the primary reasons for selecting the CPW geometry as its characteristic impedance can remain unchanged over a wide range of transverse dimensions. This allows one to couple to large circuit board features easily while attaining high electric field densities and confinement (high Q) in the actual resonator.

5.1.2 Optical Lithography

The resonator patterns are made using optical lithography, based on a resist system which uses *Microchem* lift off resist (LOR5A) as a sacrificial bottom layer and *Shipley* (S1808) photoresist as a primary layer. The base recipe is presented in table D. In this resist system, the pattern is transferred through a chrome mask via “hard contact” lithography to the top layer which is sensitive to UV. The bottom layer behaves as though “pre-exposed,” due to a chemical additive and its etch rate depends only on how it was pre-baked, not on the exposure. Areas which are exposed etch through the top layer, exposing the sacrificial layer. The same developer can then uniformly etch the bottom layer below the exposed regions at a well defined rate. With appropriately selected bake temperatures and development time, an undercut profile such as the one shown in Fig. 5.3 can be realized. Figure 5.3b is an example of how successful lithography should look, with the top layer possessing a steep vertical wall, with no sagging, and an undercut of approximately two to three times the LOR thickness.

¹For both the old and new resonator designs the dimensions were chosen such that all dimensions are small compared to the substrate thickness allowing a simple linear taper to be used.

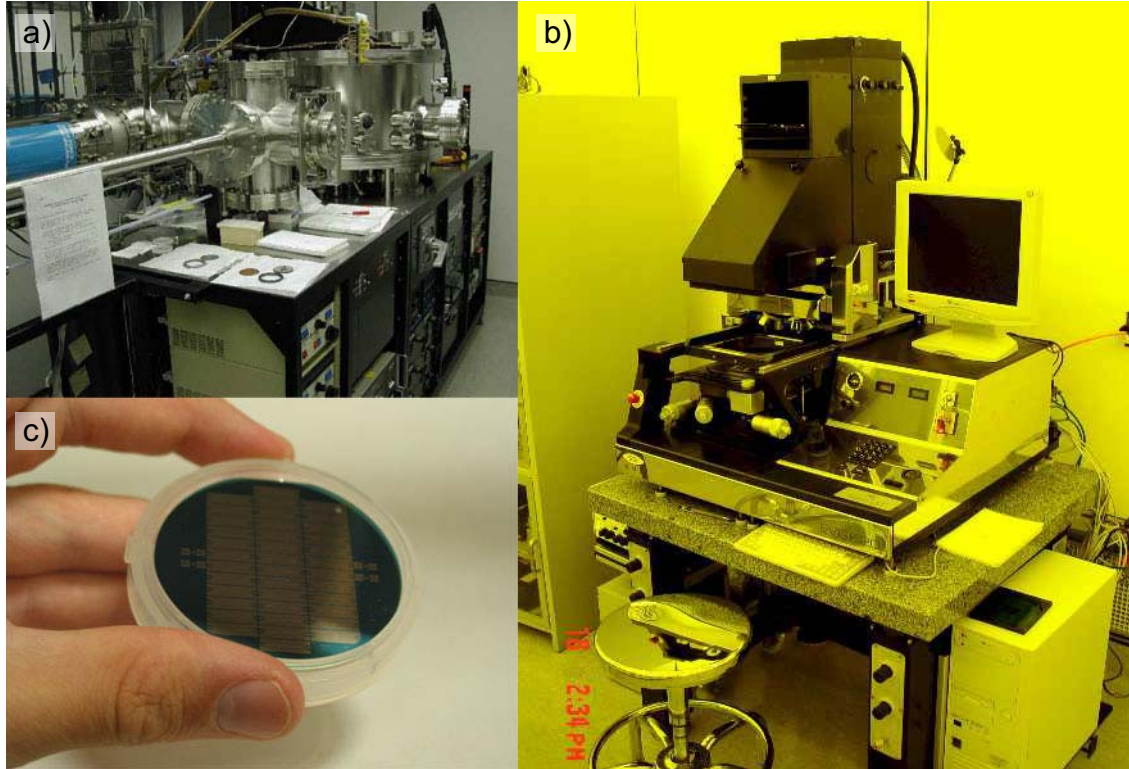


Figure 5.2: **a)** Lesker sputtering system. This system is used to deposit Nb via DC magnetron sputtering. **b)** EVG mask aligner used in hard-contact mode to expose the photoresist through a chrome mask. It is capable of sub-micron accuracy. **c)** A processed wafer of resonators prior to dicing (hand modeling by Andreas Wallraff).

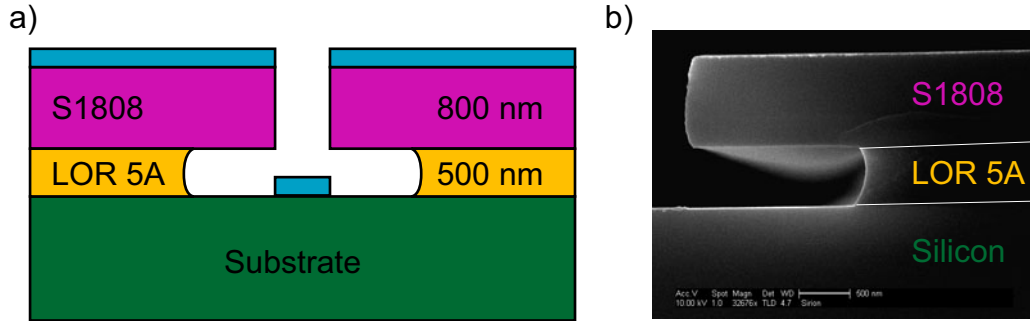


Figure 5.3: **a)** Ideal bi-layer resist profile. The wafer is spun with two layers of photoresist. The undercut layer is made from LOR5A a photoresist with an additive which makes it etch at a rate dependent only on the prebake temperature, not on exposure to light, and spins to about 500 nm. The top layer is S1808, a positive photoresist, which spins to about 800 nm. When an exposed portion is placed in a solution of developer it will dissolve. The bottom layer will then etch at a uniform, slow, rate which can be used to control the “undercut.” This profile facilitates smooth liftoff by ensuring that the deposited film on top of the resist is not connected to the film on the substrate. **b)** SEM image of resist profile. Note that the top layer has a nearly vertical sidewall. If the sidewall is not vertical the exposure is bad possibly due to poor contact with the mask. The top layer should not sag and the thicknesses of both layers should be as desired.

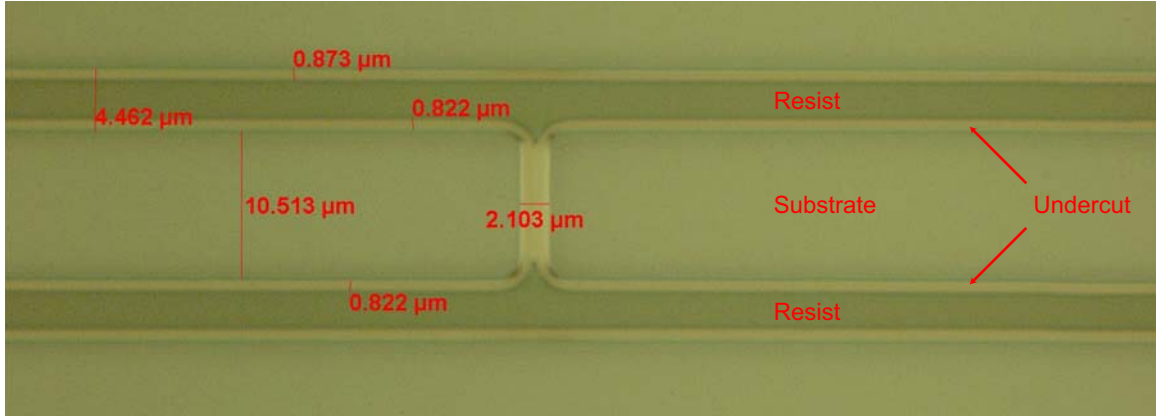


Figure 5.4: This image shows the a gap capacitor in resist. Note that all resist characteristics except the resist cross-section (shown in Fig. 5.3b) can be seen in this optical image, which can be taken immediately after development (and before deposition). The top, bottom, and centerpin appear as exposed substrate (beige). The gaps of the resonator are formed by continuous sections of unexposed (and undeveloped) resist (darker). Finally the light beige on the border between the two regions is the undercut. Note that the undercut still has resist on top, and so the final metal pattern will be determined by the border between the undercut ring and the substrate, not the undercut and the resist (which is substantially rounded). This sample had a little bit to much undercut and so the resist protecting the gap capacitor is completely suspended. While this sample would be fine, other resonators with longer gap capacitors might be damaged, so this is something to pay extra attention too.

This process can be very sensitive to the baking temperature of the first layer, which determines the etch rate. If developing this process on new equipment, one must check the hotplate uniformity and temperature with a calibrated thermometer. If uniformity is a problem or if the surface is dirty one can use an eighth inch thick piece of aluminum plate to spread the heat. It is probably also wise to limit air flow over the wafer by placing it under a beaker cover (raised on glass slides to allow some air flow).

The recipe in Table D should serve as a good starting point for optically patterning the resonators. Because all optical mask aligners have slightly different spectral characteristics one must calibrate the exact dosing to the specific machine. One should first start with a single layer of S1808 making sure that the top layer will faithfully reproduce the edges.

Characterization of the resist processing is most easily done directly after development via optical microscope (see Fig. 5.4). At this stage the patterns should be visible, as should the undercut. One should check the dimensions against the design, and pay extra attention to the undercut making sure there are no suspended regions.

5.1.3 Deposition and Liftoff

When making a metallic pattern, one must decide between an etching process and a liftoff process. In the etching process, one deposits a film and then defines an etch mask to protect the parts that are needed. This has the advantage that the film can be deposited under more ideal conditions, without being contaminated by resist outgassing, and at high temperatures without fear of burning the resist. Etching processes can be either dry, involving physical etching or reactive gasses, or alternatively it can be wet, involving submersion in liquid etchants. Unfortunately, until recently we did not have facilities to perform dry etching, and wet etching was found to be difficult to control, so in this work we chose a lift-off process. In this type of deposition, the wafer is coated with resist and patterned before the deposition. Areas of the resist which are removed expose the substrate, and metal is deposited on the whole wafer. The resist is then dissolved, and only metal in direct contact with the substrate is left, with the rest lifted off with the resist.

The ideal metal for this work would probably have been tantalum, with a T_c above 4 K and a single high quality oxide. Unfortunately, tantalum is only deposited well at high temperatures, and so is not compatible with our lift-off process which uses polymer resists. The next best choice would be niobium with $T_c \sim 9.2$ K, but it has many oxides with low temperature behavior varying from insulator to superconductor. Niobium, like tantalum, is a refractory metal, and cannot be thermally evaporated, but good film quality can be achieved by DC magnetron sputtering at room temperature (see Table D for recipe and Fig. 5.2a for picture of sputtering machine).

Unfortunately, as shown in Fig. 5.5, sputtering is not a very directional deposition technique. It is certainly possible to make resonators using sputtering and a liftoff technique, but the edge quality is often quite poor. At the lowest temperatures (20 mK), it is still possible to get high quality factors in the $10^5 - 10^6$ range. However, the properties of these poor edges make it difficult to place the qubit close to an edge, which hurts the coupling. Its behavior in the presence of a magnetic field is also not well known and may affect the qubit.

For this reason, the most recent devices have been made with aluminum. The major disadvantage of Al is its low critical temperature $T_c \sim 1.2$ K, meaning that it cannot be measured at 4 K in a storage dewar or at 1.5 K in a pumped helium system. It does, however, have a low melting point, making it suitable for thermal or electron-beam evaporation. These are very directional deposition techniques, and they are well-suited to clean liftoff. For this reason, most of the original development

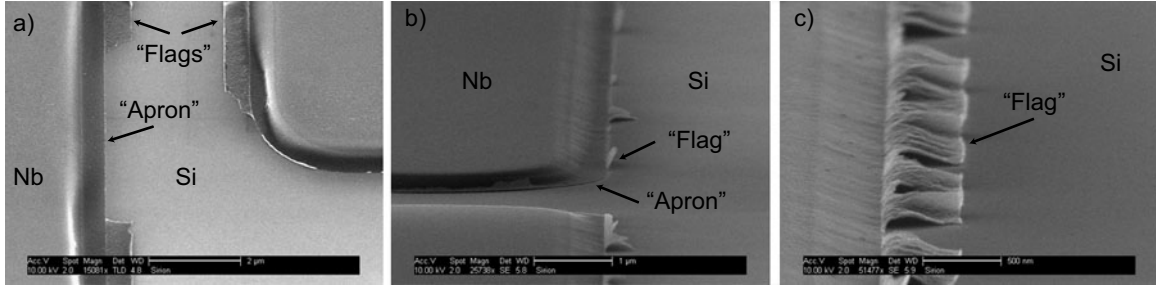


Figure 5.5: Pictures of sputtered Nb resonators showing the “apron” and “flagging.” **a)** A tilted SEM image of a gap capacitor in a sputtered Nb resonator, showing the edge profile. Nb must be sputtered because it is a refractory metal with melting temperature too high for clean thermal or electron-beam evaporation. Notice that there are two distinct pathologies, a slow tapering of the film thickness which extends for several hundred nanometers, referred to as the “apron,” and thin films of metal which are partially detached from the substrate, called “flags.” **b)** A closer view of the apron and flags. The apron occurs because sputtering is not very directional, so it spreads underneath the undercut region of the resist, getting somewhat thinner but extending far beyond the region defined by the top layer. **c)** Zoomed image of some flags, which are formed by parts of the apron coating up the sidewall of the undercut layer. When the resist is dissolved the film remains and is not well attached to the substrate. The superconductivity of these films is not well known and could be a source of loss in Nb resonators. Further, these flags make it difficult to align a CPB to close tolerance inside the resonator.

was done using niobium despite its rough edges. Once aluminum resonators were known to work well and reliably, they became the preferred option, for their ease of deposition and liftoff.

It is often useful to be able to control the slope of the edge profile of a deposited film. Because the aluminum deposition is so directional it is possible to use the shadow between the top and bottom of the upper layer of resist to tailor the slope of the film edge (see Fig. 5.6 for description). This technique has been used very successfully (see Fig. 5.7) and is a dramatic improvement over the poor control (see Fig. 5.5) afforded by sputtered niobium.

5.1.4 Substrates

Three substrates were used throughout this work, sapphire, thermally oxidized silicon, and silicon with only native oxide. All substrates were able to support high quality factor resonators. While sapphire worked well for cavities, it has not been used yet for actual qubit experiments because it is slightly more difficult to define the qubit pattern, because, as a good insulator, it is susceptible to charging. Some lithography tests were performed successfully but no devices were actually measured cold. Undoped (or lightly doped) silicon has the convenient property for lithography that it is somewhat (though weakly) conductive at room temperature, but an excellent insulator when

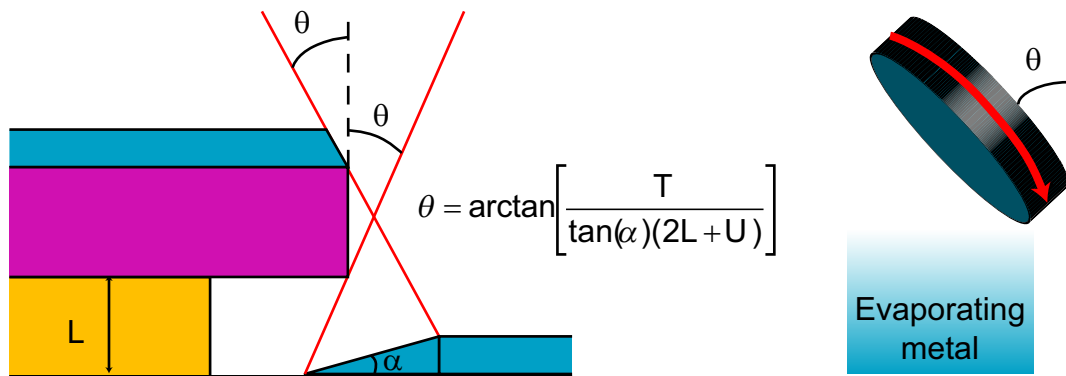


Figure 5.6: Diagram of rotating angle evaporation process. If one wants to place something inside the gap of a resonator and make good contact with the ground planes or centerpin it is helpful to have an angled sidewall. One way to do this is to tilt the substrate and rotate it rapidly as the metal is being deposited. By adjusting the angle of tilt one can change the steepness of the sidewall from shallow to nearly vertical.

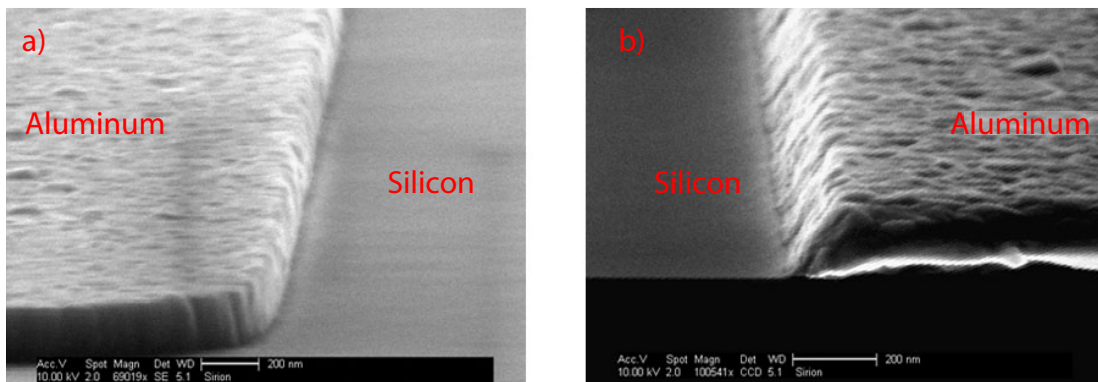


Figure 5.7: Edge profiles of deposited Aluminum. **a)** An aluminum film with nearly vertical sidewalls. Note that there is no “apron” nor “flagging.” **b)** An aluminum film with a slight slope to make it easier to coat continuously with a film.

at cryogenic temperatures. Both thermally oxidized and bare silicon were measured with qubits. Excellent results were achieved with both substrates, though there is some suspicion that the bare silicon might leak at high gate voltages.

5.2 Cooper Pair Box

The CPB has three primary parameters, the Josephson energy, E_J , the charging energy, E_C , and the coupling strength g , which is most closely related to the voltage division, β . It is possible to realize nearly arbitrary combinations of these parameters, but in doing so one must navigate a host of ancillary variables including, parasitic capacitances, critical current densities, proximity effect, and many other less glamorous occurrences, which must be exploited and compensated for. This section describes how to calculate and then realize these energy scales, and couplings.

5.2.1 Josephson Energy

In the traditional CPB, the atom transition frequency, $\omega_a \approx E_J/\hbar$, is set by the Josephson energy. This energy is chosen to be much larger than the thermal energy scale $k_B T \approx 20\text{ mK}$, but not so high that microwave engineering becomes a significant obstacle. Throughout this work, I aimed to create CPB's with transition frequencies from $\sim 4 - 8\text{ GHz}$, corresponding to thermal energy scales of $\sim 200 - 400\text{ mK}$. The Josephson junction is created by making a small overlap junction of two pieces of aluminum separated by a thin barrier of thermally grown oxide. The Josephson energy depends on the critical current, I_c , which in turn depends on two parameters of the junction, its area, A , and the thickness of the oxide barrier. The barrier is typically around 1 nm , only a few atoms thick, and conduction can be dominated by imperfections which make the barrier locally thinner. Therefore a more empirical measure, the critical current density, $J_c = I_c/A$, or sometimes the resistance-area product RA is used. The critical current of a Josephson junction is related to the junction resistance by the Ambegoakar-Baratoff relation

$$I_c = \frac{\pi\Delta}{2eR} \tanh\left(\frac{\Delta}{2k_B T}\right) \quad (5.2)$$

The important dependence is that the critical current is proportional to Δ , which here refers to the gap energy of the superconductor, and is inversely proportional to the resistance R . The resistance is an exponentially-sensitive function of the effective barrier thickness, and proportional to the area. Hence the RA product is a constant, measuring the effective barrier thickness. Luckily, the

thermal growth of aluminum oxide, is self-limiting and is relatively insensitive to the exact oxidation conditions, allowing the RA product to be controlled. The critical current density is related to the resistance area product by Eq. 5.2 as $J_c \approx \pi\Delta/2eRA$. Expressed in terms of the critical current, the Josephson energy is

$$E_J = \frac{\hbar I_c}{2e} \quad (5.3)$$

For typical oxidation parameters in our evaporator (see Tab. D), the critical current density is approximately $J_c \approx 30 - 40 A/cm^2$, but can change substantially for small junctions (see Table XX). These correspond to a resistance area product $RA \approx 1 - 0.75 k\Omega$. These are the two common metrics for expressing junction transparency, and while the resistance area product is useful for basic testing, our primary experiment measures E_J , so I prefer to characterize devices in terms of their Josephson energy density E_J/A , which is typically around $150 - 200 \text{ GHz}/\mu\text{m}^2$. This last metric clearly states that to get $E_J/h \approx 5 \text{ GHz}$ we must fabricate sub-micron ($\sim 150 \times 150 \text{ nm}^2$) junctions, a task beyond standard optical patterning, but easily obtainable with electron beam lithography.

5.2.2 Charging Energy and Voltage Division

Both the charging energy, E_C , and voltage division, β , are related to the capacitive network formed by the two CPB reservoirs and resonator. The goal of this section, is to explain how one expresses the complicated capacitive network in Fig. 5.8c as the simple effective network in Fig. 5.8d. In the simplified circuit, the charging energy is $E_C = e^2/2C_\Sigma$, and the voltage division is just $\beta \equiv V_g/V_j = C_g/C_\Sigma$.

There are many pieces of metal, and while one is not likely to call the exact expressions beautiful, using a little linear algebra, one can compute all of the island voltages and charges, analytically and quite compactly. Let C_{ij} be the capacitance between nodes i and j in Fig. 5.8c. One can then define a capacitance matrix

$$C_{ji} = -C_{ij} \quad (5.4)$$

$$C_{ii} = \sum_{j \neq i} C_{ij}$$

This capacitance matrix has the property that

$$\vec{q} = C \cdot \vec{v} \quad (5.5)$$

where \vec{q} is a vector of island charges, and \vec{v} is a vector of island voltages. If all of the charges are known, or all of the voltages are known, the capacitance matrix C allows one to easily find the other

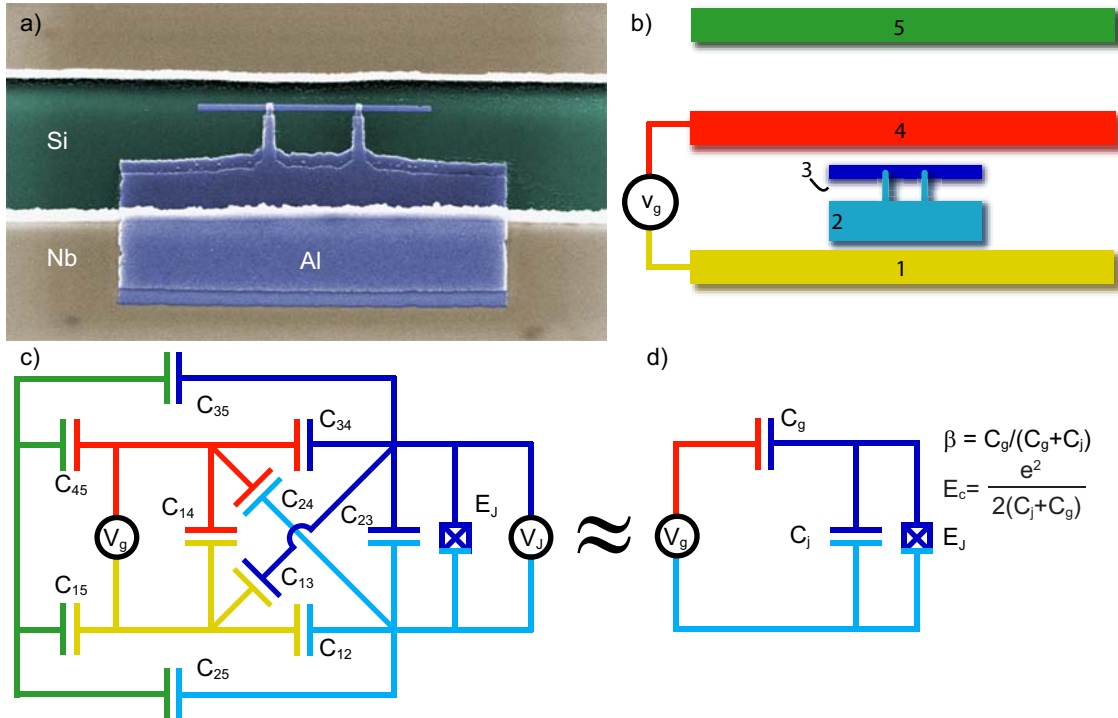


Figure 5.8: **a)** False colored SEM image of a CPB, blue is the aluminum CPB, beige is the niobium resonator, and green is the silicon substrate. The CPB consists of two reservoirs joined by a pair of tunnel junctions in a SQUID formation. There is some flagging of the resonator which shows up as white. Because of the flagging, there is (intentionally) no DC contact between the lower reservoir and the ground plane of the resonator as depicted in the model in part **c**. **b)** A color coded cartoon model of the CPB inside of a resonator with each conductor labeled (does not include input and output capacitors). **c)** Circuit diagram including capacitances between each pair of conductors. Also shown is the location of relevant voltage sources, or places that the voltage should be measured. Source V_g can be thought of as photons or zero-point energy in the resonator, while V_j can be thought of as the voltage measured across the junction due to V_g or as a voltage created by an excess charge on the CPB island, depending on whether one is trying to find β or E_c . **d)** Despite the apparent complexity of the circuit diagram in **c** there are only two relevant parameters, which can be represented by this simple CPB circuit.

quantity. Unfortunately for the box, there are typically mixed boundary conditions, with the charge of the box specified, and voltage on the gate specified. One can phrase the problem of finding β and E_C in terms of solving this mixed boundary condition problem. From there, it is easy to find a voltage between any two nodes, or the electrostatic energy XX cite Michel XX, given a voltage or charge bias across the junction. Let us write Eq. 5.5 explicitly as a sum in terms of the voltage biased nodes and charge biased nodes,

$$q_\alpha = \sum_{\beta \in I} C_{\alpha\beta} v_\beta + \sum_{i \in S} C_{\alpha i} v_i \quad (5.6)$$

where q_α is the charge on island α , v_i is the voltage on island i , and both of these are specified by the boundary conditions. From this point forward we will use a convention that greek indices are used for nodes in the set of islands (I), and roman indices are used for voltage source nodes (S). If we knew all of the v_β then we would know everything about the system, but unfortunately only the charge of the island nodes is held fixed by the boundary conditions. Like any algebra problem one should attempt to separate the knowns and unknowns. Equation 5.6 can be reexpressed as

$$\begin{aligned} q_\alpha + \tilde{q}_\alpha &= \sum_{\beta \in I} \tilde{C}_{\alpha\beta} v_\beta \\ \tilde{q}_\alpha &= - \sum_{i \in S} C_{\alpha i} v_i \end{aligned} \quad (5.7)$$

The result is just a simple linear matrix equation, where \tilde{C} is just a reduced matrix containing only island nodes $\tilde{C}_{\alpha\beta} = C_{\alpha\beta}$ for $\alpha, \beta \in I$. The solution to this equation is

$$v_\alpha = \sum_{\gamma \in I} \tilde{C}_{\alpha\gamma}^{-1} (q_\gamma + \tilde{q}_\gamma) \quad (5.8)$$

With this knowledge any electrostatic property of the system can be calculated. To calculate $\beta = V_j/V_0$ one imagines a voltage V_0 put between the resonator ground planes and center pin. Then one calculates the voltage across the junction¹, V_j , with the charge boundary condition that the islands start off neutral, that is $q_\alpha = 0$ for all island nodes. For calculating E_C , one can imagine putting a voltage across the junction and look at the resulting energy given by

$$E = \frac{1}{2} \vec{v}^T C \cdot \vec{v} = \frac{1}{2} C_\Sigma V_j^2 \quad (5.9)$$

which is easy to calculate now that we know all of the voltages. Once an effective C_Σ is known the

¹For electrostatic purposes the junction is just modeled as a capacitor. When calculating dynamics, one accounts for tunneling by allowing the island charge to change by integer electrons.

charging energy is just $E_C = e^2/2C_\Sigma$. Once β and E_C are calculated, one can solve for an effective C_g and C_Σ for the simplified CPB circuit.

This analysis can also be used to determine the DC gate voltage necessary to bias the CPB to $n_g = 1$. For a small input capacitor to the resonator, the effective gate capacitance, as seen from outside the resonator, is reduced¹ by a factor C_{in}/C_r and of course there can be some direct capacitance as well if the CPB is close to the gate². For DC gating³ it is also straightforward to extend this to gating from both sides, which allows independent biasing of two qubits. Using this approach one can control two qubits inside a resonator without adding dedicated gate lines.

5.2.3 Electron Beam Lithography

The desired junction size about 150×150 nm is too small to reliably use optical lithography, but it is in an ideal range for electron beam lithography. Such feature sizes do not push the limits of our scanning electron microscope (SEM), on which 50 nm features are regularly fabricated, and it is not so large that substrate charging, or prohibitive write times are problematic. Like the optical process, a bilayer resist system is used, but this time both layers are sensitive to electrons rather than UV light. The top layer is made using PMMA A3 (955k weight) from *Microchem*, which forms a layer approximately 120 nm thick. This sits on top of a copolymer MMA-MAA EL13 (Ethyl-lactate 13%), which spins to about 550 nm. The bottom layer is more sensitive than the top, and so a natural undercut of about ~ 80 nm will occur when writing features. This natural undercut is enough to get good liftoff with aluminum.

For making junctions one needs a three dimensional structure which overlaps two pieces of metal. To do this we use a Dolan bridge technique (see Fig. 5.9) which creates a suspended bridge of resist, used to cast a shadow in the deposited film. This technique is ideal because it allows one to make small junctions, in a single step, which are self-aligned, and can be made without breaking vacuum (necessary for high quality junctions). In order to expose PMMA, one needs to deposit approximately $\sim 150 - 200 \mu\text{C}/\text{cm}^2$ of charge at 30 keV. The copolymer can be sensitized with just $\sim 60 \mu\text{C}/\text{cm}^2$ of exposure. By exploiting this difference in sensitivity, it is possible to expose only the underlayer

¹This reduction provides some intrinsic protection against DC gate noise.

²When putting the CPB close to the gate, one must make sure that the direct coupling to the input lead does not exceed the desired Purcell effect limited decay rate.

³While it is possible to use this method to find the DC voltage division from the input to the junction, one cannot apply this treatment which assumes that the circuit is made from lumped elements to RF drives. The best approach for that is to use this technique to calculate the lumped element behavior near the qubit. Then the local resonator voltage can be found taking into account the mode structure of the cavity. This drive can then be put into the lumped element model.

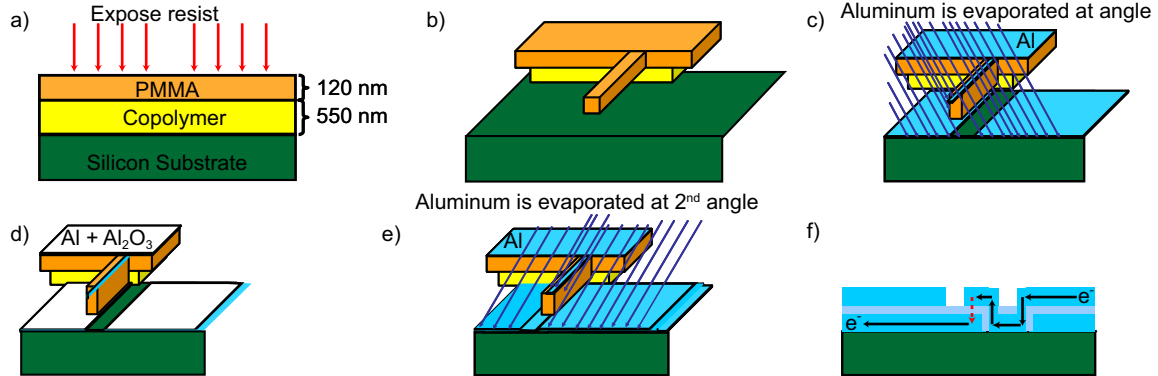


Figure 5.9: a) A bilayer of resist is patterned. b) A suspended bridge of top layer material is left after the exposed resist is dissolved in the development step. c) Next, aluminum is evaporated at an angle. The bridge creates a shadow leaving a gap in the film. d) Then a small pressure of O_2 is let into the evaporation chamber and allowed to create a thin film of aluminum oxide, which will act as the tunnel barrier. e) A second layer of aluminum is deposited at a different angle. In most areas this results in a double layer of aluminum, but under the bridge the shadows create regions where there is only a single layer. d) A side profile of the metal after the resist is lifted off. In order for an electron to get from one side of where the bridge was to the other it must tunnel from the top layer to the bottom layer.

without damaging the top layer¹.

Using this technique, one can easily design small overlap junctions. There are a few things worth mentioning, which can be observed in Fig. 5.10. In general, using this technique, all features are doubled. A notable exception can be seen in Figs. 5.10 and 5.8a. A copy of the island would be small enough that it might have resonances at similar frequencies to the box. By clever design the image of the island is made to land on the sidewall of the resist, where it is lifted off. In order to minimize errors due to imprecision of angles and or charging based misalignments, one can make the junctions in a cross geometry² (see Fig. 5.10). This makes the area of the junction first order insensitive to errors in the deposition angle, the rotation angle, and vertical or horizontal shifts. To make sure that the top layer is able to continuously coat the island, the island is deposited to be 30 nm thick while the second layer is ~ 100 nm thick. Additionally, the different thicknesses is used as a form of superconducting gap energy engineering, which suppresses quasiparticle decoherence as discussed in section 4.1.3. This gap engineering is thought to be the reason that parity improves at

¹While it takes $\sim 150 - 200 \mu C/cm^2$ to expose PMMA reliably, damage (holes/weak bridges) can set in as early as $80 - 100 \mu C/cm^2$. The exposure time for small undercut doses is often short enough that the limited bandwidth of the deflecting coils can give significant variation in the exposure. One must be careful to not damage the top layer too much.

²There is some worry that this makes the tip of the junction susceptible to breaking off which might cause excess charge noise.

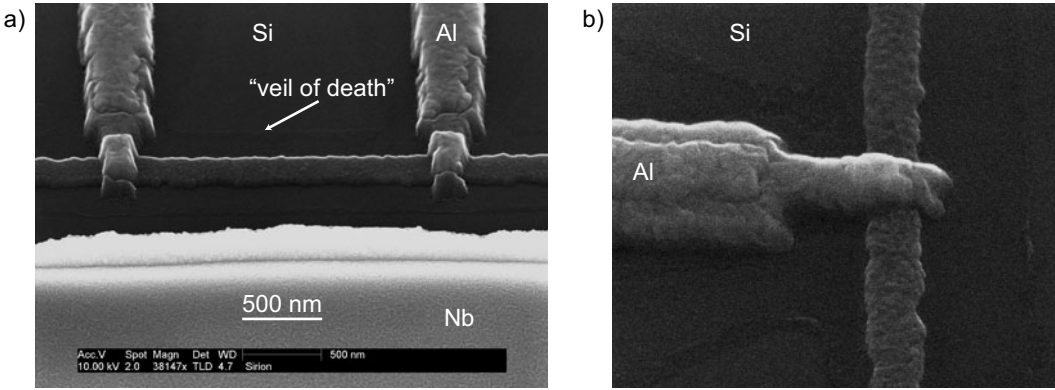


Figure 5.10: SEM images of tunnel junctions. **a)** An image from sample CQED63 showing two junctions. The shifted image is visible in the fingers. The island is ~ 30 nm thick and the overlapping fingers are ~ 100 nm thick. **b)** A junction from a different sample (CQED97). Both images show a thin film surrounding the metal features known as the “veil of death” which is a film of unknown composition (thought to be oxidized aluminum). This seems to show the region of resist that was undercut during the development process.

increased (but still small) magnetic fields (see Fig. 7.11).

5.2.4 Veil of Death

During the evaporation process we have observed a mysterious thin film around the defined features, colloquially known as the “veil of death” because we fear that it may be hurting the coherence times of our qubits (see Fig. 5.10). This film is thought to be composed of aluminum scattered by residual pressure due to outgassing of the resist. It is also possible that it is some sort of organic residue from the development process. Because it appears to be extremely thin (~ 1 nm) and has not completely destroyed the qubit it is thought that if the film was aluminum that it is fully oxidized. However, the loss tangent of this dielectric which is very close to the qubit could be particularly pathological. Ideas to eliminate this film in future samples include, using an inorganic mask, etching the film away after the fact (briefly exposing chip to acid or base), or using an all optical process (which does not seem to have this residue). Losses from this mechanism should scale with the ratio of capacitance inside and outside of the junction itself and studies measuring this dependence could provide a window into decay due to this film.



Figure 5.11: **a)** An FEI XL30 Sirion scanning electron microscope. It is capable of 4 nm viewing resolution, and has been modified with the Nanometer Pattern Generation System **NPGS** to allow it to act as electron beam lithography tool. It has successfully been used to write features as small as 40 nm, well beyond the requirements of this project. **b)** A custom made (by **Plassys**) electron beam evaporator. It is capable of depositing aluminum, gold, copper, titanium, chrome, and alumina. It features a stage which can be rotated about two axes to allow multi-angle depositions. This feature is used to create the overlap junctions and to control the edge profile of aluminum resonators. It is a load locked system which can pump down to $\sim 1 \times 10^{-7}$.

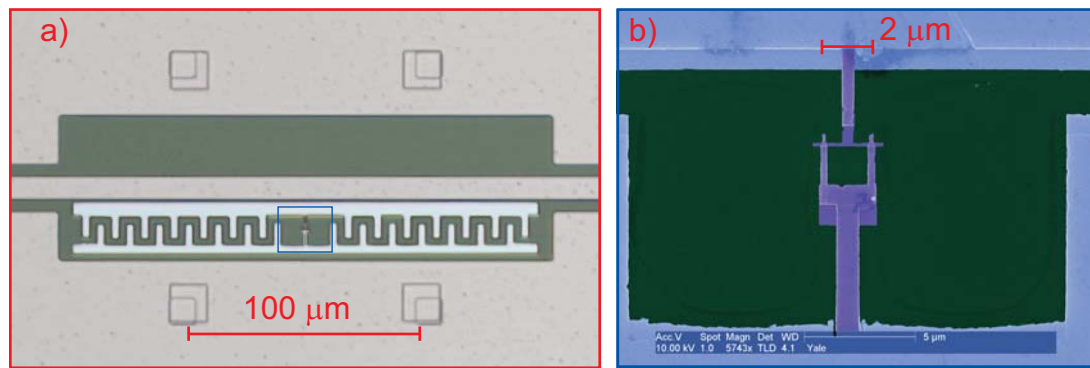


Figure 5.12: **a)** Optical image of transmon inside of a resonator. Visible are the two reservoirs which have interdigitated fingers to help increase the shunt capacitance, and lower the vacuum Rabi coupling, g . There is also a capacitance between the top island and the center-pin, and the bottom island and the ground plane, as well as other stray capacitances. The actual junctions and SQUID loop are indicated with a blue box. **b)** Zoomed in image with a scanning electron microscope which shows the Josephson tunnel junctions and the loop. The junctions are approximately $150 \times 150 \text{ nm}^2$ and the loop is approximately $4 \mu\text{m}^2$.

5.3 Transmon

The transmon design is really identical to the traditional CPB design. The only major difference is the parameters which one tries to realize. In the traditional CPB, the natural junction capacitance $C_{\Sigma} \sim C_j \approx 4 \text{ fF}$ is sufficient to provide the desired charging energy $E_C \approx 5 \text{ GHz}$. However, for the transmon one would like to have $C_{\Sigma} \approx 75 \text{ fF}$ for a charging energy $E_C \approx 250 \text{ MHz}$. In terms of fabricating capacitors, nothing fundamental changes, bigger pieces of metal give larger capacitances. A primary consideration is making sure that as one increases C_{Σ} , that the vacuum Rabi coupling g , controlled by way of β , does not become too large. If one wanted to maximize the vacuum Rabi coupling, one could push β towards unity by adding all of the capacitance in between the reservoirs and the resonator. That would increase C_g until $C_g \approx C_{\Sigma}$ and $\beta \rightarrow 1$. However, if one were to do that they would actually get too much vacuum Rabi coupling! In circuit QED it is possible to get enough coupling that one begins to violate the rotating wave approximation¹. While one could possibly still operate in such a regime, at this early stage of exploration we choose to be more conservative. Thus, we need a way of lowering β . This can be easily done by lowering the effective C_j . One could make the junction area larger but that would change the Josephson energy. Rather we add an interdigitated capacitor which shunts away much of the coupling gained by having larger effective gate capacitance. By interdigitating the shunting capacitor and not the gate capacitors we can keep $\beta < 0.2$, which is relatively safe from a rotating wave standpoint. When looking at Fig. 5.12 it is tempting to think that the interdigitating capacitance, the most prominent new feature, is responsible for increased g compared to the traditional CPB. In fact the opposite is the case, and the interdigititation is added specifically to shunt the gate capacitor lowering g .

5.4 Printed Circuit Boards and Sample Holders

The primary design consideration for the printed circuit board (PCB), see Figs. 5.14 and 5.15, and the sample holder (see Fig. 5.13) is the suppression of parasitic resonances. The circuit boards launch from SMP to coplanar waveguide via a right angle surface mount SMP connector from *Rosenberger*. These are specified up to 40 GHz and have good performance up to about 20 GHz. In order to suppress parasitic modes between the ground planes between the top and bottom of the circuit board, the top ground planes are periodically connected to the bottom using copper vias spaced by

¹Due to a common way of writing the vacuum Rabi coupling $\propto C_g E_C$, we were initially worried that by lowering E_C we would lose g . However, of course since E_C can be lowered by making C_g large this is not an issue.

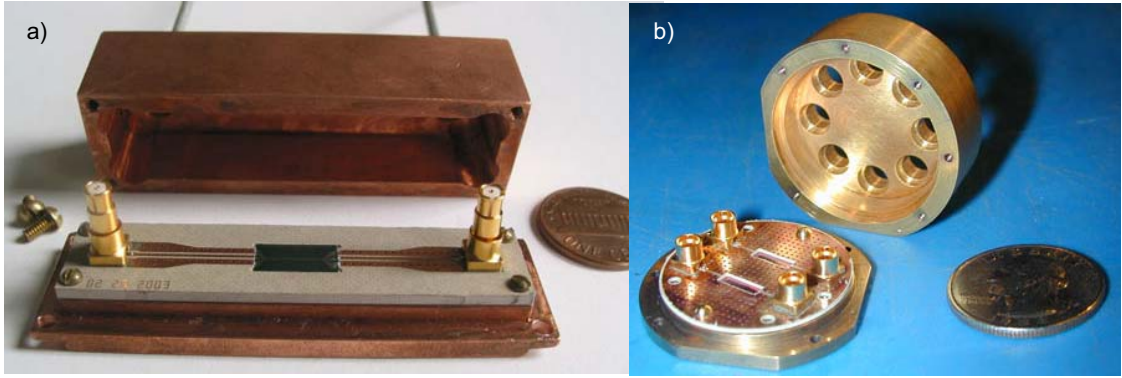


Figure 5.13: **a)** “Coffin” style sample mount with penny for size comparison. The PCB connects to semirigid coaxial cables via SMP surfacemount connectors and a compliant “bullet.” An inner lip is used to press the PCB against its backing for good ground contact. **b)** A next generation sample mount and PCB. This sample holder accepts eight incoming RF lines, and is sometimes called the “octobox” or more flavorfully the “arachnipus.” Using different PCB designs shown in Fig. 5.15 one can either measure two devices simultaneously or use all eight connections to measure a single device, allowing for flux bias lines or multiple cavities on a single chip. This sample holder is also designed to fit in the vacuum line of site port of the cryostat, allowing the possibility of transferring the sample to the cold stage without cycling the cryostat to increase sample throughput.

40 mil, which should provide protection to any modes until well above 100 GHz.

However, while the circuit boards are well protected, there can still be impedance mismatches when coupling to the chip, creating opportunities for parasitic resonances. One way that there can be a mode mismatch is due to differences in the dielectric constant between the chip and PCB substrate. This was minimized by using *Arlon*, a low loss, high dielectric (XX), teflon and ceramic based microwave substrate. One must also connect the on-chip CPW to the circuit board CPW, via wirebonds. The inductance of these wirebonds is approximately proportional to the length of the wire bond with about (1 nH/mm). In order to minimize this length, and also match the on-chip and circuit board modes as closely as possible, the circuit board has a recess (see Fig. 5.13), making the chip flush with the top of the circuit board. The circuit board is connected to the chip via as many wirebonds as can easily fit around the edges of the chip, to lower the inductance as much as possible.

Even if all of these measures could be implemented perfectly, one would still have to contend with parasitic resonances of the chip itself. Unfortunately, we do not possess the equipment to make vias in the silicon substrate, and suppress such modes, as was done with the printed circuit boards. To minimize this effect, we made the chip itself small to raise the minimum cutoff frequency of such a mode.

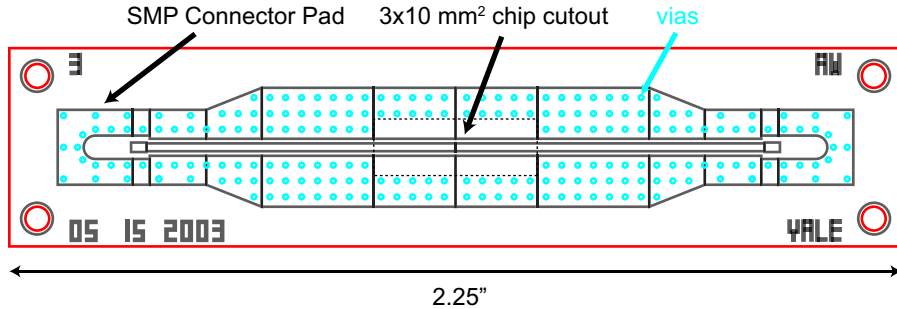


Figure 5.14: “Coffin” style printed circuit board. Visible on the circuit board are mounting pads for the SMP surface mount connectors. There is also a $3 \times 10 \text{ mm}^2$ cutout for the chip, which is milled out by the PCB manufacturer, such that the chip will be flush with the top surface. Initial versions were 25 mil thick and milled only 12 mil deep, but more recent versions are only 15 mil thick and milled down to the ground plane.

In the end the sample holders both perform nearly perfectly up to 9 GHz with reasonable performance but some parasitic resonances up to about 20 GHz.

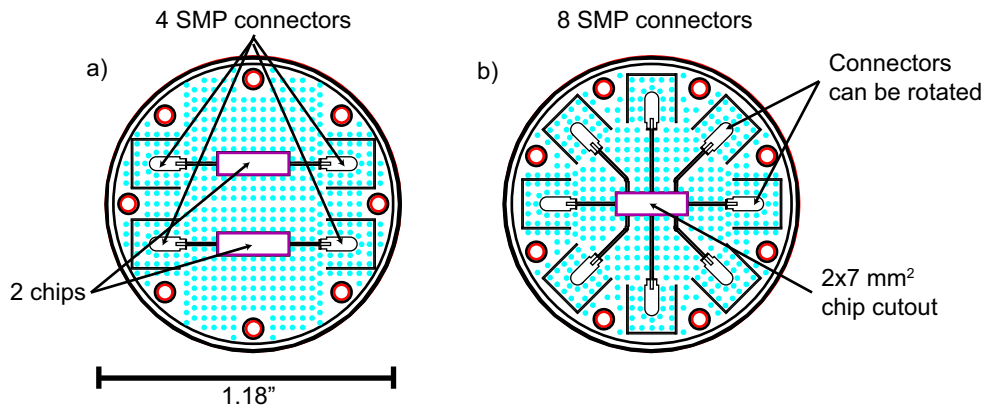


Figure 5.15: The next generation “octobox” PCB is substantially more versatile than the initial design. Most importantly it provides more RF lines which can be tasked for a variety of purposes. These designs use thinner boards (15 mil) and narrower traces (3 mil). Allowing more chips and CPW’s to fit in a smaller package than the “Coffin” style shown in Fig. 5.14 a) This version allows one to measure two devices simultaneously, and is primarily used to speed up resonator characterization. b) This design can use all eight connections for interacting with a single chip. The extra lines enable future experiments with multiple cavities, independent dedicated gate and flux biasing, and additional dedicated qubit readouts. Note that the rotational degree of freedom given by the bullet connectors is used to place the surface mount connectors at different angles than in a).

Chapter 6

Measurement Setup

This section is intended to be a brief discussion of the cryogenic, microwave, and digital signal processing techniques used to interrogate the circuit QED system. First, a rough outline of the measurement setup will be given. Next, the cryogenic design and filtering will be discussed. Then, back at room temperature, the qubit is controlled by a variety of RF and low frequency gate pulses. Finally, the demodulation hardware and software will be discussed, and in particular the digital homodyne technique will be explained.

The system state will be probed by monitoring microwave transmission through the resonator as described in section 3.4. In principle one can probe the resonator (qubit) properties either in reflection or transmission, but for all experiments in this work transmission was used. Transmission is beneficial because the signal does not sit on a large background of reflected measurement/control pulses¹. The measurement setup diagram is shown in figure 6.1. Microwave control and measurement pulses are generated at room temperature and fed through semirigid coaxial cable to the sample. The bias charge n_g is set via a DC voltage at room temperature, combined at low temperature with the RF signals, and applied on the input of the resonator. Unfortunately, these same coaxial cables that transmit desired signals can also carry thermal noise to the sample. Several layers of filters are employed to reduce the room temperature fluctuations down to acceptable levels at the sample.

The signals transmitted are quite small, with the resonator only having on average a few photons, corresponding to a power $P = n\hbar\omega_r\kappa \approx 10^{-17}$ W. In order to measure this faint signal, many stages of amplification are employed. The signal is then mixed down to a low frequency which can then be digitally sampled and processed by a computer.

¹While careful microwave design can be used to cancel these reflected pulses, such interference techniques, place a heavy burden on the microwave calibration and can limit the bandwidth of applied pulses. Dispersion in the line could make particularly annoying pulse length dependent effects.

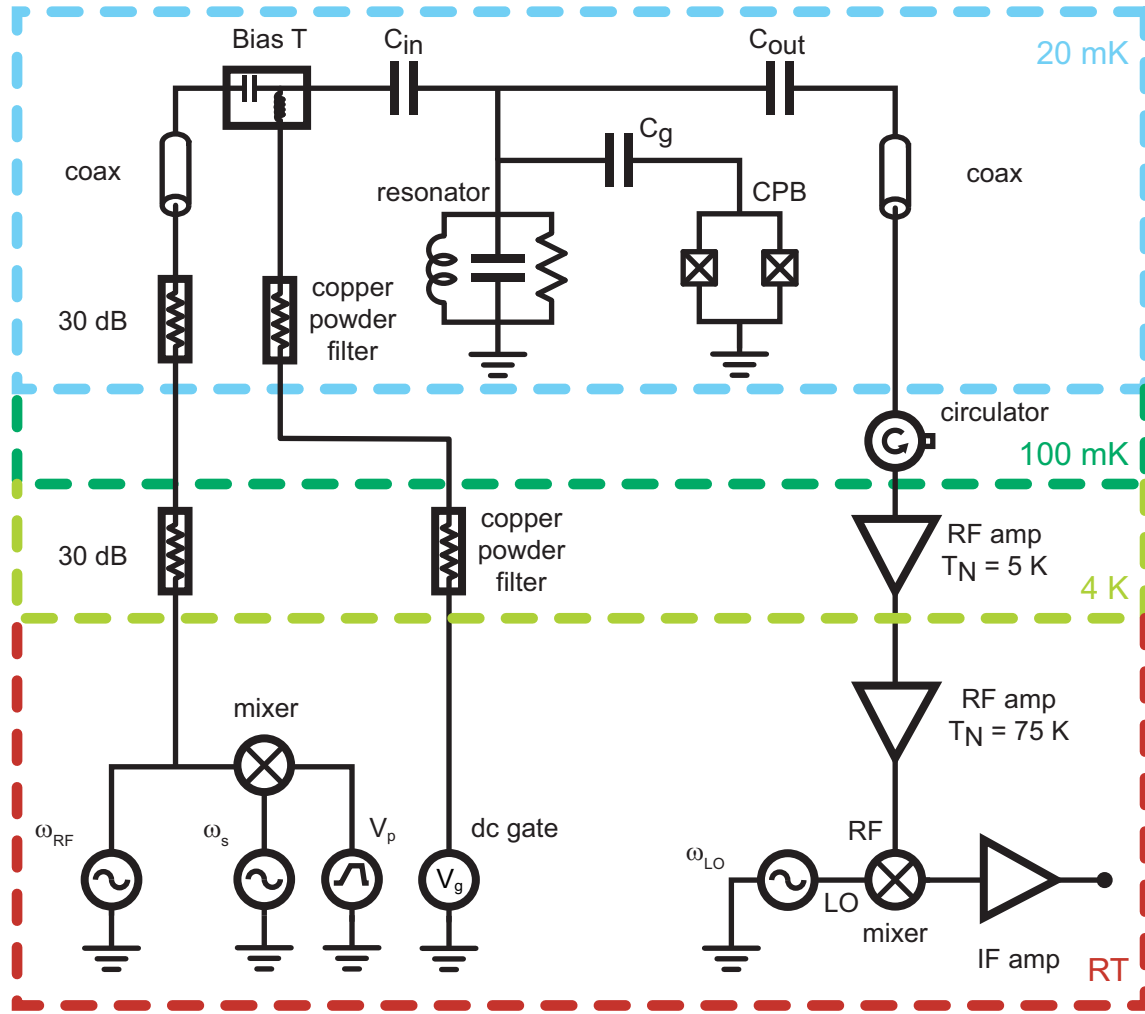


Figure 6.1: Measurement setup for cQED experiments. The control and measurement pulses, as well as any DC gate sweeps are synthesized at room temperature. Pulses are then sent down an RF pathway which attenuates the signal at 4 K and then again at 20 mK to eliminate thermal Johnson noise from room temperature and warmer parts of the cryostat. The DC gate signals are low pass filtered to about 1 GHz using Copper powder filters and then joined with the RF using a bias-tee. After interacting with the sample, the transmitted signal passes through a circulator which diverts noise from the cold amplifier. The signal is then amplified by a low noise temperature HEMT $T_N \sim 5$ K, and sent to room temperature where it is further amplified. Finally the signal is mixed down to low frequencies using an IQ mixer, where it is digitally acquired and post-processed by a computer using *LabView* software.

6.1 Cryogenics and Filtering

These experiments were performed using a Kelvinox 400 μW dilution cryostat capable of reaching a base temperature of $\sim 6 \text{ mK}$ and the sample is measured at $\sim 15 - 20 \text{ mK}$. Principles of cryostat design and operation can be found in [Pobell2006]. The primary cryogenic design concern is to minimize the amount of heat and noise that reach the sample from thermal or terrestrial microwave sources. There are three types of pathways, the RF input, the DC lines, and the RF output, each of which requires a different style of filtering.

The RF drive on the sample requires only nanowatts of power, but operates at the qubit frequency of $\sim 5 \text{ GHz}$. At all temperatures above 100 mK thermal Johnson noise will be significant at these frequencies. Since the signal and noise are in the same band and we require a large bandwidth, the easiest way to “filter” is to attenuate. If the effective temperature of interest is much less than the thermal temperature then the voltage noise is just linear in temperature $S_V(\omega) \approx 4k_{\text{B}}TR$. In order to kill noise from a high temperature at a lower temperature, one can just attenuate, at the cold stage, by a factor, $\alpha = T_{\text{hot}}/T_{\text{cold}}$. For going from room temperature (290 K) to liquid helium temperature (4 K), a 23 dB of attenuation is used. To go from 4 K to 20 mK another 30 dB of attenuation was used. The cables provide an additional $\sim 10 \text{ dB}$ of attenuation, for a total of $\sim 63 \text{ dB}$. With so much attenuation one must worry about not having enough power to perform fast pulses, and heating the attenuators at the cold stage. Measurement requires only a few photons per cavity lifetime $\sim -110 \text{ dBm}$, and 1 ns control pulses typically take a few thousand photons $\sim -80 \text{ dBm}$, neither of which heats the fridge or provides a challenge at room temperature. Off resonant pulses or multiphoton processes which require substantially larger powers, can noticeably raise the base temperature of the fridge if the duty cycle isn’t small enough. Overall this hasn’t been a substantial limitation thus far.

The DC lines have very different requirements. They do not require high bandwidth like the RF pulses, but they employ much higher voltages. For example, the sample studied in [Wallraff2004], one electron of gate charge corresponded to about 1 V . If one tried to use a line with 65 dB of attenuation, one would require a megavolt at room temperature! Since only a small bandwidth is needed, we can use a low pass filter which has no attenuation at DC, but very large attenuation at RF frequencies where most of the thermal noise power is located. There are many different flavors of low pass filter available but for this experiment, copper and stainless steel powder filters (see

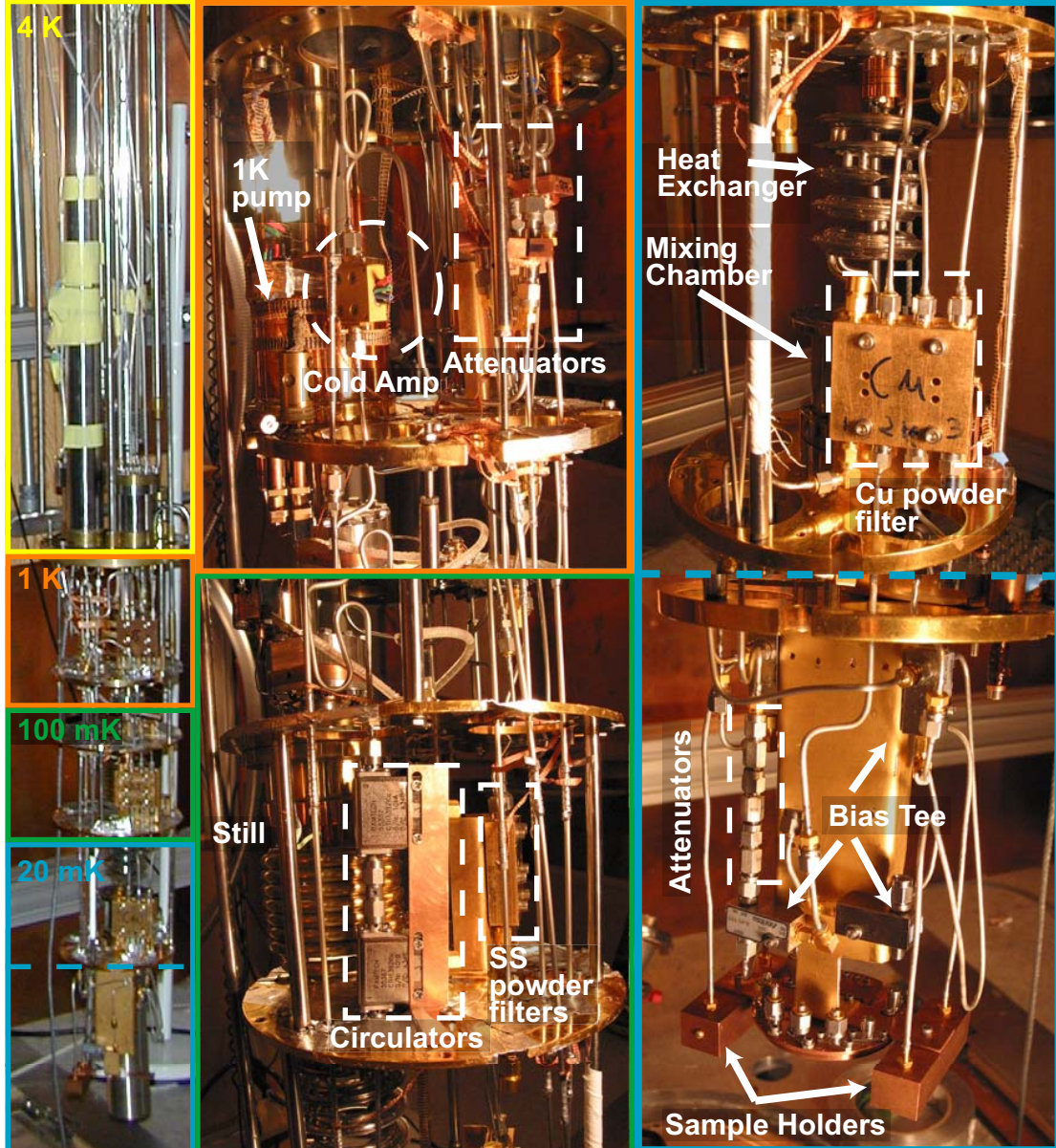


Figure 6.2: Annotated images of the cryostat (left), color coded by temperature. Everything shown in the larger images is inside the vacuum can. The 1 K pot is visible in orange section, which has the cold amplifier as well as thermalizing attenuators and copper powder filters. The 100 mK section has the still, which recovers the 3He from the mix. In early experiments the circulators were also at 100 mK though they have since been moved to the cold stage. There is also another stage of copper powder filtering. The cold stage is cooled by the mixing chamber and holds two samples. There is a final layer of filtering and attenuation, as well as the bias tees which combine the DC and RF signals. Note that the cryostat has a very large cross-sectional area which allows for the bulky RF components to be placed inside.

Fig. 6.2) were chosen, because they attenuate strongly (> 80 dB) and have no resonances at high frequencies (often a problem with lumped element filters). They consist of a long wire traveling through an epoxy/partially oxidized metal powder mixture, which is a good insulator at DC but very lossy at RF. One filter is placed at each temperature stage. Both copper and stainless steel powder filters work well, but it is feared that stainless may not thermalize at the lowest temperatures so it is generally used only at 100 mK and above. These filters begin to cutoff around 30 MHz but the DC port of the bias tee, used to join the RF and DC signal at the base temperature, actually cuts off at ~ 5 MHz, limiting the performance of the DC gate. That could be a limitation for trying to sweep the CPB through the resonator quickly using the gate voltage. That method is not ideal as the it would require leaving the sweet spot ($n_g = 1$) which would degrade performance. It would have been easy and probably would have worked if we had had ~ 100 MHz of bandwidth on those lines.

Finally, the signal must get to the amplifier which is at the 1 K stage. Here there is a delicate balance. While one needs to avoid noise from above, attenuation reduces the signal, and thus the signal-to-noise ratio. Ideally, this would be accomplished by a one-way microwave valve which lets the signal through without attenuation, but lets none of the noise back through. Amazingly, a circulator does exactly this, using a ferrite component to break time reversal symmetry. Circulators typically provide about 20 dB of isolation and have a bandwidth up to one octave (*Pamtech 4–8 GHz* in our setup). We use two of them in series to increase the isolation (see Fig. 6.2). Circulators often have resonances outside of their specified operating band. This can be obviated to some extent by using a bandpass filter to protect the sample, which was not done in this case, but probably should have been.

At low temperatures, thermal conductivity, especially due to phonons is substantially reduced. This is good, because it lowers the heat load on the cold stages, but also means that care must be taken to ensure that cables and components are properly heat sunk. The filtering elements actually serve an additional purpose of providing thermal anchoring of the cable (especially the center pin) to the cryostat. Attenuators provide a resistive connection through which heat can be dissipated from the center pin to cable shield (and cryostat). The copper powder filters also allow the center pin to come to thermal equilibrium, as there is only a very thin layer of oxide on the metal grains. The circulators are typically used as an isolator with the third port terminated with a $50\ \Omega$ resistor to ground, which can be anchored to the base temperature (though in early experiments it was

actually at 100 mK). Semi-rigid coax with both the center pin and shield made out of stainless steel (UT85 SS-SS) was used to provide isolation between temperature stages. Unfortunately, in addition to its high thermal resistance, it is also quite lossy electrically, attenuating signal as well as noise. While this is not terribly important on the input side where there is already a lot of attenuation, the short section of stainless cable between the output of the sample and the input of the amplifier have around 3 dB of attenuation raising the system noise temperature substantially. It is possible to use superconducting coax to have good thermal isolation while retaining high electrical conductivity, but it is somewhat difficult to make the cables and it was not done for this experiment.

6.2 Pulse Synthesis

All of the fast control and measurement of the qubit is performed using RF pulses. These envelopes of the pulses are generated by a *Tektronix* 520 arbitrary waveform generator (AWG) capable of generating pulses with 1 ns resolution. This AWG can hold waveforms of up to 4 million points per channel, with two analog channels, and 4 digital markers, and the second channel can also be used as 10 digital channels, all at the full speed. The analog channels are used for pulsing and the digital markers are used to trigger gate sweeps, and RF generators. Pulse sequences are designed in *Mathematica* and loaded into the AWG memory. Two types of pulses are used. Square pulses are simple to design and easy to time relative to one another, but in frequency space, they have frequency components in a wide band, which can create crosstalk between the qubit and resonator. One can also define gaussian pulses which use the minimum bandwidth. These pulse envelopes are then upconverted to the qubit or resonator frequency by mixing them with an RF tone generated by an *Agilent* 20 GHz continuous wave source. Various models of generator are used, depending on the model, the mixer can be internal or external and either vector (IQ) or scalar. Initial experiments, used two external mixers in series (model ZMX-8GH from *minicircuits*) to make a pulse with enough contrast. A high degree of contrast is necessary in order to make fast pulses when the mixer is “open,” but not create any excited state population when the mixer is “closed.” With the external mixer it was difficult to get good linearity while maintaining good contrast with these mixers. Using the internal IQ mixer of a newer vector microwave source, it is possible to get very linear response without sacrificing contrast. The vector capability also allows one to synthesize the pulses necessary to perform tomography. In both cases, it is difficult to prevent leakage below about 30 dB, so the internal switch of the source (which has \sim 80 dB of contrast) was used as a backup in both cases. The

pulse is essentially stopped by turning off the mixer, and having the backup prevents any residual population from building up while the experiment is resetting.

6.3 Demodulation

The state of the qubit is encoded in the phase (and amplitude) of a pulse transmitted at ~ 5 GHz. To extract this information two stages of demodulation are required. The eventual goal is to acquire the phase and amplitude information digitally on a computer, but unfortunately no acquisition boards can stably acquire at 5 GHz. In order to slow the signal down to below 1 GHz, where it can be sampled, the signal once amplified cold and at room temperature, must be mixed down to an intermediate frequency (IF) by an IQ demodulator. The two quadratures of this IF signal can be mixed down to anywhere from DC-500 MHz, and are then amplified by either a *mini-circuits* model ZFL-500LN RF amplifier, or a *SRS* 350 MHz preamplifier, before being acquired by an *Acqiris* data acquisition board.

The acquisition board has two channels so that it can acquire both quadratures simultaneously at 1GS/s. Because this experiment primarily measures phase, frequency synchronization between all components of the utmost importance. An *SRS* 10 MHz rubidium frequency standard is used to provide a reference frequency to all RF sources, arbitrary waveform generators, and the data acquisition card which can take an external clock source. If the internal clock rather than the frequency standard is used, a noticeable phase drift will occur during long acquisitions. This particular board also has an onboard FPGA hard-coded to average the signals in real time. This feature is useful because of the quantity of data which is taken. At the full acquisition rate of the board, the large amount of data, which is transferred into memory takes almost one hundred times longer than actually acquiring the data. This means that one is only doing useful experiments for 1% of the time. If one is performing single shot measurements, where every trace must be stored separately, this poor duty cycle is unavoidable. For any measurement which studies ensembles that can be averaged, this board will allow up to 65,000 averages to be taken without having to transfer the buffer to memory. If more than $\sim 1,000$ averages are taken the transfer time becomes negligible compared to the acquisition time.

At very high amounts of averaging, one begins to notice that there is correlated noise on the card, which arises from cross-talk between the digital components and analog-to-digital converter. This card noise is noticeable on timescales less than 20 ns and averages around 65,000. It can be

measured and digitally subtracted, to reduce its magnitude significantly but not completely. For slow phenomena, I suggest filtering it out, and for fast things it helps to subtract it off, but it will always be present to some extent.

Once the data is acquired, the phase and amplitude information must be extracted. If the signal is mixed down to DC in hardware, it can simply be averaged and decimated, and then converted from I and Q to phase and amplitude. If there is a finite IF frequency, the I and Q must first be extracted, in a process I call digital homodyne.

6.3.1 Digital Homodyne

There are two flavors of digital homodyne, which can either use a single or both quadratures to extract the phase and amplitude. The first method, which uses a single channel, does not require an IQ mixer and is very robust to imperfections and offsets in the mixer or amplifier chain, but its bandwidth is limited to the IF frequency. The second method, which uses both quadratures, allows one to have more bandwidth than the IF frequency! However, it is much more sensitive to any imbalance between the arms of the mixer and IF amplification chain. The following subsections will explain these two methods, describing the effect of various imperfections and how one can compensate.

Definition of problem

There is a signal of the form

$$S(t) = A(t) \sin(\omega t + \phi(t)) \quad (6.1)$$

The goal is to extract $A(t)$ and $\phi(t)$.

IQ Mixer

An IQ mixer has two inputs. One is used for the signal and the other is typically driven with a local oscillator (LO). The LO signal $LO = B \sin((\omega + \omega_{if})t)$ is split and one branch is phase shifted by $\pi/2$. The signal is split and multiplied with each branch of the LO. The resulting signals are then low-passed by a filter with a cutoff at IF_{max} . For our *Miteq* IQ-mixer $IF_{max} \sim 500\text{MHz}$. After low passing each branch has the form

$$I_{IF}(t) = A(t) \cos(\omega_{if}t + \phi(t)) \quad (6.2)$$

$$Q_{\text{IF}}(t) = (A(t) + \epsilon_A) \sin(\omega_{\text{if}} t + \phi(t) + \epsilon_\phi) \quad (6.3)$$

The amplitude and phase of the original signal have been mapped onto two lower frequency signals, the ϵ 's represent small imbalances between the two arms of the mixer. If $\omega_{\text{if}} = 0$ and only a single quadrature is mixed down, then the measurement is called homodyne, whereas if $\omega_{\text{if}} \neq 0$ then it is called heterodyne. Both techniques are mathematically equivalent¹, however the homodyne signal is at DC, making it easy to work with, but also susceptible to $1/f$ noise and drifts. The original signal can be reconstructed from either of these two signals alone and will be correct within a bandwidth of ω_{if} around the original signal. Imagine finding $A(t)$ from one arm alone, say I . At the point where the signal is maximum, one has very good sensitivity. However, at the zero crossing where one is sensitive to the phase, one has absolutely no information about $A(t)$. Therefore, with a single channel, it is impossible to know both the phase and amplitude precisely at the same time. While it is not possible to measure both quantities instantaneously, one can recover the average of both quantities during a complete IF period. This single channel technique will be discussed in detail in the next section. Using two channels separated by $\phi = \pi/2$, whenever I is maximum, Q is at a zero-crossing. These two channels simultaneously determine $A(t)$ and $\phi(t)$ at every point. In the third section I will discuss how to extract this information, and discuss how imbalances manifest themselves and how they can be compensated for.

Single Channel Digital Homodyne

In this method a single channel IF signal of the form

$$\text{IF}(t) = A(t) \cos(\omega_{\text{if}} t + \phi(t)) \quad (6.4)$$

is digitally mixed down to DC in an IQ fashion. The low pass is accomplished by integrating over exactly one period of the IF frequency to extract two signals.

$$I(t) = \frac{1}{2\pi/\omega_{\text{if}}} \int_t^{t+2\pi/\omega_{\text{if}}} \cos(\omega_{\text{if}} \times \tau) \text{IF}(\tau) d\tau \quad (6.5)$$

and

$$Q(t) = \frac{1}{2\pi/\omega_{\text{if}}} \int_t^{t+2\pi/\omega_{\text{if}}} \sin(\omega_{\text{if}} \times \tau) \text{IF}(\tau) d\tau \quad (6.6)$$

This yields

$$\bar{I}(t) = \bar{A}(t) \cos(\bar{\phi}(t)) \quad (6.7)$$

¹Homodyne and (IQ) heterodyne are equivalent methods for any classical signal. In quantum mechanics the extra port introduced when splitting the signal, results in a minimum addition of $\hbar\omega/2$ of extra noise.

$$\overline{Q}(t) = \overline{A}(t) \sin(\overline{\phi}(t)) \quad (6.8)$$

Where the bar represents the average value in a window size $T_{\text{IF}} = 2\pi/\omega_{\text{if}}$. This is equivalent to knowing the amplitude and phase which are just

$$\overline{A}(t) = (\overline{I}(t)^2 + \overline{Q}(t)^2)^{1/2} \quad (6.9)$$

and

$$\overline{\phi}(t) = \arctan(\overline{Q}(t)/\overline{I}(t)) \quad (6.10)$$

Since in practice the data is in discrete timesteps, the integrals become sums. This method has many advantages. With a single input channel, one can extract both the amplitude and phase information. Because there is a single IF channel, there is no error due to any imbalances between arms of the IQ mixer (which is effectively just a regular mixer in this mode). However, the bandwidth is reduced from IF_{max} to ω_{if} . If we would like to get the full bandwidth out of the mixer we will need to use both arms.

Dual Channel Digital Homodyne

In the previous section, we used a digital technique which was very analogous to how a real IQ mixer works. It multiplied the desired signal by two LO's that were $\pi/2$ apart and then low-passed (by integrating). If you have only one channel, you can't really do much better. With both channels however, one should be able to extract the information from each IQ point, rather than requiring a whole IF period. Even if one channel is only sensitive to the amplitude, the other will measure the phase, so at each point we are sensitive to all of the information. To think about extracting I and Q, imagine plotting them in cartesian coordinates, where $x = I_{\text{IF}}(t)$ and $y = Q_{\text{IF}}(t)$. If there were no imbalances, this would just trace out a circle with an angular frequency ω_{if} . What we would like to do, is go to a rotating frame where the IF frequency is stationary. This is accomplished by applying a transformation which rotates the IQ coordinates at ω_{if} .

$$R(t) = \begin{pmatrix} \cos(\omega_{\text{if}}t) & \sin(\omega_{\text{if}}t) \\ -\sin(\omega_{\text{if}}t) & \cos(\omega_{\text{if}}t) \end{pmatrix} \quad (6.11)$$

If there are no imbalances then when $R(t)$ is applied to $(I_{\text{IF}}(t), Q_{\text{IF}}(t))$, one gets.

$$I(t) = A(t) \cos(\phi(t)) \quad (6.12)$$

$$Q(t) = A(t) \sin(\phi(t)) \quad (6.13)$$

but now there is no averaging. The transformation can be applied point-by-point making it more efficient and having the maximal time resolution allowed by the acquisition and the bandwidth of the mixer.

Unfortunately, because there are now two arms, there can be slight imbalances between them. This transformation preserves all of the signal but also acts on these imbalances. If they are constant as suggested by the form given in Eqs. 6.5 and 6.6 then they can be compensated for relatively easily.

The first step is to measure all of the ϵ 's. This can be done for a large data set or for every period separately. In order to correct for amplitude imbalances one simply rescales the data which in matrix form looks as.

$$E_A = \begin{pmatrix} (1 + \epsilon_{a1})^{-1} & 0 \\ 0 & (1 + \epsilon_{a2})^{-1} \end{pmatrix} \quad (6.14)$$

The phase correction matrix R_ϵ is a little more complicated. One could obtain the transformation by some educated guess and check, however, a more formal method solves the problem based on the following criteria:

1. The transformation must work $(I_{IF}(t), Q_{IF}(t)) \rightarrow (I(t), Q(t))$.
2. Because it is a rotation it must be unitary $\det(R_\epsilon) = 1$.
3. It must be antisymmetric.

This gives four constraints which define the 4 matrix coefficients. The equations can then be solved to yield,

$$R_\phi = \frac{1}{\cos \epsilon_\phi} \begin{pmatrix} \cos \omega t + \epsilon_\phi & \sin \omega t \\ \sin \omega t + \epsilon_\phi & -\cos \omega t \end{pmatrix} \quad (6.15)$$

Essentially, the transformation just rotates one of the quadratures a little extra to make up the phase offset. This transformation works well for small ϵ_ϕ , but near $\epsilon_\phi \approx \pi/2$ the prefactor blows up and the matrix maps both quadratures to the same value. This effect describes the transition between having two orthogonal IQ ports and the behavior of a single channel mixer. As one might expect, if the phase of the two quadratures is the same, the second channel provides no additional information.

The error corrected $R_\epsilon = R_\phi E_A, (I_{IF}(t), Q_{IF}(t))$ perfectly reproduces a digital version of the DC IQ homodyne signal. After this the resulting signals can be averaged, filtered, and decimated as desired.

Advantages of the Digital IQ method

The main advantage of the digital IQ over single channel version, centers on the fact that it is a point-by-point method, where all information (at the sample time) about the amplitude and phase are known (quantum limit notwithstanding¹). The method can have higher bandwidth for a given IF frequency. The BW limiting factor for the IQ method is the maximum IF *bandwidth* of the mixer, whereas for the single channel it is the IF *frequency*. So with the IQ one can work at an IF just high enough to avoid $1/f$ noise. In the single channel one has to make the IF frequency as high as possible and can run into limits of the data acquisition card (in order to oversample the IF) .

Digital IQ Pitfalls

Unfortunately, there are some issues with the DIQ measurement technique. Because it is a point-by-point method it can be very sensitive to certain types of noise. Any kind of DC voltage noise is ‘mixed’ up to the IF frequency. Further any noise or signals at the harmonics or ‘negative’ fundamental frequency will not be suppressed. These can come from non-idealities in the mixer, acquisition card or other sources. At the time of this writing some remaining sources of noise exist. Since these seem to be at the fundamental and its harmonics, they can be easily filtered out by averaging over an integral number of IF periods. However, this essentially eliminates the advantages of the IQ over the single channel.

Digital Homodyne Summary

The digital homodyne techniques allow one to use RF amplifiers which are stable with high bandwidth, rather than DC amplifiers which are susceptible to drift and are harder to find with high bandwidth. As an additional practical benefit, they allow a lot of flexibility in tuning measurement parameters within software.

Post processing

In addition to the digital homodyne process, one typically does some minor postprocessing to the data. One can apply a digital low pass filter, which is equivalent to averaging the data over some interval, and eliminate some of the experiment and acquisition card noise. After that, one can safely decimate the data to lessen the load on the acquisition program, save storage space, and improve

¹At this stage there is much more noise than just the half photon required by the quantum limit and so the signals can be treated classically. If this procedure was done in a quantum limited set up it would be impossible to determine both quadratures without introducing an extra port (and thus extra noise).

analysis performance. One can also digitally apply a phase or amplitude offset, to the data and display it in terms of I and Q, or phase and amplitude. In addition, one can apply filters to do a quick analysis of data to extract Rabi or Ramsey oscillations as the data is acquired.

Chapter 7

Characterization of CQED

This chapter begins the presentation of circuit QED experimental results. In this chapter we will develop methods to measure all of the basic circuit QED parameters, including the energy scales, decay rates, as well as the gate capacitance and loop mutual inductance. The first section will discuss cavities without CPB's inside. The transition frequency and decay rate (Q) of resonators made from aluminum and niobium will be studied as a function of temperature and magnetic field. Then we will use the cavity to interrogate an embedded CPB/transmon to determine its spectral properties and coupling to the cavity.

7.1 Cavity

Transmission line cavities are incredibly sensitive tools to measure any quantity that can be mapped to an electric or magnetic reactance. In this thesis we focus on using them as a means of reading out a superconducting qubit, or to store photons which can be measured by the qubit (and eventually lead to non-local quantum logic gates). While circuit QED is only one application of this very promising technology, the task requires the quality factors ranging from $Q = 100$ to as high as possible. This has led us to develop a wide range of quality factors, and test the magnetic field and temperature dependence of the cavity resonance frequency and quality factor.

The frequency dependence of the transmission through the resonators was measured using a vector network analyzer¹. The equivalent circuit of the measurement setup is shown in the inset of Fig. 7.1. The sample was mounted on a PC board in a closed copper sample box (Fig. 5.13a) equipped with blind mate SMP connectors that launch the microwaves onto the PC board CPW's. The sample

¹The power transmission is measured in $\text{dB} = 10 \log |V_2/V_1|^2$, where V_2 is the voltage measured at the input port of the analyzer and V_1 is the voltage applied at the output port of the analyzer for equal input and output line impedances.

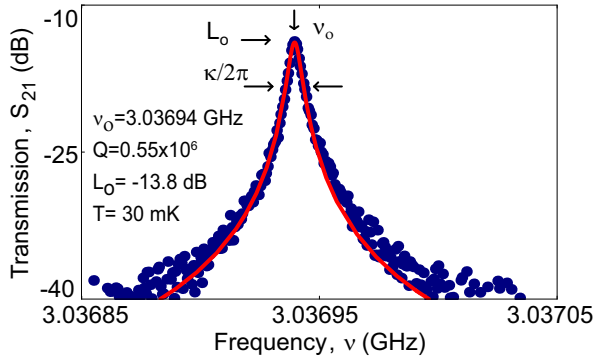


Figure 7.1: Measured transmission power spectrum of an under-coupled resonator. The solid line is a fit to a lorentzian line.

was cooled to temperatures ranging from the critical temperature, T_c of the superconducting films down to $T = 30\text{ mK}$.

The transmission S_{21} through the resonator around its fundamental resonant frequency ν_1 is shown in Fig. 7.1 at $T = 30\text{ mK}$. The curve was acquired using a -60 dBm input power and a room temperature amplifier. The input power was lowered until no distortion of the resonance curve due to excessive input power could be observed. The network analyzer was response calibrated (S_{21}) up to the input and output ports of the cryostat and the absorption of the cabling in the cryostat was determined to be approximately -7 dB in a calibrated S_{11} and S_{22} reflection measurement. The quality factor of the resonator is determined by fitting a Lorentzian line to the measured power spectrum as shown by the solid line in Fig. 7.1. This is the transmission spectrum of an under-coupled resonator and from the fit we have extracted $\nu_1 = 3.03694\text{ GHz}$. At this frequency the insertion loss, defined as the ratio of transmitted power to input power, is $L_1 = -13\text{ dB}$. The quality factor is determined from the full width at half max of the fitted power spectrum and is found to be $Q_L \approx Q_{\text{ext}} = \nu_1/2\delta\nu_1 = 2\pi\nu_1/\kappa = 0.55 \times 10^6$.

7.1.1 Temperature Dependence

In Fig. 7.2, we show the temperature dependence of the quality factor of an under-coupled (see Fig. 7.2a) and an over-coupled (see Fig. 7.2b) Nb resonator. In both cases the harmonics have lower Q than the fundamental. This is expected for both intentional coupling via the input/output capacitors and resistive losses.

In Fig. 7.3a, we show the measured temperature dependence of the quality factor Q for an under-coupled resonator (solid dots) and an over-coupled one (open dots). The lines in Fig. 7.3a

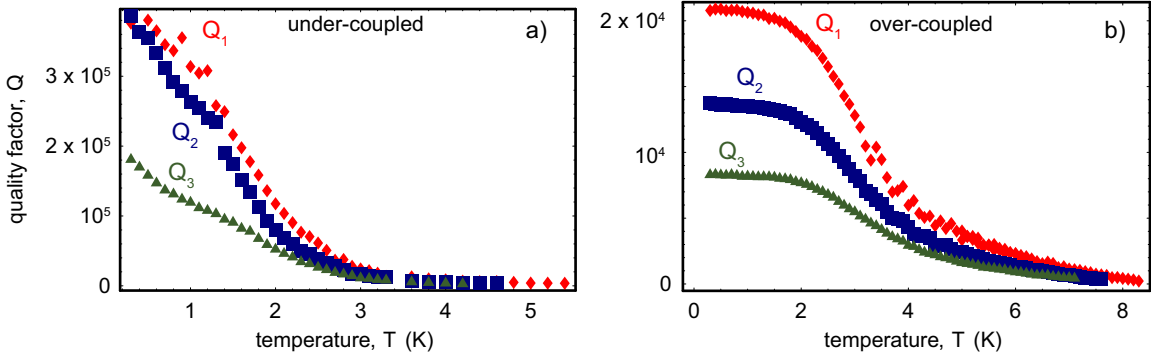


Figure 7.2: Temperature dependence of the fundamental and harmonics of an under (a) and over (b) over coupled Nb resonator.

are generated by summing a Q_{ext} that scales exponentially with the reduced temperature, T_c/T , in parallel with a constant Q_{int} . At low temperature, the coupling saturates the Q of the over-coupled resonator, while it seems that Q for the under-coupled one has still some weak temperature dependence whose nature is still unknown. We speculate that either vortices or losses in the dielectrics could limit the Q of this resonator but neither of these interpretations offer an easy understanding of the weak temperature dependence.

In Fig. 7.3b, we plot the ratios of the quality factors for the first (Q_2/Q_1) and second harmonics (Q_3/Q_1). According to calculations in sections 3.1.4 and 3.1.7, both quality factor due to capacitive coupling to the transmission line and resistive losses should scale like $Q_n/Q_1 = 1/n$, for the n^{th} resonance of the cavity. In both cases this results from the competition between having more wavelengths which tends to increase $Q \propto \omega$ and the losses which tend to decrease $Q \propto \omega^2$. In the measured data, the general trend is obeyed. There is more loss at higher harmonics and the ratios are similar whether the Q is dominated by resistive loss or by capacitive coupling. However, there doesn't appear to be quantitative agreement as one can see by comparing the dashed lines in Fig. 7.3b, to the experimental data. The under-coupled resonator also has some non-trivial dependence which appears to be non-uniform in harmonic number. This might be due to the onset of some other frequency dependent loss mechanism.

We have observed a shift of the resonant frequency ν_1 with temperature as shown in Fig. 7.4, which can be understood in terms of the temperature dependent kinetic inductance of the resonator [Day2003, Yoshida1995]. ν_1 is proportional to $1/\sqrt{L}$, where the total inductance of the resonator L is the sum of the temperature independent geometric inductance L_m and the temperature de-

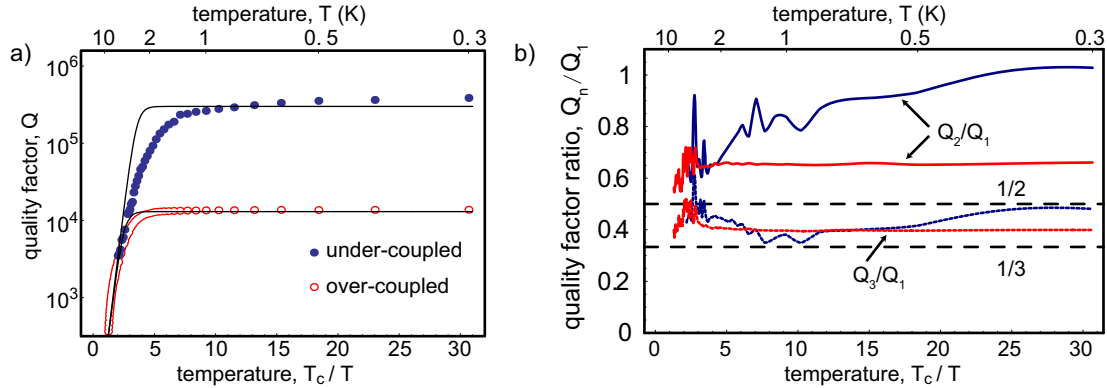


Figure 7.3: Temperature dependence of the quality factor Q of two 3 GHz superconducting Nb coplanar waveguide resonators at their first harmonic resonant frequency (6 GHz). Solid dots are data collected on a under-coupled resonator and open dots are from an over-coupled one. The lines are generated by summing a Q_{ext} that scales exponentially with the reduced temperature, T_c/T , in parallel with a constant Q_{int} . b) Plot of the ratios between the Q of the fundamental and higher harmonics for under (blue) and over (red) coupled cavities. Dashed lines indicate expected values of $Q_2/Q_1 = 1/2$ and $Q_3/Q_1 = 1/3$.

pendent kinetic inductance L_K . The kinetic inductance scales as $L_k \propto \lambda_L(T)^2$, where $\lambda_L(T)$ is the temperature dependent London penetration depth. The best fit in Fig. 7.4 was achieved for a ratio $L_K/L_m \approx 7\%$ and a critical temperature of $T_c \approx 9.1$ K, which we have independently measured on a test sample fabricated on the same wafer.

7.1.2 Magnetic Field Dependence

As explained in section 3.2, we need to apply a magnetic field perpendicular to the qubit loop in order to tune E_J . It is important that small these small fields ($\sim \mu\text{T}$) not destroy the resonator quality factor. In Fig. 7.5, we measure the quality factor of two resonators as a function of the magnetic field at $T = 300$ mK, as shown in Fig. 7.5. It is evident that the Nb film (a) is less sensitive to the applied field than the Al film (b). In both cases there seems to be a reproducible and irreversible hysteretic behavior that can be reset by thermal cycling the sample. In our initial experiments (see Sec. 7.2), we have observed a magnetic field focusing effect, such that the effective field in the gap of the resonator was approximately two orders of magnitude larger than the applied magnetic field. We believe that the hysteretic phenomena could be a result of vortices being trapped in the resonator film due to these large effective fields.

A magnetic field not only affects the quality factor of a resonator, it also slightly changes the kinetic inductance, shifting the resonance frequency. The magnetic field dependence of Nb and Al

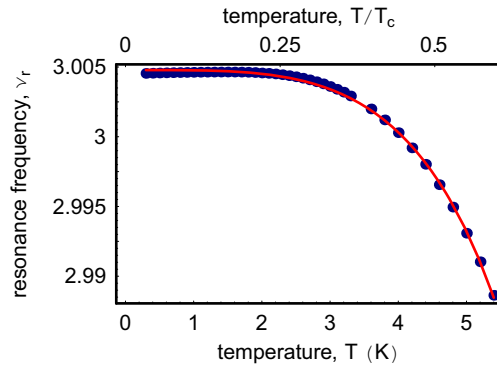


Figure 7.4: Temperature dependence of the fundamental resonant frequency ν_r of a superconducting Nb coplanar waveguide resonator. Solid line is a fit to a kinetic inductance model.

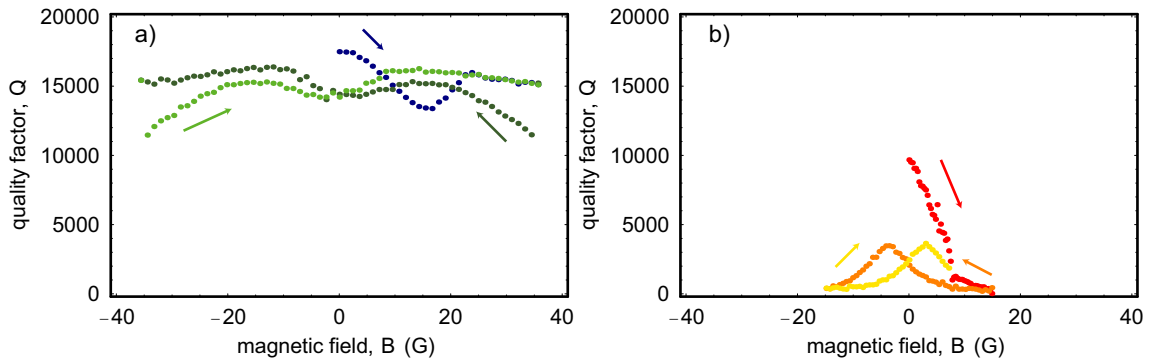


Figure 7.5: Magnetic field dependence of the quality factor Q of two different superconducting coplanar waveguide resonators at $T = 300\text{ mK}$. In the upper part data refer to a Nb resonator, while in the lower part they refer to an Al resonator. Arrows indicate the direction in which the magnetic field was swept in both cases starting from zero.

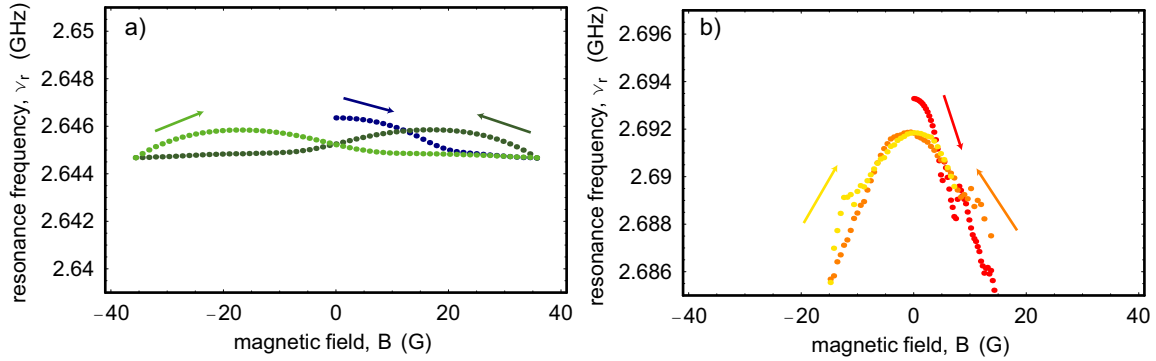


Figure 7.6: Magnetic field dependence of the fundamental resonance frequency of two different superconducting resonators at $T = 300$ mK. Both the Nb (**a**) and Al datasets are plotted on the same scale (10 MHz). The arrows indicate the direction in which the magnetic field was swept in both cases starting from zero.

resonators is plotted in Fig. 7.6. Both plots are on a 10 MHz scale and show that the Al resonator shifts significantly more than the Nb one. However, though it shifts more it has significantly less hysteresis. While tuning the qubit in circuit QED experiments, both the shift and the different hystereses are quite noticeable. This lends further weight to the suspicion that vortices are trapped. Vortices should be less stable in Al than in Nb and therefore have less hysteresis once the field is removed. Though these vortices clearly affect the quality factor of the resonators it is unclear whether they have a negative impact on the qubit decay.

The resonators are quite stable drifting much less than a linewidth over many months of data taking. They are very reproducible upon warming and cooling (with no field) returning to the same frequency within less than a few MHz. Run to run the cavities can be made with resonant frequencies repeatable to ~ 100 MHz and with Q' 's generally repeatable to $\sim 20\%$, with variation due mainly to over or under exposure of the optical resist. In practice the exact values are not critical as the dispersive coupling falls off slowly (like $1/\Delta$) and the qubit is also tunable allowing one to accommodate a wide range of resonator parameters.

7.2 Cooper pair box

To characterize the effect of the Cooper pair box on the cavity, we will continuously probe the amplitude and phase of a microwave tone at frequency $\nu_{RF} = \nu_r$. Most parameters can be extracted from cavity response to the qubit in its ground state, via its dependence on bias voltage, V_g , and flux, Φ_B . Such a ground state characterization process is advantageous because such probes

are relatively insensitive to the qubit decay rates and require no additional tones or pulse synthesis. A very similar inductive technique has also been used to characterize the CPB [Born2004], but this was done at low frequency using a magnetic coupling rather than at high frequency (and with electric coupling). By interacting with the qubit on energy scales greater than the thermal background we are able to study cavity QED with the same coupling.

The resonator frequency is given a dispersive shift due to the presence of the qubit.

$$\omega'_r = \omega_r \pm \chi \quad (7.1)$$

The dispersive shift is $\chi \approx \frac{g^2}{\Delta}$ with the \pm is determined by the qubit state. This qubit state-dependence of the cavity frequency is used for the qubit readout. However, even in the ground state the resonator frequency depends on the qubit detuning, Δ and coupling strength g , which both in turn depend on the bias parameters of the CPB. The qubit frequency ω_a (plotted in Fig. 7.7a) can be tuned with either gate or flux. The phase (or amplitude) of a tone at the bare resonator frequency ($\nu_{RF} = \nu_r$) is a sensitive probe of the dispersive shift. As the gate voltage or flux is tuned so that the qubit frequency approaches the resonator frequency, the frequency shift gets larger, resulting in a phase shift of the probe beam (Fig. 7.7b top). When the qubit transition frequency crosses the resonator (Δ changes sign) the dispersive shift, and thus the phase shift will also change sign (Fig. 7.7b bottom). This large feature can act as a marker as to how the gate and flux biases affect the CPB. The location of these sign changes can be thought of as the intersection of the transition frequency landscape with a plane at $\nu = \nu_r$ (see Fig. 7.7c).

The resulting response, resembling “footballs,” has several important features. The first is that it is periodic along both the flux and charge axes. This periodicity results from the quantized nature of charge on the island and flux in the loop of the CPB. We can find the effective gate capacitance by equating the periodicity of the gate voltage with one Cooper pair¹, $C_g V_g = 2e$. The periodicity in the magnetic field (vertical) direction measures the field necessary to apply a single flux quantum (giving the effective loop area).

In addition to the periodicity one can learn about the CPB energy scales, E_j^{\max} and E_C by looking at the major and minor axes of the “footballs” relative to the periodicity. Considering the

¹According to the CPB Hamiltonian the periodicity of the gate charge should be $2e$. However, if there are quasiparticles (single electrons) which are free to tunnel the response can appear to be $1e$ periodic. To eliminate this possibility the periodicity was observed as it was cooled and heated to about 250 mK where the number of quasiparticles increases dramatically. At low temperatures the curves (of the type in Fig. 7.7b) were $2e$ periodic with occasional $1e$ jumps, where as when the temperature was increased, the number of jumps increased, and eventually the curves became $1e$ periodic.

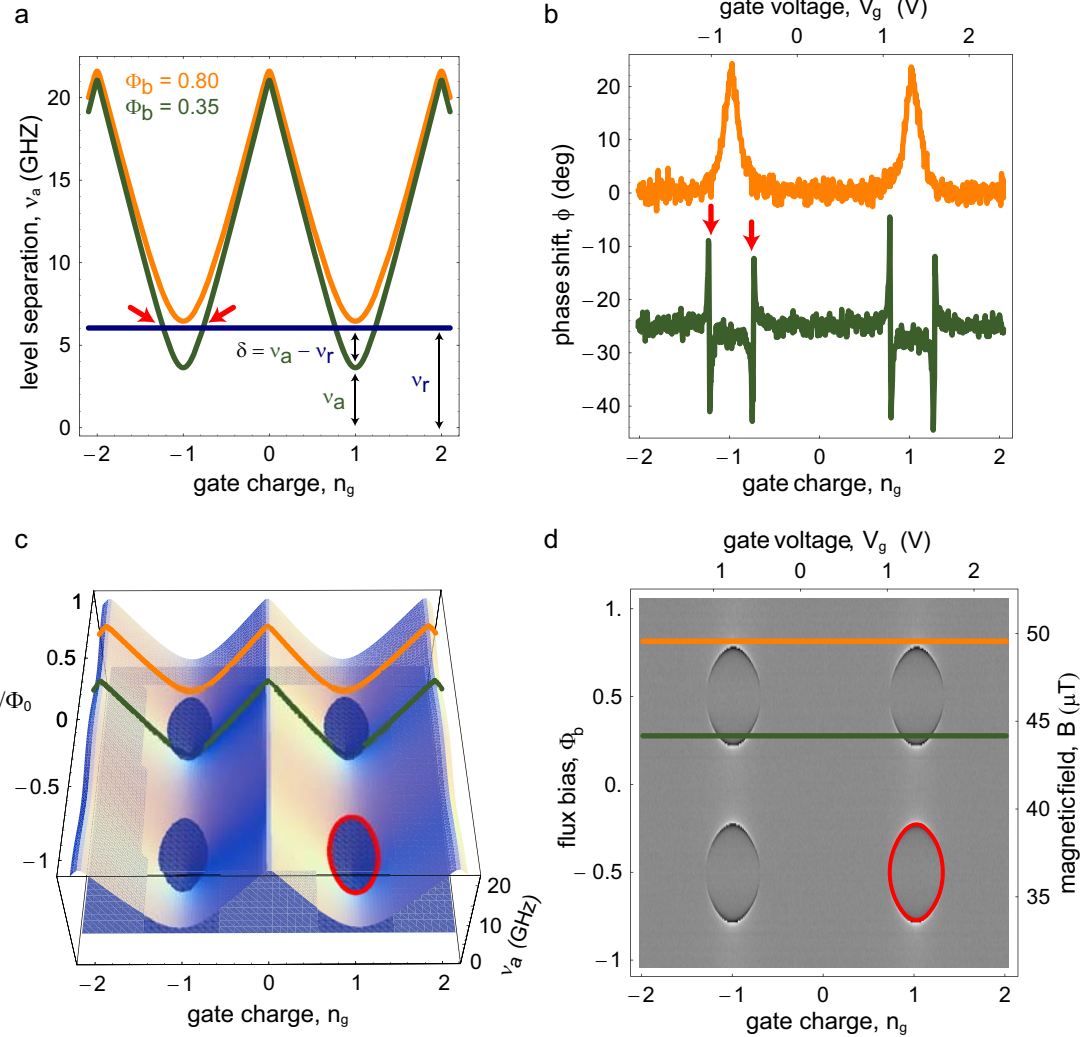


Figure 7.7: Response of cqed system to charge and flux bias, using data taken from sample CQED057 [Wallraff2004]. **a)** Calculated level separation $\nu_a = \omega_a/2\pi = E_a/h$ between ground $|g\rangle$ and excited state $|e\rangle$ of qubit for two values of flux bias $\Phi_B = 0.8$ (orange line) and $\Phi_B = 0.35$ (green line). The resonator frequency $\nu_r = \omega_r/2\pi$ is shown by a blue line. Resonance occurs at $\nu_a = \nu_r$ symmetrically around degeneracy $n_g = 1$, see red arrows. The detuning $\Delta/2\pi = \delta = \nu_a - \nu_r$ is indicated. **b)** Measured phase shift ϕ of the transmitted microwave for values of Φ_B in a. Green curve is offset by -25 deg for visibility. **c)** Calculated qubit level separation ν_a versus bias parameters n_g and Φ_B . The resonator frequency ν_r is indicated by the blue plane. At the intersection, also indicated by the red curve in the lower right hand quadrant, resonance between the qubit and the resonator occurs ($\delta = 0$). For qubit states below the resonator plane the detuning is $\delta < 0$, above $\delta > 0$. **d)** Density plot of measured phase shift ϕ versus n_g and Φ_B . Light colors indicate positive ϕ ($\delta > 0$), dark colors negative ϕ ($\delta < 0$). The red line is a fit of the data to the resonance condition $\nu_a = \nu_r$. In c and d, the line cuts presented in a and b are indicated by the orange and the green line, respectively. The microwave probe power P_{RF} used to acquire the data is adjusted such that the maximum intra-resonator photon number n at ν_r is about 10 for $g^2/\Delta\kappa \ll 1$. The calibration of the photon number has been performed in situ by measuring the ac-Stark shift of the qubit levels [Schuster2005].

extent of the “football” in the flux direction yields

$$E_J^{\max} = \frac{\hbar\omega_r}{\cos(\pi\Phi_r/\Phi_0)} \quad (7.2)$$

where Φ_r/Φ_0 is the ratio of the bias flux when the qubit and resonator are degenerate to the periodicity (one flux quantum). When attempting to find the charging energy in a similar way, one immediately notices that the signal is absent along the “football’s” gate charge axis. The magnitude of the phase response is expected to vary with both gate charge and flux. The phase shift is largest when the transition frequency (ω_a) intersects the resonator frequency (ω_r) at degeneracy $n_g = 1$. This is because the coupling strength is proportional to the charge transition matrix element

$$g^2 \propto |\langle g | \hat{N} | e \rangle|^2 \approx E_J^2 / (16E_C^2(1 - n_g) + E_J^2) \quad (7.3)$$

which as $E_J = E_J^{\max}|\cos(\pi\Phi_B/\Phi_0)|$ approaches zero¹ at $\Phi_B = \Phi_0/2$.

To get a rough idea of the charging energy one can extrapolate the qubit-resonator degeneracy curve to $\Phi_B \rightarrow \Phi_0/2$ which would (in the charge regime) yield

$$E_C \approx \frac{\hbar\omega_r}{4(1 - n_g)} \quad (7.4)$$

While looking at these two slices is the most conceptually simple way to find E_J^{\max} and E_C , one can improve the accuracy by extracting the qubit-resonator degeneracy contour and numerically fitting it to an exact expression for the CPB transition energy. This method is a good way of getting the energy scales to $\sim 10\%$ accuracy, with little initial idea of the box parameters. However, it is a quite inefficient method with only an infinitesimal curve being selected out of the entire area of the large 2D data set in figure 7.7d. So while its ability to capture the rough behavior of a device with nearly any parameters is a great asset, the absolute accuracy is limited by the large dynamic range required in the presence of potentially large amounts of charge noise.

Using an additional spectroscopy tone (at $\omega_s \neq \omega_r$) and measuring the transmitted phase shift of a tone at the resonator frequency, ω_r , one can probe the qubit at frequencies away from degeneracy with the cavity. This allows the qubit spectrum to be determined directly, with accuracy of γ_2 , better than a part in 10^{-4} relative accuracy. When the qubit is excited, the phase shift of the probe tone is opposite from when the qubit is in the ground state (see Fig. 7.9a). When the spectroscopy frequency matches the qubit transition frequency $\omega_s = \omega_a$ and the qubit is excited, reducing the

¹ $E_J \rightarrow 0$ at $\Phi_B = \Phi_0/2$ if the junctions are perfectly symmetric. If there is an asymmetry then some Josephson coupling will remain. For more details about the effects of junction asymmetry see section 3.2.3.

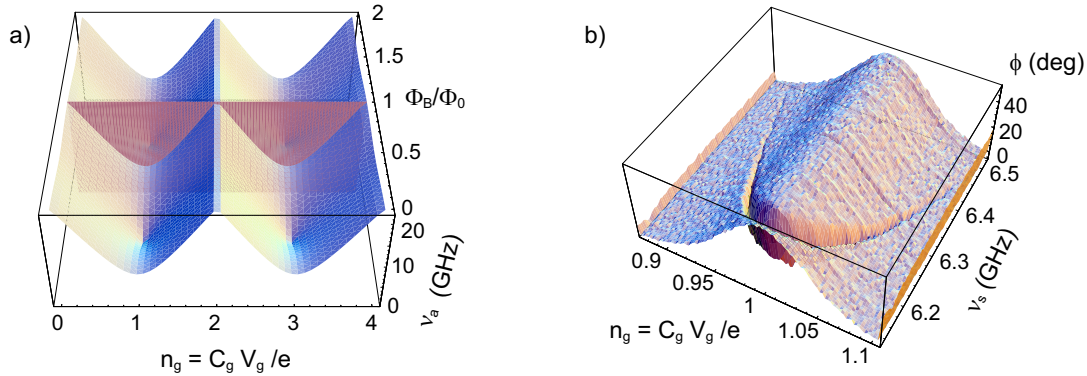


Figure 7.8: **a)** The spectroscopy experiment can be thought of as taking the intersection between the transition energy surface and a plane at constant Φ_B . **b)** A surface plot of spectroscopy data from sample CQED057.

phase shift. For example, when the qubit is saturated, the qubit has an equal chance of being in the ground or excited state, resulting in zero phase shift. The reduction in phase shift (see Fig. 7.9b) allows one to directly trace out the transition energy of the qubit. While the “footballs” plot in Fig. 7.7 can be thought of slicing the transition energy landscape with a plane at constant frequency, such spectroscopy experiments can be thought of as taking a slice at constant Φ_B . By tuning the flux to $\Phi_B = n\Phi_0$, and measuring the transition frequency at $n_g = 1$, one can calculate E_J^{\max} to better than a Megahertz¹. Fitting to the whole spectroscopy curve gives a good estimate of the charging energy, E_C , as well.

The width and the saturation level of the spectroscopic lines discussed above, depend sensitively on the power (P_s) of the spectroscopic drive. Both quantities are related to the excited state population

$$P_e = 1 - P_g = \frac{1}{2} \frac{n_s(2g)^2 T_1 T_2}{1 + (T_2 \Delta_{s,a})^2 + n_s(2g)^2 T_1 T_2}, \quad (7.5)$$

where $\Delta_{s,a}$ is the detuning between the spectroscopy drive and the qubit frequency, and n_s is the number of photons in the spectroscopy drive. The lineshape of the qubit is given by the steady state Bloch equations [Abragam1961], where $2g$ is the vacuum Rabi frequency, n_s the average number of spectroscopy photons in the resonator, T_1 the relaxation time and T_2 the dephasing time of the qubit. We have extracted the transition line width and saturation from spectroscopy frequency scans for different drive powers (P_s) with the qubit biased at charge degeneracy ($n_g = 1$). We observe that the spectroscopic lines have a lorentzian line shape (also see Fig. 7.10a), with width and depth

¹In order to get the best value for E_J^{\max} one can measure the transition frequency at degeneracy and sweep the flux to find its maximum.

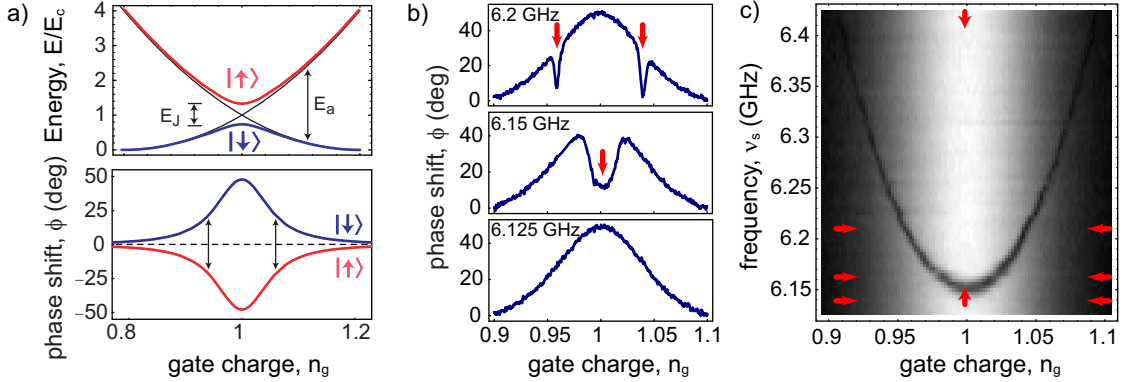


Figure 7.9: Spectroscopic interrogation of qubit transition energy using data from CQED057 [Schuster2005]. **a)** Ground $|g\rangle$ and excited $|e\rangle$ state energy levels of CPB *vs.* gate charge n_g and calculated phase shift ϕ in ground and excited state *vs.* n_g for $\Delta_{a,r}/2\pi = 100$ MHz. **b)** Plots of measured dispersive shift *vs.* n_g showing qubit response to an applied spectroscopy tone. **c)** Plot of phase shift (intensity) *vs.* gate charge, n_g and spectroscopy frequency, ν_s . The curve of suppressed phase shift is a direct measurement of the qubit transition frequency, ν_a .

in accordance with Eq. (7.5). The half width at half max (HWHM) of the line is found to follow the expected power dependence $2\pi\delta\nu_{\text{HWHM}} = 1/T'_2 = \sqrt{1/T_2^2 + n_s(2g)^2 T_1/T_2}$ [Abragam1961], where the input microwave power P_s is proportional to $n_s(2g)^2$, see Fig. 7.10a. In the low power limit ($n_s(2g)^2 \rightarrow 0$), the unbroadened line width is found to be small $\delta\nu_{\text{HWHM}} \approx 750$ kHz, corresponding to a long dephasing time of $T_2 > 200$ ns at $n_g = 1$, where the qubit is only second order sensitive to charge fluctuations limiting the dephasing time in this sample. At larger drive, the width increases proportionally to the drive amplitude. The depth of the spectroscopic dip at resonance ($\Delta_{s,a} = 0$) reflects the probability of the qubit to be in the excited state P_e , and depends on P_s as predicted by Eq. (7.5), see Fig. 7.10b. At low drive the population increases linearly with P_s and then approaches 0.5 for large P_s . From time resolved measurements (data not shown), T_1 is found to be on the order of a few microseconds, a value which is much shorter than that expected for radiative decay of the qubit in the cavity [Blais2004], indicating the existence of other, possibly non-radiative, decay channels.

7.2.1 Charge Noise

A significant obstacle to performing long duration experiments with high fidelity on the CPB is charge noise, which comes in several flavors. White noise blurs the features along the bias charge axes in Figs. 7.7-7.8, limiting the resolution of these features and coherence time of the qubit. In addition

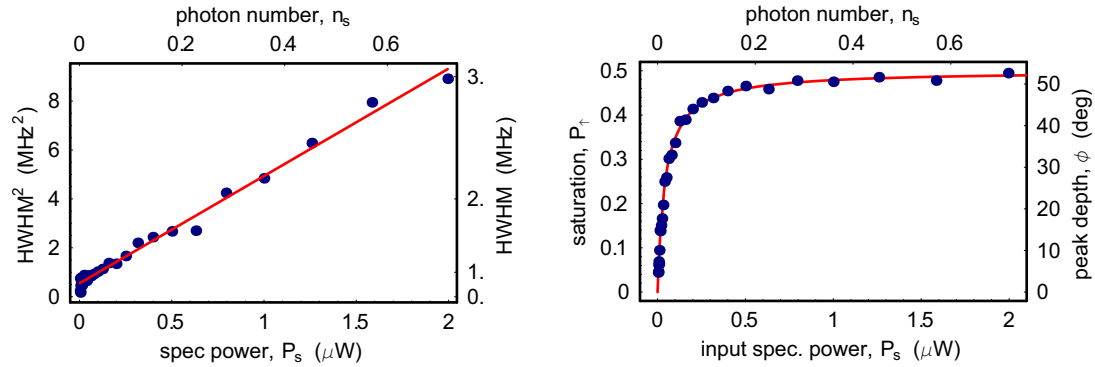


Figure 7.10: a) Measured qubit line width $\delta\nu_{\text{HWHM}}$ vs. input spectroscopy power P_s (solid circles) with fit (solid line). Probe beam power P_{RF} is adjusted such that $n < 1$. (b) Measured peak depth ϕ and excited state population probability P_e on resonance $\Delta_{s,a} = 0$ vs. P_s (solid circles) with fit (solid line).

to this disruptive, but well-behaved noise, there are also two types of discrete events known as charge “switchers.” These switchers cause discrete jumps in the apparent bias charge, n_g . One class of switchers are due to quasiparticles tunneling, which cause jumps with magnitude $1e$ (see Fig. 7.11a). In our devices at zero flux, there are usually many parity jumps in one averaging time, causing a shadow pattern to appear shifted by one electron. As magnetic field is increased, the shadow can be reduced significantly. While the exact cause of this effect is unknown, we suspect that the superconducting gap of the island and fingers are reduced differently by application of the magnetic fields. This would not eliminate quasiparticles, but does prevent them from tunneling across the junction. The preferred parity can also change on timescales of seconds to hours depending on the exact device and bias conditions (see Fig. 7.11). One also notices sub-electron switching events, such as the particularly pathological switcher in figure 7.11c, and barely noticeable deviations in the spectrum shown in figure 7.9c. Particularly, bad switchers can sometimes be eliminated by warming and cooling the sample, or by careful selection of the bias point. In decent samples, data can be taken for periods of $\sim 1\text{hr}$ (see Fig. 7.11c) without a large switching event ($> 0.01e$). Every device cooled showed working samples, and could be characterized. Of these, about two thirds could have had sufficiently long windows of stability that more intense investigations were deemed worthwhile. These discrete jumps have in practice caused the most difficulty in acquiring the data, as they make it difficult to bias the qubit for a long enough time to measure.

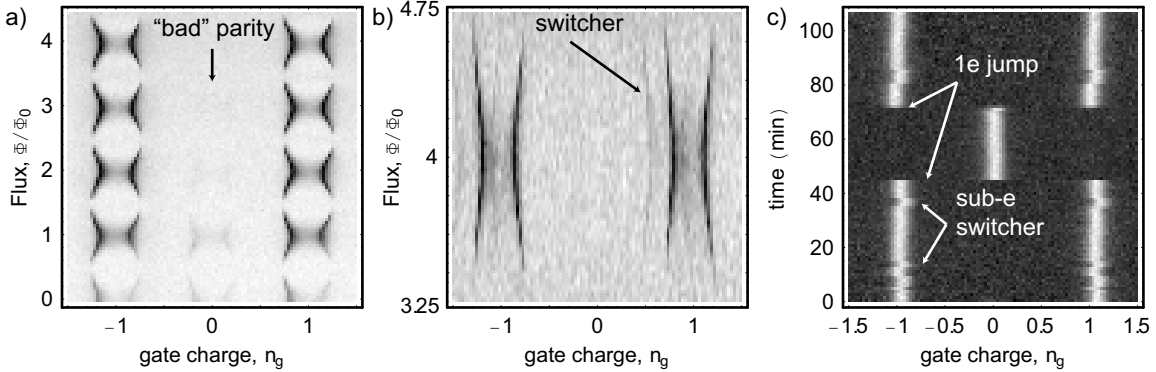


Figure 7.11: **a)** A plot of transmitted amplitude as a function of charge and flux bias, showing a preferred parity and residual off-parity “shadow.” At $n_g = 0$ there is a repetition of the pattern at $n_g = 1$, due to imperfect parity. As the magnetic field is increased it the parity improves significantly. **b)** A sub-electron charge switcher which switches fast (compared to the averaging time of ~ 1 s), relatively even duty cycle, and is large $\sim 0.3e$. Both **a** and **b** use data from CQED061 the device used in [Wallraff2005]. **c)** In **a** and **b** the switching is so fast that it just looks like a shadow. In **c** the magnetic field is fixed, and the same trace is repeated (this measurement done on CQED097). It clearly shows both parity jumps (infrequent) and sub-e switching events (more frequent). This sample is fairly typical, and the best data would be taken in an interval (typically 20 – 30 minutes) where no switching events occurred.

7.2.2 Measured CPB properties

It is useful to take a survey of all of the samples that were measured. Despite a small number of samples table 7.1 explores a large range of parameters. Quality factors from $10^2 – 10^4$ were explored allowing experiments based on fast measurements (single photon generation) and long photon coherence (number splitting). Less intentionally a large range of E_J^{\max} was also explored. These fluctuations were largely due to drift in fabrication parameters. More interestingly, the charging energy, E_C , which is very well controlled, was varied from 5 GHz a typical CPB scale to as low as 370 MHz well into the new transmon regime. By varying size of the island and capacitive division a large range of vacuum Rabi couplings, g , were explored from rather small (but still well into the strong coupling limit) values of 2.25 MHz to values approaching the fine structure limit, 115 MHz.

7.3 Transmon

The transmon, gloriously, has no charge dependence, so we must measure its energy scales without exploiting the charge dependence of the energy levels as we did when measuring the traditional CPB. Because the transmon has one less degree of freedom, it is actually much easier to characterize. In the traditional CPB, the parameter space was sufficiently large that one had to do a first pass to

ID	Cavity	ν_r (GHz)	Q	E_J^{\max} (GHz)	E_C (GHz)	$g/2\pi$ (MHz)	T_1 (μ s)	T_2 (ns)
052	R5-008	6.0413	8534	6.7	5	2.25	1.2	48
057	R5-005	6.0435	10469	8	5.2	5.8	0.6	227
061	R6-008	5.4262	7807	4.312	5.2	17	7	500
063	R6-005	5.4139	8462	8.2	3.45	10	4.1	159
80a	R22-107	5.0987	6101	40	2.49	58	0.52	159
80b	R22-107	5.0987	6101	43	2.65	25		> 31
971R	R49-105	5.5331	10300	12	5.25	17	3	200
971R	R49-105	5.5331	24822	13	5.25	25		
120c	R062-06	5.6705	24822	18.5	0.518	105		53
128	R96-C1	5.173	120	20.19	0.371	115	0.09	145

Table 7.1: Summary of sample parameters.

get an approximate idea of the energy scales, then use this knowledge to set up a spectroscopy experiment rather carefully. With the transmon, the lack of charge dependence and the extra stability that provides, one can immediately jump to spectroscopy. In a single two dimensional data acquisition, one can scan transition frequency vs. magnetic flux (see Fig. 7.12). By fitting this flux dependence, one can determine both E_J^{\max} and E_C . Because of the transmon's small anharmonicity, another technique, which is even more accurate, becomes available. One can measure the transition frequencies of auxiliary levels, which are now at accessible frequencies. Because the whole spectrum is determined by E_J and E_C , a measurement of any two transition frequencies, uniquely determines the both energy scales. By using two photon spectroscopy, one can easily measure ω_{12} in addition to the usual transition energy. This method is especially good because it does not require the qubit bias point to be changed, so it can be performed immediately before an experiment. In the asymptotic limit, where the energy levels are given by Eq. 4.78, E_J and E_C are given by

$$E_J \approx \hbar \frac{(\omega_{12} - 2\omega_{01})^2}{8(\omega_{01} - \omega_{12})} \quad (7.6)$$

$$E_C \approx -\hbar\alpha = \hbar(\omega_{01} - \omega_{12}) \quad (7.7)$$

For more accurate results, one can numerically solve for E_J and E_C , using the exact expression based on the Mathieu functions given in appendix C.1.

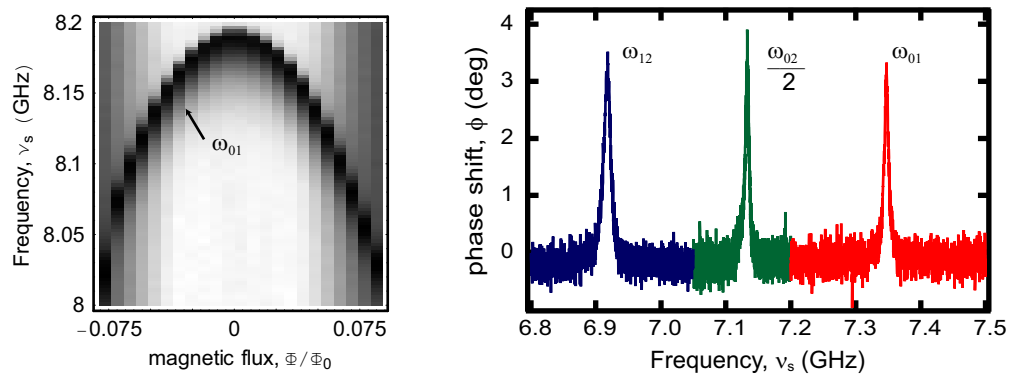


Figure 7.12: **a)** Spectroscopy of the qubit transition frequency ω_{01} vs. flux near E_J^{\max} . **b)** The transition frequencies from the ground to the first and second excited states can be used to determine E_J and E_C . To find ω_{01} conventional spectroscopy is used. To find $\omega_{02}/2$ a single spectroscopy tone is used at very high powers to exciting a two photon process. One can find ω_{12} by taking $\omega_{02} - \omega_{12}$ but it can also be measured directly by using two spectroscopy generators, tuning the first to ω_{01} and sweeping the second near ω_{12} .

Chapter 8

Cavity QED Experiments with Circuits

This chapter will focus on exploring the different regimes of cavity QED as depicted by the phase diagram in figure 8.1. First, in the resonant regime (Fig. 8.1 blue region where $\Delta < g$), we observe strong coupling for the first time in a solid state system, in the form of vacuum Rabi mode splitting. We explore tuning the qubit in and out of resonance with the cavity, using both charge and flux. When the qubit is detuned sufficiently ($\Delta \gg g$), the qubit enters the dispersive regime.

We study the transition from resonant to dispersive measuring the Purcell effect, a mechanism of indirect qubit decay through the cavity, which enhances decay near resonance, and suppresses it when far detuned. Once firmly in the dispersive regime, we first study the weak dispersive limit (Fig. 8.1 red region where $\Delta \gg g$ and $\chi < \max \kappa, \gamma$). Here, the effects of the dispersive coupling can be seen through the AC Stark shift on the qubit. This study explores the mechanism of quantum backaction in the cavity-based qubit measurement. A slight modification allows the effect to be used without backaction (and making no measurement) to create a frequency shift/phase gate.

While in the resonant regime there are spontaneous vacuum Rabi oscillations between qubit excitations and photons, in the dispersive regime such transitions must be stimulated. By exciting the qubit-cavity sidebands, one can make simultaneous qubit-photon transitions, which could allow for teleportation and quantum logic over centimeter distances. While we most commonly think of the cavity as measuring the qubit, the nature of the dispersive Hamiltonian implies that the qubit also measures the photon number.

When the coupling strength is large enough, but still dispersive (Fig. 8.1 white region where $g^2/\Delta > \kappa$ and $g < \Delta/10$), we observe the qubit spectrum resolving into separate photon number

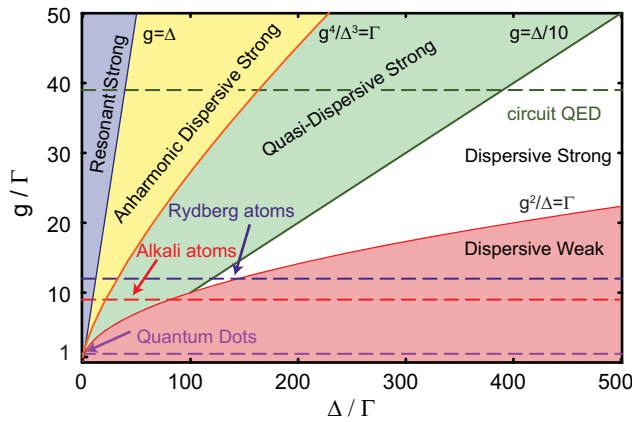


Figure 8.1: A phase diagram for cavity QED. The parameter space is described by the atom-photon coupling strength, g , and the detuning, Δ , between the atom and cavity frequencies, normalized to the rates of decay represented by $\Gamma = \max[\gamma, \kappa, 1/T]$. Different cavity QED systems, including Rydberg atoms, alkali atoms, quantum dots, and circuit QED, are represented by dashed horizontal lines. In the blue region the qubit and cavity are resonant, and undergo vacuum Rabi oscillations. In the red, weak dispersive, region the ac Stark shift $g^2/\Delta < \Gamma$ is too small to dispersively resolve individual photons, but a QND measurement of the qubit can still be realized by using many photons. In the white region, quantum non-demolition measurements are in principle possible with demolition less than 1%, allowing 100 repeated measurements. In the green region single photon resolution is possible but measurements of either the qubit or cavity occupation cause larger demolition. In the yellow region the cavity becomes anharmonic, allowing it to create squeezed states and inherit some inhomogeneous broadening, and the Stark shift becomes non-linear.

peaks. Finally, in a hint of the anharmonic coupling regime, (Fig. 8.1 yellow region where $g^4/\Delta^3 > \Gamma$ and $\Delta > g$), the cavity becomes non-linear with even just a few photons in the cavity.

8.1 Resonant Limit

Cavity QED at its heart seeks to create a coherent coupling between a two level system and a single photon. Once established, the qubit-photon coupling can be used to detect and generate quantum states of light, cool or invert the qubit, and make logical gates between distant qubits. This section discusses perhaps the most important result in this thesis, a direct measurement of the qubit-photon coupling. Using bias charge (n_g) or flux (Φ_B), the qubit is tuned into resonance with the cavity. Two experiments will be discussed. In the first case, a traditional CPB is used with charge as the primary control parameter, while employing a modest dipole coupling ($g = 6\text{ MHz}$), and similar cavity ($\kappa/2\pi = 0.8\text{ MHz}$) and qubit ($\gamma_2/2\pi = 0.7\text{ MHz}$) linewidths. In the second case, a transmon is used with flux as the control parameter and employs a dipole coupling which approaches the limit set by the fine structure constant ($2g = 228\text{ MHz}$)! For this sample, a much higher cavity decay rate $\kappa = 43\text{ MHz}$ relative to qubit decay rate ($\gamma_2/2\pi = 2.5\text{ MHz}$) was chosen, both to increase visibility of coupled peaks, and to observe fast dynamics in other experiments (see Sec. 9.3).

8.1.1 Vacuum Rabi Mode Splitting with CPB

To perform this experiment, the qubit is first characterized (see Sec. 7.2), and then tuned by magnetic flux to have its minimum transition frequency $\nu_a \approx E_J/h$ degenerate with (see Fig. 8.2a) or just below the resonator frequency, ν_r (see Fig. 8.2b). To acquire the data in figure 8.2, the transmitted amplitude of a single tone is measured in a narrow band via a heterodyne technique as a function of ν_{RF} . The gate charge bias is then stepped near $n_g = 1$. As described in chapter 2, when the cavity and qubit approach degeneracy ($\Delta \rightarrow 0$), excitations become shared between them. The eigenstates of the system are no longer $|e, 0\rangle$ and $|g, 1\rangle$, but even and odd superpositions of those states $(|g, 1\rangle \pm |e, 0\rangle)/\sqrt{2}$. In order to see transmission, the drive tone must be resonant with the transition from the ground state $|g, 0\rangle$ to one of these eigenstates of the strongly coupled system. The measured spectra in figure 8.2 are compared with the eigenfrequencies predicted by the Jaynes-Cummings Hamiltonian for the parameters found in section 7.2, and have very good agreement.

In figure 8.3, a spectrum extracted from Fig. 8.2a at $\Delta = 0$ (Fig. 8.3b) is compared with one taken at $\Delta \gg g$. Fig. 8.2b also visually, and dramatically, demonstrates that the system is in

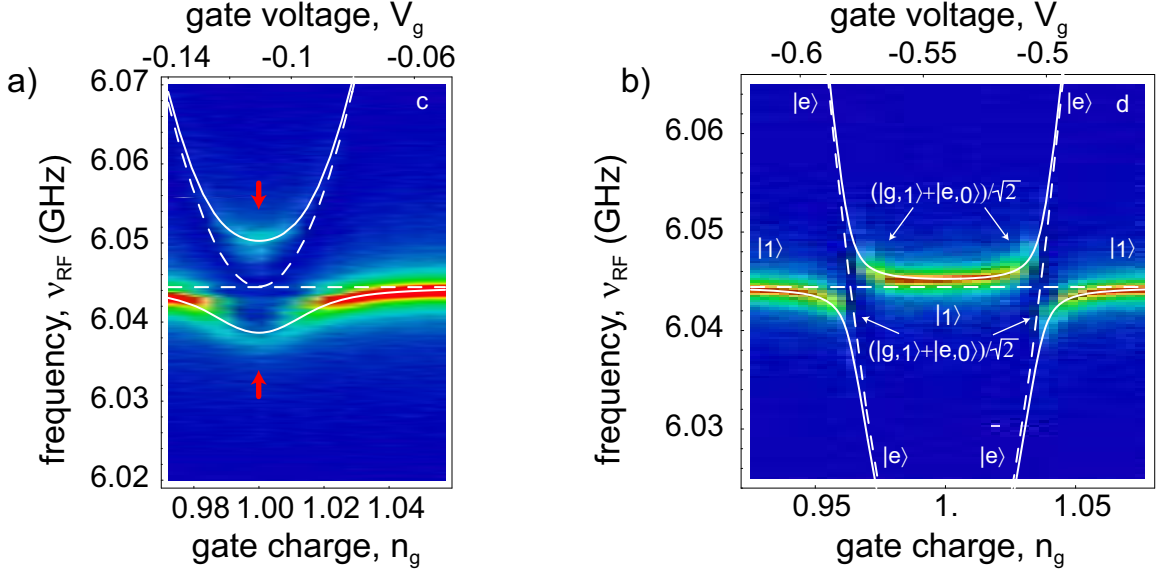


Figure 8.2: **a)** Vacuum Rabi avoided crossing as function of gate charge (n_g) where the qubit and cavity are resonant at charge degeneracy $n_g = 1$. Color shows transmission (blue is low, red is high) of a microwave probe tone at ν_{RF} . The dashed white curve shows the transition frequency as a function of n_g , of an uncoupled cavity and qubit ($g = 0$). The solid white line shows the expected transition frequencies from the ground state to first and second excited states of the strongly coupled cavity-qubit system. **b)** The same as **a** except that the cavity-qubit degeneracy does not occur at $n_g = 1$ but slightly away, yielding two avoided crossings. The states far away from the avoided crossing resemble either a single photon or qubit excitation, but near the cavity-qubit where the transition spectrum is curved the excitations have both photon and qubit character. At these points the upper and lower branch are whimsically called a phobit and quon, to signify their joint nature.

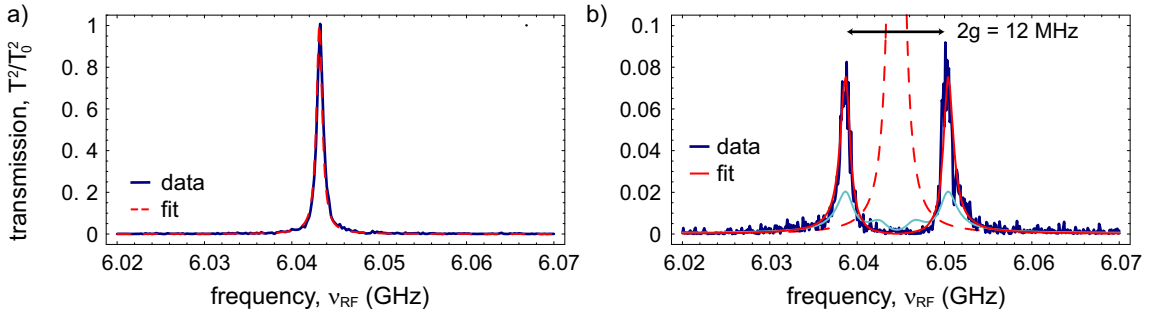


Figure 8.3: Vacuum Rabi mode splitting. **a)** Measured transmission T^2 (blue line) versus microwave probe frequency ν_{RF} for large detuning ($g^2/\Delta\kappa \ll 1$) and fit to Lorentzian (dashed red line). The peak transmission amplitude is normalized to unity. **a)** Measured transmission spectrum for the resonant case $\Delta = 0$ at $n_g = 1$ (blue line) showing the vacuum Rabi mode splitting compared to numerically calculated transmission spectra (red and light blue lines) for thermal photon numbers of $n = 0.06$ and 0.5 , respectively. The dashed line is the calculated transmission for $g = 0$ and $\kappa/2\pi = 0.8$ MHz. **b)** Measured transmission spectrum for the resonant case $\Delta = 0$ at $n_g = 1$ (blue line) showing the vacuum Rabi mode splitting compared to numerically calculated transmission spectra (red and light blue lines) for thermal photon numbers of $n = 0.06$ and 0.5 , respectively and $2g = 12$ MHz. The dashed line is the calculated transmission for $g = 0$ and $\kappa/2\pi = 0.8$ MHz.

the strong coupling regime. The fact that there are two well-resolved peaks clearly shows that the vacuum Rabi mode splitting of the cavity line ($2g = 12$ MHz), is much larger than the average of the cavity and qubit line widths, $(\kappa + \gamma_2)/2$, the definition of strong coupling. In fact, $4g/(\kappa + \gamma_2) = 16$, putting the system well into the strong coupling regime. We claim that this is evidence of a *single* photon interacting with the qubit. In a harmonic oscillator spectrum (see Fig. 8.3a) it is difficult to perform an absolute calibration of the photon number. However, the transmission spectrum of the joint system, which is highly anharmonic when degenerate, is very sensitive to the intracavity photon number. Theory predictions for $n = 0.06$, and $n = 0.5$ photons are plotted on top of the measured spectrum (see Fig. 8.3b). There is excellent agreement¹ with the $n = 0.06$, and the shape would be noticeably distorted with even $n = 0.5$ photons present in the cavity. Another significant feature of the spectrum in Fig. 8.3b is the significantly reduced transmission of both peaks. In some sense, this is the strongest evidence that the states are truly the entangled states of a qubit and harmonic oscillator. The reason they are reduced is that the qubit (and thus the joint system) is very anharmonic, leading to inhomogenous broadening and also decay into a non-radiative bath. Because the excitation is shared between the two systems, the decay of the qubit into non-radiative channels “eats” the photons, and the inhomogenous broadening scatters them into other frequencies filtered out by the heterodyne spectroscopy technique used. The qubit has in effect stolen some of the photons from the cavity, which reduces the overall transmission significantly.

8.1.2 Vacuum Rabi Mode Splitting With Transmon

The strong coupling limit can also be reached using the transmon (see Fig. 8.4). Though the principles of the experiment are similar, there are several differences from the previous experiment. The transmon itself is quite different, having effectively no bias charge dependence due to the ratio of $E_J = 9.1$ GHz and $E_C = 371$ MHz with $E_J/E_C = 24$. The flux bias is much more stable than the charge bias as there appear to be no large fluctuations due to local sources. Therefore the avoided crossing in flux (see Fig. 8.4a) was measured with much higher resolution. In addition, the vacuum Rabi splitting, $2g = 228$ MHz is more than an order of magnitude larger than the previous result (see Fig. 8.4a). In the previous experiment, the transmission was significantly reduced by absorption and scattering to out-of-band frequencies by the qubit. In order to avoid this problem, and allow efficient generation of single photons (see Sec. 9.3), we significantly increased the output coupling

¹While $n = 0.06$ was used in the plot, this should not be construed as a lower bound on the photon number as the spectrum is normalized and smaller n's might also fit well.

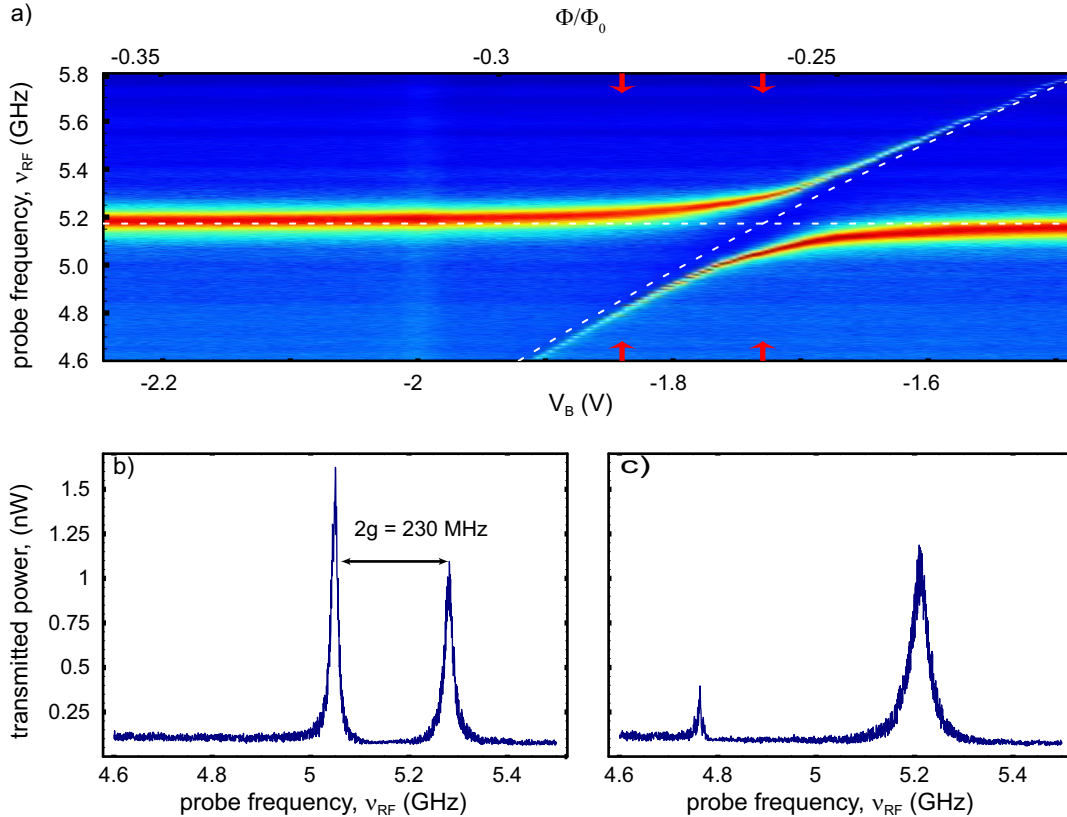


Figure 8.4: **a)** A transmon qubit has its transition frequency, ν_a , tuned through the resonator frequency, ν_r , and the vacuum Rabi coupling results in an avoided crossing. The transition frequency, by modulating the Josephson energy E_J by applying a small magnetic flux. The color represents transmission (blue is low, red is high) of a probe beam at ν_{RF} . The dashed white curve shows the transition frequency as a function of Φ_B/Φ_0 , of an uncoupled cavity and qubit ($g = 0$). The solid white line shows the expected transition frequencies from the ground state to first and second excited states of the strongly coupled cavity-qubit system (with $2g = 228$ MHz). The asymmetry in these peaks is not well understood and is thought to be due to a parasitic resonance on the circuit board. **b)** Transmission spectrum when qubit and cavity are degenerate ($\Delta = \nu_a - \nu_r = 0$), showing vacuum Rabi mode splitting. **c)** Transmission spectrum for cavity-qubit system when $\Delta = 550$ MHz $> g$. The larger peak is mostly cavity while the smaller peak is mostly qubit with only a little bit of photon character (hence the smaller amplitude). The widths of the two lines are $\kappa = 42.9$ MHz for the larger one, and $\gamma = \gamma_\perp + \gamma_\kappa = 2.5$ MHz + 1.85 MHz ≈ 4 MHz. The qubit-like state is slightly broader on the low frequency side of the cavity because its E_J/E_C ratio is smaller making it more sensitive to charge noise.

of the cavity, with $\kappa/2\pi = 43$ MHz. Because the cavity decay rate is much greater than the rate ($\gamma/2\pi = 2.5$ MHz) at which the qubit decays¹, nearly all of the excitations should decay as photons. To ensure that all photons are emitted into the amplifier, the cavity was made asymmetric, with much larger coupling to the output side than the input side.

In comparing the resonant case (see Fig. 8.4b), having $\Delta = 0$, to the dispersive case (see Fig. 8.4b), with $\Delta = 550$ MHz $> g$, one can immediately see that the (larger) peaks are nearly the same size, in both cases indicating that few of the photons are being absorbed or scattered significantly by the qubit. Unfortunately, one also immediately notices that as in the degenerate case (see Fig. 8.4b) the two peaks are asymmetric. While the exact cause of this is unknown, it is thought to be due to a low Q parasitic resonance, which gives some frequency structure on the 200 MHz scale of the vacuum Rabi splitting. The amplitude difference in the dispersive trace (see Fig. 8.4c) is not an artifact, but is actually a direct observation of the Purcell effect [Purcell1946]. The large peak (right) is the state which is mostly cavity and thus easily visible. The small state (left) is the qubit, normally invisible to direct detection, but it can be seen because it acquires a small photonic component. Because the dipole coupling, $g \sim \Delta$, and the cavity decay rate, κ , is so large compared to γ_{\perp} , the indirect decay through the cavity $\gamma_{\kappa} = (g/\Delta)^2 \kappa$ becomes the dominant decay mechanism, even though $g/\Delta \sim 1/5$. The qubit excitations are emitted into the output line and fed to our amplifier where they contribute to the spectrum. This effect will be the basis for an on-demand single photon generator.

One good way to quantify the wavefunction overlap between the qubit and cavity is to look at the peak widths. When the state is qubit-like the linewidth should approach γ , while the linewidth of cavity-like states should approach κ . The peak information is extracted by fitting a lorentzian to a small region around the modeled peak locations in figure 8.4a for each branch. The level separation and peak widths are plotted in figure 8.5. The minimum level separation gives the vacuum Rabi splitting ($2g = 228$ MHz), for a strong coupling ratio $4g/(\gamma + \kappa) = 10$. The peak widths can be examined closely in figure 8.5b, and show the qualitatively correct behavior. There is some asymmetry in the widths as well as the amplitudes and this may also be due to the same parasitic resonance, either directly or indirectly due to small amplitude induced errors in the fit.

It is also interesting to look at the vacuum Rabi splitting as a function of input power (see

¹The linewidth is a conservative measure of the decay rate, as it is also affected by dephasing. In fits to time domain data (see Fig. 9.8) it is likely that the actual non-radiative decay rate is closer to $\gamma_{\perp} = 200$ kHz corresponding to $T_1 \approx 800$ ns.

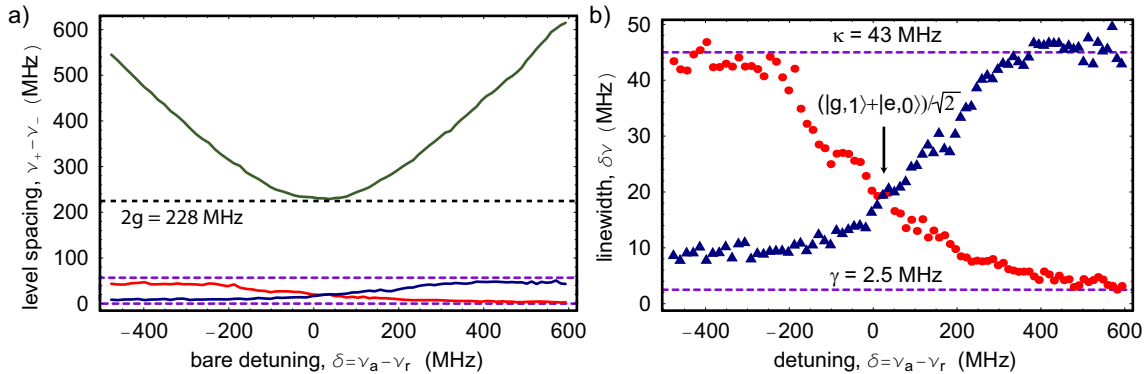


Figure 8.5: **a)** Level separation (solid green) between first and second excited states of joint cavity-qubit system. The minimum level separation is a direct measure of the vacuum Rabi splitting $2g = 228$ MHz. Below on the same scale, are the linewidths of the first (blue) and second (red) excited states, as a function of the bare detuning Δ . **b)** shows the linewidths of the first (blue triangles) and second (red circles) excited states as a function of detuning. The width gives an indication of the amount of wavefunction overlap, with small linewidth indicating the excitation is mostly qubit, and large linewidth indicating mostly cavity.

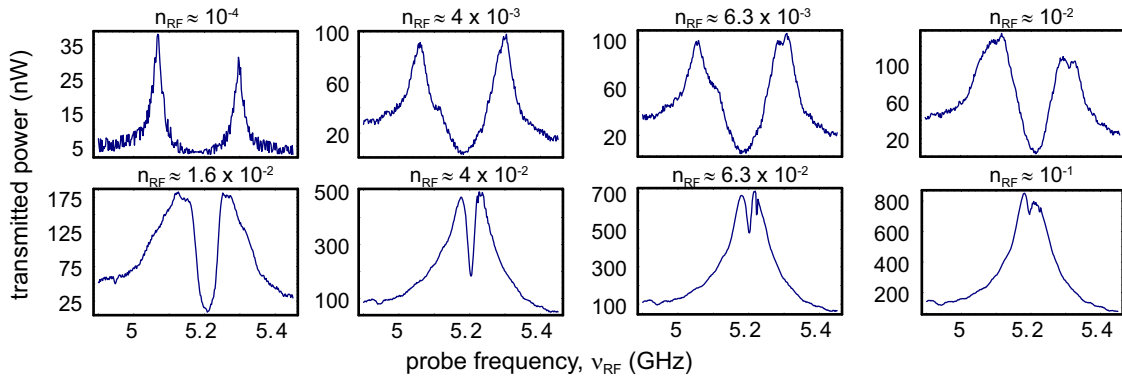


Figure 8.6: Plots of the transmission spectrum at $\Delta = 0$ at different drive powers. The powers are referenced to the output and displayed in terms of n_{RF} given by the relation $P_{RF} = \hbar\omega_r n_{RF}\kappa$. They should not be confused with the actual photon occupation of the cavity which can be much smaller or larger depending on the probe frequency ν_{RF} . At low powers the vacuum Rabi splitting splitting is clearly visible. At higher powers inherited non-linearity from the qubit causes the peaks to become inhomogeneously broadened. At intermediate powers additional bumps in the spectrum are suggestive of multiphoton transitions to higher excited states.

Fig. 8.6). The first thing one notices is that, unlike a harmonic oscillator, the peaks are inhomogeneously broadened with power. This is consistent with a harmonic oscillator coupled to a highly non-linear system, like a qubit, and is further evidence that this is not simply the avoided crossing of two harmonic oscillators. Also note that this non-linearity sets in at what seem to be very small photon numbers, but due to the non-linear nature of the cavity-qubit system, even small drives can quickly saturate the system. In the range of $4 - 6 \times 10^{-3}$ photons, there is a small bump inside the main peaks, suggestive of multiphoton transitions to the next excitation manifold which is split by $2\sqrt{2}g$. Quantitative predictions were not made for this sample due to the inability to model the asymmetry properly and also because while this data is suggestive, it is not clean enough to be definitive. Further experiments might understand this better, using a slightly higher Q resonator perhaps with $\kappa \sim 5 - 10$ MHz and a similar (or ideally better) qubit. To see the higher levels, one could also use an additional tone to populate the first excited state, and then measure transitions from that to the two excitation manifold. This was attempted briefly but without much initial success, in the same sample.

8.2 Dispersive Weak Limit

In this section we will discuss experiments in the dispersive limit, where the qubit is detuned from the cavity by much more than the vacuum Rabi frequency ($\Delta \gg g$). The focus will be to study the effect of the cavity photons on the qubit. We will study the AC Stark effect and show how it is responsible for the measurement backaction. After explaining this backaction using both a first order model, and adding non-linear corrections, we demonstrate a technique to AC Stark shift the qubit transition frequency without any dephasing. Such a tool could in principle allow the creation of a phase gate, or be used to move the qubit in or out of resonance with the cavity or another qubit. The resonant limit reveals the qubit-photon coupling very directly, but because the qubit and cavity are so strongly coupled, it is difficult to work them independently at small detunings. In the section on sidebands, we hope to regain the ability to make joint transitions, but with the coupling controlled by an RF tone, which can be switched on or off at gigahertz speeds.

8.2.1 AC Stark Effect

In the chapter 7 on characterization, we saw the effect on the cavity of having a qubit inside. In this section, the effect of the cavity photons on the qubit will be explored. The Jaynes-Cummings

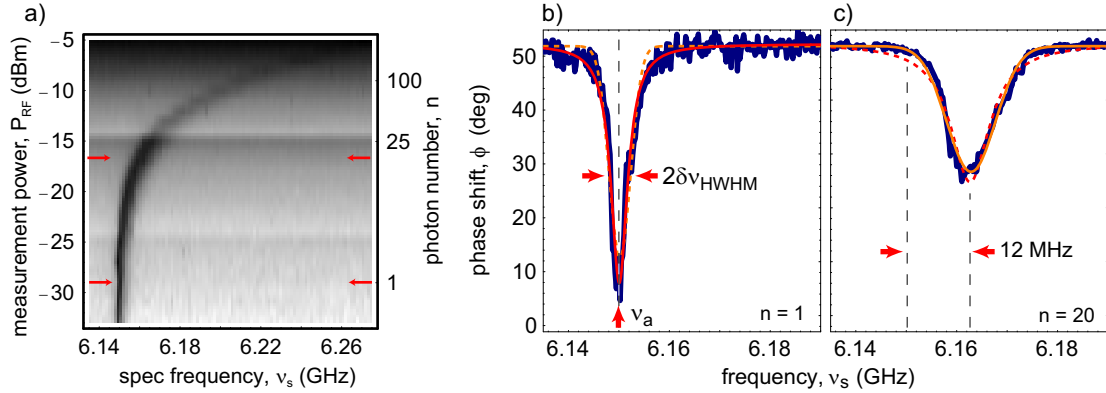


Figure 8.7: a) Density plot showing transmitted phase shift (dark is negative, white is positive) as function of spectroscopy frequency, ν_s , and measurement drive power, P_{RF} . The dip corresponding to the qubit transition frequency is AC Stark shifted as the power is increased. Discontinuities are due to phase delays when switching attenuators, and are not due to the physics of the system. b) Slice at $n_{RF} \approx 1$ and fits. The dephasing rate is given by the linewidth, $\delta\nu_{HWHM}$. c) A slice at $n_{RF} \approx 20$, which is AC stark shifted by 12MHz. It is also significantly broadened when compared to the $n_{RF} = 1$ lineshape. At low intracavity photon numbers the lineshape is predicted to be Lorentzian while at high photon numbers it should be Gaussian. In both plots the red is a fit to a Lorentzian lineshape, while the orange is a fit to a gaussian, and the solid is expected to be the correct choice. The Lorentzian to Gaussian crossover is certainly noticeable in these two plots.

Hamiltonian in the dispersive limit is as derived in chapter 2,

$$H \approx \hbar\omega_r (a^\dagger a + 1/2) + \frac{\hbar}{2} \left(\omega_a + \frac{2g^2}{\Delta} a^\dagger a + \frac{g^2}{\Delta} \right) \sigma_z \quad (8.1)$$

The quantity $\omega'_a = \omega_a + \frac{2g^2}{\Delta} a^\dagger a + \frac{g^2}{\Delta}$ can be interpreted as the dressed frequency of the qubit, which is shifted by $2\chi \approx 2g^2/\Delta$ per photon in the cavity. By changing the power of the measurement, we can easily vary the average number of photons $\bar{n} = \langle a^\dagger a \rangle$. Figure 8.7 shows spectroscopy of the qubit at different RF powers. Two effects are immediately noticeable. The qubit response peak can be shifted by many linewidths, and it also gets much broader.

First, let us investigate the mean behavior. For the powers shown in figure 8.8a, the Stark shift is proportional to the input power. Because the vacuum Rabi coupling $g/2\pi = 6$ MHz is known, and the Δ can be determined from the y-intercept of the figure 8.8a, one can calculate the Stark shift per photon to be $2\chi = 2g^2/\Delta = 2\pi 0.6$ MHz. That means that the Stark shift per photon is almost as large as the qubit linewidth $\chi \sim \gamma_2$. The Stark shift per photon, 2χ also corresponds to the slope of the line in figure 8.8a. This provides a calibration for the power of a single photon, which in this case is $P_{RF}(\bar{n} = 1) = -29$ dBm with the 63 dB and 40 dB of cold and warm attenuation, giving an input power at the resonator of $\sim 5 \times 10^{-17}$ W which is within a few dB of predictions based

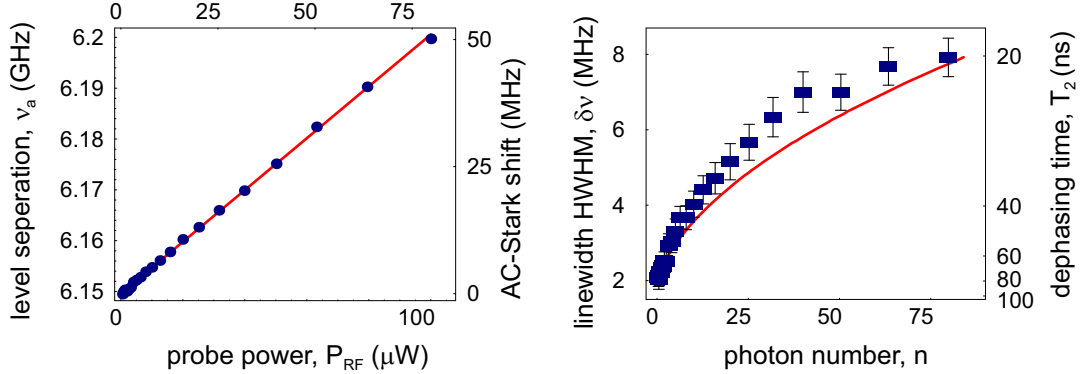


Figure 8.8: **a)** Measured qubit level separation $\tilde{\nu}_a$ and fit (solid line) *vs.* input microwave probe power P_{RF} . The ac-stark shift and the intra-resonator photon number n extracted from the fit are also indicated. **b)** Measurement broadened qubit line width $\delta\nu_{\text{HWHM}}$ *vs.* n_{RF} . Error bars are reflecting estimated systematic uncertainties in the extracted line width. The corresponding total dephasing time $T_\varphi = 1/2\pi\delta\nu_{\text{HWHM}}$ is also indicated. The solid line is obtained from Eq. 8.3 with a spectroscopy power broadened $T'_2 \approx 80$ ns.

on explicit attenuations. The remaining is likely due to reflections from connectors and launching onto the circuit board. This method is used to calibrate the power in terms of intra-cavity photon number in each experiment.

If figure 8.8a describes the mean behavior of cavity photons, then figure 8.8b gives insight into the photon quantum fluctuations δ_n about that mean. When we drive the cavity, we use a coherent signal, which does not create a photon number state in the cavity. Rather, it creates a Poisson distribution of photons, which have fluctuations of order \sqrt{n} . These fluctuations in photon number translate into fluctuations in the qubit precession frequency. One can make this notion quantitative, by defining the phase accumulated due to the AC Stark effect as,

$$\varphi(t) = \frac{2g^2}{\Delta_{a,r}} \int_0^t dt' \delta n(t') \quad (8.2)$$

The linewidth which can be thought of as a dephasing rate, is thus related to the correlator of photon number $\langle \delta n(t)\delta n(0) \rangle$. If the Stark shift per photon is not too large ($\chi < \gamma$) then one can make a gaussian approximation [Gambetta2006] yielding the absorption spectrum

$$\tilde{S}(\omega) = \frac{1}{2\pi} \sum_j \frac{(-\frac{2\tilde{\Gamma}_m}{\kappa})^j}{j!} \frac{\frac{1}{2}\tilde{\Gamma}_j}{(\omega - \tilde{\omega}_a - 2\bar{n}\chi)^2 + \left(\frac{1}{2}\tilde{\Gamma}_j\right)^2} \quad (8.3)$$

where $\tilde{\Gamma}_j = 2(\gamma_2 + \tilde{\Gamma}_m) + j\kappa$. The spectroscopic line shape is given by a sum of Lorentzians, all

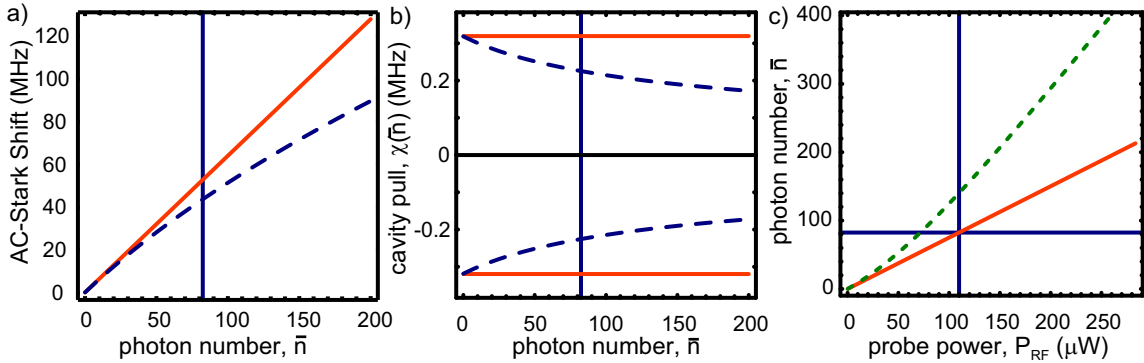


Figure 8.9: a) solid, red curve: ac-Stark shift as a function of the average intra-cavity photon number using the lowest order dispersive approximation. Dashed, blue curve: ac-Stark shift as a function of photon number calculated from the exact eigenvalues of the Jaynes-Cummings Hamiltonian. b) Cavity pull as a function of average photon number \bar{n} . The red solid line is the result of the dispersive approximation ($\pm\chi$) while the dashed blue curve is obtained from the exact eigenvalues of the Jaynes-Cummings model. c) Average photon number as a function of input power. The full red line is the result of the lowest order dispersive approximation 8.4 fit to the data in (b) at low power. The dotted green line is the non-linear model with χ replaced by $\chi(\bar{n})$ in 8.4. The vertical line in all plots indicates the critical photon number $n_{\text{crit}} = \Delta^2/4g^2$ which indicates the scale at which the lowest order dispersive approximation breaks down. For the experimental parameters $n_{\text{crit}} \sim 82$ which corresponds (within the lowest order dispersive approximation) to $P_{\text{RF}} \sim 110 \mu\text{W}$ corresponding to about 10^{-15} W at the input of the resonator .

centered on the ac-Stark shifted qubit transition but of different widths and weights. From Eq. 8.3 we see that if the measurement rate $\tilde{\Gamma}_m$ is much smaller than the cavity decay rate $\kappa/2$, then only a few terms in the sum contribute and the spectrum is Lorentzian, with width $\tilde{\Gamma}_m \approx 2\bar{n}\kappa\theta_0^2$ where $\theta_0 = 2\chi/\kappa = 2g^2/\Delta\kappa$ the ground-excited state phase shift. On the other hand, when the measurement rate is fast compared to the cavity damping, the spectrum will be a sum of many Lorentzians, resulting in a gaussian profile, with a standard deviation $\sigma = \sqrt{\bar{n}}\kappa\theta_0$. In this situation, dephasing occurs before the cavity has had time to significantly change its state, leading to inhomogeneous broadening. This Lorentzian to Gaussian crossover is evident in figures 8.7b-c.

The expression 8.3 for the spectrum can be summed analytically but yields an unsightly result which is not reproduced here. To compare with the experimental results, we evaluate numerically the half-width at half maximum from $S(\omega)$. The results are plotted as a function of probe power in figure 8.8 (red line). The agreement with the experimental results (symbols) is good, especially given that there are no adjustable parameters apart from γ_2 which only sets the value of the dephasing at $\bar{n} = 0$.

The measured AC-Stark shift is remarkably linear. While one expects linearity at low powers,

there should be some non-linearity due to higher order corrections to the simple dispersive Hamiltonian of Eq. 8.1. In this case, the apparent linearity masks competing non-linear effects. In the lowest order dispersive approximation (Eq. 8.1), the predicted ac-Stark shift $\omega_{\text{AC}} = 2\chi\bar{n}$ will be a linear function of the mean photon number, \bar{n} . However, this approximation only holds at low photon numbers, and breaks down on a scale given by the critical photon number $n_{\text{crit}} = \Delta^2/4g^2$ [Blais2004]. This is illustrated in Fig. 8.9a where the ac-Stark shift, calculated from the lowest order dispersive approximation (red solid line) and the exact eigenvalues (blue dashed line) of the Jaynes-Cummings model [Blais2004] are plotted for the experimental parameters. Also shown in this figure is n_{crit} (vertical blue line) which for the experimental parameters is about 82 photons. Here we see that as \bar{n} increases, the exact Stark shift begins to fall below the lowest order dispersive approximation even before \bar{n} reaches n_{crit} .

In Fig. 8.9b, the experimental results (solid blue points) are plotted as a function of probe power, P_{RF} (extending up to powers larger than those presented in Fig. 8.8). To convert between \bar{n} and P_{RF} , we assume that $P_{\text{RF}} = \lambda\hbar\omega_{\text{RF}}p$ where p is the photon flux at the resonator and λ is a scaling factor that takes into account the large attenuation that is placed between the probe generator and the resonator (to eliminate black body radiation). From the lowest order dispersive approximation, the average photon number when driving the cavity at $\Delta_r = 0$ is

$$\bar{n} = \frac{p\kappa/2}{(\kappa/2)^2 + \chi^2}. \quad (8.4)$$

By using the lowest order dispersive approximation for the ac-Stark shift and the line of best fit to the experimental points (in the linear regime at low power), λ can be determined. Doing this gives the red solid line in Figs. 8.9b and d. The calibration shows that n_{crit} occurs at $\approx 110 \mu\text{W}$. The experimental results clearly show the breakdown of the lowest order dispersive approximation. The data points fall below the linear prediction, but not nearly as much as the blue dashed curve in (a) predicts. In fact, the data points follow fairly closely the linear in \bar{n} dependence of the lowest order dispersive approximation in 8.1 for larger powers than expected (up to and well above n_{crit}).

It is possible to understand why the experiment agrees with the simple dispersive approximation for larger probe powers than expected by considering the following simple model. We assume that, at these large powers, the ac-Stark shift is still given by the dispersive approximation $2\chi\bar{n}$, but we now take into account the non-linear cavity pull (which is χ at low \bar{n}). From the eigenvalues of the Jaynes-Cummings Hamiltonian the cavity pull can be calculated as a function of \bar{n} . This is shown

in Fig. 8.9b. From this figure, we see that the cavity pull reduces as the number of photons in the resonator is increased. We thus replace χ by $\chi(\bar{n})$. The second aspect of our simple model is the non-linear dependence of the average photon number \bar{n} with input power P due to the power-dependence of the cavity frequency. To account for this we simply replace χ in Eq. 8.4 with $\chi(\bar{n})$ and \bar{n} becomes a non-linear function of input power. This non-linear dependence of the photon number on the input power is illustrated in Fig. 8.9c as the green dotted line. This is a precursor to bistability in this system [Walls2006]. Using these two expressions, we have for our simple model of the non-linear ac-Stark shift $2\chi(P)\bar{n}(P)$. This expression is plotted in Fig. 8.10a (green dotted line) with a new scaling factor $\lambda' \approx 0.905\lambda$ calculated by the best fit for the experimental data (here we use the complete data set). This simple model produces a result that is linear for a larger range of powers and is closely consistent with the experimental results. It happens that for the particular experimental parameters, the two non-linear effects almost cancel each other out and result in the green dotted line being more linear than expected. Comparison with the results of the non-linear model shown here in Fig. 8.9c, shows that the calibration of the cavity photon number in terms of the drive power is low by approximately 50% at the highest power, for the simple linear model used in Fig. 8.8. It should be emphasized that the treatment here of the non-linearities is only approximate.

8.2.2 Off-Resonant AC Stark Effect

Study of the AC-Stark effect, created by measurement photons in the cavity, elucidates the role of photon number fluctuations in dephasing the qubit. The ability to manipulate the qubit transition frequency by application of an RF tone could be very useful in the construction of conditional phase gates. When resonant cavity photons are used to measure the qubit state, corresponding qubit dephasing is demanded by the uncertainty principle. So in order to make a coherent gate one must use a tone which does not measure the qubit state (and can thus avoid dephasing it). If the Stark shifting tone at ν_{AC} , is applied at a detuning from the resonator, $\delta_{AC} = \nu_{AC} - \nu_r$, that is much larger than the state-dependent cavity pull, $2\chi \approx 2g^2/\Delta$, then it will not reveal much information about the qubit state, and also not cause much dephasing. Quantitatively, the information leakage

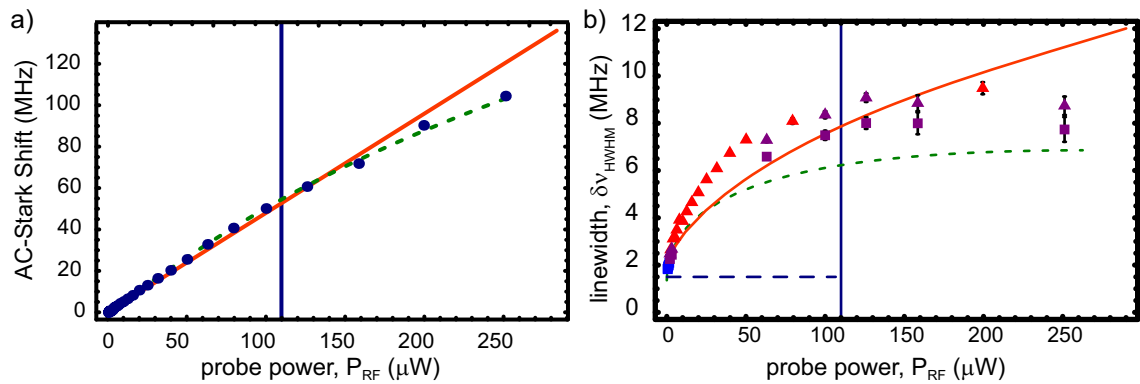


Figure 8.10: **a)** AC Stark shift as function of input power P_{RF} . Includes points past $n_{\text{crit}} \approx 110 \mu\text{W}$ (indicated by vertical blue line) with fits to the simple dispersive approximation (solid red line) and a model which includes non-linearity of the photon number in input power as well as the reduction in Stark shift per photon at high photon numbers. Blue dots: experimentally measured ac-Stark shift as a function of external microwave input power. The conversion factor from photon number to external microwave drive power was determined by fitting the red curve to the linear portion of the data at low power. Green, dotted curve: Same as red but taking into account the non-linear reduction in the cavity pull (see Fig. 8.9b) and the non-linear increase in the average photon number (see Fig. 8.9c) with microwave drive power. For the particular experimental parameters these two effects almost cancel each other out and result in the green dotted line being nearly linear out to much greater input powers than expected. **b)** Measurement broadened qubit line width $\delta\nu_{\text{HWHM}}$ as a function of the input measurement power or average photon number as predicted by the lowest order dispersive approximation (solid red). Dispersive prediction with a non-linear reduction in the cavity pull and plotted as a function of input power (dotted green). The symbols are the experimental results. Symbols and color scheme are described in the text. The vertical line indicates the critical photon number n_{crit} . The blue dashed line is the calculated HWHM for $\Delta_R/2\pi = 32$ MHz. It clearly shows that measurement induced dephasing is small at large Δ_R where information about the state of the qubit in the transmitted signal is also small and should be compared with the experimental measurement in Fig. 8.13.

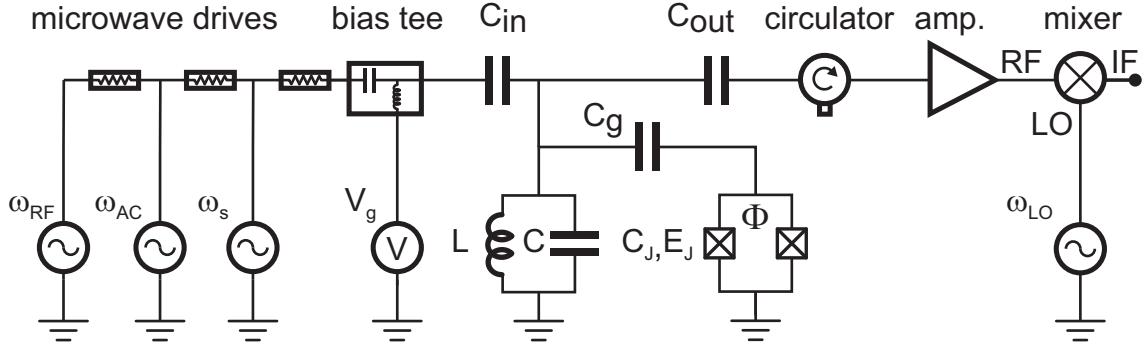


Figure 8.11: The qubit is measured via the digital homodyne technique, using a weak tone ω_{RF} , at the cavity frequency, and comparing it to a local oscillator ω_{LO} . A spectroscopy tone at ω_s is used to interrogate the qubit state and transition frequency. In addition a new tone at ω_{AC} is applied at a small detuning from the cavity δ_{AC} , to modify the qubit transition frequency, or help excite sideband transitions.

rate due to the Stark photons is given by Eq. 3.93, which is approximately¹

$$\Gamma_m = \frac{2\bar{n}\chi^2\kappa}{\delta_{AC}^2 + (\kappa)^2/4 + \chi^2} \quad (8.5)$$

For given experimental parameters the Stark shift is given by $2\bar{n}\chi$. Therefore we can define a dimensionless Stark dephasing factor

$$\frac{2\bar{n}\chi}{\Gamma_m} = \frac{\delta_{AC}^2 + \kappa^2/4 + \chi^2}{\chi\kappa} \quad (8.6)$$

By using a suitably large detuning this can be approximated as δ_{AC}^2/χ , which can be made quite large. Adjusting the amplitude accordingly it is possible to get a large AC Stark shift without any noticeable dephasing. By setting $\delta_{AC} \rightarrow 0$ in Eq. 8.5, we can recover the earlier (weak measurement) result, $\kappa/4\chi = 1/2\theta_0$. To perform such experiments, we use a weak measurement tone at the resonator frequency as a probe, while adding an additional generator to produce the AC Stark tone (see Fig. 8.11). The Stark tone detuning is chosen such that it is large enough to not dephase the qubit substantially, while also not filtered so strongly that the input power required heats the cryostat (see Fig. 8.12).

To observe the off-resonant Stark effect, one performs the same types of experiments, but in place of the RF measurement power, P_{RF} , one sweeps the AC-Stark power, P_{AC} as shown in figure 8.13. When one can compares figure 8.13 with figure 8.7, one immediately sees that for an even larger

¹In Eq. 3.93 Γ_m is written in terms of n_+ and n_- which are the average photon numbers in the ground or excited state. Since for the large detunings $\delta_{AC} \gg \chi$ or very small detunings $\delta_{AC} \ll \kappa$ $\bar{n} \approx n_+ \approx n_-$ we use $n_+ + n_- \rightarrow 2\bar{n}$ for simplicity.

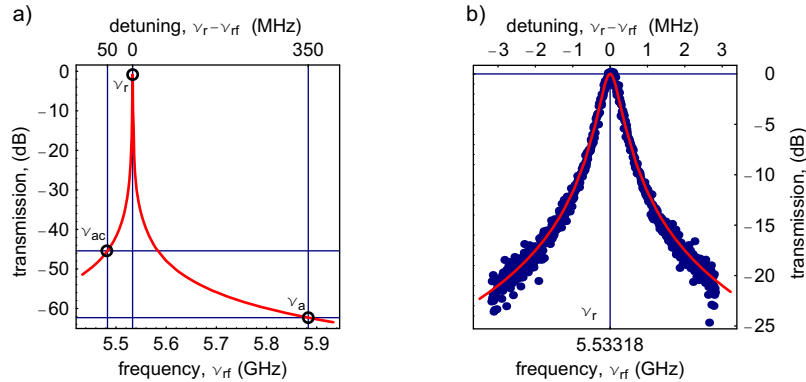


Figure 8.12: **a)** Calculated lorentzian cavity transmission spectrum over large frequency range. The cavity drives at frequencies $\nu_s \approx \nu_a$, $\nu_{RF} \approx \nu_r$ and ν_{AC} and the cavity transmission at these frequencies are indicated. **b)** Measured cavity spectrum (dots) and lorentzian fit (line) around cavity resonance frequency.

Stark shift (32 MHz vs. 12 MHz) the linewidth remains essentially unchanged. By fitting the peaks as a function of P_{AC} we can extract the dressed transition frequency and linewidth (see Fig. 8.14). This shows that the line can be shifted by many linewidths without any significant broadening, meaning that it could be used to create a coherent phase gate.

8.2.3 Sideband Experiments

In the resonant limit, the cavity-qubit coupling directly manifests itself in the form of vacuum Rabi splitting, which naturally creates coherent oscillations between a qubit excitation and a photon. Unfortunately, it can be difficult to control these oscillations¹. In the dispersive limit, the system exists as an independent qubit and cavity, with state-dependent dressed states, rather than real transitions as evidence of their interaction. The ability of cavity QED to convert a qubit excitation into a cavity photon, spontaneous in the resonant case, requires stimulation in the dispersive regime. One natural way of driving a qubit-photon transition, is to exploit the state-dependence of the qubit and cavity frequencies, using energy conservation to make a simultaneous change of qubit state and photon number. Such sideband transitions allow one to switch the qubit-cavity coupling on and off using an RF pulse. This can be done with very high contrast and on nanosecond timescales.

More concretely, imagine applying an RF tone at $\omega_{\text{red}} = \omega_a - \omega_r$, which would drive a transition

¹This is mainly due to our current experimental configuration which has heavily low-passed (< 5 MHz) electrostatic gates, and extremely (unintentional) strong magnetic low passing (< 1 Hz) due to inductive shielding of the very high conductivity OFHC copper sample holder. Fast flux control will be added in future experiments, which will make control substantially easier by tuning the qubit transition frequency on timescales comparable to the vacuum Rabi coupling rate.

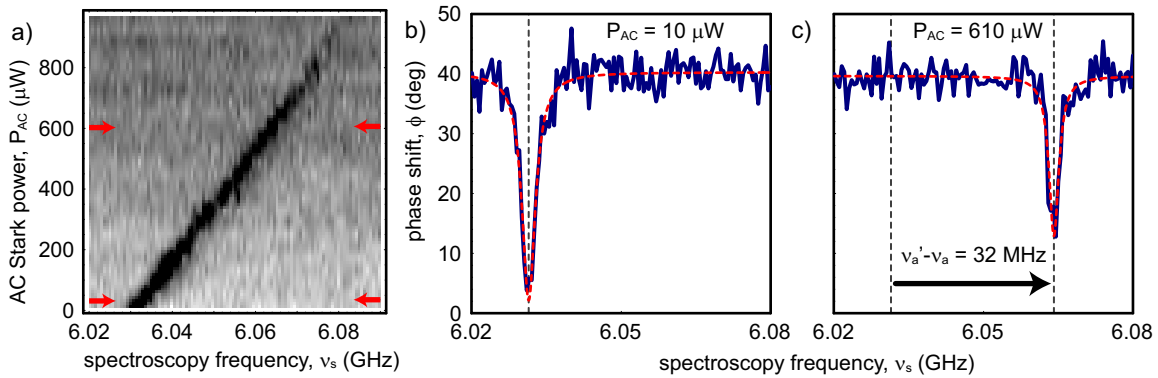


Figure 8.13: a) Density plot of spectroscopy taken as a function of the power of the AC stark tone, ω_{AC} . The tone is detuned by $\delta_{AC} = \omega_{AC} - \omega_r = -50 \text{ MHz}$, and so does not excite any real photons in the cavity. b) Slice taken at $P_{AC} = 10 \mu\text{W}$, where the AC Stark shift shift is negligible. The linewidth is due to power broadening by the spectroscopy tone and the intrinsic qubit dephasing. c) Slice taken at $P_{AC} = 610 \mu\text{W}$, showing that the qubit transition has been shifted by $\nu_a' - \nu_a = 32 \text{ MHz}$, without significant broadening.

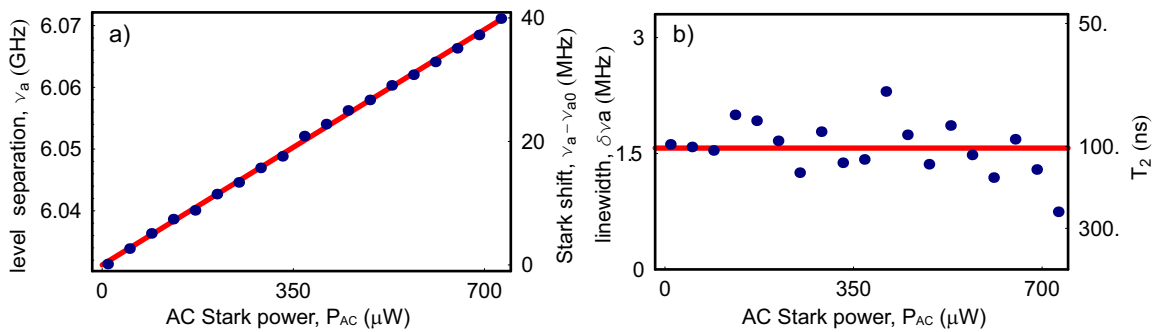


Figure 8.14: a) Plot of the AC-Stark shift as function of Stark tone power P_{AC} . The qubit transition frequency is shifted by more than 30 linewidths. b) Plot of linewidths/ T_2 , which essentially do not change in the experimental power range. The linewidth is limited by the intrinsic dephasing rate and power broadening due to the spectroscopy tone.

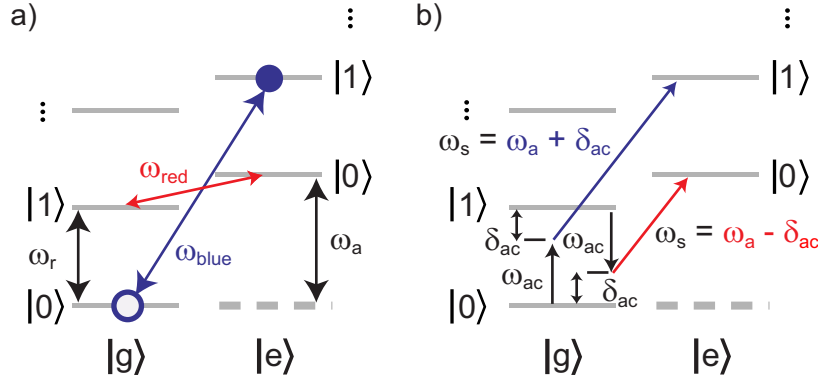


Figure 8.15: Qubit-cavity energy levels illustrating sideband transitions. **a)** Illustration of direct sideband transitions from $|g, 0\rangle \rightarrow |e, 1\rangle$ at $\omega_{\text{blue}} = \omega_a + \omega_r$ and from $|g, 1\rangle \rightarrow |e, 0\rangle$ at $\omega_{\text{red}} = \omega_a - \omega_r$. **b)** At the CPB charge degeneracy point ($n_g = 1$) where the qubit is most coherent, direct sideband transitions are forbidden by a parity selection rule. Sidebands transitions can still be driven by using two tones, at ω_{AC} and ω_s . Two-photon transitions can occur when the sum ($\omega_{\text{AC}} + \omega_s = \omega_{\text{blue}}$) or difference ($\omega_{\text{AC}} + \omega_s = \omega_{\text{red}}$) of these tones satisfies energy conservation.

between $|e, n - 1\rangle$ and $|g, n\rangle$, effectively converting a qubit excitation into a photon (see Fig. 8.15). Energy conservation demands that the photon number and qubit state are changed simultaneously. Similarly driving at $\omega_{\text{blue}} = \omega_a - \omega_r$, one can couple $|g, n\rangle$ and $|e, n + 1\rangle$, which adds or subtracts a photon and a qubit excitation. These transitions are particularly special when the system starts in the ground state, $|g, 0\rangle$. In that case, only the blue sideband is allowed, as there is no state, $|e, -1\rangle$, that would satisfy energy conservation. Similarly, when the system starts in the $|e, 0\rangle$ state, only the red sideband is allowed, as there is no $|g, -1\rangle$ state with which the blue sideband can couple. These “dark” states can act as the basis of quantum SWAP gate between a qubit and photon, using the following protocol. Assume the cavity is empty to start, then apply a π strength pulse on the red sideband. If the qubit is in the ground state, nothing will happen since a transition would require absorption of a photon which is not present (see 8.15). While the SWAP is a classical gate, using a $\pi/2$ pulse would create the entangled state, $(|e, n - 1\rangle + |g, n\rangle)/\sqrt{2}$ and could be used as the basis for universal quantum logic. Even the “classical” swap gate would allow the teleportation of a state between two qubits present in the cavity. This could be accomplished, by first swapping a qubit possessing an unknown quantum state into a photon. Then the other qubit, initialized to the ground state, could be swapped with the cavity photon (superposition) state, restoring the qubit in the new location. In a standard cavity, this could be done over distances ~ 1 cm.

Unfortunately, at the charge degeneracy point, $n_g = 1$, there is a parity selection rule that does

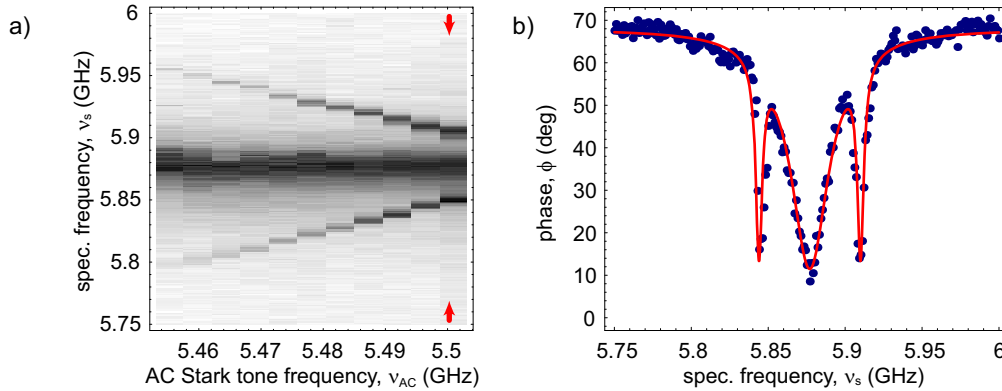


Figure 8.16: **a)** Density plot showing the spectrum near the qubit transition frequency, ν_a as a function of the (off-resonant) AC Stark tone frequency and spectroscopy frequency (at $P_{AC} = -20$ dB and $P_s = -14$ dB). The central line is the Stark shifted bare qubit transition. Also present are blue and red sidebands which result in a simultaneous change of the qubit state and the addition or subtraction of a photon from the cavity. **b)** A line cut of the spectroscopy near the qubit transition frequency, ν_a , at $\delta_{AC} = 50$ MHz. The sidebands are clearly visible.

not allow direct transitions involving an even number of energy quanta. Because of this it is not possible to do single tone sidebands as can be done with a flux qubit[Chiorescu2004]. However, two photon transitions are not forbidden and can be exploited to the same end. Nominally any two tones, which together satisfy the condition that $\omega_{AC} + \omega_s = \omega_{\text{red/blue}}$ or even a single tone at half the frequency $2\omega_s = \omega_{\text{red/blue}}$, can be used to create the sideband (see Fig. 8.15b). The strong filtering property of the cavity, encourages one to choose the tones such that one tone is relatively close to the cavity, $\omega_{AC} \sim \omega_r$, and the other is near the qubit transition frequency, $\omega_s \sim \omega_a$. One way to think about this is that, we know we can make transitions in the qubit and cavity with one beam at ω_r and the other ω_a . That is just normal spectroscopy, but in that case because each process is individually relevant, there are no correlations between the addition of a photon and the flipping of a qubit. By detuning both beams by δ_{AC} , but keeping the difference of the two beams fixed to Δ , energy conservation is only satisfied by simultaneous flips (see Fig. 8.15b). Thus the challenge is to detune as little as possible (to keep the rate high), while detuning by enough (so that there is no independent absorption).

In this experiment, a qubit with vacuum Rabi coupling strength $g/2\pi = 17$ MHz, is placed at one end of a $\omega_r/2\pi = 5.5$ GHz resonator with decay rate $\kappa/2\pi = 0.5$ MHz, at a detuning of $\Delta/2\pi \approx 350$ MHz $\gg g$. Figure 8.16b shows spectroscopy near the qubit, while a second tone drives the cavity at a detuning of $\delta_{AC} = -50$ MHz, and clearly shows the sidebands as well as the Stark

shifted direct qubit transition. This experiment is identical in setup to the off-resonant Stark effect, but now (using higher powers and larger detunings) we focus on the sidebands, rather than the Stark shift. The sideband spectroscopy is a line cut taken from the density plot of cavity transmission in response to a scan of the two beam frequencies, ω_s and ω_{AC} (see Fig. 8.16a). At the relatively low powers used in the scan, the sideband detuning is roughly proportional to the AC-Stark tone detuning δ_{AC} . At higher powers or smaller detunings significant non-linearities are present. These arise due to the Stark shifts, which necessarily accompany the two off-resonant tones at detuning of δ_{AC} and $\delta_{AC} + \Delta$. The resulting dressed atom frequency is given by

$$\omega'_a = \omega_a + 2\frac{\Omega_{AC}^2}{\omega_a - \omega_{AC}} + 2\frac{\Omega_s^2}{\omega_a - \omega_s} \quad (8.7)$$

which depends on the drive strengths $\epsilon_{ac,s}$ (expressed as frequencies) that we parameterize in terms of their Rabi frequencies

$$\Omega_{AC} = \frac{g\epsilon_{ac}}{\omega_r - \omega_{AC}} \quad (8.8)$$

$$\Omega_s = \frac{g\epsilon_s}{\omega_r - \omega_s} \quad (8.9)$$

That means that the correct frequencies for ω_s must be determined self consistently from the non-linear equation,

$$\omega_s = \omega'_a \pm \delta_{AC} \quad (8.10)$$

The drive amplitudes can be calibrated using the resonant AC-stark effect which gives the power for a single photon ($n = 1$) to be $P_{RF} = -28$ dBm, corresponding to a power at the input of the resonator of 1.2×10^{-17} . The cavity's lorentzian line shape then gives

$$n = \frac{\epsilon^2}{\Delta^2 + (\kappa/2)^2}, \quad (8.11)$$

where ϵ has units of frequency and is related to the incident photon put power by $\epsilon^2 = P_{in}/\hbar\omega$ and the output power is just $P_{out} = n\hbar\omega\kappa$.

Figure 8.17 plots the location of the qubit transition and its sidebands as a function of the detuning δ_{AC} and the power of the two beams. Figure 8.17a shows that the sidebands are nearly proportional to the detuning but begin to be shifted significantly at small detunings. This is in some sense an artifact of performing the scan at constant input power, rather than as a function of cavity occupation. This becomes clear when looking at 8.17b which shows the shift due to changes

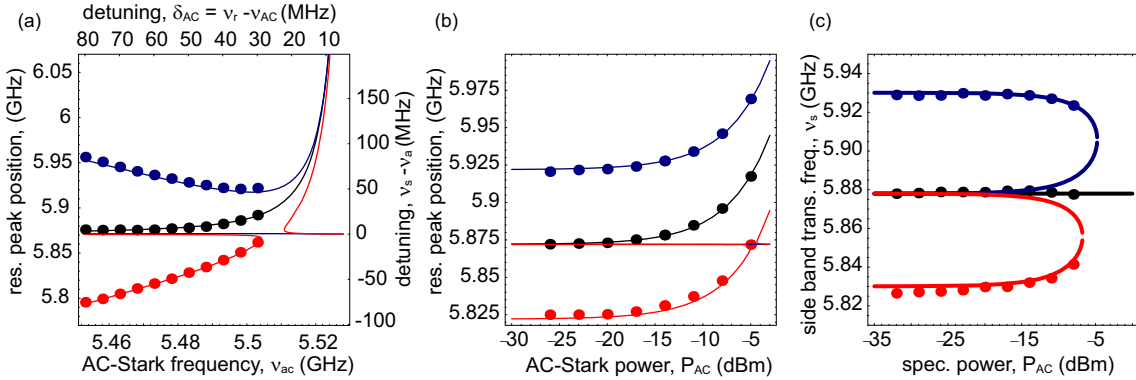


Figure 8.17: **a)** Two-tone red and blue sidebands (red/blue dots) and fundamental (black dots) qubit transition frequencies for fixed P_s and P_{AC} varying ω_{AC} . Lines are fits to Eqs. (8.7-8.11) **(b)** For fixed ω_{AC} , and varying P_{AC} . **(c)** For fixed ω_{AC} , P_{AC} and varying P_s . **(a-c)** All measurements are done at fixed measurement frequency $\omega_{RF} = \omega_r$ and power P_{RF} weakly populating the resonator with $n_{RF} \approx 2$ photons.

in amplitude. Finally we can see that ω_s is self-consistently matching Eq. 8.10, by monitoring the peak position as a function of the spectroscopy power, P_s , in figure 8.17b. The data fits remarkably well over two orders of magnitude of power in both the tones and to detunings which are nearly resonant with the cavity.

There were some aspects of the sidebands experiment that were unable to observe that would be very interesting to study in the future. One issue was the finite width of the direct qubit transition. Looking at figure 8.16b, one can see that though the sideband is well-resolved, there is some overlap between the direct transition (which is very power broadened at these amplitudes) and the sideband. For this reason, we were unable to observe any time domain oscillations associated with the sideband transitions. In future experiments, this could be addressed by increasing the coupling strength, which would allow larger detunings and smaller amplitudes. Of course, improving the qubit dephasing time would help immensely. Reducing the cavity decay rate, which can easily done by at least an order of magnitude, would allow one to operate at smaller detunings and drive the transition rates higher. It is also possible that another beam at the direct qubit transition could be used to compensate for the direct precession. Another interesting phenomena that we were unable to observe conclusively is the asymmetry of the red and blue sidebands when the system is in its ground state. Though in the ground state only the blue sideband should be allowed, we observed only a slight asymmetry between the two sidebands. This was likely due to photons in the cavity from the weak measurement, or possibly due to direct excitation of the qubit. A pulsed measurement protocol, would allow one

to eliminate the former possibility and the direct excitation could be reduced by the ways stated above.

8.3 Dispersive Strong Limit

In the dispersive limit, the cavity and qubit frequencies are shifted by their interaction, which is characterized by the shift per photon, 2χ . In the previous section, the dispersive coupling was relatively weak compared with the decoherence rates, resulting in a small state-dependent phase shift ($\chi < \kappa$) of the cavity and small AC Stark shift per photon ($\chi < \gamma$). Despite this, by using many photons, we were able to make a strong measurement of the qubit state and (equivalently) AC Stark shift the qubit by many linewidths. In principle, the quantum Stark Hamiltonian (Eq. 8.1) allows one to make a strong measurement of the cavity photon number state, using the qubit as well. Because there is only a single qubit, a measurement of the exact photon number requires each photon to shift the qubit by more than one linewidth, and for the number of photons to stay constant during the measurement, $\chi > \gamma, \kappa$. When this additional constraint is met, (and the dispersive condition $\Delta \gg g$) then one enters the strong dispersive regime, the hallmark of which is the ability to measure the photon number state of the cavity. When the qubit is so strongly coupled to the cavity, the anharmonic dispersive regime (see Fig. 8.1). The defining characteristic of this regime is that the second order non-linearity the cavity dispersively inherited from the qubit, leads to single-photon level anharmonicity, and inhomogeneous power broadening of the cavity.

8.3.1 Photon Number Splitting

In this experiment, we would like to make a quantum non-demolition (QND) measurement of cavity the photon number state using the AC Stark effect of those photons on the qubit. This measurement could be performed by driving the atom at its Stark shifted atom frequency $\omega_n = \omega_a + 2n\chi$ (see Fig. 8.18a), followed by an independent measurement of the atom state. If the atom is excited, then the field must have exactly n photons. Because the photon number is not changed in this process, the QND protocol can be repeated indefinitely. In practice, all measurements have some demolition, which limits the number of repetitions before the measurement process changes the measured variable (the number of photons). In our experiment, the cavity transmission is used to measure the atom state, so while the interaction is QND, the detection performed here is not. Any cavity QED experiment that employs a fixed coupling, will have demolition arising from the overlap of the atomic

and photonic wavefunctions, creating a probability, $(g/\Delta)^2$, that a measurement of photon number will absorb a photon or a measurement of the atomic state will induce a transition, demolishing the measured state. If the coupling strength, g , can be changed adiabatically the demolition can be substantially reduced[Gleyzes2007]. In that work despite having a ratio of $g/\Delta \approx 1$, the demolition was still $\sim 10^{-4}$, but in our current implementation g is fixed, and this limit applies.

In order for this measurement protocol to have single photon resolution, the Stark shift per photon must be greater than the qubit and cavity lifetimes, $\chi > \gamma, \kappa$. It has been proposed that the dispersive photon shift could be used to make a QND measurement of photon number state of the cavity using Rydberg atoms [Brune1990]. Previously attainable interaction strengths required photon number detection experiments to employ absorptive quantum Rabi oscillations in the resonant regime[Brune1996], allowing a QND measurement [Nogues1999], restricted to distinguishing only between zero and one photon. More recently, a non-resonant Rydberg atom experiment entered the strong dispersive limit, measuring the single photon Wigner function with demolition $(g/\Delta)^2 = 6\%$, in principle allowing ~ 15 repeated measurements [Bertet2002]. For the parameters in this experiment, $g/2\pi = 105$ MHz, and $\Delta = 1.2$ GHz it is possible to have a demolition less than $(g/\Delta)^2 < 1\%$, which should allow up to ~ 100 repeated measurements.

The primary innovation that allowed this experiment to succeed was the incredibly large vacuum Rabi coupling $g/2\pi = 105$ MHz afforded by the transmon which sees its first realization here. The dimensionless coupling strength $g/\omega = 2\%$ of the total photon energy. This approaches the fine structure limit (Eq. 3.79) and is 10^4 times larger than currently attainable in atomic systems, which allows the system to overcome the larger decoherence present in the solid-state environment. This experiment was capable of making $g/\gamma_{\text{eff}} = 40$ possible coherent vacuum Rabi oscillations in the strong resonant regime, where $\gamma_{\text{eff}} = (\gamma + \kappa)/2$ is the combined photon-qubit decay rate. The equivalent comparison, of the dispersive interaction to decoherence, examines the Stark shift per photon in relation to the qubit decay, $2\chi/\gamma = 6$, and determines the resolution of the photon number peaks. Comparing instead to the cavity lifetime yields an estimate of the maximum number of peaks that could possibly be resolved, $2\chi/\kappa = 70$, and determines the contrast of a qubit measurement by a single cavity photon. The charge stability of the transmon, though not the focus of this experiment, is attested to by signal-to-noise ratio in the data (see Fig. 8.19). The experiment would have also been far more difficult, if not impractical without this stability.

The photon number-dependent frequency shift of the qubit is detected by performing spec-

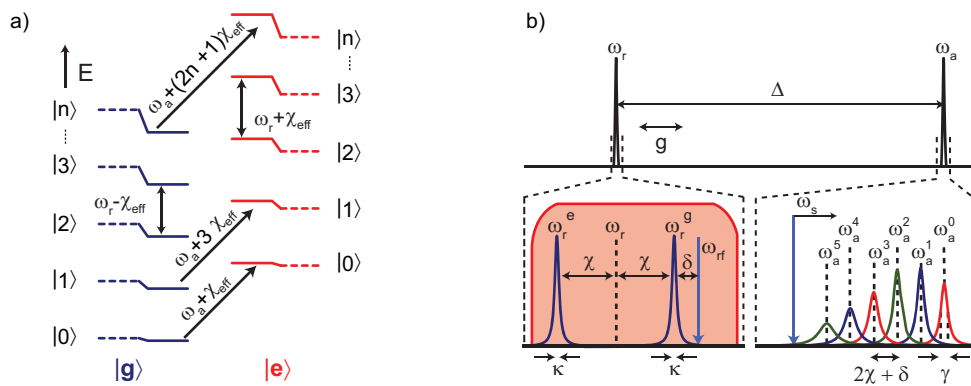


Figure 8.18: a) Dispersive cavity-qubit energy levels. Each level is labeled by the qubit state, $|g\rangle$ or $|e\rangle$, and photon number $|n\rangle$. Dashed lines are qubit/cavity energy levels with no interaction ($g = 0$), where solid lines show eigenstates dressed by the dispersive interaction. Transitions from $|n\rangle \rightarrow |n+1\rangle$ show the qubit-dependent cavity shift. Transitions at constant photon number from $|g\rangle|n\rangle \rightarrow |e\rangle|n\rangle$ show a photon number dependent frequency shift $2n\chi_{\text{eff}}$. b) Cavity-qubit spectral response. To measure the qubit state and populate the cavity, a coherent tone is driven at ω_{rf} (bottom left), which is blue detuned from the cavity by several linewidths, reducing any cavity nonlinearity. Thermal fields are generated with gaussian noise applied in the red envelope, spanning the cavity. The qubit spectrum (bottom right), is detuned from the cavity by $\Delta/2\pi = 1.2 \text{ GHz} \gg g/2\pi$. Information about photon number is measured by monitoring transmission at ω_{rf} while driving the qubit with a spectroscopy tone at ω_s . Each photon shifts the qubit transition by more than a linewidth ($\chi/2\pi > \gamma/2\pi = 1.9 \text{ MHz}$, $\kappa/2\pi = 250 \text{ kHz}$) giving a distinct peak for each photon number state. The maximum number of resolvable peaks is $2\chi/\kappa$.

troscopy on the qubit-cavity system (Fig. 8.18b). The cavity is coherently excited by applying a microwave signal (the cavity tone) at frequency (ω_{rf}) near the cavity resonance (Fig. 8.18b). A spectrum is taken by sweeping the frequency (ω_s) of a second microwave signal (the spectroscopy tone), which probes the qubit absorption, without significantly populating the resonator as it is detuned by many linewidths ($\omega_s - \omega_r \gg \kappa$). The detection is completed by exploiting the dual nature of the qubit-photon coupling, reusing the cavity photons as a measure of cavity transmission, as in Sec. 7.2, to measure the qubit excited state population. The measured transmission amplitude (Fig. 8.19) is an approximate measure of the actual qubit population, which could in principle be measured independently. For clarity, the transmission amplitude in Figure 8.19 is plotted from high to low frequency. In order to reduce non-linearities in the response, the cavity tone was applied at a small detuning from the resonator frequency when the qubit is in the ground state $\delta/2\pi = (\omega_{\text{rf}} - \omega_r^g)/2\pi = 2$ MHz which also slightly modifies the peak splitting[Gambetta2006] (Fig. 8.18b).

The measured spectra reveal the quantized nature of the cavity field, containing a separate peak for each photon number state (Fig. 8.19)[Gambetta2006, Irish2003]. These peaks approximately represent the weight of each Fock state in a coherent field with mean photon number \bar{n} , which is varied from zero to seventeen photons. At the lowest photon powers, nearly all of the weight is in the first peak, corresponding to no photons in the cavity, and confirming that the background cavity occupancy is $n_{\text{th}} < 0.1$. It is reasonable to wonder how one can measure a zero photon peak when information is only extracted from the cavity when photons are transmitted. The solution to this apparent paradox is that the qubit can be excited while the cavity is empty which then prevents photons from entering. Another interesting feature in Fig. 8.19 at the lowest power is the dip (representing an overall increase in transmission). While this feature is not well-understood it appears in both the experiment and numerical simulations, and is thought to be an interference effect of some sort. As the input power is increased, more photon number peaks can be resolved and the mean of the distribution shifts proportional to \bar{n} . The data agree well with numerical solutions at low powers (solid lines in Fig. 8.19) to the Markovian Master equation[Walls2006, Gambetta2006] with three damping sources, namely the loss of photons at rate $\kappa/2\pi = 250$ kHz, energy relaxation in the qubit at rate $\gamma_1/2\pi = 1.8$ MHz and the qubit dephasing rate $\gamma_\phi/2\pi = 1.0$ MHz. However, adequate numerical modeling of this strongly coupled system at higher photon numbers is quite difficult and has not yet been achieved.

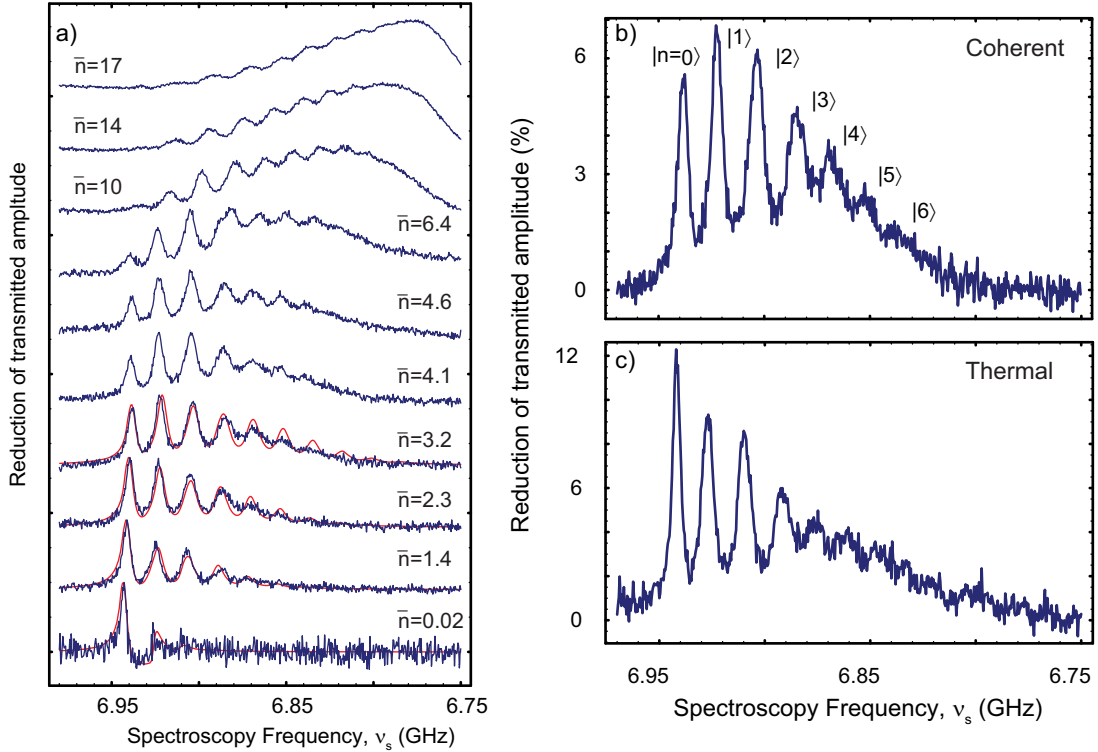


Figure 8.19: Direct spectroscopic observation of quantized cavity photon number. **a)** Qubit spectra with coherent cavity drive at different average cavity occupations (\bar{n}). The spectra have resolved peaks corresponding to each photon number. The peaks are separated by $2|\chi_{\text{eff}}|/2\pi = 17$ MHz. Approximately ten peaks are distinguishable. The data (blue) is well described by numerical simulations (red) with all parameters predetermined except for a single frequency offset, overall power scaling, and background thermal photon number ($n_{\text{th}} = 0.1$) used for all traces. Computational limitations prevented simulations of photon numbers beyond ≈ 3 . At the lowest power nearly all of the weight is in the $|0\rangle$ peak, meaning that the cavity has a background occupation less than ($n_{\text{th}} < 0.1$). Peaks broaden as $(n + \bar{n})\kappa/2$ plus some additional contributions due to charge noise. At higher powers the peaks blend together and the envelope approaches a gaussian shape for a coherent state. Since $\chi < 0$, spectra are displayed from high to low frequency, and also have been normalized and offset for clarity. **b)** Reduction in transmitted amplitude is plotted as a proxy for qubit absorption for the case of a coherent drive with $\bar{n} = 3$ photons. **c)** Spectrum when cavity is driven with Gaussian white noise approximating a thermal state also with $\bar{n} = 3$. The coherent spectrum is clearly non-monotonic and qualitatively consistent with the Poisson distribution, $P(n) = e^{-\bar{n}}\bar{n}^n/n!$, while the thermal spectrum monotonically decreases consistent with the Bose-Einstein distribution $P(n) = \bar{n}^n/(\bar{n} + 1)^{n+1}$.

In earlier work[Brune1994, Schuster2005] in the weak dispersive limit ($\chi/\gamma < 1$), the measured linewidth resulted from an ensemble of Stark shifts blurring the transition, while here in the strong limit ($\chi/\gamma > 1$) each member of the ensemble is individually resolved. In the spectra measured here (Fig. 8.19), the linewidth of a single peak can be much less than the frequency spread of the ensemble, but changes in photon number during a single measurement can still completely dephase the qubit. Taking this into account, yields a predicted photon number dependent linewidth, $\gamma_n = \gamma/2 + \gamma_\phi + (\bar{n} + n) \kappa/2$ for the n^{th} peak[Gambetta2006]. The lowest power peak (in the $\bar{n} = 0.02$ trace) corresponds to zero photons and measures the unbroadened linewidth, $\gamma_0/2\pi = 1.9$ MHz. When $\bar{n} = 2\chi_{\text{eff}}/\kappa$ the peaks should begin to overlap once more, returning the system to the classical field regime. If this effect were the only limitation, we might hope to count as many as 70 photon number peaks before they merge. In practice the higher number peaks are also more sensitive to charge fluctuations in the Cooper pair box, which limits us to about 10 resolvable photon states in this measurement.

The relative area under each peak in the transmission amplitude (Fig. 8.19) contains information about the photon statistics of the cavity field. We can compare two cases having the same average cavity occupation ($\bar{n} \sim 3$), but containing either a coherent field (Fig. 8.19b) or a thermal field (Fig. 8.19c). To create the thermal field, gaussian noise was added in a wide band around the cavity (red in Fig. 8.18b). The coherent and thermal states are clearly distinguishable. The weights of the peaks are non-monotonic for a coherent distribution while in the thermal distribution they monotonically decrease[Dykman1987] for all noise intensities measured. However, for the sample parameters and measurement protocols used here, several effects prevent quantitative extraction of photon number probabilities from the data. First, the inhomogeneous broadening of the higher number peaks due to charge noise prevents independent extraction of their areas. Additionally, though it has been analytically shown that the qubit absorption spectrum should accurately represent the cavity photon statistics[Gambetta2006], this experiment did not have an independent means to measure the qubit, and there are imperfections in mapping the qubit spectrum onto the cavity transmission. Finally, numerical simulations show that spectroscopic driving of the qubit results in complex dynamics which squeezes the cavity photon number, pointing to a path to create exotic states of light, but also obscuring the initial photon statistics. The measured data is consistent with numerical predictions which do take into account such squeezing effects (see Fig. 8.19) for photon numbers ($\bar{n} \leq 3$) which we could simulate. While these effects are large in the present

experiment, an independent measurement of the qubit could be introduced using a second cavity or Josephson-bifurcation amplifier[Siddiqi2006], allowing the realization of a quantitative photon statistics analyzer. Previous experiments have also measured analogous statistics of other Bosonic systems including phonons in an ion trap[Leibfried1996, Leibfried1997], excitations in a single electron cyclotron oscillator[Peil1999], and the number of atoms in a Bose-Einstein condensate passing through a cavity[Ottl2005].

The results obtained here also suggest a method for photon-qubit conditional logic. The qubit response is now strongly dependent on the number of photons in the cavity. For example, a controlled-not (CNOT) gate between a photon and qubit could be implemented by applying a π control pulse at the frequency corresponding to one photon in the cavity. This would flip the qubit if there were exactly one photon in the cavity, but do nothing for all other number states. Since the qubit does not absorb the cavity photon, the number is unchanged after the operation and could be used to entangle with distant qubits. A photon number based gate is analogous to the phonon common mode coupling used in ion-traps[Monroe1995], but since the photons travel along transmission lines and not through qubits themselves, many qubits can be placed in a single wavelength, and the photons could be sent to distant qubits, including those in other cavities.

8.3.2 Anharmonic Strong Dispersive Limit

The dispersive limit is conventionally defined as having $g/\Delta \ll 1$. This limit has many physical implications. One, which we've explored at length, is that the wavefunction overlap will be small allowing for quantum non-demolition measurements. Mathematically, one can also think of this as the condition for perturbation theory to converge¹. Typically, this perturbation is only taken to second order, but the fourth order effect is also quite interesting. Expanding Eq. 2.4 to fourth order gives,

$$\frac{E_{\pm,n}}{\hbar} = n\omega_r + \frac{\omega_a}{2} \pm \left(\frac{\Delta}{2} + n\frac{g^2}{\Delta} - n^2\frac{g^4}{\Delta^3} + \dots \right) \quad (8.12)$$

As a result of this new fourth order coupling term the resonator transition frequency becomes photon number dependent,

$$\omega_{r,n} = \frac{E_{\pm,n+1} - E_{\pm,n}}{\hbar} = \omega_r \pm \frac{1}{2} \left(\frac{g^2}{\Delta} - \frac{g^4}{\Delta^3} - 2n\frac{g^4}{\Delta^3} \right) \quad (8.13)$$

¹The convergence criteria is best seen as the condition for a Taylor series expansion in g/Δ of Eq. 2.4, describing the exact energies, to converge.

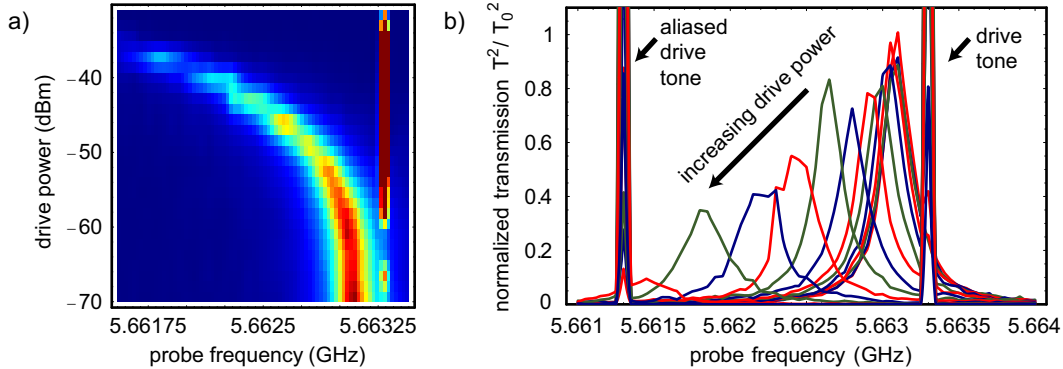


Figure 8.20: **a)** Density plot showing the dispersive cavity’s inherited non-linearity from its coupling to the qubit. The cavity is driven with a tone of order $\bar{n} \sim 1$ at a slight positive detuning, $\delta_d = 210$ kHz. A weak probe signal is then scanned as the drive tone’s power is increased. **b)** A waterfall plot of the same data, normalized to the low power transmission. As the power is increased the cavity transmission peak shifts downward in frequency and the linewidth decreases. The two large features are the drive tone, and an aliased version of it at twice the IF frequency below.

The fourth order correction makes the cavity anharmonic! This non-linearity can be thought of as coming from the small part of the photon which lives in the qubit. More amazing still, while the sign of the anharmonicity depends on the qubit state, it is present even when the qubit never leaves the ground state. The dispersive limit implies that the number dependent term will always be much smaller than the first order light shift, but when considering the anharmonicity of the cavity, it is appropriate to compare instead to the cavity linewidth κ . The cavity can be considered anharmonic at a new critical photon number, $n_\kappa = \kappa\Delta^3/2g^4$, which is the condition for the non-linear shift to be equal to the linewidth. For this experiment $n_\kappa \approx 3$.

To observe this non-linearity most directly, two-tone spectroscopy of the cavity is performed. A drive tone at is applied at a detuning from the cavity δ_d and has its power scanned near $n \approx 1$ photons. If the detuning is chosen so as to repel the cavity line from the drive tone, it will be more heavily filtered as the power is increased. In this case photon number fluctuations are suppressed potentially below the vacuum noise. If it is detuned such that the anharmonicity brings the line closer it will tend towards bistability, which is very similar to a Josephson bifurcation amplifier[Siddiqi2004]. In this experiment, we will focus on the case where number fluctuations are suppressed rather than enhanced. A second probe tone, at very low powers, is used to interrogate the cavity resonance. As the drive power is increased (see Fig. 8.20), the cavity line is red-shifted and becomes broadened. The broadening occurs because the line is moved by $2g^4/\Delta^3$ whenever the photon number changes, so in addition the homogenous broadening due to decay, the line is also shifted by significant fraction of

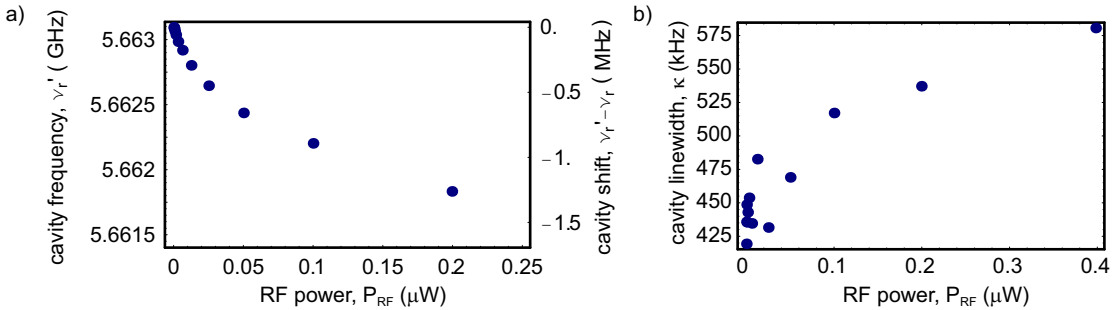


Figure 8.21: **a)** Anharmonic cavity frequencies ν_r' , as extracted from fitting the data in Fig. 8.20. The total shift is 1.5 MHz about 3κ . **b)** As the peak is shifted it is also broadened increasing by about 20% in the dataset. The peak amplitude is also reduced because the cavity now experiences inhomogenous broadening due to its significant non-linearity.

a linewidth. This can be thought of as a manifestation of the uncertainty principle, which demands that any reduction of uncertainty in photon number be accompanied by a corresponding increase in the fluctuations of its conjugate variable, the phase.

This experiment presents a first glance a cavity which is anharmonic on the single photon level. A better understanding of this regime will be especially important for understanding experiments with two strongly coupled cavities. It could be used to make a single photon detector, or eventually perhaps even a photonic qubit. There is much yet to be done along this direction. Future experiments might increase the dispersive coupling (or decrease the cavity linewidth) to see still stronger anharmonic effects. The positive feedback regime has been studied a little (though is not presented here) and should be studied more closely. Such investigations could see how the discrete nature of the photon affects the transition from qubit (non-linearity strong even at one excitation) to Josephson bifurcation effects[Siddiqi2004] (quasi-classical non-linearity at hundreds of photons).

Chapter 9

Time Domain Measurements

All of the experiments discussed until now have been spectroscopic in nature. These allow one to efficiently study the energy levels of the cavity-qubit system over decades of frequency scales with incredible precision. Each of these spectroscopic studies has a dual in the time domain, and many of the cavity QED or quantum computation concepts, such as gates or single shot measurements are expressed more naturally in the time domain. In the first section, I present single qubit gates, demonstrating full control over the qubit state. The quantum non-demolition measurement process is explained and used to demonstrate $> 95\%$ visibility of qubit control. The next section goes a step further, looking at single shot detection rather than ensemble measurements, realizing a measurement fidelity of $30 - 40\%$. Finally, the ability to manipulate the qubit is mapped onto the state of a single photon creating an “on-demand,” single photon source, which can provide arbitrary superposition states of zero and one photon.

9.1 Single Qubit Gates

An outstanding question for superconducting qubits, and in fact for all solid-state implementations of quantum information processors, is whether the qubits are sufficiently well-isolated to allow long coherence times and high-fidelity preparation and control of their quantum states. This question is complicated by inevitable imperfections in the measurement. A canonical example is a Rabi oscillation experiment, where the experimenter records the oscillations of a meter’s response as a function of pulse length to infer the qubit’s excited state population immediately after the pulse. The measurement contrast (e.g. the amplitude of the meter’s measured swing relative to its maximum value) is reduced in general by both errors in the qubit preparation and readout, and sets a lower

limit on the visibility of oscillations in the qubit population. Most experiments with superconducting qubits to date have reported only the measurement contrast, setting only a lower limit on the visibility in the range of 10–50 % [Nakamura1999, Vion2002, Martinis2002, Yu2002, Chiorescu2004, Collin2004, Yamamoto2003].

A full understanding of the measurement process is required to extract the qubit population from the meter’s output. The qubit control is then characterized by the visibility, defined as the maximum qubit population difference observed in a Rabi oscillation or Ramsey fringe experiment. It is essential to demonstrate that a qubit can be controlled without inducing undesired leakage to other qubit states or entanglement with the environment. Some experiments [Simmonds2004] observe a substantial reduction of the visibility due to entanglement with spurious environmental fluctuators [Meier2005]. In the few experiments in which the contrast has been characterized, it was close to the expected value [Duty2004, Astafiev2004], which implies that high visibility should be achievable with superconducting qubits.

In the experiments presented here, we coherently control the quantum state of a Cooper pair box in the resonator by applying microwave pulses of frequency ω_s , which are resonant or nearly resonant with the qubit transition frequency $\omega_a/2\pi \approx 4.3$ GHz, to the input port C_{in} of the resonator, see Fig. 9.1a. Even though ω_s is strongly detuned from the resonator frequency ω_r , the resonator can be populated with n_s drive photons which induce Rabi oscillations in the qubit at a frequency of $\nu_{\text{Rabi}} = \sqrt{n_s}g/\pi$. Simultaneously, we perform a continuous dispersive measurement of the qubit state by determining both the phase and the amplitude of a coherent microwave beam transmitted through the resonator at frequency ω_{RF} which is resonant or nearly resonant with the resonator frequency $\omega_r/2\pi \approx 5.4$ GHz [Blais2004, Wallraff2004]. The phase shift $\phi = \tan^{-1}(2g^2/\kappa\Delta)\sigma_z = \pm\theta_0$ is the response of our meter from which we determine the qubit population. For the measurement, we chose a resonator that has a quality factor of $Q \sim 0.7 \times 10^4$ corresponding to a photon decay rate of $\kappa/2\pi = 0.73$ MHz. The resonator is populated with $n \sim 1$ measurement photons on average, where n is calibrated using the ac-Stark shift [Schuster2005]. All experiments are performed in a dilution refrigerator at a temperature of 20 mK. The charging energy of the box is $E_C = e^2/2C_\Sigma \approx h 5.2$ GHz. Details on the device fabrication can be found in Ref. [Frunzio2005].

We initially determine the maximum swing of the meter in a calibration measurement by first maximizing the detuning Δ to minimize the interaction ($g^2/\Delta \rightarrow 0$) and defining $\phi = 0$. We prepare the Cooper pair box in the ground state $|g\rangle$ by relaxation, the thermal population of excited states

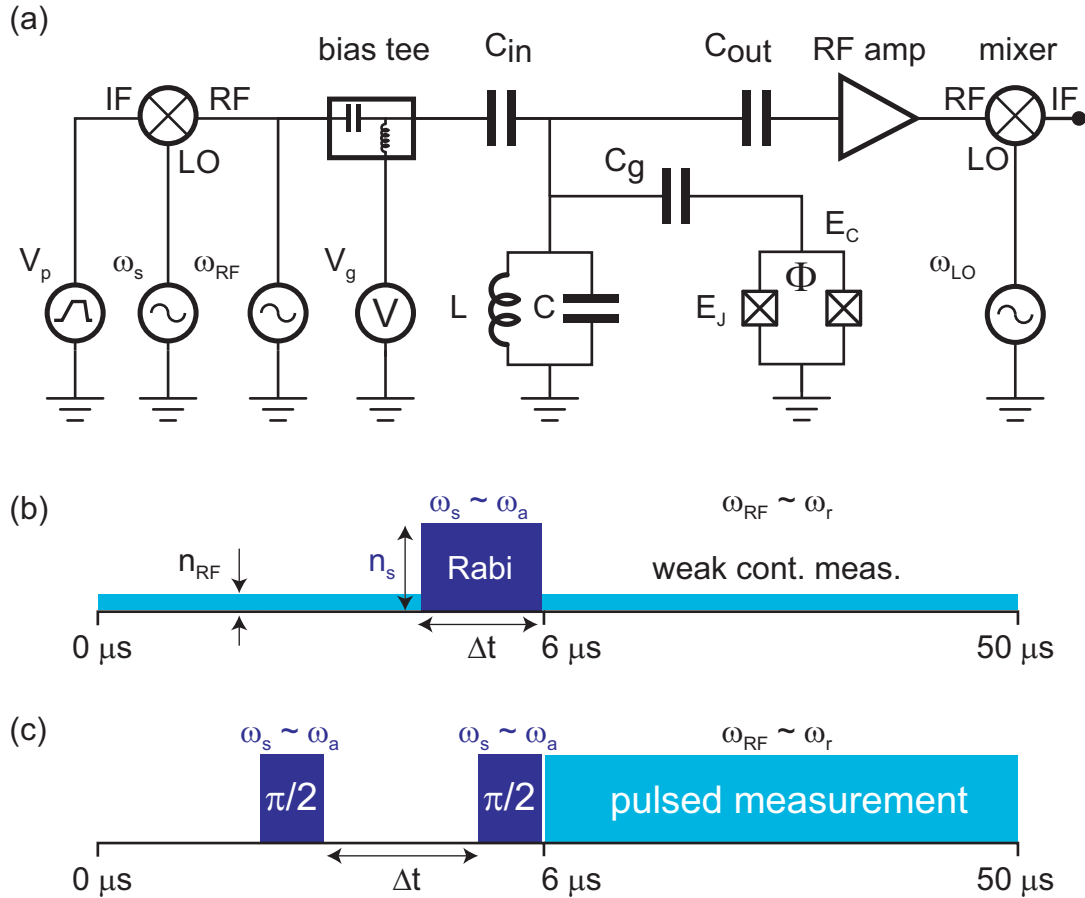


Figure 9.1: **a)** Simplified circuit diagram of measurement setup. A Cooper pair box with charging energy E_C and Josephson energy E_J is coupled through capacitor C_g to a transmission line resonator, modeled as parallel combination of an inductor L and a capacitor C . Its state is determined in a phase sensitive heterodyne measurement of a microwave transmitted at frequency ω_{RF} through the circuit, amplified and mixed with a local oscillator at frequency ω_{LO} . The Cooper pair box level separation is controlled by the gate voltage V_g and flux Φ_B . Its state is coherently manipulated using microwaves at frequency ω_s with pulse shapes determined by V_p [Collin2004]. **b)** Measurement sequence for Rabi oscillations with Rabi pulse length Δt , pulse frequency $\omega_s \sim \omega_a$ and amplitude $\propto \sqrt{n_s}$ with continuous measurement at frequency $\omega_{RF} \sim \omega_r$ and amplitude $\propto \sqrt{n_{RF}}$. **c)** Sequence for Ramsey fringe experiment with two $\pi/2$ -pulses at ω_s separated by a delay Δt and followed by a pulsed measurement.

being negligible. The box is biased at charge degeneracy ($E_{\text{el}} = 0$), where its energy is to first-order insensitive to charge noise [Vion2002]. Using flux bias, the detuning is adjusted to $\Delta/2\pi \approx -1.1$ GHz corresponding to a maximum in the Josephson coupling energy of $E_J/h \approx 4.3$ GHz $< \omega_r/2\pi$. In this case we measure a minimum meter response of $\phi_{|g\rangle} = -35.3$ deg corresponding to a coupling strength of $g/2\pi = 17$ MHz. Saturating the qubit transition by applying a long microwave pulse which incoherently mixes the ground and excited states such that the occupation probabilities are $P_{|g\rangle} = P_{|e\rangle} = 1/2$, the measured phase shift is found to be $\phi = 0$, as expected [Schuster2005]. From these measurements, the predicted phase shift induced by a fully polarized qubit ($P_{|e\rangle} = 1$) would be $\phi_{|e\rangle} = 35.3$ deg. Thus, the maximum swing of the meter is bounded by $\phi_{|e\rangle} - \phi_{|g\rangle}$.

In our measurement of Rabi oscillations, a short microwave pulse of length Δt is applied to the qubit in its ground state with a repetition rate of 20 kHz while the measurement response ϕ is continuously monitored and digitally averaged 5×10^4 times, see Fig. 9.1b. The signal to noise ratio (SNR) in the averaged value of ϕ in an integration time of 100 ns is approximately 25, see Fig. 9.2, corresponding to a SNR of 0.1 in a single shot. For the present setup the single shot read-out fidelity for the qubit state integrated over the relaxation time ($T_1 \sim 7 \mu\text{s}$) is approximately 30 % (see Sec. 9.2). Either a read-out amplifier with lower noise temperature or a larger signal power would potentially allow a high fidelity single shot measurements of the qubit state in this setup.

The time dependence of the averaged value of ϕ in response to a π pulse of duration $\Delta t \sim 16$ ns applied to the qubit is shown in Fig. 9.2b. Before the start of the pulse the measured phase shift is $\phi_{|g\rangle} \approx -35.3$ deg corresponding to the qubit being in the ground state. Due to the state change of the qubit induced by the pulse, the resonator frequency is pulled by $2g^2/\Delta$ and, thus, the measured phase shift is seen to rise exponentially towards $\phi_{|e\rangle}$ with the resonator amplitude response time $2/\kappa \approx 400$ ns, i.e. twice the photon life time. After the π pulse, the qubit excited state decays exponentially with its energy relaxation time $T_1 \sim 7.3 \mu\text{s}$, as extracted from the decay in the measured phase shift, see Fig. 9.2b. As a result, the maximum measured response ϕ_{\max} does not reach the full value of $\phi_{|e\rangle}$. In general, the measurement contrast $C = (\phi_{\max} - \phi_{\min})/(\phi_{|e\rangle} - \phi_{|g\rangle})$ will be reduced in any qubit read-out for which the qubit lifetime is not infinitely longer than the measurement response time. Additionally, in non-QND measurements the contrast is reduced even further due to mixing of the qubit states induced by the interaction with the measurement apparatus. In our QND measurement presented here, the qubit lifetime is about 15 times the response time of the measurement, allowing us to reach a high maximum contrast of $C \sim 85$ % in the bare measurement response ϕ .

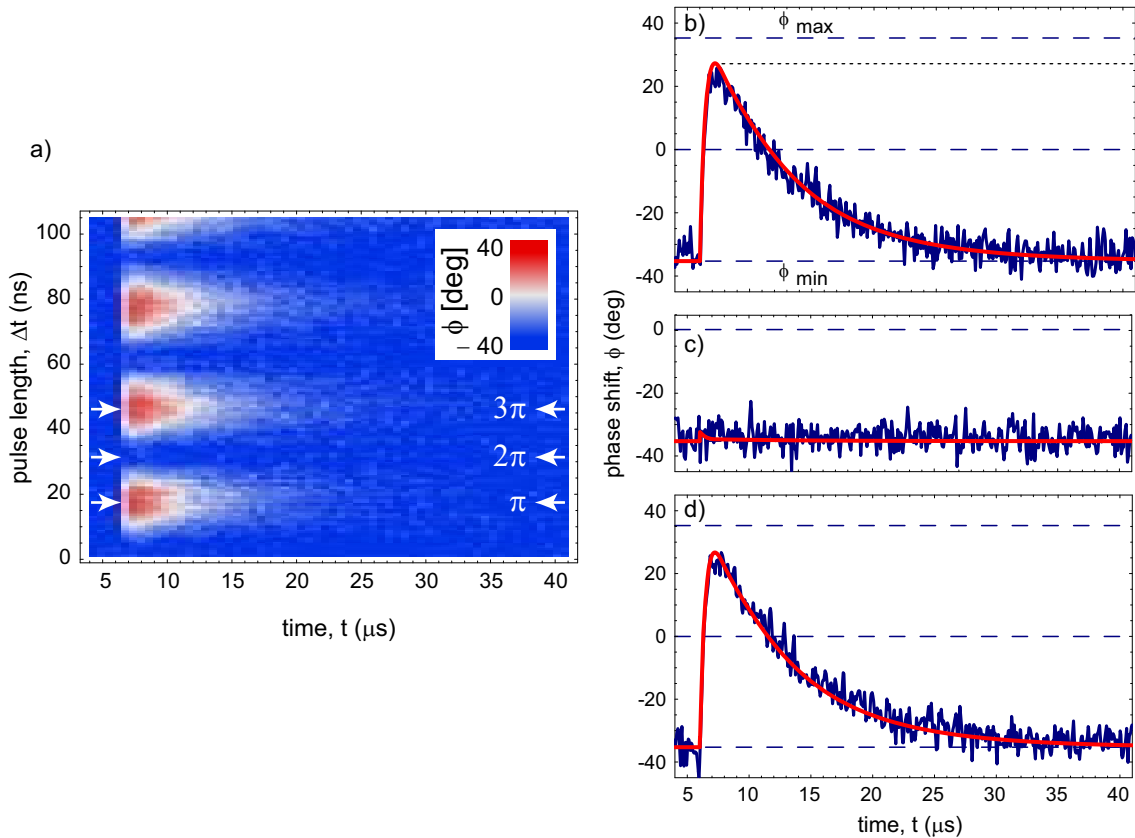


Figure 9.2: **a)** Color density plot of phase shift ϕ (see inset for scale) versus measurement time t and Rabi pulse length Δt . Data shown in **b-d** are slices through this data set at the indicated pulse lengths. They show the measurement response ϕ (blue lines) and theoretical prediction (red lines) vs. time. At $t = 6\ \mu\text{s}$ (a) a π pulse, (b) a 2π pulse, and (c) a 3π pulse is applied to the qubit. In each panel the dashed lines correspond to the expected measurement response in the ground state $\phi_{|g\rangle}$, in the saturated state $\phi = 0$, and in the excited state $\phi_{|e\rangle}$.

In Figs. 9.2c and d, the measured response ϕ of the meter to a 2π and a 3π pulse acting on the qubit is shown. As expected, no phase shift is observable for the 2π pulse since the response time of the resonator is much longer than the duration $\Delta t = 32$ ns of the pulse. In agreement with the expectations for this QND scheme, the measurement does not excite the qubit, i.e. $\phi_{\min} = \phi_{\max} = \phi_{|g\rangle}$. The response to the 3π pulse is virtually indistinguishable from the one to the π pulse, as expected for the long coherence and energy relaxation times of the qubit. In the 2D density plot Fig. 9.2a, Rabi oscillations are clearly observed in the phase shift acquired versus measurement time t and Rabi pulse length Δt .

The observed measurement response ϕ is in excellent agreement with theoretical predictions, see red lines in Fig. 9.2, demonstrating a good understanding of the measurement process. The temporal response $\phi(t) = \arg\{i\langle a(t)\rangle\}$ of the cavity field a is calculated by deriving and solving Bloch-type equations of motion for the cavity and qubit operators using the Jaynes-Cummings Hamiltonian in the dispersive regime [Blais2004] as the starting point. A semi-classical factorization approximation is done to truncate the resulting infinite set of equations to a finite set (e.g. $\langle a^\dagger a \sigma_z \rangle \sim \langle a^\dagger a \rangle \langle \sigma_z \rangle$; all lower order products are kept). This amounts to neglecting higher order correlations between qubit and field which is a valid approximation in the present experiment. The calculations accurately model the exponential rise in the observed phase shift on the time scale of the resonator response time due to a state change of the qubit. They also accurately capture the reduced maximum response ϕ_{\max} due to the exponential decay of the qubit. Overall, excellent agreement in the temporal response of the measurement is found over the full range of qubit and measurement time scales with only T_1 as a fit parameter, see Fig. 9.2.

The visibility of the excited state population $P_{|e\rangle}$ in the Rabi oscillations is extracted from the time dependent measurement response ϕ for each Rabi pulse length Δt . We find $P_{|e\rangle}$ by calculating the normalized dot product between the measured response ϕ and the predicted response, taking into account the systematics of the measurement. This amounts to comparing the area under a measured response curve to the theoretically predicted area, see Fig. 9.2. The averaged response of all measurements taken over a window in time extending from the start of the Rabi pulse out to several qubit decay times T_1 is used to extract $P_{|e\rangle}$. This maximizes the signal to noise ratio in the extracted Rabi oscillations.

The extracted qubit population $P_{|e\rangle}$ is plotted versus Δt in Fig. 9.3a. We observe a visibility of $95 \pm 6\%$ in the Rabi oscillations with error margins determined from the residuals of the experi-

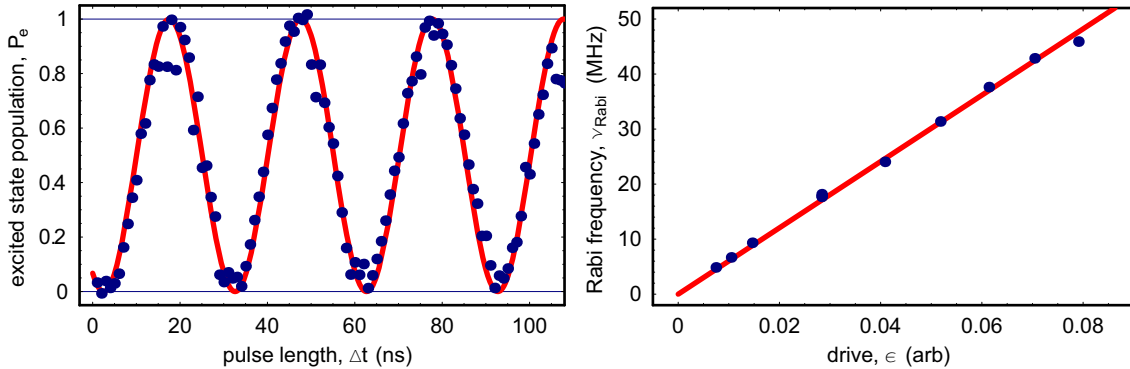


Figure 9.3: **a)** Rabi oscillations in the qubit population P_e vs. Rabi pulse length Δt (blue dots) and fit with unit visibility (red line). **b)** Measured Rabi frequency ν_{Rabi} vs. pulse amplitude ϵ_s (blue dots) and linear fit.

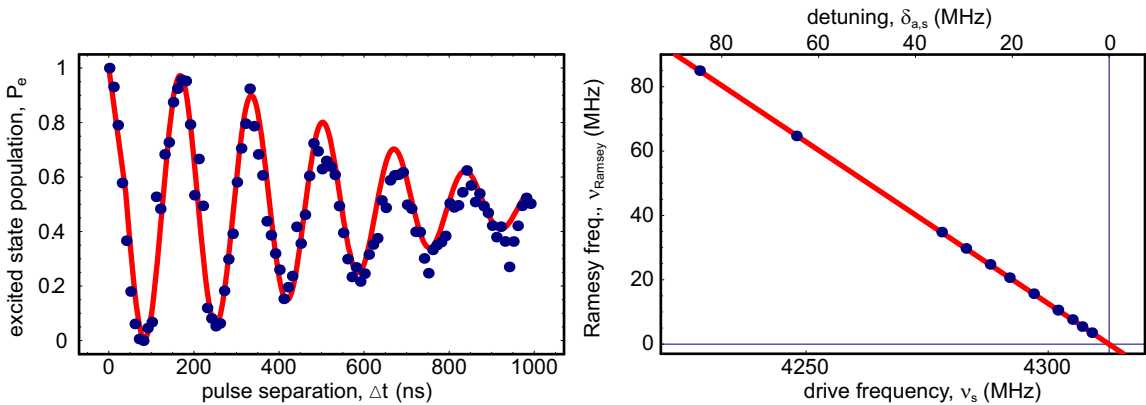


Figure 9.4: **a)** Measured Ramsey fringes (blue dots) observed in the qubit population P_e vs. pulse separation Δt using the pulse sequence shown in Fig. 9.1b and fit of data to sinusoid with gaussian envelope (red line). **b)** Measured dependence of Ramsey frequency ν_{Ramsey} on detuning $\delta_{a,s}$ of drive frequency (blue dots) and linear fit (red line).

mental $P_{|e\rangle}$ with respect to the predicted values. Thus, in a measurement of Rabi oscillations in a superconducting qubit, a visibility in the population of the qubit excited state that approaches unity is observed for the first time. Moreover, the decay in the Rabi oscillation amplitude out to pulse lengths of 100 ns is very small and consistent with the long T_1 and T_2 times of this charge qubit, see Fig. 9.3a and Ramsey experiment discussed below. We have also verified the expected linear scaling of the Rabi frequency ν_{Rabi} with the pulse amplitude $\epsilon_s \propto \sqrt{n_s}$, see Fig. 9.3b.

We have determined the coherence time of the Cooper pair box from a Ramsey fringe experiment at charge degeneracy using $\pi/2$ pulses of 20 ns duration, see Fig. 9.1c. To avoid dephasing induced by a weak continuous measurement beam [Schuster2005] we switch on the measurement beam only after

the end of the second $\pi/2$ pulse. The resulting Ramsey fringes, oscillate at the detuning frequency $\delta_{a,s} = \omega_a - \omega_s \sim 6$ MHz, decaying with a long coherence time of $T_2 \sim 500$ ns (see Fig. 9.4a). The corresponding qubit phase quality factor of $Q_\varphi = T_2 \omega_a / 2 \sim 6500$ is similar to the best values measured so far in qubits biased at an optimal point [Vion2002]. The Ramsey frequency is shown to depend linearly on the detuning $\delta_{a,s}$, as expected, see Fig. 9.4b. We note that a measurement of the Ramsey frequency is an accurate time resolved method to determine the qubit transition frequency $\omega_a = \omega_s + 2\pi \nu_{\text{Ramsey}}$.

9.2 Single Shot Readout

Quantum computation, like its classical counterpart, operates on digital information. While performing computations, a qubit can be prepared in any superposition of $|g\rangle$ and $|e\rangle$. When the qubit is measured though, it will produce a digital, 0 or 1 result. From the data presented thus far the binary nature of the qubit is only expressed subtly through oscillatory behavior in response to being driven, and agreeing well with the predictions for a two-level system interacting with a harmonic oscillator. The reason the binary nature is masked in the previous experiments is that they are always composed of many (tens of thousands) of individual experiments ensemble averaged again. These experiments measured the expectation value rather than the projection of the qubit state. In this section, we will store each experiment consisting of preparation of the qubit state and subsequent measurement of the qubit state individually, histogramming them to see not only the mean behavior as studied in section 9.1, but also the distribution of the measurements. We find that our measurement has a fidelity of approximately $\sim 33 - 40\%$ meaning that in an individual experiment we get about 1/3 of a bit of information. This means that the measurement is currently suitable for ensemble measurements where we get 1/3 of the available information (given the qubit decay time). The measurement fidelity should be $> 99\%$ for reliable quantum computation, a goal for future experiments.

This measurement is somewhat unique for superconducting qubits in that it is a continuous measurement whereas most experiments employ latching measurements[Lupascu2006, Steffen2006, Siddiqi2006]. When measuring a small signal one uses an amplifier which adds noise in addition to amplifying the signal, and can obscure the original signal. In our system the noise temperature is $T_N = 5$ K, giving an efficiency $\eta = 0.025$. This corresponds to approximately 40 photons of amplifier noise in one cavity bandwidth, meaning that we must acquire that many photons in order to achieve

a signal-to-noise ratio (SNR) of one. To have high fidelity ($> 90\%$) one must have a $\text{SNR} > 30$ in a decay time, T_1 . This corresponds to having $\text{SNR} = 10$ by the time there is a 10% chance of decay. A continuous measurement must acquire that SNR by averaging away any classical noise before the qubit decays. A latching measurement attempts to reduce the effect of the amplifier noise by first mapping the fragile quantum state onto a more robust classical state, such as the switching current of a SQUID[Lupascu2006], a phase slip in a phase qubit[Steffen2006] or a meta-stable oscillation state in a non-linear cavity[Siddiqi2006]. Once latched into this robust state, the signal can be averaged until the amplifier noise has been reduced sufficiently. Though latching can be advantageous, there is typically a finite arming time which must be much faster than the qubit lifetime ($t_{\text{arm}} \ll T_1$). Latching measurements also often involve large unknown excursions in parameter space during the measurement which can lead to reduced contrast, though this problem has been addressed to some extent. The latching measurement of [Siddiqi2006] is compatible with our system and could be used as a readout, though currently it has a similar fidelity to our continuous measurement.

The continuous measurement protocol used here consists of preparing the qubit in the excited state (by applying a π pulse) or ground state (by doing nothing) and then measuring the transmission of the cavity. The local oscillator phase is configured such that in the ground state the amplitude is all in the in-phase channel (I), and that when in the excited state most of the amplitude is in the out-of-phase (Q) channel. To first order the Q can be considered the phase, and I the amplitude (though there are deviations if the phase shifts are large). The measurement tone can be left on during the pulse (if the dephasing rate is small compared to the π pulse time $\sim 10\text{ ns}$), or turned on after the preparation pulse has been completed. Several T_1 's worth of data is collected and stored individually for each experiment.

Once collected each trace must be analyzed individually to assess the most likely prepared qubit state[Braff2007]. The simplest method is to just average the data for a certain period of time. In this method one has to find an optimum measurement time. By measuring longer, one can reduce the uncertainty due to random amplifier noise, but the chances that an excited state qubit has decayed also grows. Using this simple scheme, the fidelity is fairly sensitive to the exact measuring time used[Braff2007]. A better technique takes into account the decay of the qubit by weighting the average with an exponential. While there is still an optimal measurement time, the fidelity is much less sensitive to measuring a little bit too long[Braff2007]. The best method relies on a non-linear filtering method which uses the early data to assess the value of data taken later (in the same trace),

which gives a substantial improvement compared with the linear simple or weighted average filters. This non-linear filter gives the most improvement at very high fidelities, where a substantial amount of information is revealed even after a short period of time. At the current level of fidelity 30 – 40% all of these methods, once optimized, give similar results.

For this data a slight variation on the exponential weighting method was used. To see how the weighting function was chosen we first discuss the behavior of an arbitrary filter function. The score, s , is just the weighted average of the data is just the dot product of the filter function $f(t)$, and the signal $\psi(t)$.

$$s = \int_0^{t_m} f(t)\psi(t)dt \quad (9.1)$$

For these experiments rather than using an exponential filter function, a calibration trace of a measurement of the excited state (like in Fig. 9.2b) was used. The ensemble average is very similar to an exponential decay and gives similar results to those described in [Braff2007], but has the convenient property that it is self-aligning in time. In the case of pulsed measurements, where there might be transients in both the ground and excited states, one can use a Graham-Schmidt orthonormalization procedure to adjust the weighting accordingly, creating a filter function with the following prescription

$$\vec{f} = \frac{1}{\vec{\psi}_e^{\text{avg}} \cdot \vec{\psi}_g^{\text{avg}}} \left(\vec{\psi}_e^{\text{avg}} - (\vec{\psi}_e^{\text{avg}} \cdot \vec{\psi}_g^{\text{avg}}) \vec{\psi}_g^{\text{avg}} \right) \quad (9.2)$$

where $\vec{\psi}_{g/e}^{\text{avg}}$ are averages taken over many shots and the dot product represents integration over time as in Eq. 9.1. This function has the property that the average value of the $\vec{f} \cdot \vec{\psi}_{g/e}^{\text{avg}}$, will be zero or one respectively for averages of the ground or excited state. It gives a good measure of how much information is at each timestep and is convenient to apply. In the future, the non-linear filter should not be significantly more complex and may improve performance once our signal to noise improves to get higher fidelity.

With this filtering technique we took many single shot measurements, (10,000,000 for Fig. 9.5a), and histogrammed the scores. The histograms can be thought of as probability distributions of getting a certain score given that the qubit was prepared in the ground or excited state. The two distributions in figure 9.5a are resolved, but have substantial overlap indicating that there was too much amplifier noise broadening the distributions. To determine the fidelity of the measurement we have to define a threshold which decides between scores belonging to the ground state or excited state. This can easily be found by integrating the distributions (in Figs. 9.5a and d) to compute

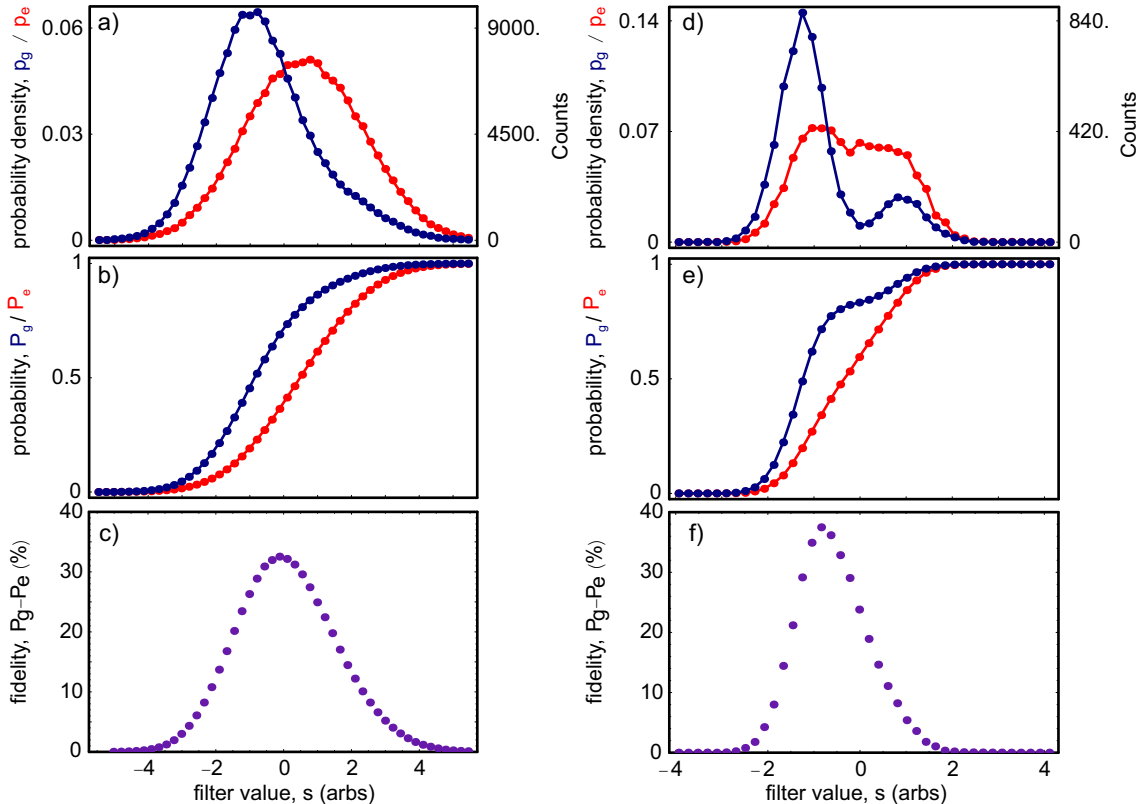


Figure 9.5: Histograms of single shot measurements after preparation with a π pulse (red) and no pulse (blue), using measurement power equivalent to $\bar{n} \approx 7$ photon (a-c) and $\bar{n} \approx 30$ photons (d-f). The data in a and d are obtained by histogramming, the filter value (method described in the text) of many single shots (approximately 10,000,000 in a and 6,000 in d), to form a probability density p_e/p_g of excited/ground state *vs.* filter value. By integrating these probability distributions one can create “s-curves” (b and e), which give the probabilities $P_g(s)/P_e(s)$ of the qubit being in the ground/excited state if the measured filter value is less than s . The fidelity (c and f) for a given threshold s is given by the quantity $P_g(s) - P_e(s)$. The maximum threshold at $\bar{n} \approx 7$ is $F \approx 32\%$, whereas it is $\bar{n} \approx 30$ is $F \approx 38\%$. The histogram in d shows the effects of demolition with evidence of an excited state population in the ground state histogram and excess ground state in the excited state histogram. This demolition prevents the fidelity from increasing as expected with photon number. The histograms have been scaled and offset such that the mean of the excited and ground state distributions lie at ± 1 for clarity.

the probability $P_g(s)/P_e(s)$ of being in the ground/excited state and measuring a score below a given threshold (see Figs. 9.5b and e). The difference of these two, $P_g(s) - P_e(s)$, gives the average fidelity of a measurement at that particular threshold. The maximum fidelity was about 32% for the distribution in figure 9.5a which had $n \approx 7$ photons and 38% for the distribution in figure 9.5d.

While the fidelities are (disappointingly) similar, the cause of errors is quite different. In figure 9.5a the distributions are broad and basically symmetric (though a little asymmetry is noticeable in the ground state distribution), while the in figure 9.5d they are quite narrow but they are asymmetric, even bimodal. The width of the histograms arises from the random noise from the amplifier, while the asymmetry gives information about the effect of decay (or measurement induced demolition). Ideally the signal to noise ratio should improve by increasing the power from $n \approx 7$ to $n \approx 30$, improving the fidelity significantly. While the signal to noise ratio (as evident by the width of the ground state peaks in Fig. 9.5d) does improve the fidelity does not because the measurement itself induces transitions in the qubit.

The exact cause of this demolition is not well understood. One known source of measurement based demolition arises from the wavefunction overlap, described in Eq. 2.7. For small photon number ($n \ll n_{\text{crit}} = 3000$ for this sample), this overlap should be $\sim n(g/\Delta)^2 < 1\%$. This implies that an effect outside the simple Jaynes-Cummings Hamiltonian is responsible for the demolition. One possibility is that the measurement excites the Cooper pair box out of the qubit Hilbert space into higher excited states, via a multiphoton process. Such processes have been seen at certain bias points and powers and could be responsible but we haven't been able to definitively confirm or deny that this is the culprit here.

Solving this mystery and improving the single shot fidelity should be considered one of the top priorities for future experiments. Higher fidelity readout would allow us to study quantum measurement, observing quantum jumps, and with qubit gates also to perform tests of Bell's inequalities. It is also possible that the same type of process which causes demolition in the presence of the measurement is responsible for the relaxation of the qubit when the measurement is off, which is the biggest unsolved mystery in all superconducting quantum computing applications.

9.3 Single Photon Source

Conventional electronic circuits are only capable of interacting with classical electromagnetic signals, which consist of superpositions of many different photon number states [Schuster2007]. Though

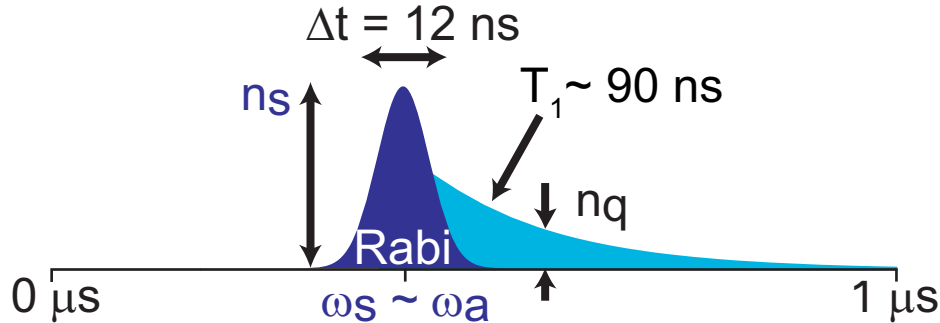


Figure 9.6: The single photon source is made by applying a short (~ 12 ns) gaussian control pulse (dark blue), to prepare the desired qubit state. The qubit then decays in a time $T_1 \sim 90$ ns, primarily through radiating into the transmission line through the cavity, resulting in the release a single photon or superposition state.

recently developed quantum circuits have the ability to interact with single photons, they are still usually controlled and measured using classical voltages and currents [Nakamura1999, Vion2002, Martinis2002, Yu2002, Chiorescu2004, Collin2004, Yamamoto2003]. Here, we demonstrate an on-chip single photon source which employs the circuit quantum electrodynamics architecture to map an arbitrary state of a superconducting qubit onto a single photon in a transmission line resonator with 80% efficiency [Houck2007]. A photon is created via enhanced fluorescence of the qubit due to the Purcell effect of the cavity, allowing single photons to be requested, “on-demand,” every ~ 100 ns. Tomography of both the qubit and photon states demonstrate the ability to convert the stationary qubit into a flying qubit. The ability to generate and detect [Schuster2007] single photons are key tools to study microwave quantum optics on a chip.

The underlying principle for generating single photons from atoms or qubits is simple. An excited qubit can relax to its ground state by emitting a photon, so a pulse that excites the qubit can trigger a single photon emission [Clauser1974, Kimble1977] (see Fig. 9.6). Early experiments demonstrated this photon generation from ions [Diedrich1987], atoms [Darquie2005], molecules [Basche1992, Brunel1999, Lounis2000], nitrogen vacancies [Kurtsiefer2000], and quantum dots [Michler2000, Michler2000a, Pelton2002] though radiation in all directions made efficient collection difficult. Collection is also difficult in solid state turnstile approaches to photon generation[Imamoglu1994, Kim1999]. In a cavity QED source, the atom or qubit is coupled to a single photonic mode of a cavity, enhancing the rate of decay to that mode through the Purcell effect [Purcell1946] and allowing a source where photons are emitted into a controlled chan-

nel. Atoms [Brattke2001, Kuhn2002, Maitre1997, McKeever2004], ions [Keller2004] and quantum dots [Moreau2001, Santori2002, Pelton2002] have been used to generate optical photons efficiently in this manner.

Here, we implement a cavity QED system in a circuit, where a superconducting qubit and transmission line resonator are coupled such that the dominant channel for relaxation of the qubit is to spontaneously emit a photon into the resonator. Each time the qubit is excited, the mostly likely outcome is the generation of one (and only one) photon on a timescale given by the characteristic decay rate of the qubit. The challenge is to create a system where spontaneous emission dominates other relaxation channels.

When in the dispersive limit ($\Delta \gg g$), the artificial atom (qubit) has a small photonic component of the wavefunction, of magnitude $(g/\Delta)^2$ (see App. B). This opens a new source of decay for the qubit, as the photonic component of the qubit can decay at the cavity decay rate, κ , resulting in a new qubit decay rate $\gamma_\kappa = (g/\Delta)^2\kappa$. The qubit can be an efficient photon source if this new decay rate (the Purcell effect [Purcell1946]) dominates over other non-radiative decay rates, $\gamma_\kappa > \gamma_\perp$.

Verifying the single photon output is a substantial challenge in on-chip microwave experiments. At this time, microwave single photon detectors are in their infancy [Schuster2007] and there isn't yet an equivalent to the optical single photon detector such as a photomultiplier or avalanche photodiode. Fortunately, several unique characteristics of the source are evident in the average signal generated by many single photon events, together yielding a convincing verification even with noisy detectors. Most simply, the output of the single photon source is expected to be oscillatory in the amplitude of the control pulse. Second, the average amplitude produced should agree well with the expected value for a single photon. Finally, and most importantly, if the output of the system depends only on the state of the qubit, the measured photons should show complete agreement with that expected from independent measurements of the qubit. The source reported here meets all three of these criteria.

The circuit designed to generate photons consists of a superconducting transmon qubit, an optimized version of the Cooper Pair Box, capacitively coupled to a half-wave transmission line resonator with fundamental frequency $\omega_r/2\pi = 5.18$ GHz. Two important design differences between this circuit and previous incarnations of circuit QED are needed to achieve efficient single photon generation. First, the cavity is asymmetric in that the capacitors (mirrors) at either end of the transmission line are no longer equally coupled (reflective), resulting in asymmetric decay rates to the input and output ports ($\kappa_{\text{in}}/2\pi \approx 200$ kHz for the input side and $\kappa_{\text{out}}/2\pi = 44$ MHz for the output). As a

result, photons generated in the cavity are emitted at the output port more than 99% of the time. In addition, the total decay rate for the cavity, $\kappa/2\pi = 44$ MHz, is substantially higher than in previous samples, a necessary change for spontaneous emission to be the dominant relaxation channel for the qubit. The qubit dephasing rate in the absence of spontaneous emission, γ_ϕ , is frequency dependent, with $\gamma_2/2\pi < 3$ MHz for all measured frequencies between 4.3 and 7.3 GHz.

Transmission measurements are used to probe the energy spectrum of this system while the qubit frequency is tuned via an external magnetic field (see Fig. 8.4). When the qubit is far detuned from the cavity, only a single transmission peak is expected, centered at the cavity frequency with a Lorentzian lineshape and width given by the bare cavity width. When the qubit and cavity are resonant, two peaks in transmission are expected, a phenomenon known as the vacuum rabi splitting. Each peak corresponds to one of the two single-excitation eigenstates of the system, superpositions of the separate qubit and photon excitation states (see Fig. 8.4b). The width of each peak is the average of the qubit and photon decay rates, $(\gamma + \kappa)/2$. In the dispersive limit, where the detuning Δ is much larger than the coupling g , spontaneous emission is enhanced by the Purcell effect, resulting in decay rates $[1 - (g/\Delta)^2]\kappa + (g/\Delta)^2\gamma$ and $[1 - (g/\Delta)^2]\gamma + (g/\Delta)^2\kappa$ (see Fig. 8.4c). Experimentally determined linewidths agree well with theoretical predictions (see Fig. 8.5), demonstrating the ability to tune the rate of radiative decay of the qubit by changing its resonant frequency.

By choosing the qubit-resonator detuning, ($\omega_a/2\pi = 4.66$ GHz and $\Delta/2\pi$) one can make the radiative channel dominate the qubit decay. With a coupling $g/2\pi = 107$ MHz, the qubit wave functions had a $(g/\Delta)^2 = 4\%$ photonic nature, resulting in a spontaneous emission lifetime of $\gamma_\kappa/2\pi = 1.7$ MHz. When the qubit was tuned to this frequency, the measured relaxation rate of the qubit was $\gamma/2\pi = 1.9$ MHz, indicating a non-radiative decay time $T_1 = 1/2\pi\gamma_\perp \approx 800$ ns. With the current experimental parameters the expected radiative efficiency is $\eta = \gamma_\kappa/\gamma \approx 90\%$.

To verify single photon generation, we first show that the output of the cavity is an oscillatory function of the input drive, as at most one photon is generated, regardless of the magnitude of the input drive. A 24 ns gaussian control pulse rotates the qubit state by a Rabi angle that is proportional to the pulse amplitude. After the control pulse leaves the cavity, the excited qubit will relax, generating a new photon state at the qubit frequency. Because the control pulse leaves the cavity at a rate κ that is much faster than the rate of spontaneous emission γ_κ , the control pulse and generated photons can easily be separated in time. As seen in Figure 9.7a, the measured control signal increases monotonically, while the spontaneous emission oscillates as the qubit is

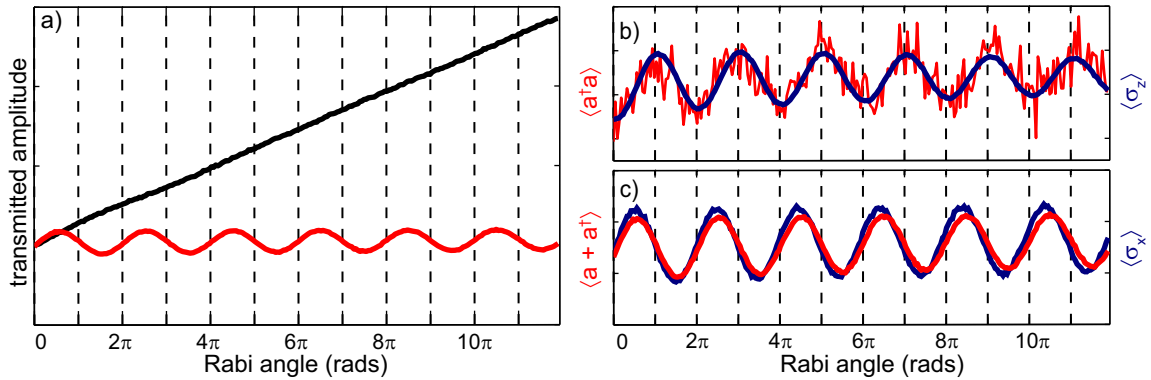


Figure 9.7: Mapping of qubit state onto photon states. **a)** Measured drive and spontaneous emission voltage. When the drive rotating the qubit is increased, the initial output of the cavity increases linearly, while after many lifetimes the output voltage of the cavity is oscillatory, due to photons stored in the qubit. **b)** Output power of the cavity ($\langle a^\dagger a \rangle$) measured with a diode, and measured qubit state ($\langle \sigma_z \rangle$). These peak when the qubit is in the excited state, after a π pulse; the agreement between qubit and photon states verifies the photon generation occurs as expected. The peak power is 80% of the power expected from an ideal qubit, indicating that 1/5 of the time, the qubit decays non-radiatively. Because of measurement transients, spontaneous emission can be collected earlier after the drive than the qubit state can be measured. While the qubit and photon states do agree in amplitude at this time, the earlier emission is plotted here with a scaled version of the qubit state for signal to noise reasons. **c)** Average voltage of the output photons ($\langle a + a^\dagger \rangle$) compared with the qubit state ($\langle \sigma_x \rangle$) measured with a Ramsey experiment. The agreement shows that the phase of superpositions states is also transferred from qubit to photon. The photon output here is only 50% of that expected for an ideal qubit due to non-radiative decay in b. and dephasing. The qubit amplitude here agrees with the qubit amplitude at later times, but is again scaled to match the photon amplitude at the earlier measurement time presented here.

rotated through increasing angles from the ground to the excited state and back, confirming that the spontaneous emission is proportional to the qubit state, not simply the applied drive amplitude.

We characterize both the power and electric field of the single photon source, using independent measurements of the qubit state and control pulse to verify performance (see Fig. 9.7). If the qubit state is mapped to the photon state, then an arbitrary superposition of the ground and excited states $\alpha|g\rangle + \beta|e\rangle$ will result in the same superposition of photon states: $\alpha|0\rangle + \beta|1\rangle$, where $|0\rangle$ and $|1\rangle$ refer to states with zero or one photon. The average photon number is proportional to the average qubit state in the ground-excited basis: $\langle a^\dagger a \rangle = 2\langle \sigma_z \rangle - 1$. The power output is minimum with no rotation or a 2π rotation, and maximum for a π rotation, when the qubit is in the purely excited state and a single photon is generated. The two quadratures of homodyne voltage, on the other hand, are proportional to the x and y-components of the qubit state: $\langle a + a^\dagger \rangle = \langle \sigma_x \rangle$ and $\langle a - a^\dagger \rangle = \langle \sigma_y \rangle$. The qubit emits in the conjugate quadrature from the control pulse separating the spontaneous emission from the control. Because a Fock state has no average phase the averaged voltage of spontaneous emission is exactly zero whenever the photon number is known completely. Thus, for 0, π , and 2π rotations, no voltage is expected (see Fig. 9.7). However, superpositions of ground and excited states do give a voltage, a maximum for a $\pi/2$ rotation, and a minimum for $3\pi/2$ rotations.

Both the power and voltage of the photon output match the qubit state, demonstrating the ability to generate single photons, as well arbitrary superpositions of zero and one photon, simply by controlling the qubit. Moreover, the amplitude of the pulse is as expected. The measured control pulse is used to calibrate the amplitude of the spontaneous emission. The frequency of qubit oscillations and a measurement of the control pulse on the output of the cavity together yield a calibration for the gain of the amplifiers, which in turn allows us to determine the efficiency of our single photon source. Simulations that include non-radiative channels of decay and dephasing agree well with the observed data. The homodyne voltage peaks at around 50% of the expected value for an otherwise lossless qubit, due to dephasing. The power efficiency is 80%, larger than for the voltage efficiency because only energy relaxation and not pure dephasing reduces the efficiency in power. It is likely reduced from the maximum 90% due to dephasing during the pulse and in practical use the efficiency may be reduced further from this 80% to separate the control pulse from the emission. By waiting to collect photons, some early emission events are missed, but double photon events due to the control pulse are prevented.

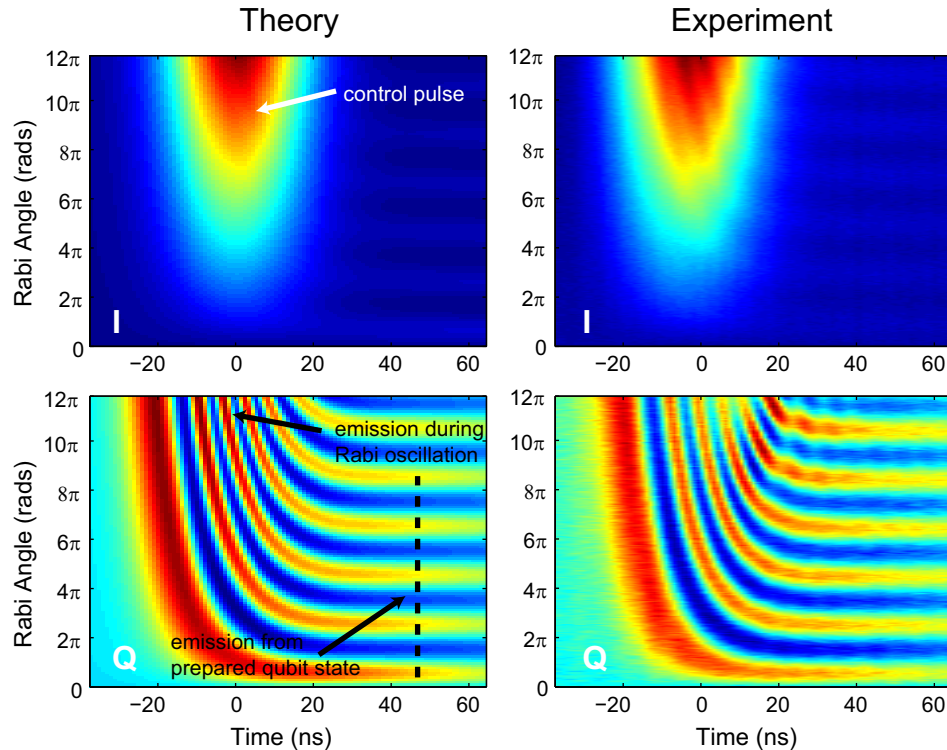


Figure 9.8: Measuring the free induction decay of a single qubit. Theoretical predictions for both quadratures of the homodyne voltage, both in-phase (a) and out-of-phase (b) with the drive, agree well with experimental measurements of the in-phase (c) and out-of-phase (d) signals. Because emission is always orthogonal to the rotation axis, the spontaneous emission and control signal are phase separable. The homodyne sine waves in the previous figure are vertical slices through the emission in d. The frequency of these oscillations, coupled with a gain known from measurements of the control pulse, provide a calibration. The theory presented in b uses this calibration and parameters known from separate measurements to predict the data in d. Because the qubit and drive are slightly detuned by a fluctuating amount due to flux instability (on the order of 3 MHz), there is a slow beat note in the time direction. This fluctuating detuning is modeled by adding two homodyne emissions predictions at ± 1.5 MHz detuning. The fast oscillations in the time domain are a direct measure of the Rabi oscillations of the qubit.

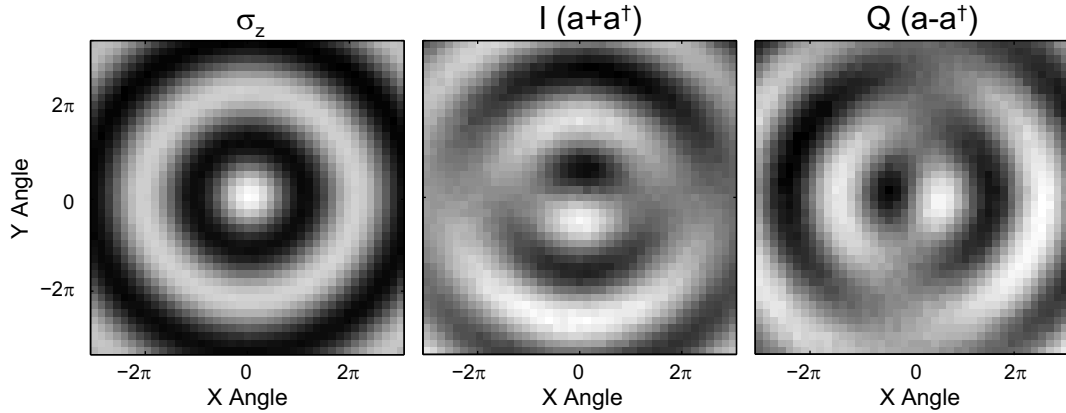


Figure 9.9: Single photon fluorescence tomography. **a)** Measurement of qubit state after rotations by pulses of arbitrary amplitude and phase. Regardless of the phase of the pulse, the qubit oscillates to a peak after a π pulse. **b** and **c.** Fluorescence tomography. The amplitude of the voltage measured in each homodyne quadrature agree with expectations for $\langle \sigma_x \rangle$ and $\langle \sigma_y \rangle$. Oscillations around the x-axis produce a signal in $\langle \sigma_y \rangle$ while none in $\langle \sigma_x \rangle$. This shows the ability to map an arbitrary qubit state onto a photon state, as well as the ability to characterize a qubit state through spontaneous emission.

Using this calibration technique and numerical simulations, complete time dynamics can be predicted to excellent accuracy, as shown for the homodyne voltage in Figure 9.8. Several features of the time dynamics are striking. First, because the control pulse sets the rotation axis, and the qubit state sets the emission phase, the control and generated photons are orthogonal in phase, which allows the two signals to be completely separated in homodyne detection. In the generated photon quadrature, rapid time oscillations are apparent during the control pulse; this is a direct observation of the Rabi oscillation of the qubit through its spontaneous emission. After the pulse, the qubit emits with a phase depending on its final state, resulting in a smooth connection between the time and power oscillations. Finally, there is a very low frequency oscillation in time. Photons are emitted at the qubit frequency, which in the data shown here, is slightly detuned from the drive frequency. The result is a beating, with a half period shown in the image. This beating indicates that there is a slight frequency separation between the input and output photons in addition to the phase and time separations.

Tomography represents an even more powerful tool for characterizing the qubit[Steffen2006] and photon states, and demonstrating a complete mapping of the qubit state onto the photons. Tomography plots a measured quantity ($\langle \sigma_z \rangle$, $\langle a + a^\dagger \rangle$, and $\langle a - a^\dagger \rangle$) as function of control pulses applied with all phases and amplitudes. Here, qubit tomography (of $\langle \sigma_z \rangle$) is measured using a

dispersive measurement of the qubit state $\langle \sigma_z \rangle$. This yields the expected concentric rings for a qubit initially in the ground state. Tomography of the photon state is performed by measuring the fluorescence directly in both homodyne quadratures ($\langle a + a^\dagger \rangle$, and $\langle a - a^\dagger \rangle$). These show excellent agreement with the expected σ_x and σ_y components of the qubit state. This means that a qubit state can be copied onto a photon state, thus transferring information from a stationary qubit to a “flying qubit”, one of the extended DiVincenzo criteria [DiVincenzo2000] for quantum computation.

The mapping of qubit states onto photon states allows for the use of photons as a true resource for quantum information on a chip. This is a convenient means of creating non-classical states of light to interact with atoms, all in the wires of an integrated circuit, allowing them to be shuttled around a chip. This work also stresses the need for true single shot, single photon detectors at microwave frequencies, which would allow for tests of many of the tenets of basic quantum mechanics on a chip. The source presented here has a high efficiency ($> 80\%$), a high repeat rate (~ 100 ns), and is robust to first order noise in the control pulse. Further, it not only generates single photon Fock states, but also any single photon superposition state. These abilities will be important tools for on-chip quantum optics in the microwave regime.

Chapter 10

Future work

The biggest results of this work are not just its current achievements, but in the tradition of science, are new questions, and new ideas for future experiments. These fall into two basic categories. The first class consists of ideas to improve the understanding of current experiments and overcoming current barriers, using this knowledge to make progress towards furthering our understanding of cavity QED and realizing a quantum information processor. The second class combines quantum circuits with other physical systems, allowing the interaction of systems with potentially disparate and interesting properties.

10.1 Evolution of Circuit QED

This work has just scratched the surface of circuit QED. The cavity and Cooper pair box, though already quite remarkable systems, have much room for improvement both in concept and in their fabrication. As we gain control over the interaction of single qubits and cavities, the next logical step is to study the interaction of multiple cavities and qubits. Finally, the knowledge gained in circuit QED can be applied to create new architectures.

10.1.1 New Cavity and Qubit Designs

Substantial progress on improving the cavities and qubits are possible and likely in the next few years. The cavities currently can have quality factors in excess of $Q > 10^5$, but this was essentially a first try. Cavities with similar geometries of $Q \sim 1,000,000$ have already been demonstrated [Day2003], but the limiting factors are not well understood. Though the cavity decay rates are not limiting current experiments they will certainly limit multi-cavity experiments (discussed in the next section). Also cavities are large distributed objects with a very simple energy spectrum; understanding their

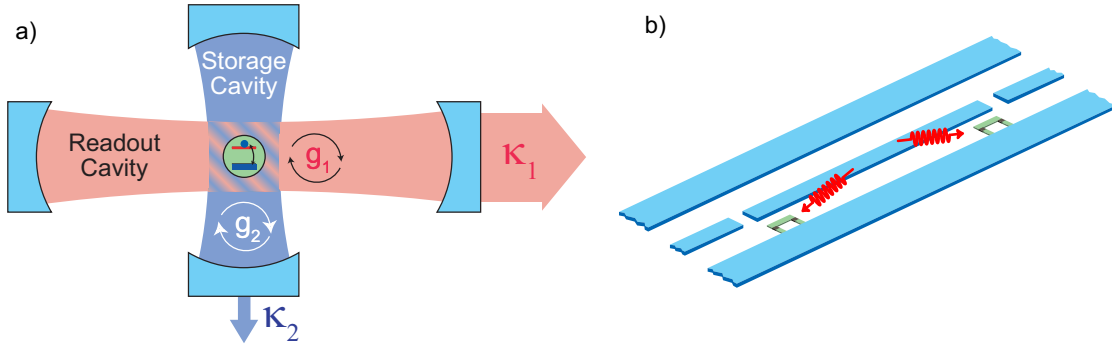


Figure 10.1: a) Schematic of a single artificial “atom” or qubit coupled to two cavities. The qubit would have a separate coupling, g , to each cavity, and the cavities could have different decay rates, κ . One cavity could be optimized for measurement with a very fast κ while the other could be optimized for coherence with very slow κ . b) One could also put two qubits inside the same cavity. Even though the qubits might be centimeters apart and have no direct contact, they could communicate through the cavity. This entanglement bus could avoid many of the pitfalls associated with nearest neighbor interactions.

decay mechanisms may shed insight onto the unknown decay mechanisms afflicting the qubits.

The Cooper pair box was chosen because of familiarity, its large dipole moment, and moderate sensitivity to known dephasing mechanisms. Recently we have begun to rethink the CPB, working with the “transmon,” a CPB in a very different regime, which is nearly immune from charge noise. If this new type of qubit can be mastered it will allow our previous experiments to be performed better, and allow experiments that were impractical or impossible due to charge-based dephasing. While no one knows what causes relaxation in the CPB, there are many culprits and means to eliminate each one. By using a balanced transmission line or by proper balanced design of the CPB-cavity coupling any possible radiation into parasitic modes could be reduced. By using materials with different gaps for the two CPB reservoirs, one might reduce the impact of quasiparticles. By using different deposition techniques, it could be possible to eliminate potentially lossy films (veil of death) that might be causing decay. In addition, other traditional types of superconducting qubits could also be coupled to the cavity in a similar manner. There are also radically different schemes which might use qubits with topological protection, or a way to turn off the coupling between the ground and excited state.

10.1.2 Scaling Circuit QED

The experiments in this work demonstrated control and readout of a single qubit inside of a cavity. Some initial experiments with two qubits in a cavity have already been performed, showing that is

possible to detect them simultaneously 10.1b. It has been difficult to measure the coupling between them because of the number of bias parameters (two charges, and two fluxes, as well as the resonator frequency) which have to be precisely set. Using the new “transmon” design, which eliminates the two charges and the larger couplings that are now regularly attained, all of the technical aspects are ready to study two qubit gates. These experiments would be different from all previous gates in a solid state system in that they would be non-local, interacting with each through the cavity, which is used as an “entanglement bus.”

Another interesting direction to explore is multiple cavities coupled to a single qubit 10.1a. In current experiments there is a trade-off between a high quality factor, useful for exploring quantum optics phenomena, and the fast readout necessary for high fidelity readout of the qubit. By having two cavities each one could be optimized for these tasks separately. Lack of an independent readout was one of the main limiting factors in the photon number splitting experiment (see Sec. 8.3.1). A two cavity implementation of this experiment might realize a practical photon detector or quantum memory.

While it is easy to make a large number of qubits using standard lithography, a functional quantum information processor will require an architecture which allows information to be processed in parallel and transported between distant qubits. An implicit requirement of scalability is direct interaction between distant qubits (or the ability to bring distant qubits together). Cavities could provide a direct long distance coupling between qubits. In order to manage the complexity inherent in having many qubits and many cavities coupled together directly and indirectly, it will be necessary to control the couplings of the cavities and qubits. By loading cavities with active elements such as a SQUID (current work at Chalmers at KTH), one can tune their frequency. A similar scheme could also be used for changing the coupling between resonators. It would be perhaps even more useful to have the ability to turn off the coupling of individual qubits to the cavity. There is a long and interesting road towards making circuit QED a viable architecture for quantum computing, and it is one that promises to be an exciting ride.

10.1.3 Other quantum circuits

The experiments here can be seen as a sample of one way that Josephson elements can be used to control microwaves on the single photon level. They are very non-linear and can be fantastically coherent, and other architectures and uses might be also be productive. One in particular that might

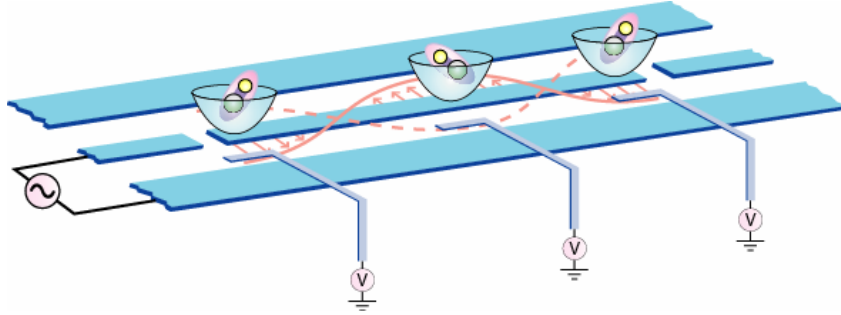


Figure 10.2: Molecules are electrostatically trapped above a coplanar waveguide resonator. The rotational modes of these molecules can be used as qubits and the cavity can be used to cool the molecules into both the rotational and translational ground, where they would be suitable for quantum computation or other investigations.

be exciting is that of transmission lines made from many Josephson elements in series[Yurke1996]. These can have impedances that are unrealizable by any geometric inductance and are quite non-linear. Such systems could be used as the microwave analog of non-linear optical quantum computation, with the advantage that the Josephson element is a much more readily accessible source of single photon non-linearity than is available in the optical domain. More immediately, these could be used as quantum-limited distributed parametric amplifiers which would be useful for all microwave cryogenic experiments.

10.1.4 Hybrid Circuit QED

Circuit QED can be thought of as a versatile platform for manipulating microwave photons, and interacting with non-linear quantum systems at microwave frequencies. Microwaves can be thought of as something of a universal language spoken by circuits, atoms, molecules, nuclear spins and electron spins, as well as phonons in ion traps or nanomechanical systems. The high energy density of the 1D transmission line resonators would allow these systems to be efficiently coupled into an electronic circuit. That would provide a natural path for readout, detection, and even cooling of these systems. One could envision performing cavity QED experiments with any or many of these diverse systems, coupled to a superconducting cavity 10.2. Atoms have hyperfine transitions exploited for atomic clocks, cooling, and quantum computation and ion traps already use microwaves for trapping, just not for computation. Molecules have rotational modes at gigahertz frequencies which could be used[Andre2006, Rabl2006]. One could also envision coupling to nuclear or electron[Lyon2006] spins which have Zeeman splittings from MHz to GHz. Nanomechanical systems can have resonant

frequencies up to about a gigahertz and be made to couple electrostatically or magnetically to a transmission line[Irish2003]. There are nearly limitless possibilities and it will be interesting to see which ones have the most impact.

Chapter 11

Conclusions

The result of this thesis work is the development of circuit QED, which is a platform upon which many interesting experiments in quantum information and cavity QED have been and will be performed. Circuits are incredibly versatile, they can be quite coherent ($Q > 10^6$), their electrical properties (like impedance) can be varied over 10 orders of magnitude, easily connecting elements from meters to nanometers, and are made through well-understood, scalable, fabrication techniques. Quantum circuits provides an immense opportunity to develop new experiments, with new geometries and topologies that might be difficult or impossible in natural physical systems. In this work we have used this versatility to explore very different regimes of cavity QED, performing many experiments which I hope will inspire even deeper study of these interesting topics.

One of the most important contributions was to harness light (the quantum aspects at least) as a resource for quantum circuits and solid-state quantum computation. The quantum nature of microwave radiation is not usually exploited, even when dealing with quantum circuits, but single microwave photons have great potential to act as carriers of quantum information. Their small energy ($\mu\text{eV's}$) and large spatial extent (cm's) stretch the limits of our concept of the photon, but have the advantage of being guided by wires, which could be up to 10 km long based on current experiments. Our first experiment[Wallraff2004] demonstrated the potential for coupling qubits to single photons. Later experiments generating[Houck2007] and measuring[Schuster2007] single photons began to provide first steps towards exploiting this coupling. I hope among other things that they will provoke interest in and perhaps create a path to the creation of quantum (un)limited amplifiers and single photon counters, which would improve the efficiency of cryogenic microwave measurements by at least two orders of magnitude (current cryogenic amplifiers have $T_N \sim 10\text{ K}$).

There is still a great mystery which remains unsolved: What causes decoherence in superconducting qubits? While we still have no definitive answer, we have made significant progress. One goal of the circuit QED architecture is to simplify the qubit circuit, making a very clean system. The cavity is used to create a well-controlled electromagnetic environment, allowing us to model and observe the radiative decay of the qubit. The simplicity of the system allowed us to fully model the measurement process of the qubit, verifying our control of the qubit. Finally, in our initial development of the “transmon,” we have begun the process of eliminating the effect of charge noise, which is primarily responsible for the inhomogeneous broadening of the qubit. Fully understanding the implications of this new type of qubit will be the subject of future theses, but is very promising for obtaining long coherence times.

I hope that the reader has come to be as excited about this subject as the author and will pardon the author’s inability to do it justice.

Appendix A

Operators and Commutation Relations

A.1 Harmonic Oscillators

$$[a, a^\dagger] = 1 \quad (\text{A.1})$$

$$[a, a^\dagger a] = a \quad (\text{A.2})$$

$$[a^\dagger, a^\dagger a] = -a^\dagger \quad (\text{A.3})$$

A.2 Spin 1/2

$$[\sigma_+, \sigma_-] = \sigma_z \quad (\text{A.4})$$

$$[\sigma_\pm, \sigma_z] = \mp 2\sigma_\pm \quad (\text{A.5})$$

$$[\sigma_i, \sigma_j] = 2i\epsilon_{ijk} \sigma_k \quad (\text{A.6})$$

Where $i, j \in \{x, y, z\}$ and ϵ_{ijk} is the Levi-Cevita tensor (if $i = j$ then $\epsilon_{ijk} = 0$ else k is the remaining index and it is $\epsilon_{ijk} = \pm 1$ if the i, j, and k are cyclic or acyclic.)

A.3 Jaynes-Cummings Operators

Note that the operator $(\sigma^+ a - a^\dagger \sigma^-, a^\dagger a)$ used is not the dipole interaction operator itself but a unitary operator which can be used to diagonalize it approximately to second order.

A.3.1 Interaction with Harmonic oscillator operators

$$[\sigma^+ a - a^\dagger \sigma^-, a^\dagger a] = \sigma^+ a + a^\dagger \sigma^- \quad (\text{A.7})$$

$$[\sigma^+ a - a^\dagger \sigma^-, a] = \sigma^- \quad (\text{A.8})$$

$$[\sigma^+ a - a^\dagger \sigma^-, a^\dagger] = \sigma^+ \quad (\text{A.9})$$

A.3.2 Interaction with Spin 1/2 Operators

$$[\sigma^+ a - a^\dagger \sigma^-, \sigma_z] = -2(\sigma^+ a + a^\dagger \sigma^-) \quad (\text{A.10})$$

$$[\sigma^+ a - a^\dagger \sigma^-, \sigma^\pm] = \pm \sigma_z a \quad (\text{A.11})$$

Appendix B

Derivation of Dressed State Atom Picture

The Jaynes-Cummings Hamiltonian:

$$H_{JC} = \hbar\omega_r(a^\dagger a + 1/2) + \hbar\frac{\omega_a}{2}\sigma_z + \hbar g(a^\dagger\sigma^- + a\sigma^+) \quad (\text{B.1})$$

has the convenient property that it conserves excitation number, or more specifically it only connects nearest atom and photon levels together. In matrix form the Hamiltonian can be represented by the ground state and an infinite block diagonal matrix of 2x2 matrices of the form:

$$\begin{pmatrix} (0) & & & & 0 \\ \left(\begin{array}{cc} \omega_r & g \\ g & (\omega_r + \Delta) \end{array} \right) & & & & \\ & \left(\begin{array}{cc} 2\omega_r & g\sqrt{2} \\ g\sqrt{2} & \omega_r + (\omega_r + \Delta) \end{array} \right) & & & \\ & & \ddots & & \\ 0 & & & \left(\begin{array}{cc} n\omega_r & g\sqrt{n} \\ g\sqrt{n} & (n-1)\omega_r + (\omega_r + \Delta) \end{array} \right) & (\text{B.2}) \end{pmatrix}$$

where $\omega_a = \omega_r + \Delta$ and n is the number of excitations (photons + 0 or 1 excitation in the atom). Because of this simple form each block can be diagonalized directly (and independently). The eigenvalues of the n^{th} submatrix are as in Eq. 2.4:

$$\begin{aligned} E_{\pm,n} &= \frac{\hbar}{2} \left((n-1)\omega_r + \omega_a \pm \sqrt{4ng^2 + \Delta^2} \right) \\ E_{g,0} &= -\frac{\hbar\Delta}{2} \end{aligned} \quad (\text{B.3})$$

The corresponding eigenstates in raw form (unnormalized and no trig substitutions) are:

$$|\overline{+,n}\rangle = A \left(-\frac{\Delta + \sqrt{4g^2n + \Delta^2}}{2g\sqrt{n}} |g,n\rangle + |e,n-1\rangle \right) \quad (\text{B.4})$$

$$|\overline{-,n}\rangle = B \left(-\frac{\Delta - \sqrt{4g^2n + \Delta^2}}{2g\sqrt{n}} |g,n\rangle + |e,n-1\rangle \right) \quad (\text{B.5})$$

The square root terms have a very Pythagorean look to them and so one can try to introduce an angle

$$\theta_n = \frac{1}{2} \arctan \left(\frac{2g\sqrt{n}}{\Delta} \right) \quad (\text{B.6})$$

With a bit of work (or the right line of Mathematica) one can arrive at the rather beautiful solution for the eigenstates

$$|\overline{-,n}\rangle = \cos \theta_n |g,n\rangle - \sin \theta_n |e,n-1\rangle \quad (\text{B.7})$$

$$|\overline{+,n}\rangle = \sin \theta_n |g,n\rangle + \cos \theta_n |e,n-1\rangle$$

Because the qubit now has a photon component it can decay into the transmission line. This corresponds to going from $|\overline{+,n}\rangle$ to $|\overline{-,n-1}\rangle$, which means that we have lost one excitation and gone from a state which was mostly excited state qubit to mostly ground state qubit (see Fig. B.1). The decay can be modeled as a term that couples the photons inside the cavity to the transmission line mode (b and b^\dagger), which looks like¹

$$H_\kappa = \sqrt{\kappa} (b^\dagger a + a^\dagger b) \quad (\text{B.8})$$

In this language the Fermi Golden Rule can be expressed as

$$\gamma_\kappa = \left| \langle \overline{-,n-1} | \langle 1 | \sqrt{\kappa} (b^\dagger a + a^\dagger b) | 0 \rangle | \overline{+,n} \rangle \right|^2 \quad (\text{B.9})$$

Note that the b will not act if the transmission line is empty (as is assumed above).² The expression can then be simplified to

¹Eq. B.8 is an approximation which is based on the coupling of a single mode cavity to a continuum of bath modes. If the bath has frequency structure on the scale of κ a more sophisticated treatment is necessary [Walls2006].

²If amplifier noise or some other source populated the transmission line one could add this in by making n in the b -mode be nonzero, which would give a rate to heat the qubit-cavity system.

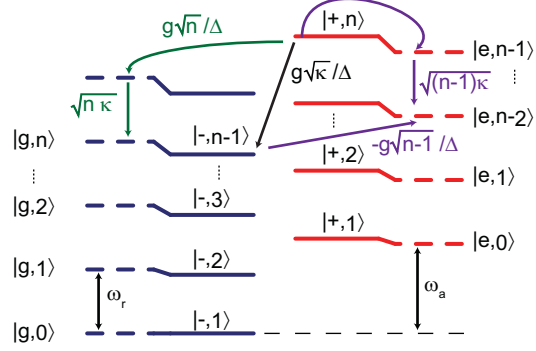


Figure B.1: Radiative atom decay paths in presence of coherent cavity coupling. The net *amplitude* for a path is found by multiplying the rate of each segment. In the green path, the small part of the qubit excitation which lives in the cavity is emitted from the cavity leaving the photon number the same but the atom decayed. At the same time as the purple path shows it is possible for the atom to absorb a photon (hence the minus sign) from this decayed state, resulting in an ordinary photon decay with no implications on the qubit state. These rates add coherently with the n's canceling leaving only a net rate amplitude (black) $g\sqrt{\kappa}/\Delta$ which gives the usual $\gamma_\kappa = (\frac{g}{\Delta})^2 \kappa$ decay rate.

$$\gamma_\kappa = \kappa |\langle \overline{-, n-1} | a | \overline{+, n} \rangle|^2 \quad (\text{B.10})$$

Expressing the eigenstates in the qubit/photon basis (rather than the \pm , excitation basis, it is straight forward to evaluate this matrix element. Though it is not hard to evaluate the exact expressions to gain a bit of intuition let us first use the approximate (to order g/Δ) eigenstates

$$\begin{aligned} |\overline{-, n}\rangle &= |g, n\rangle - \frac{g\sqrt{n}}{\Delta} |e, n-1\rangle \\ |\overline{+, n}\rangle &= \frac{g\sqrt{n}}{\Delta} |g, n\rangle + |e, n-1\rangle \end{aligned} \quad (\text{B.11})$$

Substituting into eq. B.10 and remembering that $a |n\rangle = \sqrt{n} |n-1\rangle$

$$\gamma_\kappa = \kappa \left| \left(\langle g, n-1 | - \frac{g\sqrt{n-1}}{\Delta} \langle e, n-2 | \right) a \left(\frac{g\sqrt{n}}{\Delta} |g, n\rangle + |e, n-1\rangle \right) \right|^2 \quad (\text{B.12})$$

$$\gamma_\kappa = \kappa \left| \sqrt{n} \frac{g\sqrt{n}}{\Delta} - \sqrt{n-1} \frac{g\sqrt{n-1}}{\Delta} \right|^2$$

$$\gamma_\kappa = \left(\frac{g}{\Delta} \right)^2 \kappa \quad (\text{B.13})$$

Note that due to the amazing properties of the harmonic oscillator that γ_κ does not depend on n (to first order). This can be seen as the coherent interference between the two decay paths (see Fig.

B.1), represented by the matrix elements inside eq. B.12. The expression using the full eigenstates is

$$\begin{aligned}\gamma_\kappa &= \kappa |(\cos \theta_{n-1} \langle g, n-1 | - \sin \theta_{n-1} \langle e, n-2 |) a (\sin \theta_n |g, n\rangle + \cos \theta_n |e, n-1\rangle)|^2 \\ \gamma_\kappa &= \kappa |\sqrt{n} \sin \theta_n \cos \theta_{n-1} - \sqrt{n-1} \sin \theta_{n-1} \cos \theta_n|^2\end{aligned}\quad (\text{B.14})$$

With these exact expressions we can also find the radiative decay in the resonant limit $\Delta \rightarrow 0$. Substituting this into eq. B.6 gives $\theta_n \rightarrow \pi/4$, substituting this result into eq. B.14, for $n \geq 2$ yields

$$\lim_{\Delta \rightarrow 0} \gamma_\kappa = \frac{\kappa}{4} |\sqrt{n} - \sqrt{n-1}|^2 \quad (\text{B.15})$$

When calculating the special case of $n = 1$, the unique ground state must be taken into account¹.

$$\gamma_\kappa^{n=1} = \kappa |\langle g, 0 | a |+, 1\rangle|^2 \quad (\text{B.16})$$

$$\lim_{\Delta \rightarrow 0} \gamma_\kappa^{n=1} = \kappa \left| \langle g, 0 | a \frac{1}{\sqrt{2}} (|g, 1\rangle + |e, 0\rangle) \right|^2 = \kappa/2$$

¹In the dispersive limit to first order the uniqueness of the ground state can be neglected because the matrix element for mixing is zero anyway, but in the resonant limit the mixing is by definition of order unity

Appendix C

Mathematica Notebooks

C.1 Cooper Pair Box

Appendix D

Recipes

This Appendix will present recipes and descriptions of the fabrication process.

1. Sonicate fresh wafer in NMP 60s
2. Sonicate wafer in Acetone 60s
3. Sonicate wafer in Methanol 60s
4. Sonicate wafer in DI water 60s
5. Blow dry with N_2 and then bake at 110° 120s
6. Spin LOR5A at 4000 rpm for 60s
7. Bake at 195°C for 15 minutes
8. Spin S1808 at 4000 rpm for 60s
9. Bake at 115°C for 60s
10. Expose in hard contact mode for 3.3s at 9.3mW/cm² on 365nm line.
11. Develop in 300 mL of MF-319 for 140s (for ~ 500 nm undercut)

Table D.1: This is an optical lithography recipe to achieve, resist bilayer profile of 800 nm of S1808 on top of 500 nm of LOR 5A with 500 nm undercut.

PMMA/MMA bilayer spinning recipe

1. Sonicate fresh wafer in NMP 60s
2. Sonicate wafer in Acetone 60s
3. Sonicate wafer in Methanol 60s
4. Do NOT sonicate wafer in DI water (PMMA is hydrophobic)
5. Blow dry with N_2 and then bake at 110° 120s
6. Spin MMA EL13 at 4000 rpm for 60s
7. Bake at 170°C for 60s (under petri dish propped up on slides)
8. Spin PMMA 950k A3 at 4000 rpm for 60s
9. Bake at 170°C for 30min

Table D.2: When followed correctly this recipe should result in a PMMA-MMA bilayer with ~ 550 nm of MMA and ~ 120 nm of PMMA on top.

PMMA development recipe

1. Pour 30 mL of **MIBK:IPA 1:3** at $25^{\circ}C$ into small beaker
2. Pour 30 mL of **isopropyl alcohol (IPA)** at $25^{\circ}C$ into small beaker
3. Using self-closing tweezers gently shake chip vertically in **MIBK** solution for **48s**
4. Immediately put chip into **IPA** for **10s**
5. Blow dry with N_2

Table D.3: This recipe is not very sensitive to any of the parameters. The developer should be at room temperature but in my experience \pm a one or two degrees in temperature does not hurt. To minimize fluctuations one can keep a store of MIBK solution in a hot water bath a few degrees above room temperature. One should always be very consistent with the development time but if one should leave the chip in for a few seconds to long in the developer it will probably still come out (for > 100 nm feature at least). The isopropyl alcohol is used mainly as a stop to the development, but will etch the resist, so don't just leave it in there.

Niobium Sputtering Recipe

1. Load sample in Leaker sputter system on a stainless wafer holder, with a 3/64" thick, 2" diameter copper disk on the back of the wafer.

2. Check that the base pressure is about 2x10-8 Torr before deposition.

3. Turn on all cooling water supplies.

4. Presputter Nb from the 2" torus dc magnetron sputter gun for 2 minutes. Note that the parameters should be argon=1.3 mTorr; 350 W.

5. Switch off the ion gauge;

6. Set conductance controller to 4.0;

7. Close the conductance controller switch;

8. Close the CHAM INTERLOCK valve;

9. Switch on station gas AR3;

10. Switch on the capacitance manometer;

11. Switch on the flow controller (FC) main;

12. Switch on FC channel 1;

13. Turn the capacitance manometer controller to "AUTO";

14. Set pressure to 1.3 mTorr;

15. Set the 1 kW switch to gun E (Niobium);

16. Switch on the 1 kW power supply;

17. Fix the setpoint at 40 W;

18. Switch on "OUTPUT" to start plasma (light violet);

19. Increase the setpoint to about 350 W

20. Presputter for 2 minutes;

21. Decrease the setpoint to 40 W;

22. Set pressure to 0 mTorr;

23. Open the CHAM INTERLOCK valve.

24. Ion beam clean the wafer for 1.5 minutes.

25. Sputter Nb to desired thickness: Note that the parameters should be argon=1.3 mTorr and 350 W; rate=1.25 nm/s. Source to sample distance is approximately 3 inches. The Nb thickness should be kept below 300 nm to reduce the probability of photoresist cracking or peeling during the sputter deposition.

26. Close the CHAM INTERLOCK valve;

27. Set pressure to 1.3 mTorr;

28. Switch on "OUTPUT" to start plasma (light violet);

29. Increase the setpoint at 350 W;

30. Open shutter E (sputtering time 150 seconds for Nb thickness of 190 nm);

31. To shut down, close shutter E;

Electron Beam Evaporation Recipe

1. Pump out chamber to $\sim 3 \times 10^{-7}$. Takes about 2 hours.
2. Evaporate a few nanometers of **titanium** (not on the sample) to lower the pressure to $\sim 1 \times 10^{-7}$.
3. Evaporate 30 nm aluminum at **0°** from normal
4. Wait **2 min.**
5. Put 85/15 Argon/Oxygen mix in at **3 Torr** for **12 min.**
6. Pump chamber down, should get to 5×10^{-7} in a few minutes.
7. Evaporate 100 nm aluminum at **32°** from normal
8. Wait **2 min.**
9. Put 70/30 Argon/Oxygen mix in at **3 Torr** for **10 min.**
10. Place sample in a vertical or slightly inverted holder, for 20 minutes in 50 mL of acetone at 70°C
11. Squirt sample with hot acetone from a syringe, this should take the whole metal film off in one squirt.
12. Place beaker in sonicator, wait 30s for it to cool, then sonicate for 60s.

Table D.5: This is the deposition recipe for making tunnel junctions. It typically results in a critical current density of approximately $\sim 40 \text{ A/cm}^2$. The junctions can be evaporated at pressures as high as 2×10^{-6} but they seem to age less consistently than when a longer pump down time is used. I have not systematically varied the length of time or pressure of the oxidation step, so I cannot say how sensitive this parameter is, with any certainty, though others say that it is not very sensitive. A wide degree of lift-off times and temperatures can be used. If it lifts off smoothly its probably fine.

Bibliography

- [Aragam1961] Abragam. *The principles of nuclear magnetism*. Oxford University Press, 1961.
- [Andre2006] A. Andre, D. Demille, J. M. Doyle, M. D. Lukin, S. E. Maxwell, P. Rabl, R. J. Schoelkopf, and P. Zoller. A coherent all-electrical interface between polar molecules and mesoscopic superconducting resonators. *Nature Physics*, 2(9):636–642, September 2006.
- [Arscott1964] F. M. Arscott. *Periodic Differential Equations*. Pergamon Press, 1964.
- [Astafiev2004] O. Astafiev, Y. A. Pashkin, T. Yamamoto, Y. Nakamura, and J. S. Tsai. Single-shot measurement of the Josephson charge qubit. *Physical Review B*, 69(18):180507, May 2004.
- [Aumentado2004] J. Aumentado, Mark W. Keller, John M. Martinis, and M. H. Devoret. Nonequilibrium quasiparticles and $2e$ periodicity in single-cooper-pair transistors. *Phys. Rev. Lett.*, 92(6):066802–4, February 2004.
- [Averin2003] D. V. Averin and C. Bruder. Variable electrostatic transformer: Controllable coupling of two charge qubits. *Physical Review Letters*, 91(5):057003, August 2003.
- [Basche1992] Th. Basch, W. E. Moerner, M. Orrit, and H. Talon. Photon antibunching in the fluorescence of a single dye molecule trapped in a solid. *Phys. Rev. Lett.*, 69(10):1516–, September 1992.
- [Bennett1982] C. H. Bennett. The thermodynamics of computation - a review. *International Journal Of Theoretical Physics*, 21(12):905–940, 1982.

- [Bennett1984] C. H. Bennett and G. Brassard. Proceedings of ieee international conference on computers, systems, and signal processing, bangalore, india. page 175. IEEE, New York, 1984, 1984.
- [Bennett1992] C. H. Bennett, G. Brassard, and N. D. Mermin. Quantum cryptography without Bell theorem. *Physical Review Letters*, 68(5):557–559, February 1992.
- [Berman1994] P. R. Berman, editor. *Cavity quantum electrodynamics*. Academic Press, 1994.
- [Bertet2002] P. Bertet, A. Auffeves, P. Maioli, S. Osnaghi, T. Meunier, M. Brune, J. M. Raimond, and S. Haroche. Direct measurement of the Wigner function of a one-photon Fock state in a cavity. *Physical Review Letters*, 89(20):200402, November 2002.
- [Bertet2004] P. Bertet, I. Chiorescu, G. Burkard, K. Semba, C. J. P. M. Harmans, D.P. DiVincenzo, and J. E. Mooij. Relaxation and dephasing in a flux qubit. *cond-mat/0412485*, 2004.
- [Bertet2007] P. Bertet (private communication). 2007.

- [Birnbaum2005] K. M. Birnbaum, A. Boca, R. Miller, A. D. Boozer, T. E. Northup, and H. J. Kimble. Photon blockade in an optical cavity with one trapped atom. *Nature*, 436(7047):87–90, July 2005.

Comment: 10.1038/nature03804

- [Blais2004] A. Blais, R.S. Huang, A. Wallraff, S. Girvin, and R. J. Schoelkopf. Cavity quantum electrodynamics for superconducting electrical circuits: an architecture for quantum computation. *Physical Review A*, 69:062320, 2004.
- [Born2004] D. Born, V. I. Shnyrkov, W. Krech, T. Wagner, E. Il’ichev, M. Grajcar, U. Hubner, and H. G. Meyer. Reading out the state inductively and microwave spectroscopy of an interferometer-type charge qubit. *Physical Review B*, 70(18):180501, November 2004.
- [Boroditsky1999] M. Boroditsky, T. F. Krauss, R. Caccioli, R. Vrijen, R. Bhat, and E. Yablonovitch. Light extraction from optically pumped light-emitting diode by thin-slab photonic crystals. *Applied Physics Letters*, 75(8):1036–1038, August 1999.

- [Bouchiat1998] V. Bouchiat, D. Vion, P. Joyez, D. Esteve, and M. H. Devoret. Quantum coherence with a single Cooper pair. *Physica Scripta*, T76:165–170, 1998.

- [Braff2007] and Gambetta J. Braff, W. A., S. M. Girvin, and R. J. Schoelkopf. Protocols for optimal readout of qubits using a continuous quantum nondemolition measurement. *submitted to PRA*, 2007.
- [Brattke2001] Simon Brattke, Benjamin T. H. Varcoe, and Herbert Walther. Generation of photon number states on demand via cavity quantum electrodynamics. *Phys. Rev. Lett.*, 86(16):3534–, April 2001.
- [Brune1990] M. Brune, S. Haroche, V. Lefevre, J. M. Raimond, and N. Zagury. Quantum nondemolition measurement of small photon numbers by Rydberg-atom phase-sensitive detection. *Physical Review Letters*, 65(8):976–979, August 1990.
- [Brune1994] M. Brune, P. Nussenzveig, F. Schmidtkaler, F. Bernardot, A. Maali, J. M. Raimond, and S. Haroche. From Lamb shift to light shifts: vacuum and subphoton cavity fields measured by atomic phase-sensitive detection. *Physical Review Letters*, 72(21):3339–3342, May 1994.
- [Brune1996] M. Brune, F. SchmidtKaler, A. Maali, J. Dreyer, E. Hagley, J. M. Raimond, and S. Haroche. Quantum Rabi oscillation: A direct test of field quantization in a cavity. *Physical Review Letters*, 76(11):1800–1803, March 1996.
- [Brunel1999] Christian Brunel, Brahim Lounis, Philippe Tamarat, and Michel Orrit. Triggered source of single photons based on controlled single molecule fluorescence. *Phys. Rev. Lett.*, 83(14):2722–, October 1999.
- [Buttiker1987] M. Buttiker. Zero-current persistent potential drop across small-capacitance josephson junctions. *Phys. Rev. B*, 36(7):3548–, September 1987.
- [Caves1980] C. M. Caves, K. S. Thorne, R. W. P. Drever, V. D. Sandberg, and M. Zimmermann. On the measurement of a weak classical force coupled to a quantum-mechanical oscillator. *Reviews of Modern Physics*, 52(2):341–392, 1980.
- [Chiorescu2004] I. Chiorescu, P. Bertet, K. Semba, Y. Nakamura, C. J. Harmans, and J. E. Mooij. Coherent dynamics of a flux qubit coupled to a harmonic oscillator. *Nature*, 431(7005):159–162, September 2004.

- [Clauser1974] John F. Clauser. Experimental distinction between the quantum and classical field-theoretic predictions for the photoelectric effect. *Phys. Rev. D*, 9(4):853–, February 1974.
- [Collin2004] E. Collin, G. Ithier, A. Aassime, P. Joyez, D. Vion, and D. Esteve. NMR-like control of a quantum bit superconducting circuit. *Physical Review Letters*, 93(15):157005, October 2004.
- [Cory1997] D. G. Cory, A. F. Fahmy, and T. F. Havel. Ensemble quantum computing by NMR spectroscopy. *Proceedings of the National Academy of Sciences of the United States of America*, 94(5):1634–1639, March 1997.
- [Cottet2002] A. Cottet. *Implementation of a quantum bit in a superconducting circuit*. PhD thesis, l'Universite Paris VI, 2002.

- [Darquie2005] B. Darquie, M. P. A. Jones, J. Dingjan, J. Beugnon, S. Bergamini, Y. Sortais, G. Messin, A. Browaeys, and P. Grangier. Controlled single-photon emission from a single trapped two-level atom. *Science*, 309(5733):454–456, July 2005.

Abstract: By illuminating an individual rubidium atom stored in a tight optical tweezer with short resonant light pulses, we created an efficient triggered source of single photons with a well-defined polarization. The measured intensity correlation of the emitted light pulses exhibits almost perfect antibunching. Such a source of high-rate, fully controlled single-photon pulses has many potential applications for quantum information processing.

Comment: 10.1126/science.1113394

- [Day2003] P. K. Day, H. G. LeDuc, B. A. Mazin, A. Vayonakis, and J. Zmuidzinas. A broadband superconducting detector suitable for use in large arrays. *Nature*, 425(6960):817–821, October 2003.

- [Deutsch1985] D. Deutsch. Quantum-theory, the Church-Turing principle and the universal quantum computer. *Proceedings of the royal society of London series A - mathematical physical and engineering sciences*, 400(1818):97–117, 1985.

- [Deutsch2000] I. H. Deutsch, G. K. Brennen, and P. S. Jessen. Quantum computing with neutral atoms in an optical lattice. *Fortschritte Der Physik-Progress of Physics*, 48(9-11):925–943, 2000.
- [Devoret2003] M. Devoret. Superconducting qubits. In *Les Houches Summer School Proceedings 79*, 2003.
- [Devoret2004] M. H. Devoret, A. Wallraff, and J. M. Martinis. Superconducting qubits: A short review, 2004.
- [DiVincenzo2000] David P. DiVincenzo. The physical implementation of quantum computation. *Fortschritte der Physik*, 48(9-11):771–783, 2000.
- [Diddams2001] S. A. Diddams, T. Udem, J. C. Bergquist, E. A. Curtis, R. E. Drullinger, L. Hollberg, W. M. Itano, W. D. Lee, C. W. Oates, K. R. Vogel, and D. J. Wineland. An optical clock based on a single trapped Hg-199(+) ion. *Science*, 293(5531):825–828, August 2001.
- [Diedrich1987] Frank Diedrich and Herbert Walther. Nonclassical radiation of a single stored ion. *Phys. Rev. Lett.*, 58(3):203–, January 1987.
- [Duan2001] L.-M. Duan, M. D. Lukin, J. I. Cirac, and P. Zoller. Long-distance quantum communication with atomic ensembles and linear optics. *Nature*, 414(6862):413–418, November 2001.
- [Duty2004] T. Duty, D. Gunnarsson, K. Bladh, and P. Delsing. Coherent dynamics of a josephson charge qubit. *Physical Review B*, 69(14):140503, April 2004.
- [Duty2005] T. Duty, G. Johansson, K. Bladh, D. Gunnarsson, C. Wilson, and P. Delsing. Observation of quantum capacitance in the cooper-pair transistor. *Physical Review Letters*, 95(20):206807, November 2005.
- [Dykman1987] M. I. Dykman and M. A. Krivoglaz. Profiles of no-phonon lines of impurity centers interacting with local quasilocal vibrations. *Sov. Phys. Solid State*, 29:210 – 214, 1987.
- [Eroms2006] J. Eroms, L. C. van Schaarenburg, E. F. C. Driessens, J. H. Plantenberg, C. M. Huizinga, R. N. Schouten, A. H. Verbruggen, C. J. P. M. Harmans, and J. E. Mooij. Low-

- frequency noise in Josephson junctions for superconducting qubits. *Applied Physics Letters*, 89(12):122516, September 2006.
- [Feynman1982] R. P. Feynman. Simulating physics with computers. *International journal of theoretical physics*, 21(6-7):467–488, 1982.
- [Frunzio2005] L. Frunzio, A. Wallraff, D. Schuster, J. Majer, and R. Schoelkopf. Fabrication and characterization of superconducting circuit QED devices for quantum computation. *IEEE Transactions On Applied Superconductivity*, 15(2):860–863, June 2005.
- [Gambetta2006] J. Gambetta, Blais A., Schuster D. I., A. Wallraff, L. Frunzio, J. Majer, S. M. Girvin, and R. J. Schoelkopf. Qubit-photon interactions in a cavity: Measurement induced dephasing and number splitting. *Physical Review A*, 74:042318, 2006.
- [Gershenfeld1997] N. A. Gershenfeld and I. L. Chuang. Bulk spin-resonance quantum computation. *Science*, 275(5298):350–356, January 1997.
- [Gleyzes2007] Sebastien Gleyzes, Stefan Kuhr, Christine Guerlin, Julien Bernu, Samuel Deleglise, Ulrich Busk Hoff, Michel Brune, Jean-Michel Raimond, and Serge Haroche. Observing the quantum jumps of light: birth and death of a photon in a cavity, 2006.
- [Griffiths1999] David J. Griffiths. *Introduction to electrodynamics*. Prentice Hall, 3 edition, 1999.
- [Grover1997] L. K. Grover. Quantum mechanics helps in searching for a needle in a haystack. *Physical review letters*, 79(2):325–328, July 1997.
- [Hauser1964] J. J. Hauser and H. C. Theuerer. Superconducting tantalum films. *Rev. Mod. Phys.*, 36(1):80–83, Jan 1964.
- [Hood2000] C. J. Hood, T. W. Lynn, A. C. Doherty, A. S. Parkins, and H. J. Kimble. The atom-cavity microscope: Single atoms bound in orbit by single photons. *Science*, 287(5457):1447–1453, February 2000.
- [Houck2007] A. A. Houck, D. I. Schuster, J. M. and Schreier J. A. , Gambetta, B. Johnson, J. Majer, A. Wallraff, A. Blais, L. Frunzio, M. H. Devoret, S. M. Girvin, and R. J. Schoelkopf. Generating single microwave photons in a circuit. *submitted to Nature*, 2007.

- [Huelga1997] S. F. Huelga, C. Macchiavello, T. Pellizzari, A. K. Ekert, M. B. Plenio, and J. I. Cirac. Improvement of frequency standards with quantum entanglement. *Physical Review Letters*, 79(20):3865–3868, November 1997.
- [Imamoglu1994] A. Imamoglu and Y. Yamamoto. Turnstile device for heralded single photons: Coulomb blockade of electron and hole tunneling in quantum confined p-i-n heterojunctions. *Phys. Rev. Lett.*, 72(2):210–, January 1994.
- [Ioffe2004] L. B. Ioffe, V. B. Geshkenbein, C. Helm, and G. Blatter. Decoherence in superconducting quantum bits by phonon radiation. *Physical Review Letters*, 93(5):057001, July 2004.
- [Irish2003] E. K. Irish and K. Schwab. Quantum measurement of a coupled nanomechanical resonator - Cooper pair box system. *Physical Review B*, 68(15):155311, October 2003.
- [Josephson1962] B. D. Josephson. Possible new effects in superconductive tunnelling. *Physics Letters*, 1(7):251–253, 1962.
- [Keller2004] Matthias Keller, Birgit Lange, Kazuhiro Hayasaka, Wolfgang Lange, and Herbert Walther. Continuous generation of single photons with controlled waveform in an ion-trap cavity system. *Nature*, 431(7012):1075–1078, October 2004.

Comment: 10.1038/nature02961

- [Kim1999] J. Kim, O. Benson, H. Kan, and Y. Yamamoto. A single-photon turnstile device. *Nature*, 397(6719):500–503, February 1999.

Comment: 10.1038/17295

- [Kimble1977] H. J. Kimble, M. Dagenais, and L. Mandel. Photon antibunching in resonance fluorescence. *Phys. Rev. Lett.*, 39(11):691–, September 1977.

- [Kittel1996] C. Kittel. *Introduction to Solid State Physics*. Wiley, 1996.

- [Knill2001] E. Knill, R. Laflamme, and G. J. Milburn. A scheme for efficient quantum computation with linear optics. *Nature*, 409(6816):46–52, January 2001.

- [Koch2007] J. Koch, A. Houck, Schuster D. I., J. Gambetta, Blais A., , A. Wallraff, L. Frunzio, J. Majer, S. M. Girvin, and R. J. Schoelkopf. Transmon paper. *submitted to PRA*, 2007.

- [Kuhn2002] Axel Kuhn, Markus Hennrich, and Gerhard Rempe. Deterministic single-photon source for distributed quantum networking. *Phys. Rev. Lett.*, 89(6):067901–, July 2002.
- [Kuhr2006] Stefan Kuhr, Sébastien Gleyzes, Christine Guerlin, Julien Bernu, Ulrich Busk Hoff, Samuel Deleglise, Michel Brune, Jean-Michel Raimond, Serge Haroche, Stefano Osnaghi, E. Jacques, P. Bosland, and B. Visentin. An ultrahigh finesse fabry-perot superconducting resonator as a photon box for cavity-qed experiments, 2006.
- [Kurtsiefer2000] Christian Kurtsiefer, Sonja Mayer, Patrick Zarda, and Harald Weinfurter. Stable solid-state source of single photons. *Phys. Rev. Lett.*, 85(2):290–, July 2000.
- [Landauer1991] R. Landauer. Information is physical. *Physics Today*, 44(5):23–29, May 1991.
- [Leibfried1996] D. Leibfried, D. M. Meekhof, B. E. King, C. Monroe, W. M. Itano, and D. J. Wineland. Experimental determination of the motional quantum state of a trapped atom. *Physical Review Letters*, 77(21):4281–4285, November 1996.
- [Leibfried1997] D. Leibfried, D. M. Meekhof, C. Monroe, B. E. King, W. M. Itano, and D. J. Wineland. Experimental preparation and measurement of quantum states of motion of a trapped atom. *Journal of Modern Optics*, 44(11-12):2485–2505, 1997.
- [Loss1998] Daniel Loss and David P. DiVincenzo. Quantum computation with quantum dots. *Physical Review A*, 57(1):120–126, Jan 1998.
- [Lounis2000] B. Lounis and W. E. Moerner. Single photons on demand from a single molecule at room temperature. *Nature*, 407(6803):491–493, September 2000.
- Comment:** 10.1038/35035032
- [Lupascu2006] A. Lupascu, E. F. C. Driessens, L. Roschier, C. J. P. M. Harmans, and J. E. Mooij. High-contrast dispersive readout of a superconducting flux qubit using a nonlinear resonator. *Physical Review Letters*, 96(12):127003, March 2006.
- [Lutchyn2005] R. Lutchyn, L. Glazman, and A. Larkin. Quasiparticle decay rate of josephson charge qubit oscillations. *Physical Review B*, 72(1):014517, July 2005.

- [Lutchyn2006] R. M. Lutchyn, L. I. Glazman, and A. I. Larkin. Kinetics of the superconducting charge qubit in the presence of a quasiparticle. *Physical Review B*, 74(6):064515, August 2006.
- [Lyon2006] S. A. Lyon. Spin-based quantum computing using electrons on liquid helium. *Physical Review A*, 74(5):052338, November 2006.
- [Mabuchi2002] H. Mabuchi and A. C. Doherty. Cavity quantum electrodynamics: Coherence in context. *Science*, 298(5597):1372–1377, November 2002.
- [Maitre1997] X. Matre, E. Hagley, G. Nogues, C. Wunderlich, P. Goy, M. Brune, J. M. Raimond, and S. Haroche. Quantum memory with a single photon in a cavity. *Phys. Rev. Lett.*, 79(4):769–, July 1997.
- [Makhlin2004] Y. Makhlin and A. Shnirman. Dephasing of solid-state qubits at optimal points. *Physical Review Letters*, 92(17):178301, April 2004.
- [Martinis2002] J. M. Martinis, S. Nam, J. Aumentado, and C. Urbina. Rabi oscillations in a large josephson-junction qubit. *Physical Review Letters*, 89(11):117901, September 2002.
- [Martinis2003] J. M. Martinis, S. Nam, J. Aumentado, K. M. Lang, and C. Urbina. Decoherence of a superconducting qubit due to bias noise. *Physical Review B*, 67(9):094510, March 2003.
- [Mazin2002] B. A. Mazin, P. K. Day, H. G. LeDuc, A. Vayonakis, and J. Zmuidzinas. Superconducting kinetic inductance photon detectors. In *Proc. SPIE Vol. 4849*, 2002.
- [Mazin2004] B. Mazin. *Microwave Kinetic Inductance Detectors*. PhD thesis, California Institute of Technology, 2004.
- [McKeever2004] J. McKeever, A. Boca, A. D. Boozer, R. Miller, J. R. Buck, A. Kuzmich, and H. J. Kimble. Deterministic generation of single photons from one atom trapped in a cavity. *Science*, 303(5666):1992–1994, March 2004.

Abstract: A single cesium atom trapped within the mode of an optical cavity is used to generate single photons on demand. The photon wave packets are emitted as a Gaussian beam with temporal profile and repetition rate

controlled by external driving fields. Each generation attempt is inferred to succeed with a probability near unity, whereas the efficiency for creating an unpolarized photon in the total cavity output is $0.69 +/- 0.10$, as limited by passive cavity losses. An average of 1.4×10^4 photons are produced by each trapped atom. These results constitute an important step in quantum information science, for example, toward the realization of distributed quantum networking.

Comment: 10.1126/science.1095232

[Meier2005] F. Meier and D. Loss. Reduced visibility of rabi oscillations in superconducting qubits. *Physical Review B*, 71(9):094519, March 2005.

[Michler2000] P. Michler, A. Imamoglu, M. D. Mason, P. J. Carson, G. F. Strouse, and S. K. Buratto. Quantum correlation among photons from a single quantum dot at room temperature. *Nature*, 406(6799):968–970, August 2000.

Comment: 10.1038/35023100

[Michler2000a] P. Michler, A. Kiraz, C. Becher, W. V. Schoenfeld, P. M. Petroff, Lidong Zhang, E. Hu, and A. Imamoglu. A quantum dot single-photon turnstile device. *Science*, 290(5500):2282–2285, December 2000.

Comment: 10.1126/science.290.5500.2282

[Monroe1995] C. Monroe, D. M. Meekhof, B. E. King, W. M. Itano, and D. J. Wineland. Demonstration of a fundamental quantum logic gate. *Physical Review Letters*, 75(25):4714–4717, December 1995.

[Mooij1999] J. E. Mooij, T. P. Orlando, L. Levitov, L. Tian, C. H. van der Wal, and S. Lloyd. Josephson persistent-current qubit. *Science*, 285(5430):1036–1039, August 1999.

[Moreau2001] E. Moreau, I. Robert, J. M. Gerard, I. Abram, L. Manin, and V. Thierry-Mieg. Single-mode solid-state single photon source based on isolated quantum dots in pillar microcavities. *Appl. Phys. Lett.*, 79(18):2865–2867, October 2001.

- [Nakamura1999] Y. Nakamura, Y. A. Pashkin, and J. S. Tsai. Coherent control of macroscopic quantum states in a single-Cooper-pair box. *Nature*, 398(6730):786–788, April 1999.
- [Nogues1999] G. Nogues, A. Rauschenbeutel, S. Osnaghi, M. Brune, J. M. Raimond, and S. Haroche. Seeing a single photon without destroying it. *Nature*, 400(6741):239–242, July 1999.
- [Ottl2005] A. Ottl, S. Ritter, M. Kohl, and T. Esslinger. Correlations and counting statistics of an atom laser. *Physical Review Letters*, 95(9):090404, August 2005.
- [Peil1999] S. Peil and G. Gabrielse. Observing the quantum limit of an electron cyclotron: QND measurements of quantum jumps between Fock states. *Physical Review Letters*, 83(7):1287–1290, August 1999.
- [Pelton2002] Matthew Pelton, Charles Santori, Jelena Vuckovi, Bingyang Zhang, Glenn S. Solomon, Jocelyn Plant, and Yoshihisa Yamamoto. Efficient source of single photons: A single quantum dot in a micropost microcavity. *Phys. Rev. Lett.*, 89(23):233602–, November 2002.
- [Pobell2006] F. Pobell. *Matter and Methods at Low Temperatures*. Springer, 3 edition, 2006.
- [Pozar1990] David M. Pozar. *Microwave Engineering*. Wiley, 3 edition, 1990.
- [Purcell1946] E. M. Purcell. Spontaneous emission probabilities at radio frequencies. *Physical Review*, 69(11-1):681–681, 1946.
- [Rabl2006] P. Rabl, D. DeMille, J. M. Doyle, M. D. Lukin, R. J. Schoelkopf, and P. Zoller. Hybrid quantum processors: Molecular ensembles as quantum memory for solid state circuits. *Physical Review Letters*, 97(3):033003, July 2006.
- [Raimond2001] J. M. Raimond, M. Brune, and S. Haroche. Manipulating quantum entanglement with atoms and photons in a cavity. *Reviews of Modern Physics*, 73(3):565–582, July 2001.
- [Reithmaier2004] J. P. Reithmaier, G. Sek, A. Löffler, C. Hofmann, S. Kuhn, S. Reitzenstein, L. V. Keldysh, V. D. Kulakovskii, T. L. Reinecke, and A. Forchel. Strong coupling in a single quantum dot-semiconductor microcavity system. *Nature*, 432(7014):197–200, November 2004.

[Rivest1978] R. L. Rivest, A. Shamir, and L. Adleman. A method for obtaining digital signatures and public-key cryptosystems. *Commun. ACM*, 21(2):120–126, 1978.

[Sakurai1994] J. J. Sakurai. *Modern quantum mechanics*. Addison-Wesley, 1994. see Sec. 3. 8.

[Santori2002] Charles Santori, David Fattal, Jelena Vuckovic, Glenn S. Solomon, and Yoshihisa Yamamoto. Indistinguishable photons from a single-photon device. *Nature*, 419(6907):594–597, October 2002.

Comment: 10.1038/nature01086

[Schoelkopf2001] R. J. Schoelkopf, A. A. Clerk, S. M. Girvin, K. W. Lehnert, and M. H. Devoret. *Qubits as Spectrometers of Quantum Noise*. Springer, 2001.

[Schuster2005] D. I. Schuster, A. Wallraff, A. Blais, R. S. Huang, Majer J., S. Girvin, and R. Schoelkopf. AC-Stark shift and dephasing of a superconducting qubit strongly coupled to a cavity field. *Physical Review Letters*, 94:123602, 2005.

[Schuster2007] D. I. Schuster, A. A. Houck, J. A. Schreier, A. Wallraff, J. M. Gambetta, A. Blais, L. Frunzio, B. Johnson, M. H. Devoret, S. M. Girvin, and R. J. Schoelkopf. Resolving photon number states in a superconducting circuit. *Nature*, 2007.

[Shor1994] P. Shor. Algorithms for quantum computation: discrete logarithms and factoring. In *Proceedings of the 35th Annual Symposium on Foundations of Computer Science*, page 124, 1994.

[Siddiqi2004] I. Siddiqi, R. Vijay, F. Pierre, C. M. Wilson, M. Metcalfe, C. Rigetti, L. Frunzio, and M. H. Devoret. RF-driven Josephson bifurcation amplifier for quantum measurement. *Physical Review Letters*, 93(20):207002, November 2004.

[Siddiqi2006] I. Siddiqi, R. Vijay, M. Metcalfe, E. Boaknin, L. Frunzio, R. J. Schoelkopf, and M. H. Devoret. Dispersive measurements of superconducting qubit coherence with a fast latching readout. *Physical Review B*, 73(5):054510, February 2006.

[Simmonds2004] R. W. Simmonds, K. M. Lang, D. A. Hite, S. Nam, D. P. Pappas, and J. M. Martinis. Decoherence in Josephson phase qubits from junction resonators. *Physical Review Letters*, 93(7):077003, August 2004.

- [Simons2002] Rainee N. Simons. *Coplanar Waveguide Circuits, Components, and Systems*. Wiley, 2002.
- [Steffen2006] M. Steffen, M. Ansmann, R. McDermott, N. Katz, R. C. Bialczak, E. Lucero, M. Neeley, E. M. Weig, A. N. Cleland, and J. M. Martinis. State tomography of capacitively shunted phase qubits with high fidelity. *Physical Review Letters*, 97(5):050502, August 2006.
- [Tian2000] L. Tian, L. S. Levitov, C. H. van der Wal, J. E. Mooij, T. P. Orlando, S. Lloyd, C. J. P. M. Harmans, and J. J. Mazo. Decoherence of the superconducting persistent current qubit. In I. Kulik and R. Ellatioglu, editors, *Quantum Mesoscopic Phenomena and Mesoscopic Devices in Microelectronics*, number 559 in NATO Science Series C: Mathematical and Physical Sciences, page 429. Kluwer Academic, Dordrecht, 2000.
- [Tinkham2004] M. Tinkham. *Introduction to Superconductivity*. Dover, 2004.
- [Vahala2003] K. J. Vahala. Optical microcavities. *Nature*, 424(6950):839–846, August 2003.
- [VanHarlingen2004] D. J. Van Harlingen, T. L. Robertson, B. L. T. Plourde, P. A. Reichardt, T. A. Crane, and J. Clarke. Decoherence in josephson-junction qubits due to critical-current fluctuations. *Phys. Rev. B*, 70:064517, 2004.
- [Vion2002] D. Vion, A. Aassime, A. Cottet, P. Joyez, H. Pothier, C. Urbina, D. Esteve, and M. H. Devoret. Manipulating the quantum state of an electrical circuit. *Science*, 296(5569):886–889, May 2002.
- [Wakai1986] R. T. Wakai and D. J. Vanharlingen. Low-frequency noise and discrete charge trapping in small-area tunnel junction dc squids. *Applied Physics Letters*, 49(10):593–595, September 1986.
- [Wallraff2004] A. Wallraff, D. I. Schuster, A. Blais, R.-S. Huang, J. Majer, S. Kumar, S. M. Girvin, and R. Schoelkopf. Circuit quantum electrodynamics: Coherent coupling of a single photon to a Cooper pair box. *Nature*, 431:162, 2004.
- [Wallraff2005] A. Wallraff, D. I. Schuster, A. Blais, L. Frunzio, J. Majer, S. M. Girvin, and R. J. Schoelkopf. Approaching unit visibility for control of a superconducting qubit with dispersive readout. *Physical Review Letters*, 95:060501, 2005.

- [Walls2006] D. F. Walls and G. J. Milburn. *Quantum optics*. Springer, 2006.
- [Wellstood1987] F. C. Wellstood, C. Urbina, and J. Clarke. Low-frequency noise in DC superconducting quantum interference devices below 1-K. *Applied Physics Letters*, 50(12):772–774, March 1987.
- [Widom1984] A. Widom, G. Megaloudis, T. D. Clark, J. E. Mutton, R. J. Prance, and H. Prance. The Josephson pendulum as a nonlinear capacitor. *Journal Of Low Temperature Physics*, 57(5-6):651–658, 1984.
- [Yamamoto2003] T. Yamamoto, Y. A. Pashkin, O. Astafiev, Y. Nakamura, and J. S. Tsai. Demonstration of conditional gate operation using superconducting charge qubits. *Nature*, 425(6961):941–944, October 2003.
- [Yoshida1995] K. Yoshida, K. Watanabe, T. Kisu, and K. Enpuku. Evaluation of magnetic penetration depth and surface-resistance of superconducting thin-films using coplanar waveguides. *IEEE Transactions On Applied Superconductivity*, 5(2):1979–1982, June 1995.
- [Yoshie2004] T. Yoshie, A. Scherer, J. Hendrickson, G. Khitrova, H. M. Gibbs, G. Rupper, C. Ell, O. B. Shchekin, and D. G. Deppe. Vacuum Rabi splitting with a single quantum dot in a photonic crystal nanocavity. *Nature*, 432(7014):200–203, November 2004.
- [Yoshihara2006] F. Yoshihara, K. Harrabi, A. O. Niskanen, Y. Nakamura, and J. S. Tsai. Decoherence of flux qubits due to 1/f flux noise. *Phys. Rev. Lett.*, 97:16001, 2006.
- [Yu2002] Y. Yu, S. Y. Han, X. Chu, S. I. Chu, and Z. Wang. Coherent temporal oscillations of macroscopic quantum states in a Josephson junction. *Science*, 296(5569):889–892, May 2002.
- [Yurke1996] B. Yurke, M. L. Roukes, R. Movshovich, and A. N. Pargellis. A low-noise series-array josephson junction parametric amplifier. *APPLIED PHYSICS LETTERS*, 69(20):3078–3080, November 1996.
- [Zorin1996] A. B. Zorin, F.-J. Ahlers, J. Niemeyer, T. Weimann, H. Wolf, V. A. Krupenin, and S. V. Lotkhov. Background charge noise in metallic single-electron tunneling devices. *Phys. Rev. B*, 53(20):13682–, May 1996.